Phyllosilicates and Sulfates on Mars

Case Studies from Terra Cimmeria and Valles Marineris

Inauguraldissertation zur Erlangung des
Grades eines
Doktors der Naturwissenschaften
am Fachbereich Geowissenschaften der
Freien Universität Berlin

Vorgelegt von
Lorenz Wendt

Berlin, 2012

Ersttgutachter: Prof. Dr. Ralf Jaumann
Fachbereich Geowissenschaften
Institut für Geologische Wissenschaften
Fachrichtung Planetologie und Fernerkundung
und
Deutsches Zentrum für Luft- und Raumfahrt DLR
Institut für Planetenforschung, Abteilung Planetologie
Zweitgutachter: Prof. Dr. Stephan van Gasselt
Freie Universität Berlin
Fachbereich Geowissenschaften
Institut für Geologische Wissenschaften
Fachrichtung Planetologie und Fernerkundung

Datum der Disputation: 13. Juli 2012

Eidesstattliche Erklärung

Hiermit erkläre ich, die vorliegende Arbeit selbständig und nur unter Verwendung der angegebenen Quellen und Hilfsmittel erstellt zu haben.

Lorenz Wendt

Danksagung

Ich möchte zuallererst Herrn Prof. Neukum meinen Dank aussprechen. Seine High Resolution Stereo Camera (HRSC), die er mit viel Durchhaltevermögen nach dem Absturz der Mars 96 Mission auf Mars Express auf die Reise schickte, gab mir überhaupt erst die Möglichkeit, mich an der Freien Universität Berlin mit der Geologie des Mars zu beschäftigen. Herr Prof. Neukum hat mir damit die Tür zur Planetenforschung geöffnet, und mir auch in vielerlei anderer Hinsicht Möglichkeiten zur wissenschaftlichen Weiterentwicklung eröffnet.

Herrn Prof. van Gasselt danke ich für die Begutachtung der vorliegenden Arbeit, die fachlichen Diskussionen und die kritische Durchsicht meiner Manuskripte, sowie die menschliche Unterstützung an manch einem schwierigen Punkt, der sich im Lauf der Arbeit an dieser Dissertation ergab. Und natürlich danke ich ihm für die viele Mühe im Hintergrund, die er sich mit der Betreuung der wissenschaftlichen Anträge gemacht hat, aus denen viele meiner Kollegen und auch ich ihren Lebensunterhalt bestritten haben.

Ich danke Herrn Prof. Jaumann, Herrn Prof. Kaufmann, Herrn Prof. Heubeck und Frau Dr. Sowe für Ihre Rollen als Gutachter der vorliegenden Arbeit.

Ich danke Dr. Jean-Philippe Combe, Dr. Janice Bishop, Dr. Patrick McGuire, Dr. Laetitia Le Deit und Dr. Damien Loizeau für ihre Lehrstunden zum Thema Infrarotspektroskopie. Sie haben mich an dieses komplexe Thema herangeführt und mich auf seine Feinheiten und Fallstricke aufmerksam gemacht. Ich freue mich über die gute Zusammenarbeit und hoffe auf deren Fortsetzung in Zukunft.

Ich danke auch Hern Prof. Tom McCord und seinen Mitarbeitern für zwei interessante Forschungsaufenthalte im "Bear Fight Institute" in den Bergen von Washington. Ebenso bedanke ich mich bei Dr. Ted Roush und seiner Familie und Dr. Giuseppe Marzo für die Zusammenarbeit und freundliche Betreuung bei einem Forschungsaufenthalt am NASA Ames Research Center.

Ich bedanke mich bei Prof. Foing, Prof. Ehrenfreund und ihren Mitarbeitern und Studenten für die vorweggenommene Reise zu unserem Nachbarplaneten. Dies war eine wirklich interessante und inspirierende Erfahrung.

Mein Dank geht an meine Kollegen an der Freien Universität Berlin, insbesondere Herrn Dr. Kneissl, Herrn Gross und Frau Musiol sowie Herrn Walter, Herrn Platz, Herrn Dr. Michael und Frau Balthasar, mit denen ich viel Zeit verbracht habe, um unsere Forschungsergebnisse zu diskutieren, uns gegenseitig auf die Sprünge zu helfen oder uns anderweitig bei Laune zu halten.

Und schließlich bedanke ich mich von Herzen bei Marie Espinasse, die mich auf so viele Weisen auf meinem Weg unterstützt hat.

Abstract

The Martian history has recently been divided into three eras, based on the predominating aqueous sediments formed in them, with a "phyllosian" during the Noachian period, during which relatively warm and wet climatic conditions led to the formation of phyllosilicates, a "theiikian era" in the Hesperian, dominated by sulfate-rich deposits formed during relatively shortlived climatic excursions from an otherwise cold and dry climate caused either by episodes of enhanced volcanic activity or variations of the orbital parameters of Mars, and a "siderikian era" in the Amazonian, in which anhydrous conditions allowed only the anhydrous formation of ferric oxide, giving Mars its red colour.

In this thesis, these hypotheses are tested by investigating phyllosilicate-rich and sulfate-rich deposits in three selected regions of Mars using data from the imaging spectrometers Observatoire pour la Minéralogie, l'Eau, les Glaces et l'Activité (OMEGA) and the Compact Reconnaissance Imaging Spectrometer for Mars (CRISM). Both instruments operate in the visible to short-wave infrared spectrum. The hyperspectral data are analyzed using dedicated software and interpreted together with topographic data and imagery from various sensors combined in a geographical information system.

The study area located between Terra Cimmeria and Terra Sirenum features enigmatic knob fields, comprising Ariadnes Colles, Atlantis Chaos and Gorgonum Chaos. They have previously been mapped as Hesperian or Amazonian units and contain Mg-Fe bearing smectites and locally Al-rich phyllosilicates. This thesis shows that the mounds are erosional remnants of a once contiguous layer, the "Electris deposit", described in previous studies as a fine-grained, possibly glass-rich unit of proposed eolian origin, altered into phyllosilicates. Based on cross-cutting relationships, an upper Noachian age below the Hesperian "ridged plains" unit (Hr) is proposed. A younger, precipitation-fed valley network filled a lake in the Gorgonum basin and small bodies of water in which chlorides formed.

The second and third study investigate sulfate-rich light-toned deposits (LTD) in the Vallis Marineris region (Juventae Chasma and Ophir Chasma), which are partly analyzed using the linear spectral unmixing scheme MELSUM. These deposits are spectrally dominated by kieserite or szomolnokite, which are locally overlain by polyhydrated sulfate deposits as well as jarosite, iron oxides and unidentified phases with absorptions at 2.21 μm or 2.23 μm. Various processes are proposed for the formation of the individual outcrops. The topographic distribution of the deposits in Ophir Mensa is inconsistent with a standing body of water and a formation from evaporating groundwater infiltrated into previously sulfate-free deposits is favored. In contrast, a formation in a lake, playa or under a glacier is consistent with the mineralogy of the central valley of Ophir Chasma and its flat, low-lying topography. The sulfate outcrops on the southern chasm

wall are found on local ridges, which cannot have been reached by groundwater. Here, a water supply from the atmosphere by rain, snow, fog or frost is more conceivable.

The three studies in this thesis confirm the postulated correlation between the types of aqueous mineral formation and the stratigraphic periods observed elsewhere on Mars. The phyllosilicates in the Terra Cimmeria/Terra Sirenum region formed during the Noachian at the surface, indicating a climate that allowed the existence of liquid water. The Hesperian-aged, sulfate-rich deposits in Vallis Marineris are best explained by evaporating groundwater, consistent with their location in zones of groundwater upwelling, as shown by previous researchers. The role of magmatic heating vs. climate variations caused by changes of the orbital parameters remains elusive. Although the groundwater upwelling may have been driven or facilitated by heat induced into the subsurface by volcanic activity, the post-Noachian valley networks in the Terra Cimmeria/Terra Sirenum study area and the jarosite-rich deposits on the walls of Ophir Chasma indicate precipitation and run-off, which cannot be explained by volcanic heating of the subsurface alone but require a regional or global climatic excursion towards higher temperatures, possibly related to variations in the orbital parameters of Mars.

Zusammenfassung

Aktuelle Studien unterteilen die Klimageschichte des Mars anhand der dominierenden, im Zusammenhang mit Wasser gebildeten Sedimente in drei Epochen, das "Phyllosian" während des Noachiums, in der ein wärmeres und feuchteres Klima zur Bildung von Tonmineralen führte, das "Theiikian" im Hesperium, dominiert von sulfathaltigen Ablagerungen, die in kurzen klimatischen Abweichungen von einem überwiegend kalten und hyperariden Klima, ausgelöst entweder durch verstärkte vulkanische Aktivität oder Änderungen der Orbitalparameter des Mars, abgelagert wurden, und das "Siderikian", in dem durch die hyperariden Umweltbedingungen lediglich der eisenoxidreiche rote Staub entstand, der dem Mars seine Farbe gibt.

In diese Doktorarbeit werden diese Hypothesen getestet, indem phyllosilikat- und sulfatreiche Ablagerungen in drei ausgewählten Gebieten anhand von Daten der abbildenden Spektrometer OMEGA und CRISM untersucht werden. Beide Instrumente arbeiten im Bereich des sichtbaren bis kurzwelligen Infrarotspektrum. Die Hyperspektraldaten werden mit verschiedenen Methoden ausgewertet und in Kombination mit Topographie und Bilddaten zahlreicher Kamerasysteme interpretiert.

Im Untersuchungsgebiet zwischen Terra Cimmeria und Terra Sirenum befinden sich die Hügelfelder Ariadnes Colles, Atlantis Chaos und Gorgonum Chaos. Sie wurden in früheren Arbeiten als hesperische oder amazonische Ablagerungen kartiert und enthalten Mg- und Fe-reiche Smektite und untergeordnet Al-reiche Tonminerale. Diese Arbeit zeigt, dass die Hügel Erosionsreste einer ehemals zusammenhängenden Formation waren, dem "Electris deposit", das als feinkörniges, möglicherweise äolisches Sediment beschrieben worden ist, und lokal in Tonminerale umgewandelt wurde. Die Überdeckung durch die ridged-plains-Einheit (Hr) deutet auf ein obernoachisches Alter hin. Ein jüngeres Gewässernetz führte zur Bildung eines Sees im Gorgonum Becken und zur Bildung von Chloridablagerungen.

Die zweite und dritte Studie dieser Doktorarbeit befasst sich mit den hellen Ablagerungen in der Valles Marineris Region (Juventae Chasma und Ophir Chasma), die teilweise mit der Methode der linearen spektralen Entmischung MELSUM untersucht werden. Die Spektren dieser Ablagerungen werden von Kieserit oder Szomolnokit dominiert, die örtlich von polyhydrierten Sulfaten, Jarosit, Eisenoxiden und unbekannten Phasen mit Absorptionen bei 2.21 µm oder 2.23 µm überlagert werden. Für die einzelnen Aufschlüsse werden unterschiedliche Bildungsprozesse vorgeschlagen. Die topographische Verteilung der Sulfate in Ophir Mensa lässt sich nicht durch Evaporation in einem stehenden Gewässer erklären, weshalb die Sulfatbildung aus evaporierendem Grundwasser, das in ein vorher sulfatfreies Gestein eindringt, bevorzugt wird. Im Gegensatz dazu ist die Bildung in einem See, unter einem Gletscher oder in einer Playa für die flachen, niedrig gelegenen Ablagerungen im zentralen Teil von Ophir Chasma denkbar.

Die Sulfate auf der Südwand des Beckens befinden sich auf lokalen Rücken, die nicht durch Grundwasser erreicht worden sein können. Hier ist eine Wasserzufuhr aus der Atmosphäre in der Form von Regen, Schnee, Reif oder Nebel eine mögliche Erklärung.

Die drei Studien dieser Doktorarbeit bestätigen die Korrelation zwischen durch Wasser gebildeten Mineralen und den stratigraphischen Perioden, die auch an anderen Stellen auf dem Mars beobachtet wurde. Die Tone im Gebiet zwischen Terra Cimmeria und Terra Sirenum wurden im oberen Noachium an der Oberfläche gebildet und deuten daher auf ein wärmeres und feuchteres Klima zu dieser Zeit hin. Die hesperischen, sulfatreichen Gesteine in Valles Marineris sind am besten durch die Verdunstung von Grundwasser zu erklären. Dies passt zu anderen Studien, die diese Gebiete als Grundwasseraufstiegszonen ausweisen. Die Rolle von magmatischen Wärmequellen im Gegensatz zu Klimaschwankungen durch Änderungen der Orbitalparameter ist weiterhin ungeklärt. Auch wenn der Grundwasseraufstieg durch magmatische Aktivität angetrieben oder begünstigt worden sein könnte, sind die post-noachischen Flussnetze im Terra Cimmeria/Terra Sirenum Gebiet und die jarositreichen Ablagerungen auf der Südwand von Ophir Chasma deutliche Hinweise auf Niederschlag und Oberflächenabfluss, die nicht durch magmatische Erwärmung des Untergrundes allein erklärt werden können, sondern ein wärmeres regionales oder globales Klima erfordern, möglicherweise im Zusammenhang mit variierenden Orbitalparameter des Mars.

Contents

List of Figures

1 Introduction

1.1 Motivation

Mars must once have sustained a warmer and wetter climate than today's cold and hyperarid conditions. This has been known from various morphological features on the surface, including valley networks, outflow channels, rampart craters and possible shorelines. These features have been known since the first global imagery of the Martian surface had been gathered by Mariner 9 in 1972. More specifically, the analysis of valley network types and -densities indicated that in the oldest, Noachian aged regions of Mars, the climate must have been clement enough to allow liquid water to form precipitation and run-off (e.g., Carr, 1983). Remarkably, until less than one decade ago, the Martian rock record appeared to be mostly unaffected by this. Investigations by the Viking Landers from 1976 on pointed towards a high content of sulfate in the Martian soil and the presence of phyllosilicates appeared possible (Toulmin *et al.*, 1977), yet the emerging picture drawn by Christensen and Kieffer, 2003 based on data from a thermal emission spectrometer showed the Martian surface to be mainly basaltic, dominated by pyroxene- and olivine rich rocks, which showed no sign of aqueous alteration. Only a few, isolated spots in Valles Marineris and in Meridiani Planum displayed gray hematite as chemical evidence for water-related alteration processes.

This view changed dramatically with the arrival of a new type of sensors in the orbit of Mars. The Observatoire pour la Minéralogie, l'Eau, les Glaces et l'Activité OMEGA onboard ESA's Mars Express spacecraft, an imaging spectrometer operating in the wavelength range of 0.38 to 5.1 µm, investigates the Martian surface since 2004 and has detected a variety of mineral alteration assemblages, including phyllosilicates and sulfates, but no carbonates (e.g., Bibring *et al.*, 2005). These findings were confirmed and refined by data from the Compact Reconnaissance Imaging Spectrometer for Mars CRISM, a similar instrument with a higher spatial and spectral resolution compared to OMEGA on NASA's Mars Reconnaissance Orbiter (MRO), in orbit around Mars since 2006. Several hundreds to thousands of location have since been identified, which contain either hydrated phyllosilicates or hydrated sulfates, and also other water-related minerals like zeolites, hydrated silica and iron oxides and oxyhydroxides have been found.

The presence of these aqueous minerals appears to correlate with the three geological periods defined previously based on geological mapping and cratersize-frequency relationships. Phyllosilicates have been found exclusively in the oldest, Noachian aged regions of Mars, sulfates are believed to have formed only in the Hesperian period, and only anhydrous ferric oxides in the youngest Amazonian period (Bibring *et al.*, 2006, Ehlmann *et al.*, 2011, Murchie *et al.*, 2009b).

This model allows to create a link between morphological markers for the water activity and the mineralogy, and indicates a warmer and wetter Mars in the Noachian sustaining liquid water long enough and at intermediate pH conditions to form clay minerals, a dry Mars with sporadic, short-lived events during which sulfates formed under acidic conditions in the Hesperian, and a mainly cold and hyperarid Mars during the Amazonian. Apart from the rare aqueous events in the Hesperian, which might have been triggered by

massive volcanic eruptions as proposed by Neukum *et al.*, 2010, and possible climate excursions caused by changes in the orbital parameters of Mars (Laskar *et al.*, 2004), the climate was cold and hyperarid similar to today since the end of the Noachian.

However, many questions remain open: Is the mineralogical record indeed as strongly correlated to the geological periods as claimed? What has caused the "warmer and wetter" climate in the Noachian? A strong greenhouse effect caused by CO_2 outgassing apparently was not responsible, as in this case massive carbonate deposits would be expected, which are not found. What is the exact timing of valley networks as morphological climate markers and phyllosilicate formation? Dendritic, connected valley networks, indicative for precipitation and run-off on the surface, appear to become widespread only in the late Noachian (Carr, 1995, Hynek *et al.*, 2010), when the atmosphere was declining, while some of the phyllosilicates appear to be older. Are they formed in the subsurface, by hydrothermal activity secluded from the atmosphere, as proposed by Ehlmann *et al.*, 2011?

This thesis tries to find answers to some of these questions by investigating phyllosilicate bearing deposits in the Terra Cimmeria/Terra Sirenum region of Mars as a case study. The region was selected, because these clay-bearing deposits have been mapped as Hesperian to Amazonian-aged units (Greeley and Guest, 1987, Scott and Tanaka, 1986), pointing to phyllosilicate formation after the Noachian. Data from CRISM is used together with multispectral and panchromatic imagery combined in a geographical information system (GIS) to provide an integrated view of the mineralogy, stratigraphy and morphology of the deposits in order to constrain their age relationship to surrounding units, and to investigate the facies in which they have formed, in order to conclude on the climatic at the time of their deposition. The study area is also very interesting with respect to the aqueous history after the Noachian, as precipitation-fed valley networks (Howard and Moore, 2011), lakes and chloride deposits (Osterloo *et al.*, 2010) suggest a more complex evolution than anticipated.

Similar questions arise for the Hesperian period, in which the bulk of the sulfates on Mars is believed to have formed. The best investigated sulfate-bearing deposits are those in Terra Meridiani, analyzed in situ by the Mars Exploration Rover "Opportunity" since 2004. This deposit is believed to have formed in a playa or interdune setting from sulfate-rich sand grains cemented by precipitation of sulfates from ground water (McLennan *et al.*, 2005). Is this formation model comparable to the massive, several-km-thick sulfate-bearing "Interior Layered Deposits" (ILD) within the canyons of Valles Marineris (e.g., Gendrin *et al.*, 2005b)? Or were the canyons once filled with water, which evaporated to leave the deposits behind? Did the deposits form by a single event or a succession of events? Are the types of minerals indicative for specific formation processes? Do dip anle and dip direction of layers in the deposits, measured in digital elevation models, give further clues on their formation environment? This study addresses these questions by analyzing the ILDs within Ophir Chasma, the northernmost canyon of the central part of Valles Marineris, in detail based on hyperspectral data from OMEGA and CRISM and imagery in various scales, integrated in a GIS.

While hyperspectral data are an invaluable source of information, allowing the identification of mineral types from remote sensing platforms hundreds of kilometers from the target, its interpretation is also a technical challenge. The

possession of such a wealth of information fosters the idea of automatic mineral mapping, which does not require human interaction. The full exploitation of hyperspectral data by automated or semi-interactive algorithms is an active field of science, and hundreds of methods have been published in the recent years (an overview is given by Kaufmann *et al.*, 2009). This study exploits the potential of a linear unmixing scheme, MELSUM (Combe *et al.*, 2008b) for the investigation of sulfate-bearing deposits in Juventae Chasma. These deposits are comparable to the ILDs in Ophir Chasma. The analysis of their composition provides further evidence on the origin of these enigmatic deposits.

1.2 Organization of this thesis

This thesis is organized in 5 chapters, which are bracketed by this introduction and final summary and conclusions. It contains parts that have already been published as stand-alone articles. Therefore, they contain individual introductory sections and conclusions. Chapter 2 provides a concise overview of the exploration of Mars since the beginning of the space age. This focus on the datasets provided by the various space missions occurs early in this thesis because it allows an estimation of not only what kind of observations have been done to investigate Mars, but also what the limits of these datasets are, and thus of our knowledge of Mars. Chapter 2 also gives a short insight to the mineralogical record collected on Mars, as well as its climatic evolution arising from these investigations, and points to the most important open questions.

Chapter 3 gives an introduction to hyperspectral remote sensing using reflectance spectroscopy. The origin of the observed absorption features, their location in the spectra of the detectable classes of minerals and the difficulties arising when comparing spectra measured in a laboratory and spectra measured from a remote sensing platform are introduced. The chapter also contains a description of the processing steps applied to the data of OMEGA and CRISM.

The stratigraphy and mineralogy of the phyllosilicate-bearing deposits in the Terra Cimmeria/Terra Sirenum region are addressed in chapter 4. This chapter has been submitted to the journal *Icarus* for publication. The concept, data analysis, and the preparation of the manuscript and the figures have been carried out by the author of this thesis. Results, especially those of the hyperspectral investigations, have been discussed with the co-authors.

The subject of chapter 5 is the regional study of the sulfate deposits in Juventae Chasma using linear unmixing. The concept, the data collection, processing, analysis and the writing of the manuscript and preparation of the figures have been done by the author of this thesis. Spectral analysis results and issues regarding the specific behavior of the applied linear unmixing algorithm and their implications were discussed with the co-authors. The chapter was published as "Linear spectral unmixing of near-infrared hyperspectral data from Juventae Chasma, Mars (Wendt *et al.*, 2009) in "Image and Signal Processing for Remote Sensing XV - Proceedings of SPIE Vol. 7477".

Chapter 6 deals with the stratigraphy and mineralogy of the sulfate deposits in Ophir Chasma. It has been published as "Sulfates and iron oxides in Ophir Chasma, Mars, based on OMEGA and CRISM observations" (Wendt *et al.*, 2011) in *Icarus*. In this study, the concept, the data assemblage, data processing and data analysis have been carried out by me, and the text and figures have been prepared by myself. The

results of various aspects of this study, for example the layer measurements and the spectral analysis, have been discussed with the co-authors.

Each chapter ends with conclusions. Summarizing and overarching concluding remarks are presented in chapter 7.

2 Background

2.1 Spacecraft Exploration of Mars: Missions and their Datasets

The past 47 years of Mars exploration using planetary spacecrafts and landers since the first successful fly-by of a space probe by Mariner 4 in 1962 have created a wealth of different datasets that are at hand for the researcher studying Mars. This makes it worthwhile to get an overview of the past and current Mars missions. The chapter is not intended as a complete review of the history of Mars exploration, which may be found up to the nineties in Snyder and Moroz, 1992, but rather to provide an insight to the various produced datasets and their advantages and limitations, before the next chapter 2.2 will describe the modern view of Mars in a very concise manner, with special emphasis on its mineralogy. Although the mentioned space missions carried a large number of different instruments designed for the study of different aspects of Mars, the following chapters will focus mostly on imagery and spectroscopic data, as these types of data have been used for the research of this study.

2.1.1 The pre-Viking era

The exploration of Mars by spacecraft began with the first launch of a probe designed to travel to Mars in the USSR in 1960. The mission failed, as did many of the following (at least 20) attempts during the "Space Race" between the USA and the USSR before the Viking missions in 1975 (Snyder and Moroz, 1992). The first few images of Mars taken from a spacecraft were transmitted by Mariner 4 in 1965. With an image resolution of approximately 1 km/pixel and a coverage of only 1% of the Martian surface, the main observed features on the surface were impact craters, suggesting a generally "moonlike" surface on Mars. The following unsuccessful or only partly successful fly-bys and landing attempts of both the USA and the USSR provided some new information on the Martian orbital parameters, atmosphere, magnetic field and solar wind interaction, but the overall picture of the Martian surface features remained more or less unchanged until the first successful orbiter mission of Mariner 9 in 1972. It provided a full coverage of the Martian surface at a resolution of 50-500 m/pixel. This allowed the identification of the major surface features of Mars, including the dichotomy boundary, Olympus Mons and the Tharsis bulge, Valles Marineris, outflow channels, and tectonic features like grabens and faults (Snyder and Moroz, 1992).

2.1.2 Viking

The Viking program consisted of two identical orbiters and two landers. They were launched in summer 1975. The landers contained panoramic cameras and several instruments to characterize the physical properties and composition of the Martian soil and atmosphere, and also included experiments to search for signs of organic matter and living microorganisms, which were not detected. The Viking 1 lander operated for more than six years and the Viking 2 lander for more than three and a half years.

The most important instruments of the orbiters were video cameras to map the surface, but they also carried instruments to analyze the composition and structure of the Martian atmosphere. The two cameras on each of the

orbiters were vidicon framing cameras with a focal length of 475 mm and were equipped with a filter wheel, allowing them to take images in one of five bands in the visible spectrum, if desired. Depending on the orbit of the spacecraft, the resolution of the produced images ranged from 7 to 1400 m/pixel, with most images being higher resolved than 100 m/pixel, and the surface of Mars was fully covered (Flinn *et al.*, 1977). This was a great improvement to the camera system of Mariner 9. The USGS produced the global mosaic Mars Digital Image Model MDIM with a nominal spatial resolution of 231 m/pixel at the equator (256 pixels/degree) from this imagery, which remained the best global image dataset of the surface of Mars until the renaissance of Mars exploration in the mid-nineties of the last century. The latest version of MDIM, which fixed some misalignments of images and internal inaccuracies caused by inaccurate orientation data of the Viking spacecrafts, was released in 2005 as version MDIM 2.1, when a new network of reference points based on MOLA (see below) was available. The image mosaic is in grayscale. The individual images were taken under various lighting conditions and observation angles. To adapt the images to each other, regional albedo differences where filtered out to emphasize topographic features resulting in shading rather than surface albedo variations (Kirk *et al.*, 2000).

2.1.3 Mars Global Surveyor MGS

The next successful spacecraft to study Mars or its moons after the Viking missions was Mars Global Surveyor. It was launched towards Mars in 1996. It carried three instruments that greatly improved the view of Mars and the composition of its surface, which were the Mars Orbiter Camera (MOC; Malin and Edgett, 2001), the Mars Orbiter Laser Altimeter (MOLA; Smith *et al.*, 2001) and the Thermal Emission Spectrometer (TES; Christensen *et al.*, 2001a). MGS orbited Mars on a circular, sun-synchronous orbit with an altitude of 378 km above the surface.

In November 2006, a chain reaction to an erroneous command to the spacecraft sent a few months before caused one of the spacecraft's batteries to overheat, which resulted in the loss of the spacecraft (NASA, 2007).

2.1.3.1 Mars Orbiter Camera MOC

This camera was first developed for the Mars Observer mission, which started in 1992. After the loss of the spacecraft shortly before orbit insertion in 1993, a new MOC was built from spare hardware for the following Mars Surveyor mission, now under the name Mars Orbiter Camera (Malin *et al.*, 2010). The camera consisted of three push-broom instruments, a narrow angle camera (MOC-NA) and two wide angle cameras (MOC-WA), one with a red and one with a blue filter, and common control and storage devices. The narrow angle camera MOC-NA had a field of view of 0.4° and a focal length of 3.5 m. It acquired panchromatic images with a resolution of up to 1.4 m/pixel, although most images had a resolution of 2 to 5 m/pixel. The image footprints were approximately 3 km wide from the nominal orbit of the spacecraft of 378 km above the surface.

The wide angle cameras had a field of view of 140° to image the entire planet daily in order to investigate transient phenomena especially in the Martian atmosphere, such as cloud movements. The ground resolution of MOC-WA was between 0.24 km/pixel at nadir and 1.5 km/pixel at the limbs (Malin *et al.*, 2010).

At the time of the loss of the spacecraft in November 2006, the MOC-NA camera had taken

97097 individual images, which covered 5.45% of surface of Mars. This allowed the construction of image mosaics in several locations of Mars, but in many regions, the individual MOC images did not overlap, and the step in resolution between up to 1.4 m/pixels of MOC-NA and several tens to hundreds of m/pixel of Viking and MOC-WA imagery was large. This made the mapping of medium-scale features beyond individual MOC-NA images difficult, especially due to the relatively low cross-track extent of the images of only 3 km.

2.1.3.2 Mars Orbiter Laser Altimeter MOLA

The Mars Orbiter Laser Altimeter MOLA was designed to send laser pulses at a rate of 10 Hz from the spacecraft to the ground to deduce the surface topography from the two-way-travel time between the spacecraft and the ground. Unlike modern airborne LIDAR systems, which scan in a swath below the aircraft, MOLA measured only in the nadir direction (Smith *et al.*, 2001). It operated between September 1999 and June 2001, when a critical component failure turned the instrument inoperative.

MOLA covered the entire planet between -87° and +87° latitude. The theoretical vertical accuracy of the instrument was 37.5 cm, but uncertainties in the spacecraft's orbit reduced it to 1 m over flat areas (slope < 2°). The footprint of the laser point on the surface of Mars had a diameter of 168 m. The 10 Hz pulse frequency of the laser lead to a spacing of 300 m between the shots along-track. The across-track spacing was lowest in the polar region and reached 4 km at the equator. Over 9500 profiles of the Martian surface were produced. They were interpolated to a gridded digital elevation model with a resolution of 128 pixels/degree for the sub-polar regions of Mars. This equals a post spacing of approx. 460 m in an equirectangular projection. For the polar regions, DEMs with up to 512 pixels/degree were produced (Smith *et al.*, 2003). This data compose the first global digital elevation model of Mars, and have been the basis of uncounted studies of the Martian surface. It is also the reference frame for higher resolved DEMs derived from

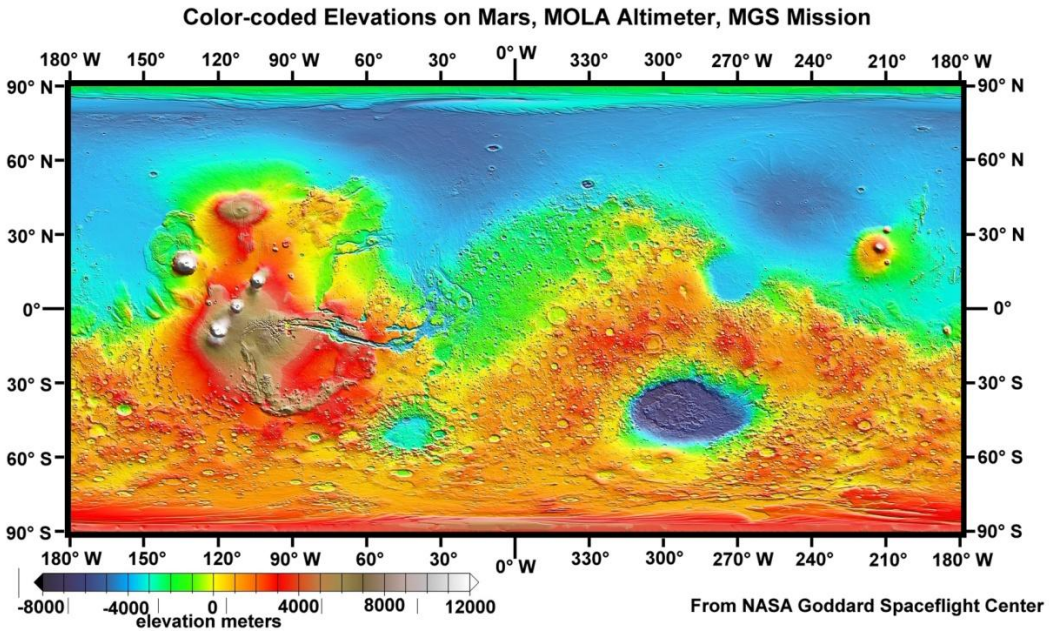

Fig. 2.1: shaded, color-coded MOLA relief.

stereoscopic data from the High Resolution Stereo Camera HRSC (see below) and other optical systems. Due to the relatively high point spacing across-track close to the equator, the interpolated dataset contains interpolation errors and smoothing of terrain features. Especially narrow and elongated features such as canyon walls and faults are deformed as they cross areas with gaps in the MOLA data record.

2.1.3.3 Thermal Emission Spectrometer TES

The Thermal Emission Spectrometer TES is a hyperspectral sensor operating in the thermal infrared wavelength range between 5 and 50 microns. It consists of an array of 3 by 2 sensors, which covered in the mapping orbit of MGS a footprint of 3 by 8 km each. The purpose of TES was to examine the composition of the Martian surface minerals, the ices, the atmosphere and the dust particles therein. TES also allowed the determination of particle sizes of sediments and dust by estimating their thermophysical properties (Christensen *et al.*, 2001a).

In the thermal infrared, all matter that is warmer than 0° K emits radiation. The wavelength of the maximum radiation can be used to determine the temperature of the object. The spectrum of the thermal emission depends on its temperature and its composition, as different minerals and molecules show absorption bands or deviations from an ideal blackbody radiator, which are specific for that particular material. By calculating the ratio of the measured spectrum and the radiation of a blackbody at the same temperature, an emissivity spectrum is obtained. This spectrum can then be compared to laboratory spectra of known minerals.

Due to the large footprint of the TES pixel, the measured spectra are always mixed spectra of different rock forming minerals on the ground, plus a contribution from the Martian atmosphere. The measured spectrum can, in the thermal infrared, be regarded as a linear combination of the spectra of the different surface minerals, weighted by their relative areal coverage of the ground. Adams *et al.*, 1986, Ramsey and Christensen, 1998). Consequently, a major outcome of the TES experiment are maps at the km scale that display the relative abundance of the main constituents of the Martian surface rocks, which are mainly mafic and contain feldspar, pyroxene, and olivine. TES identified two different compositions of Martian volcanic rocks, a "surface type 1" corresponding to plagioclase- and clinopyroxene-rich basalts, and a "surface type 2" corresponding to more evolved andesites or basaltic andesites. The transition between the units is at the dichotomy boundary (Rogers *et al.*, 2007). TES also identified grey hematite in Meridiani Planum and some of the canyons of Valles Marineris, Ophir Chasma, Candor Chasma and Aram Chaos (Christensen *et al.*, 2000, Weitz *et al.*, 2008). Another important TES product is a map of the thermal inertia of the Martian surface materials by comparing daytime and nighttime temperatures (Putzig *et al.*, 2005). The thermal inertia is correlated with the grain size and degree of consolidation, with more compact sediments displaying a higher thermal inertia. This can also be used to determine the degree of dust coverage in a region of Mars. This is used in section 6 on the light-toned deposits in Ophir Chasma.

2.1.4 Mars Pathfinder

The Mars Pathfinder mission was launched shortly after Mars Global Surveyor in December 1996 and reached Mars in July 1997. The mission consisted of a stationary lander, later named Sagan Memorial Station, and a small (~10 kg) roving probe, named Sojourner. Pathfinder

measured atmospheric profiles during its descent before landing in the mouth of Ares Valles at 193°N, 326°E. This landing site was chosen because it was expected to find a wide range of different rock types transported to this location by the Ares Vallis outflow event(s), which would be accessible for investigation by the rover within its relatively small radius of operation. The landing site is characterized by rounded and semirounded pebbles, cobbles and boulders deposited by floods. They were later modified by eolian activity.

Pathfinder operated for 82 Martian days, during which the rover traversed 52 m. It was equipped with an Alpha Proton X-ray Spectrometer (APXS) and panchromatic and color cameras. While being in part a technological demonstrator, Sojourner examined the composition of ten rock samples. The investigated rocks had an andesitic to basaltic composition, indicating a certain degree of differentiation from mantle-derived magmas, but did not display the variety of rock types hoped for (Golombek *et al.*, 1997).

2.1.5 Mars Odyssey

The Mars Odyssey spacecraft was launched in 2001 and is still in operation. As MGS, it is in a near-polar, sun-synchronous orbit at an elevation of 390 km. It carries a camera, named Thermal Emission Imaging System (THEMIS), a gamma ray spectrometer (GRS) plus a radiation measurement package (MARIE; Saunders *et al.*, 2004).

2.1.5.1 Thermal Emission Imaging System THEMIS

THEMIS is a combination of two multispectral push-broom cameras. THEMIS-VIS captures images through five narrowband filters in the visible spectrum (425±25, 540±25 654±25, 749±25 and 860±25 nm) at a ground resolution of 18, 36 or 72 m/pixel. Its purpose is to bridge the gap between the higher resolved MOC-NA images and the lower resolved Viking and MOC-WA data. The individual footprints are approximately 20 km wide (cross-track). The length of the individual image strips (along-track) is limited by the size of the internal data storage of 3.8 Mb, and therefore a trade-off has to be made between pixel binning, number of channels and image strip length. A fully resolved image at all five channels uses the entire storage after the acquisition of only 10 km of image (Christensen *et al.*, 2004a, McConnochie *et al.*, 2006). Therefore, of the ~162.000 images recorded until November 2011 (Mars Image Explorer website, 2011), only 11.000 or 6.8% were recorded with more than one band (own query, 2011). THEMIS-VIS has, however, imaged almost the entire surface of Mars at a resolution of 100 m with one band only. In the studies of this thesis, THEMIS-VIS data have not been used, because imagery of the High Resolution Stereo Camera (HRSC; see below) with a comparable resolution has been preferred. The individual HRSC strips cover larger areas, which makes the data handling for a regional study easier, and they are usually multispectral.

THEMIS-IR is a separate multispectral sensor with 9 different bands between 6.5 and 15 µm. Its ground resolution is 100 m. It is designed to complement the hyperspectral instrument TES in the assessment of the Martian surface mineralogy with its increased spatial resolution and its multispectral capability in the same wavelength range. Its purpose is also to provide night-time infrared imagery, in which the brightness of the surface is correlated to its thermal inertia.

2.1.5.2 Gamma Ray Spectrometer GRS

The Gamma Ray Spectrometer GRS consists of three instruments, the Gamma Subsystem (GSS), the Neutron Spectrometer (NS) and the High-Energy Neutron Detector (HEND). These instruments are designed to detect gamma rays that are emitted from the uppermost parts of the Martian surface, as its atoms are excited by cosmic rays (Saunders *et al.*, 2004). The cosmic rays can penetrate the subsurface up to a depth of approximately one meter. The measured gamma rays are used to calculate the elemental composition of the Martian surface with an accuracy of 10%, as well as the presence of hydrogen, which is taken as a proxy for subsurface water ice. The GRS suite receives gamma rays from the entire planetary surface underneath the Mars Odyssey spacecraft, the spatial resolution therefore is only 600 km. Data of the GRS has helped define the modern view of Mars, which is presented in chapter 0. It has not been used directly in the studies of this thesis.

2.1.6 The Mars Exploration Rover Mission (MER)

The Mars Exploration Rovers were launched in summer 2003 and arrived at Mars in early 2004. The mission consists of two identical, six-wheeled rovers, MER-A "Spirit" and MER-B "Opportunity". They are each 1.6 m long and weigh 185 kg. Each carries a panoramic camera with filter wheels (PanCam) and a thermal emission spectrometer (Mini-TES) on a mast and a Mössbauer spectrometer (MIMOS), an Alpha Particle X-ray spectrometer (APXS) and a microscopic imager on a robotic arm, which also carries a tool to grind off weathering rinds from rocks, named Rock Abrasion Tool (RAT; Crisp *et al.*, 2003).

The landing site of MER-A "Spirit" is Gusev crater, an impact crater with a diameter of 166 km near the highland-lowland boundary of Mars. It was selected, because the Ma'adim Vallis valley enters the crater and probably formed a lake (Golombek *et al.*, 2003). Most of the rocks analyzed by "Spirit" are of volcanic origin. They cover the floor of the crater and the putative lake sediments in it. Therefore, the rover was guided to a group of hills named Columbia hills, where veins and void-filling materials as signs of hydrothermal alteration were identified (Arvidson *et al.*, 2006). Spirit got stuck in a sand trap in early 2009, and all attempts to free it remained unsuccessful. The rover was not in a suitable position to gather enough solar energy to charge its batteries, so eventually, radio contact was lost in early 2010 and could not be reestablished (JPL, 2011).

MER-B "Opportunity" landed in Meridiani Planum, a relatively flat region east of Chryse Planitia. The landing site was chosen, because data from the Thermal Emission Spectrometer TES on Mars Global Surveyor indicated the presence of crystalline, grey hematite at this location (Christensen *et al.*, 1998) which is formed by liquid water. The major findings of this mission are introduced in more detail in section 2.2.2. The rover is still operational.

2.1.7 Mars Express

After the loss of the Russian Mars 96 mission shortly after launch in November 1996, the European Space Agency set up the Mars Express (MEX) mission as a recovery to carry the flight spare models of the European instruments that were on the failed Russian mission. Mars Express was launched in June 2003 and reached Mars in December 2003 and is still operational. Mars Express carries eight different instruments.

Among them are the High Resolution Stereo Camera HRSC, the Observatoire pour la Minéralogie, l'Eau, les Glaces et l'Activité OMEGA, the subsurface sounding radar (MARSIS) and spectrometer for the investigation of the Atmosphere (SPICAM and PFS). To meet the competing requirements of these instruments, Mars Express is on a highly elliptical orbit with a periapsis of 270 km and an apoapsis of ~10.000 km. Consequently, the orbit is not sun-synchronous, and highly resolved mapping operations of the surface by HRSC and OMEGA are only possible near the pericenter.

The Mars Express mission also included the lander "Beagle 2". Contact to it was lost during its descent through the atmosphere (Chicarro *et al.*, 2004).

2.1.7.1 The High Resolution Stereo Camera HRSC

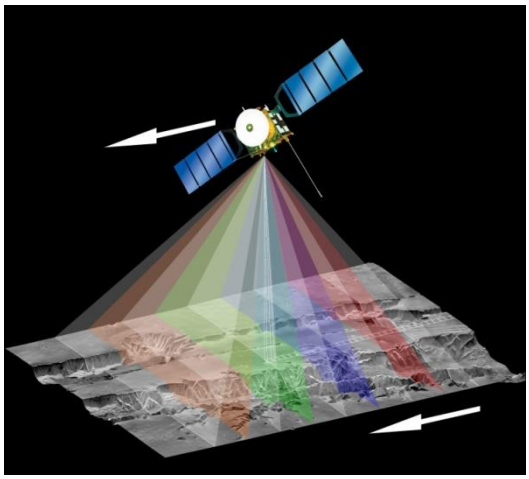

Fig. 2.2: working principle of the HRSC. From Neukum und Jaumann, 2004.

The High Resolution Stereo Camera HRSC consists of nine CCD line scanners with 5184 pixels behind a common optics with 175 mm focal length. The CCD lines operate in the push-broom principle and image the surface at different viewing angles between -18.9° and +18.9° forward and aft with respect to the nadir direction. Five of the nine scanners or "channels" (including the nadir channel) operate in the same broadband wavelength range of 675±90 nm, four channels are equipped with color bandpass filters in the blue (440±45 nm), green (530±45 nm), far-red (750±20 nm) and infrared (970±45 nm) wavelength range.

With this design, the surface of Mars is imaged simultaneously at different viewing angles, resulting in a five-fold stereo coverage by only one fly-over. This allows the systematic calculation of stereoscopic digital elevation models of the surface of Mars. The viewing geometry was also chosen to derive surface roughness estimations from the surface phase function measured at different angles. Therefore, two of the panchromatic channels were named "photometric channels" (Neukum and Jaumann, 2004).

The camera is operated only near periapsis, where the ground resolution reaches up to 10 m/pixel (at 250 km orbit height). In most observations, only the nadir channel is operated at full resolution, whereas in the color, photometric and stereo channels the resolution is degraded by a factor of two, four or eight to reduce the required transmission volume. The image footprints are approx. 50 km wide at the highest resolution. The length of the image strips is virtually unconstrained and can reach up to 4000 km.

The HRSC also carries a panchromatic frame camera with 975 mm focal length, the Super Resolution Channel SRC. Its images are nested within the nadir channel images. The SRC was designed to produce images with a resolution of 2.3 m/pixel, but a thermal distortion of the camera's optics results in a degraded image quality. Various efforts have been made in the

HRSC science team to improve the sharpness of the images (Michael and Neukum, 2009).

All data are compressed onboard with a lossy compression scheme prior to transmission to Earth. This can lead to compression artifacts that form a blocky texture in the images, especially in the color data (McCord *et al.*, 2007).

Digital elevation models (DTM) with a ground resolution of 200 m per pixel are systematically produced for all HRSC observations, using MOLA as a reference frame. Multispectral orthoimages are then produced as level 4 data products with post spacings of 12.5 m, 25 m or 50 m by projecting the image data on these DTMs (Gwinner *et al.*, 2009). The production of DTMs with resolutions of up to 50 m/pixel requires human interaction. They are produced in the HRSC science team. Imagery and DTMs are mosaiced together by bundle-block adjustment to produce quadrangle maps of Mars (Dumke *et al.*, 2010). To date (Oct. 2011), orthoimages with a resolution of 25 m/pixel or better have been produced for approx. 88% of the Martian surface. For 55% of the surface, images with a resolution better than 15 m/pixel are available (own query).

In summary, the high resolution in the order of 10 to 15 m/pixel over large image footprints, the availability of digital elevation models and color data for almost every HRSC image are the advantages of this dataset, whereas the varying illumination and atmospheric conditions of adjacent strips due to the non-sun-synchronous orbit of Mars Express are drawbacks for some applications.

2.1.7.2 The Observatoire pour la Minéralogie, l'Eau, les Glaces et l'Activité OMEGA

The Observatoire pour la Minéralogie, l'Eau, les Glaces et l'Activité OMEGA is a mapping spectrometer that measures spectra in the visible to short-wave infrared between 0.38 and 5.1 µm in 352 contiguous channels (Bibring *et al.*, 2004). Spectrometers in this wavelength range register mostly reflected sunlight. This is an advantage over spectrometers measuring emitted thermal infrared radiation, as the received signal is much stronger, allowing a higher spatial resolution. The disadvantage is that only a few minerals, including iron-bearing minerals and water-rich minerals like sulfates and phyllosilicates are active in this wavelength range, whereas important rock-forming minerals like quartz and feldspar are spectrally bland. A more detailed introduction to reflectance spectroscopy and the detectable minerals is given in chapter 3.2.

The instrument consists of two co-aligned systems, one working in the visible and near infrared (VNIR, 0.38 to 1.05 µm, named), and the other in the SWIR, (0.93 to 5.1 µm). The VNIR channel is operated in push-broom mode. One cross-track line is imaged at once over the entire field of view (FOV) of 8.8°. The line is spectrally dispersed by a grating on a CCD array, on which one direction represents the cross-track dimension and the other one the spectral dimension. The SWIR channel operates in whiskbroom mode. A moving scanning mirror controls the viewing direction from one side to the other, while each spectrum is recorded by the same detector line. The instantaneous field of view (IFOV) of the detector is 1.2 mrad, the entire FOV corresponds to 128 IFOV. The detected beam is collimated and then split by a dichroic filter on two separate spectrometers in the spectral ranges from 0.93 to 2.73 µm and 2.55 to 5.1 µm. The spectral resolution is 7 nm in the visible and 20 nm in the SWIR range.

OMEGA observes Mars globally from altitudes of 1500-4000 km above the surface as well as locally

close to periapsis. The swath width of the OMEGA observations is adapted to compensate the differences in spacecraft velocity on its elliptical orbit. At periapsis, the nadir track moves at a velocity of~ 4 km/s by one IFOV in only 100 ms. The nominal integration time is 5 ms, resulting in a swath width of 16 pixels. The resolution at periapsis is in the order of 350 m/pixel. At orbit heights between 350-700 km, OMEGA is set to acquire 32-pixel-wide strips. 64 pixel wide image strips are chosen at altitudes up to 1500 km. At higher elevations, OMEGA uses its entire 128 pixel wide field of view. In the study on Ophir Chasma (chapter 6), mostly data acquired in the 32-pixel-mode were used, because they provide a reasonably high resolution of ~700 km per pixel, a coverage of the planet of 15%, and a coregistration of spectral data and imagery is much easier than using the highest resolved, but only 16 pixel wide strips. In the 64- and 128-pixel modes, a global coverage has been reached. These data have a spatial resolution between 2 and 4 km.

2.1.8 Mars Reconnaissance Orbiter MRO

The Mars Reconnaissance Orbiter (MRO) is the latest spacecraft in orbit around Mars. It reached Mars in March 2006 and is still operational. MRO is on a near-circular, sun-synchronous orbit at an altitude between 250 and 316 km above the surface. It carries six instruments: a camera with very high resolution (HiRISE), a camera with a high resolution, providing context for the HiRISE images (CTX), a wide-angle, low-resolution camera for daily global maps in seven channels in the ultraviolet and visible range (MARCI), a VNIR-SWIR hyperspectral imager similar to OMEGA (CRISM), a low-spatial-resolution VNIR and thermal IR spectrometer for weather observations (MCS), and a ground-penetrating radar to map mainly the layering in the ice-rich polar deposits (SHARAD, similar to MARSIS; Zurek and Smrekar, 2007). The instruments HiRISE, CTX and CRISM will be introduced in the next chapters, as data from these instruments have been used extensively in this study.

2.1.8.1 The High Resolution Imaging Science Experiment (HiRISE)

The HiRISE camera is a mirror telescope with a primary mirror of 0.5 m in diameter and has a focal length of 12 m. It contains 14 frame CCDs, each 2048 pixels wide and 128 pixels long. The long-track direction of the CCD sensors are used for time-delay integration (TDI; Delamere *et al.*, 2003). In conventional line scanner cameras like MOC or HRSC, each ground element is imaged by one pixel of the sensor only, limiting the available integration or "exposure time" to the time the camera needs to pass the ground element in one IFOV. For fast-moving cameras on spacecrafts in low orbits, this can result in a high signal-to-noise ratio. TDI faces this problem by imaging a ground element not by only one pixel, but by several pixels in the long-track direction, as the spacecraft passes over the ground. The signal of the long-track pixels is then summed up to provide a better SNR. Ten of the 14 CCDs are mounted next to each other in the cross-track direction to allow a swath width of 6 km, twice the swath width of MOC. The remaining four sensor arrays are mounted in two pairs and equipped with color filters around 530 nm (blue-green) and 900 nm (infrared) to produce color images of the 1.5-km-wide central swath. The images are recorded at a radiometric resolution of 14 bit, which are compressed to 8 bit. This allows for a wide contrast in the images without over-saturating the sensors. The ground resolution of

the images is up to 0.25 cm/pixel, but can be reduced by pixel binning, if desired (McEwen *et al.*, 2007). HiRISE images are also used to produce anaglyphs and DTMs with a resolution of up to 1 m/pixel.

2.1.8.2 The Context Imager (CTX)

The Context Imager CTX is a push-broom camera with a Cassegrain optic with 350-mm focal length. It provides grayscale context images for the HiRISE and CRISM observations. Its footprints are 30 km wide and up to 160 km long. The images have a resolution of 6 m/pixel, comparable to MOC imagery (Malin *et al.*, 2007), but the coverage of the surface is much higher. More than 50% of the surface had been imaged until Feb. 2010 (MSSS, 2010). CTX images have been used in this study, because they provide the highest resolution over the entire study areas examined here. CTX images are collected in the wavelength range of 500-700 µm in a single channel.

2.1.8.3 The Compact Reconnaissance Imaging Spectrometer for Mars (CRISM)

CRISM is a hyperspectral imager operating in a wavelength range between 362 and 3920 nm, similar to OMEGA. It allows the detection of iron oxides and of minerals that contain water or hydroxyl (OH^-) groups in their crystal structure, like sulfates and clays. Two spectral sensors are mounted behind a telescope with 441 mm focal length, one sensor is used for the visible and near infrared spectrum (362-1053 nm), and one for the SWIR (1002-3920 nm). The spectral resolution is 6.55 nm for each of the 545 channels. The entire optical system is mounted on a one-axis gimbal on the nadir-facing side of the MRO spacecraft. This allows for various observation modes, most of which fall either in the "targeted" or in the "mapping" category.

In mapping mode, the instrument is pointed at nadir, and contiguous strips with a width of ~10 km are recorded for 73 selected bands. This is also called "multispectral mode". Pixels are binned in the cross-track direction to increase SNR, resulting in a resolution of 100 or 200 m/pixel. In targeted mode, individual outcrops previously identified in CRISM multispectral mode, OMEGA data or panchromatic imagery are observed in high spatial and spectral resolution by gimbaling the instrument. This takes out the along-track motion of the spacecraft and allows longer integration times and higher SNR. Full Resolution Targeted (FRT) observations have a spatial resolution of ~18 m/pixel and a footprint size of ~10 by 10 km. In Half-Resolution Long (HRL) observations, the resolution is reduced to ~36 m/pixel, and the footprints are ~10 km wide and 20 km long. Both types of observations provide the full spectral resolution of the 545 channels (Murchie *et al.*, 2007a). All three types of data have been used in the study projects in this thesis.

2.1.9 The Phoenix Mars Mission

The Phoenix Mars Mission consisted of a stationary robotic lander. It was launched in 2007 and arrived at Mars in May 2008. Phoenix landed at 68°N 234°E near the Martian north polar cap in the late Martian spring and operated until August 2008. It was equipped with a stereo imager (SSI), a combination of miniature heating ovens and a mass spectrometer (Thermal Evolved Gas Analyzer TEGA), a wet chemistry suite (Mars Environmental Compatibility Assessment MECA), which included microscopic imagers to analyze the soil samples. The soil samples were delivered to the analysis instruments by a robotic arm equipped with a shovel. Further instruments included a thermal and electrical conductivity

probe and a meteorological station (MET). The mission confirmed the presence of water ice about 5 cm below the surface. The soil at the landing site is slightly alkaline (pH 7.7, Smith *et al.*, 2009), dominated by the cations Mg^{2+} and Na^{+} and contains minor amounts of K^{+} and Ca^{2+}. The anions include perchlorate (ClO_4^-), chloride, bicarbonate and possibly small amounts of sulfate (Hecht *et al.*, 2009). Small amounts of calcium carbonate were detected and interpreted as the result of the interaction of atmospheric CO_2 with thin water films around soil particles (Boynton *et al.*, 2009).

2.1.10 The MSL Curiosity mission

At the time of writing of this thesis, the Mars Science Laboratory (MSL), named Curiosity, is on its way to Mars. This car-sized rover is the most ambitious mission to study Mars in situ, and is scheduled for landing on Mars on 6. August 2012. After a selection process over several years, Gale crater had been selected as the landing site out of several dozens of interesting locales (Grant *et al.*, 2011). Gale crater has a diameter of 155 km and is located near the dichotomy boundary. The crater contains a sequence of stratified rocks approx. 5 km in thickness (Milliken *et al.*, 2010). The origin of this deposit is unknown, but the lack of obvious volcanic features like vents, cones or lava flows suggest that it is not a volcanic construct, but a sedimentary sequence (Malin and Edgett, 2000b). The strata have also been interpreted as being volcanic ash, lacustrine, eolian, spring mound or ancient polar deposits (Cabrol *et al.*, 1999, Rossi *et al.*, 2008, Schultz and Lutz, 1988). The age of the deposit is constrained by crater counts on underlying and onlapping units to Late Noachian to Early Hesperian.

The sequence is divided in a lower and an upper formation, separated by an unconformity. The lower formation contains hydrous minerals: Sulfate-rich layers are overlain by a thin section of nontronite-rich strata, which are in turn overlain by deposits showing sulfate- and weak phyllosilicate spectral signatures, and finally sulfate-rich deposits at the top. Ferric oxides are often found associated to the sulfates. The upper formation does not exhibit spectra of hydrous minerals in CRISM data. It is planned that the rover will traverse this stratigraphic sequence in order to investigate the facies of the sulfates and phyllosilicates, which will give hints for the climatic evolution of Mars. Interestingly, this deposit shows sulfates not only on top of phyllosilicates but also below it, which is somewhat at odds with the climatic model proposed by Bibring *et al.*, 2006, if sulfates and phyllosilicates are autochthonous.

2.2 The Geology and Mineralogy of Mars

2.2.1 The Martian Stratigraphic Time Frame

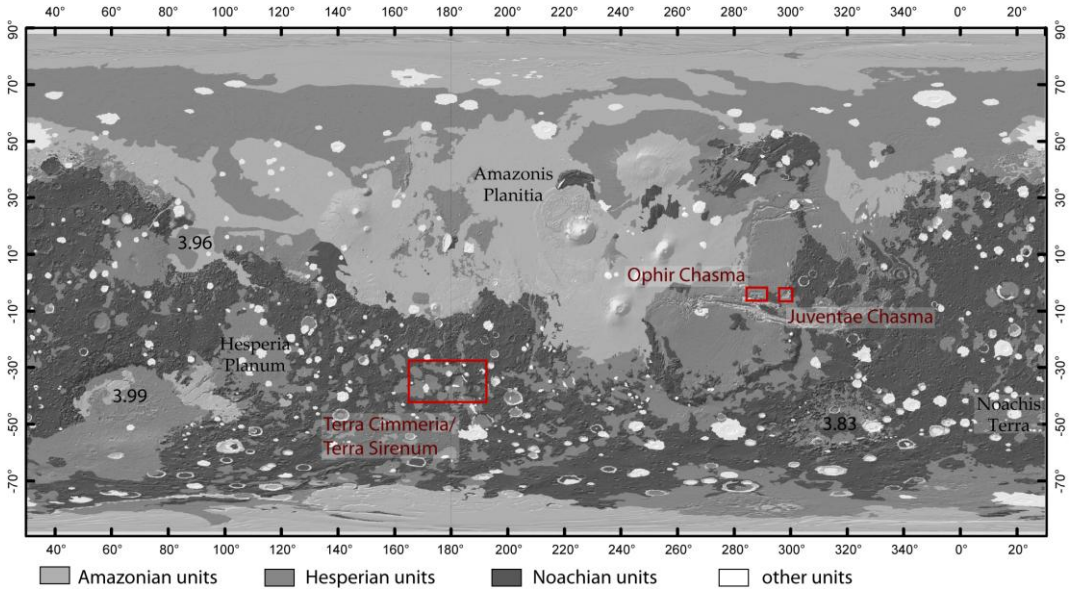

Fig. 2.3: The Martian Stratigraphic Periods.

The main stratigraphic units Amazonian, Hesperian and Noachian in different tones of gray, overlain on MOLA shaded relief map, and the study areas of this thesis. Modified after Greeley and Guest, 1987, Scott and Tanaka, 1986. Ages of major basins from Werner, 2005.

Any investigation of the timing of specific events or of the succession of environments in which observed rock units formed requires a stratigraphic time frame in order to place them at the correct point in time. The time frame on solid planetary bodies like Mars is established on one hand by geologic mapping of surface units with distinct morphologies, textures or spectroscopic characteristics following the basic stratigraphic principles of superposition and cross-cutting relationships. On the other hand, the sizes and numbers of impact craters superposed on the individual geologic units can be used to derive relative ages of the units. Assuming that the craters observed on planetary bodies and on the Moon are formed by the same family of impactors, and that the time dependency of impact cratering rates are similar to that of the Moon, these relative ages can be translated into absolute ages by relating the crater size-frequency distributions to absolute radiometric ages obtained from rock samples collected by the Apollo astronauts on the Moon. Scaling factors have to be taken into account that consider the specific conditions of the planetary body, i.e., its gravity, position in the solar system and surface properties (Neukum and Hiller, 1981, Neukum *et al.*, 2001, Neukum *et al.*, 1994, Neukum and Wise, 1976, Strom *et al.*, 2005). Several chronology models have been proposed, as newer and higher resolved image data became available, leading to two current models by Hartmann (HM) and Neukum (NM) with slightly different ages for the boundaries between the stratigraphic periods (Hartmann and Neukum, 2001). The Neukum model is shown in Fig. 2.4. The Martian surface

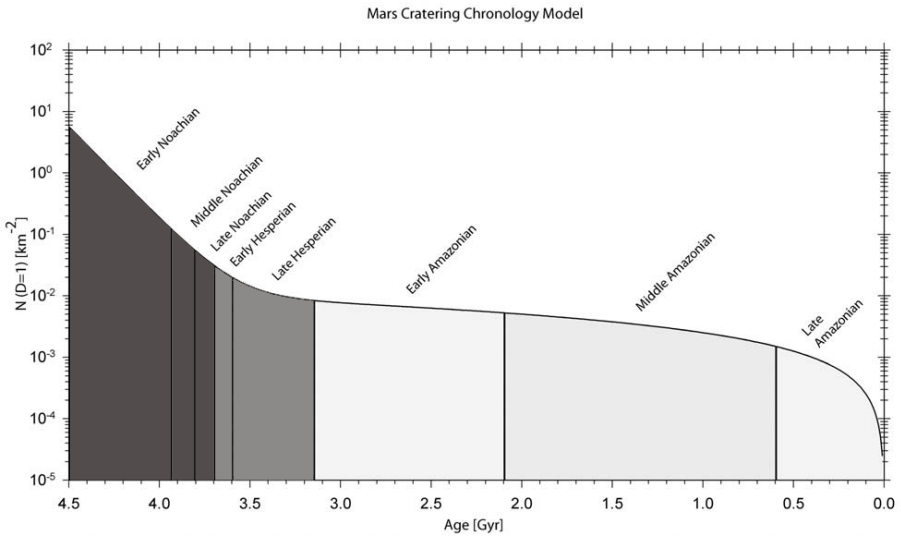

Fig. 2.4: The Martian Chronology Model

The Neukum Martian Chronology model, modified after Hartmann and Neukum, 2001, with Martian eras. The cratering rate drops exponentially in the Noachian. It transitions in the Hesperian era into the constant rate observed during the Amazonian.

morphology has been shaped extensively by impact cratering, volcanism, glacial, fluvial, and eolian activity, which allows a subdivision of the stratigraphic record into periods and epochs. Plains-forming volcanism has been used as marker horizons for the individual units (Scott and Carr, 1978, Tanaka, 1986, Tanaka *et al.*, 1992). The type localities for the resulting Noachian, Hesperian and Amazonian periods are shown in Fig. 2.3.

A tabulated overview of the most important events in the Martian geologic history is provided in Table 2-1. The Noachian Period is exposed mostly in the southern highland south of the prominent dichotomy boundary separating the smooth, low-lying northern plains from the more rugged southern highlands. This unit displays the highest impact crater densities on Mars, and is characterized by impact breccias and ejecta covered and interbedded with lava flows. The type locality is Noachis Terra between Argyre and Hellas Planitia. It displays a crater retention age of 3.97 Ga (Hartmann and Neukum, 2001, Tanaka *et al.*, 1992). If Noachis Terra is taken as the base of the Noachian period, the large impacts of Hellas, Argyre and Isidis have taken place in a pre-Noachian period. If, on the other hand, the entire time prior to the onset of the Hesperian is defined as Noachian, the core and crust of Mars and the three largest impact basins have been formed in the Noachian. At the time prior to these impacts, Mars apparently had a magnetic field, as evidenced by magnetizations of the highland crust, but the magnetic dynamo must have shut down prior to the formation of the large impact basins, as they are not magnetized (Connerney et al., 1999). Volcanism in the Tharsis region began in the Noachian, and the highland volcanic provinces, the paterae and tholi formed (Rossi and van Gasselt, 2010, Tanaka *et al.*, 1992). The Noachian period ended at 3.7 Ga (NM).

The onset of the Hesperian period is defined by the volcanism in Hesperia Planum. Large-scale volcanic activity covered extended parts of the highlands, the Tharsis region and the Martian lowlands. The most extensive unit of the

Hesperian are the Ridged Plains (Hr; Greeley and Guest, 1987), characterized by wrinkle ridges resembling similar features in the mare-basalts on the Moon. Fluvial activity declined in the Hesperian, as evidenced by a lower density of valley networks in these units. Water was stored as permafrost in the subsurface, which locally breached to form gigantic outflow channels, mostly in the circum-Chryse region (Tanaka et al., 1992). Valles Marineris, the prominent canyon system 4000 km long and several km deep, also developed mainly in the Hesperian. The Hesperian period lasted from 3.7 Ga to 3.3 Ga (NM).

The Amazonian era spans the longest part of the Martian history and began 3.3 Gyr before present (NM). It is characterized by sparsely cratered, relatively featureless plains in the northern lowlands (Fig. 2.3), which were shaped to a great extent by volcanic and eolian activity in this era (Tanaka et al., 1992). The base of the Amazonian is marked by the Arcadia Formation of inferred volcanic origin (Greeley and Guest, 1987), whereas the name-giving deposits in Amazonis Planitia define the Middle Amazonian. The Upper Amazonian is marked by "channel and flood-plain material" south of the Elysium volcanic province.

Major Events in Martian Geological History

	Volcanism	Tectonism	Fluvial Events	Cratering	Erosion and surface processes
Amazonian	Late flows in southern Elysium Planitia. Decreased volcanism in northern plains. Most recent flows from Olympus Mons. Emplacement of massive materials at S. edge of Elysium Planitia. Waning volcanism in Tharsis region. Waning volcanism in Elysium region. Widespread flows around Elysium Mons.	Tharsis tectonism continued through the Amazonian, mostly associated with the large shield volcanoes. Formation of Elysium Fossae. Initial formation of Olympus Mons aureoles.	Channeling in southern Elysium Planitia. Late period of Channel formation. Formation of channels NW of Elysium Mons.		Emplacement of polar dunes and mantle. Development of polar deposits? Formation of ridged lobate deposits on large shield volcanoes. Emplacement of massive materials at S. edge of Elysium Planitia. Local degradation and resurfacing of northern plains. Erosion of northern plains. Deep erosion of layered deposits in Valles Marineris. Development of ridges. grooves, and knobs on northern plains.
Hesperian	Volcanism at Syrtis Major. Formation of highland paterae. Volcanism at Tempe Terra. Major Volcanism in Elysium and Tharsis regions. Emplacement of ridged plains (Hr).	Formation of Noctis Labyrinthus. Formation of Valles Marineris. Formation of wrinkle ridges. Memnonia and Sirenum Fossae, fracturesaround Isidis.	Development of large outflow channels. Infilling of northern plains. Deposition of layered materials in Valles Marineris.		Degradation of northern plains materials. Dorsa Argentea formation at South Pole. Resurfacing of northern plains.
Noachian	Formation of intercrater plains. Decreasing highland volcanism. Beginning of widespread highland volcanism.	Ceraunius, Tempe, and Noctis Fossae. Tectonism south of Hellas. Archeron Fossae. Claritas Fossae.	Formation of extensive valley networks.	Waning impact flux. Intense bombardment. Argyre impact. Hellas and Isidis impacts. Formation of oldest exposed rocks.	Extensive dessication and etching of highland rocks. Formation and erosion of heavily cratered plateau surface. Deep erosion of basement rocks.

Table 2-1: Major events in the geological history of Mars. Modified after Head *et al.*, 2001.

2.2.2 The Martian Mineralogy

The following chapter provides an overview of the mineralogical record of Mars. The most important mineral groups and their outcrops on the surface are discussed together with suggested formation theories. As some of the mineral groups are formed by liquid water, the spatial and temporal distribution of morphological evidence for the presence of water are shown as well, before the next chapter will discuss the emerging picture of the Martian climate history.

2.2.2.1 Volcanic rocks

The by far most abundant mineral paragenesis on the surface of Mars is of basaltic to andesitic composition. This has been known from in situ measurements by the Viking landers and has been confirmed by measurements of TES on MGS as well as further rovers and landers. A major class of minerals in mafic volcanic rocks are pyroxenes. Pyroxenes are inosilicate minerals, built up by chains of SiO_4-tetraeders and mostly Fe^{2+}, Mg^{2+}, Ca^{2+} and Mn^{2+} cations. Si^{4+} in the tetrahedrons can also be replaced by Al^{3+} and Fe^{3+}. Pyroxenes are grouped into low-calcium, orthorhombic pyroxenes (LCP/Opx) - and high-calcium, monoclinic pyroxenes (HCP/Cpx). Low-calcium, orthorhombic pyroxenes form a solid solution of enstatite ($MgSiO_3$), ferrosilite ($FeSiO_3$) and minor modal amounts of the Ca-endmember wollastonite ($CaSiO_3$).

Fig. 2.5 shows a comparison of the Martian surface as it appears to the human eye (A) with results from TES (B), displaying red surface dust in red, low-calcium pyroxene in green and high-calcium pyroxene in blue (Bandfield, 2002). The Figure shows that regions appearing bright red in the visible imagery are dominated by surface dust. The low-albedo regions show spectral characteristics of pyroxenes, rock-forming minerals in basaltic rocks. Low-albedo regions in the lowlands are dominated by low-calcium pyroxene, whereas the highland basalts appear mostly in blue colors in Fig. 2.5 indicating high-calcium pyroxenes.

The OMEGA data confirms that the low albedo features are dominated by a basaltic composition, indicated by the presence of pyroxenes. TES data suggests two surface types: surface type 1 is found mostly in the southern highland low albedo regions and contains high-calcium pyroxene (blue in Fig. 2.5B), whereas surface type 2 is found in the northern lowlands and brighter regions of the highlands and contains predominantly low-calcium pyroxene (green in Fig. 2.5B), but both types of pyroxenes usually occur together. Plagioclase is spectrally featureless in short-wave infrared data gathered by OMEGA and CRISM, but the mafic minerals pyroxene and olivine are detectable. Global maps from OMEGA data are shown in Fig. 2.5C and D (Poulet *et al.*, 2007). They confirm the detection of pyroxenes in the low-albedo regions in the highlands. The dark, low-calcium pyroxene-rich regions (according to TES) in the lowlands have less clear spectral characteristics in OMEGA data. Olivine has been mapped globally by TES (Bandfield, 2002) and THEMIS (Hamilton and Christensen, 2005), and has also been detected in the soil and rocks at the landing sites of the Mars Exploration Rovers (Klingelhöfer *et al.*, 2004, Morris *et al.*, 2006) and in Martian meteorites (McSween, 2002). This suggests that olivine is a common rock-forming mineral on Mars, and is not restricted to the relatively few locations where it has been detected by OMEGA (Fig. 2.5D) and CRISM.

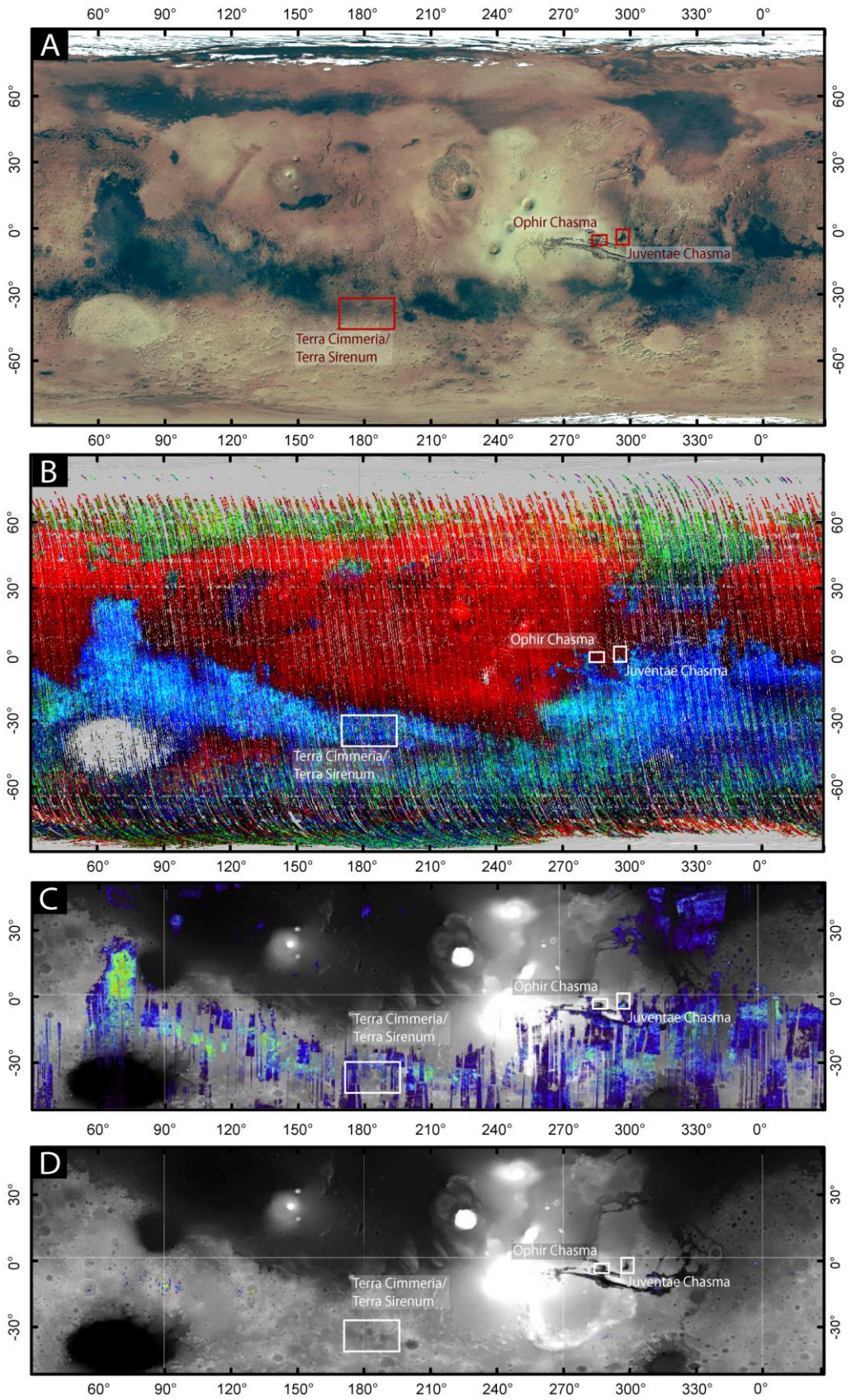

Fig. 2.5. Overview of major surface components as seen by TES and OMEGA.

A: The Martian surface in true color imagery from Viking. B: Global map of selected endmembers from the deconvolution of TES data (Bandfield, 2002). Red channel: Surface dust, green: low-calcium pyroxene, blue: high-calcium pyroxene. C: Spectral index for pyroxenes in OMEGA data on MOLA. D: Spectral index for forsterite in OMEGA data on MOLA. C and D modified from Poulet et al., 2007.

Deconvolution of TES data suggests based on the inferred plagioclase content that two surface compositions dominate the Martian surface. Surface type 1 is composed predominantly from plagioclase and clinopyroxene and is mafic in composition, while the intermediate, andesitic type 2 is composed of plagioclase and basaltic glass. The separation of the surface types roughly resembles the dichotomy boundary (Bandfield *et al.*, 2000, Bandfield *et al.*, 2004; Hamilton *et al.*, 2001). Alternative explanations for the difference between the two surface types included altered basalts rich in phyllosilicates (Wyatt and McSween, 2002). This interpretation is not consistent with OMEGA and CRISM data, which indicate that the northern plains are generally phyllosilicate-free, with the exception of a few impact craters (Carter *et al.*, 2010).

An outcrop of felsic magmatites exists in an area of approx. 230 by 125 km in two craters in northern Syrtis Mayor that contains both plagioclase and quartz (Bandfield, 2006). Poulet *et al.*, 2009 use non-linear unmixing of spectra in the VNIR range to derive plagioclase abundances from the absorption band depths of mafic minerals, as plagioclases display no spectral features in this range. They conclude that the dominating composition of the Martian low-albedo surface resembles gabbro-norites and two-pyroxene basalts and thus contains significantly less SiO_2 than estimated by Bandfield *et al.*, 2000 on TES data, especially the andesitic surface type 2. The model solves for mineralogy, grain size and aerosols in the atmosphere simultaneously. Results roughly match the surface composition known from Martian meteorites and rover data, and have been validated against laboratory measurements, but the method has not been validated against field measurements with a VNIR sensor on the Martian surface, as such an instrument has not been deployed on the surface yet. The results therefore have to be interpreted with caution. See also chapter 3 for details on the difficulties of transferring laboratory spectral measurements to remote sensing data.

Fig. 2.5D shows localized outcrops of olivine. Olivine $(Fe,Mg)_2SiO_4$ is a nesosilicate. It forms a solid solution of the iron endmember fayalite and the magnesium endmember forsterite. It is an important rock forming mineral in mafic and ultramafic rocks on Earth and has been identified in several locations on Mars, with the spatially most extensive locality at Nili Fossae. (Hamilton *et al.*, 2003, Hoefen *et al.*, 2003, Poulet *et al.*, 2007).

2.2.2.2 Phyllosilicates

Phyllosilicates form under a variety of alteration conditions and are important indicators of aqueous weathering processes of primary magmatic rocks (e.g., Bishop *et al.*, 2008b, Matthes, 1993). As they require the prolonged presence of liquid water for their formation, they are important proxies for the ancient climate on Mars, and understanding the facies in which the clay minerals have formed allows an estimation of the habitability of the planet at that time. The formation of clay minerals in contact with the current atmosphere of Mars is not possible, as the low atmospheric pressure of 7 mbar and the low temperature of 218 K on average prevent water from occurring in the liquid state. The major issue is whether the clay minerals formed at the surface in contact with the atmosphere, as in this case they would allow an estimate of the atmospheric conditions, or in the subsurface, secluded from it, in which case the climatic conditions would not play a role (Bibring *et al.*, 2006).

The presence of phyllosilicates on Mars has been expected from experiments on inorganic

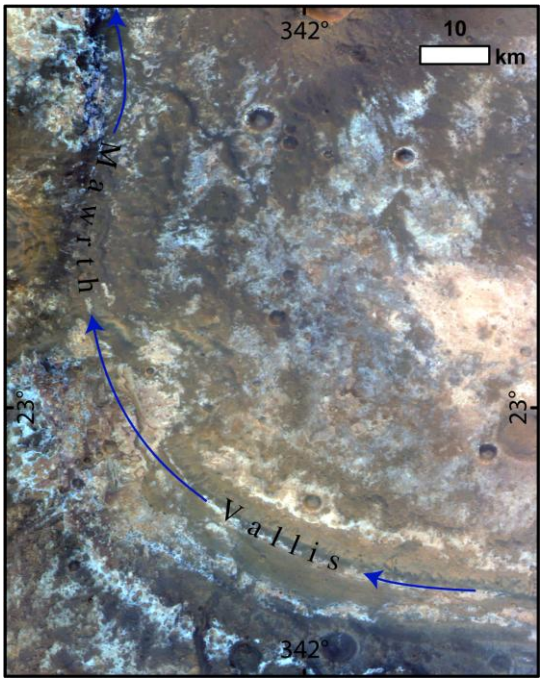

Fig. 2.6: Clay minerals in Mawrth Vallis.
This color-stretched image from HRSC orbit 1293, red, green and blue channels shows reddish Mg/Fe-smectites overlain by bluish Al-rich smectites and hydrated silica (Loizeau *et al.*, 2010, Loizeau *et al.*, 2007). This clay stratigraphy is typical for Mars and is observed globally (Mustard et al., 2008).

chemistry by the Viking landers (Toulmin *et al.*, 1977), investigations on weathering of terrestrial basaltic rocks and ashes (e.g., Bishop *et al.*, 1995, Singer, 1982) and clays in Martian meteorites (Bridges *et al.*, 2001, Bridges and Grady, 2000). Finally, phyllosilicates have been detected by the OMEGA and CRISM instruments.

An overview of the locations where phyllosilicates have been identified on Mars is given in Fig. 2.7B. It shows that the vast majority of sites are found in the Noachian-aged highlands, whereas sulfate deposits are mostly found in Hesperian units (Bibring *et al.*, 2005). This has inspired Bibring *et al.*, 2006, to suggest a "phyllosian" era, in which phyllosilicates formed, a "theiikian" era, dominated by sulfate formation, and a "siderikian" era, in which the formation of iron oxides in a hyperarid climate was the only chemical alteration process.

Clay minerals have been detected in hundreds to thousands of locations in the Martian highlands by CRISM (Fig. 2.7B; Murchie *et al.*, 2009b), but the individual outcrops are mostly small. This explains, why they had not been detected earlier using TES, and why OMEGA detected only the largest outcrops, for example in Mawrth Vallis (Loizeau *et al.*, 2007) or near Nili Fossae (Mangold *et al.*, 2007b) and only a few of the smaller clay-bearing sites in the highlands.

The most abundant clay minerals detected are smectites rich in Fe (nontronite), Mg (saponite) or Al (montmorillonite), but other species like chlorites, muscovite, illite, kaolinite, prehnite, the zeolite analcime and serpentine have also been identified (e.g., Ehlmann *et al.*, 2009, Mustard *et al.*, 2008). Phyllosilicates have been found in a number of settings, and schemes to classify them have been invoked by Murchie *et al.*, 2009b, Grotzinger and Milliken, 2011, and Ehlmann *et al.*, 2011.

Clay minerals occur deep in ancient, volcanic terrains, from where they have been exposed by impact cratering processes or tectonic movement. In these locations, chlorite and locally prehnite indicate formation temperatures between 200 and 400°C (Ehlmann *et al.*, 2009). These deposits have been classified as "deep phyllosilicates" by Ehlmann *et al.*, 2011. Phyllosilicates are also exposed in the walls of Nili Fossae (Mustard *et al.*, 2009) and Valles Marineris (Murchie *et al.*, 2009b). These deposits appear to be dominated by chlorite and saponite with minor amounts of nontronite, Al-smectite kaolinite and other minerals (Ehlmann *et al.*, 2008a), and are also exposed in numerous impact craters, where they have been excavated and form an impact breccia

(McEwen *et al.*, 2008). This class of deposits may be common in the Noachian-aged Martian southern highlands, resulting in possibly several thousands of outcrops (Mustard *et al.*, 2009), but alteration might have been controlled by the local availability of water, as easily altered olivine is still present in many locations (Hoefen *et al.*, 2003).

Layered phyllosilicates are found in Mawrth Vallis, where a sequence of >300 m thickness is observed, which consists of a lower unit of Fe/Mg-rich clay (nontronite), a middle unit of Al-rich smectite, and an upper layer of a kaolinite-group mineral and hydrated silica. The sequence is covered by spectrally bland material that shows no sign of alteration (Loizeau *et al.*, 2010, Loizeau *et al.*, 2007, Michalski and Noe Dobrea, 2007, Mustard *et al.*, 2008). These deposits extend over several thousands of km^2, formed after the incision of Mawrth Vallis, and once covered large parts of western Arabia Terra prior to erosion (Murchie *et al.*, 2009b). Similar sequences of clay deposits, yet with a higher proportion of Fe/Mg phyllosilicates are found east of Nili Fossae (Ehlmann *et al.*, 2009), and elsewhere on Mars. They have been classified as "clays in stratigraphies" by Ehlmann *et al.*, 2011.

"Sedimentary clays" according to Ehlmann *et al.*, 2011, are phyllosilicates found within layered strata of inferred sedimentary origin in suggested paleolakes and fluvial basins. Clays in these locations are dominated by Fe/Mg-rich varieties, wheras minerals indicating elevated formation temperatures have not been found. This type of occurrence includes the Jezero, Holden, Eberswalde (Milliken and Bish, 2010; Ehlmann *et al.*, 2008b, Fassett and Head, 2005, Grant *et al.*, 2008, Lewis and Aharonson, 2006), and Columbus Craters (Wray *et al.*, 2009), where clays are locally observed interbedded with sulfates or overlain by chlorides. In these locations, it is not clear whether the clays have formed in situ or have been eroded elsewhere, transported and deposited.

Another class of phyllosilicate-bearing deposits following Murchie *et al.*, 2009b, are plains sediments found in a relatively flat basin in Terra Sirenum. These Fe/Mg phyllosilicates are found together with deposits characterized as chlorides based on THEMIS data (Osterloo *et al.*, 2008). Chlorites appear to embay eroded outcrops of phyllosilicates, indicating that chlorides were deposited after the clay-rich deposits. These deposits may be similar to phyllosilicates in deltas, and might have been deposited in playas or lakes within impact basins.

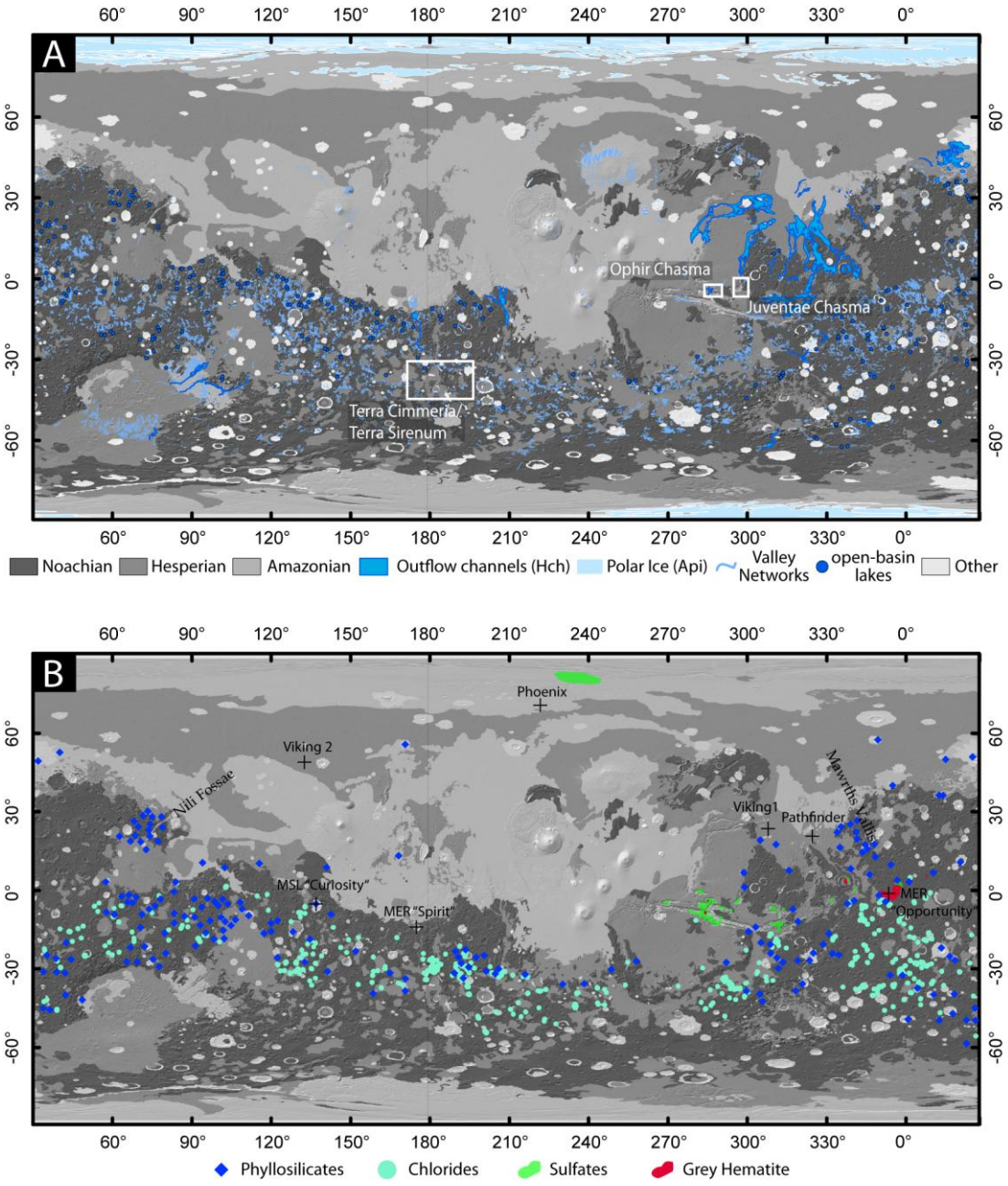

Fig. 2.7: Overview of water related surface morphologies and chemical sediments.

A: Geological map showing the main stratigraphic units, overlain with outflow channels (Hch) and polar ice (Api) from Greeley and Guest, 1987, Scott and Tanaka, 1986, valley networks from Hynek et al., 2010, and open-basin lakes from Fassett and Head, 2008, Loizeau *et al.*, 2010. B: Same geological map as A, overlain with detections of phyllosilicates, chlorides, sulfates and grey hematite, compiled from Bibring *et al.*, 2006, Christensen *et al.*, 2001b, Ehlmann *et al.*, 2011, Massé *et al.*, 2010.

The formation of clay minerals by alteration of primary silicates and glasses is controlled by several factors. The most important among them are the chemical composition of the primary minerals, the amount of available water, and the degree to which the alteration takes place in an open or closed system with respect to the atmosphere (Ehlmann *et al.*, 2011, Meunier, 2005). In a closed system in the subsurface, waters develop towards an equilibrium with the

host rock, leading to alkaline and anoxic conditions in mafic rocks, and the resulting mineral precipitates are controlled by temperature and pressure. As the fluid-rock-ratio is typically low, the elemental composition remains approximately constant, while the mineralogy changes. Typical alteration products are iron oxides and ferrous or Mg-smectites, and chlorite and serpentinite at elevated temperatures. Hydrated silica, zeolite and prehnite can form in fractures and pore spaces as well (Ehlmann *et al.*, 2011, Meunier, 2005). In an open system with abundant water in contact with the Martian atmosphere, the oxidation of ferrous iron the and solution of atmospheric CO_2 result in oxic, acidic conditions in the fluid. This leads at moderate pH conditions to the solution of Na, K, Cl, Ca and Mg from the weathered basaltic rock, leaving a residual enriched in the less soluble Fe, Al and SiO_4 behind, which forms Al-rich smectites like montmorillonite. The dissolved cations precipitate elsewhere as chlorides, carbonates or sulfates. In oxic surface conditions or in the presence of oxidized sulphurous species, the fluid becomes too acid for the precipitation of Fe/Mg smectites, and jarosite, silica, iron oxides or kaolinite are formed if enough water is available (Altheide *et al.*, 2010, Chevrier *et al.*, 2007). At lower fluid/rock ratios, only the most soluble mineral in the basalt, olivine, dissolves before the water evaporates to form amorphous coatings and salts.

A comparison between outcrops of phyllosilicates and valley networks (Fig. 2.7A,B) shows that both occur in roughly the same regions of Mars, and that they are generally constrained to the Noachian. However, Howard *et al.*, 2005, Irwin *et al.*, 2005 and Hynek *et al.*, 2010 report that valley networks during most of the Noachian were generally underdeveloped with short channels leading into local depressions and craters, but few signs of ponding and overflow of these basins, suggesting a hyperarid climate. Only in the late Noachian, fluvial activity peaked to form connected channels entering and leaving craters. The reason for an apparently higher flow rate in the late Noachian might be the formation of a duricrust or a permafrost layer at the surface, which led to the concentration of water to fewer, but longer channels (Irwin *et al.*, 2005; Barnhart *et al.*, 2009). In contrast, Hynek *et al.*, 2010 see precipitation as the only conceivable explanation for the relatively dense, dendritic valley networks in the Late Noachian, which were not visible in older, lower-resolved imagery. This would require a denser atmosphere caused, for example, by large impacts or increased volcanic outgassing.

The "deep" phyllosilicates, for example in parts of Nili Fossae, apparently formed prior to the development of extensive valley networks in the Late Noachian, and the elevated formation temperatures indicated by the specific mineral paragenesis point to a hydrothermal origin of these clay minerals. The heat source may have been a generally higher geothermal gradient during the Noachian and local volcanism. These phyllosilicates where locally excavated by impact cratering, eroded, transported and redeposited during the Late Noachian. Additional clay minerals formed by weathering of basaltic precursor material in that epoch (Ehlmann *et al.*, 2011) The relative timing of volcanic activity, valley networks, outflow events and chemical sediments is shown in Fig. 2.10.

Phyllosilicates are have also been found in a few craters in the northern lowlands, and thus in regions younger than Noachian. These clay minerals may have been excavated by the impact event from the underlying, Noachian-aged, altered strata in the subsurface (Carter *et al.*, 2010), but could locally also have been formed by

hydrothermal systems induced by the impact itself, as suggested for Toro crater (Marzo *et al.*, 2010) or for a crater in the northern lowlands at 50.55°N, 16.33°E, recently named Micoud crater (Gross *et al.*, 2011). Clay formation by surface weathering apparently did not occur after the Late Noachian/Early Hesperian, but may have continued in the subsurface, especially in the younger volcanic provinces.

2.2.2.3 Chlorides

A compositional unit showing featureless spectra with a negative slope in THEMIS data, distinct from other surface materials on Mars, was attributed to chloride deposits by Osterloo *et al.*, 2008 and further investigated by Osterloo *et al.*, 2010. The individual outcrops have a light-toned appearance in visible imagery, are spectrally featureless in CRISM data and show polygonal fractures suggestive of desiccation cracks in optical imagery. Other minerals like bromides or fluorides or sulfites are alternative candidates for these deposits, but their occurrence in local basins and as fills of inverted channels make chlorides the geologically most plausible interpretation.

The chlorides form patches up to 1300 km^2 in extent, but most outcrops cover areas of tens of km^2, which are often ancient, degraded impact craters. Chlorides are restricted to the southern highlands of Mars. Approximately 60% of the 640 sites investigated by Osterloo *et al.*, 2010 are located on Noachian-aged terrain and 40% on Hesperian-aged units (Fig. 2.7B). No chlorides have been detected on Amazonian units.

A comparison to the location of valley networks (Fig. 2.7; Hynek *et al.*, 2010) shows that many chloride outcrops are located close to fluvial features, but almost an equal number is found in regions devoid of morphological evidence of fluvial processes. Chlorides are locally found overlaying phyllosilicate-rich units, where they appear to have formed at a later time (e.g., Glotch *et al.*, 2010). The chloride deposits are best explained as evaporites formed from surface water ponding in local depressions, supplied either by precipitation or groundwater upwelling. The large number of outcrops documents that this was likely a common process in the Noachian and Early Hesperian. However, the estimated mass of chloride deposits is too low to account for the excess cations which are released during the dissolution of primary basaltic material and not incorporated into phyllosilicates (Milliken *et al.*, 2009).

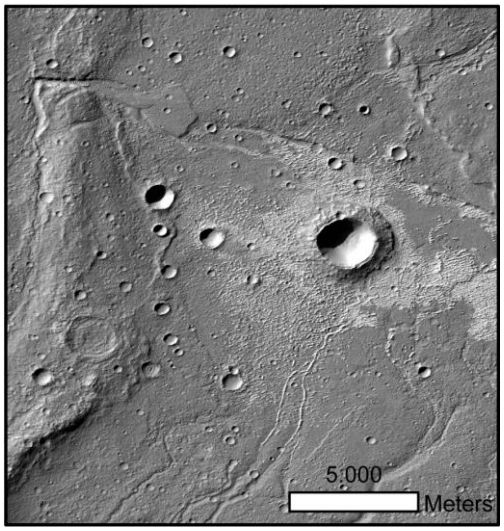

Fig. 2.8: Chloride deposit in Terra Sirenum.
This CTX image (P21_009318_1463) shows a chloride deposit in a local basin near 205.5 E, 33.3°S. Note the inverted channels and the small delta (Davila et al., 2011).

2.2.2.4 Carbonates

The presence of carbonates on the surface of Mars has been postulated for a long time. Valley networks in Noachian-aged terrains were taken as evidence for a warmer and wetter climate during the Noachian, which was caused by a strong greenhouse effect in a primitive CO_2-rich

atmosphere up to four orders of magnitude denser than at present (Haberle, 1998 and references therein). The CO_2 would have reacted with the surface waters to form carbonic acid, which in turn would have led to an accelerated weathering of the basaltic rocks, releasing Ca-, Mg- and Fe-ions, and finally leading to the formation of carbonates (Catling, 1999, Gooding, 1978). Consequently, thick carbonate deposits on the surface of Mars would be an effective storage medium for the CO_2 removed from the atmosphere near the Noachian/Hesperian boundary, if the climate models involving a thicker, CO_2-rich atmosphere are correct.

Carbonates are present on Mars. Martian meteorites contain up to 1% of carbonate by volume (Bridges *et al.*, 2001). The highest content is found in the 4.09-Ga-old (Lapen *et al.*, 2010) meteorite ALH 84001, where it has a composition of 58% magnesite, 29% siderite, 12% calcite and 1% rhodochrosite (Mittlefehldt, 1994). Ehlmann *et al.*, 2008c, and Brown *et al.*, 2010, report small (<10 km²) outcrops of magnesite-rich rocks in the Nili Fossae region of Mars, based on CRISM data. These deposits are found on top of Noachian-aged phyllosilicates and below Hesperian, olivine-rich basaltic rocks, and thus Mg- and Fe-rich rocks, implying a hydrous, possibly hydrothermal alteration of the olivines at circum-neutral pH. The carbonate content of these deposits has not been estimated. TES data suggests that carbonates might be a minor component (<5% by volume) in Martian dust (Bandfield *et al.*, 2003), which is supported by an absorption band at 3.9 µm attributed to carbonates in data from the Planetary Fourier Spectrometer PFS over both bright and dark surface units (Palomba *et al.*, 2009). Recently, data from the "Comanche" outcrops on the Columbia hills in Gusev crater, collected by the instruments of the Mars Exploration Rover Spirit, were interpreted as indicating a carbonate content by weight between 16 and 34%, with a similar composition of 62% magnesite, 25% siderite, 11% calcite and 2% rhodochrosite (Morris *et al.*, 2010). The similar compositions of ALH 84001 and the outcrops at Nili Fossae and Gusev are taken as evidence for a common formation pathway, likely under hydrothermal conditions.

Despite these localized carbonate detections, large-scale carbonates, which could have acted as sinks for the large amounts of CO_2 required to support a "warm and wet" climate are missing (Bandfield *et al.*, 2003, Bibring *et al.*, 2006, Ehlmann *et al.*, 2008c). TES and OMEGA have found no outcrop down to a scale of a few hundred meters. The apparent gap between models of the early atmosphere and the observed rock record may be bridged in three ways: (1) Mars never had a thick atmosphere, and the formation of phyllosilicates occurred mostly in the subsurface, as advocated by Ehlmann *et al.*, 2011, and/or water was kept liquid due to a high content of solutes (Fairén, 2010) or (2), the early atmosphere had a thick CO_2 atmosphere with a strong greenhouse effect, but a relatively high content of SO_2 in the order of tens of mbars, which would have reacted with surface waters to form sulfurous acid (H_2SO_3), inhibiting the formation of carbonates (Fairen *et al.*, 2004, Halevy and Schrag, 2009, Halevy *et al.*, 2007), or (3) carbonates did form on the surface of Mars during the Noachian, but subsequent conditions prevent an abundant detection, either due to burial (Banin *et al.*, 1997), alteration to sulfates (Tosca and McLennan, 2006) or photodecomposition (Mukhin *et al.*, 1996).

2.2.2.5 Sulfates

Sulfur is an important element in the Martian surface and occurs in higher overall concentrations than on Earth. A sulfur content in the order of ten percent has been detected at the landing sites of the Viking landers (Baird *et al.*, 1976, Clark *et al.*, 1976), Pathfinder (Bell *et al.*, 2000) and the Mars Exploration Rovers (Gellert *et al.*, 2004, Rieder *et al.*, 2004), and possibly at the Phoenix landing site (Hecht *et al.*, 2009). Mössbauer and mini-TES data from MER-Opportunity in Meridiani Planum suggest concentrations of up to 25 wt% of SO_3 in sedimentary outcrops (Rieder *et al.*, 2004). The most abundant sulfates here are jarosite (Klingelhöfer *et al.*, 2004), gypsum and Mg-sulfates (Squyres *et al.*, 2004). MER Spirit also detected Mg-, Fe- and Ca-sulfates in outcrops in the Columbia Hills (Gusev Crater; Ming *et al.*, 2006). Sulfates have also been detected in the Interior Layered Deposits (ILD) in Valles Marineris and neighboring depressions and chaotic terrains (e.g., Bibring *et al.*, 2005, Bishop *et al.*, 2009, Gendrin *et al.*, 2005b, Lichtenberg *et al.*, 2010, Mangold *et al.*, 2007a, Murchie *et al.*, 2009a, Roach, 2009, Roach *et al.*, 2010a, Roach *et al.*, 2010b, Sowe *et al.*, 2011), in a dune field near the north polar cap (Horgan *et al.*, 2009, Langevin *et al.*, 2005, Massé *et al.*, 2010) using orbital data from OMEGA, and in Terra Meridiani and some highland craters, using CRISM data (e.g., Murchie *et al.*, 2009b). An overview to the largest sulfate outcrops is provided in Fig. 2.7B. Hyperspectral data in the shortwave infrared allowed the identification of kieserite, szomolnokite, jarosite, gypsum and "polyhydrated sulfates". This group of minerals comprises all sulfate species with more crystal water than two water molecules per unit formula, like, e.g., epsomite or copiapite. They show very similar spectra, making a further distinction very difficult or impossible using SWIR data. A more detailed introduction to the spectral properties of sulfates is provided in chapter 3.2.4.

Sulfates form in acidic conditions, whereas clays require a neutral to slightly alkaline environment for their formation. Three main scenarios have been invoked for the formation of sulfate deposits, shown in Fig. 2.9. The first is the evaporation of a standing body of water. An Earth analog for this process would be the evaporation of the Mediterranean Sea in the Messinian stage of the Miocene (7.3 to 5.3 Ma b. p.). The second is the evaporation of groundwater near the surface, leaving cements, nodules and crusts of sulfate in the subsurface behind. This setting is called a playa. The third scenario is the formation of sulfates by the precipitation of volcanic aerosols (Settle, 1979).

The best examined outcrops of sulfate-rich rocks are those of the "Burns Formation" in Meridiani Planum, investigated by MER Opportunity. The "Burns Formation" consists of three units. The lower unit is a sandstone displaying large-scale cross-bedding formed in dunes at least 2 m high. The dune field was shaped by wind (Grotzinger *et al.*, 2005), but the sand-sized grains are composed of a mixture of basaltic siliciclasts and sulfate evaporites derived likely from a nearby playa environment (McLennan *et al.*, 2005). The cross-bedded sandstone is unconformably overlain by the middle unit, a planar-laminated sandstone deposited as eolian sand sheet. The contact between crossbedded sandstone and planar-laminated sandstone is named "Wellington contact" and is interpreted as an interdune deflation surface, created by a rise of the water table to preserve the eolian dune strata below (Grotzinger *et al.*, 2005). The upper unit contains wavy bedding, irregular lamination with

convolute bedding and possible tepee-structures and festoon cross-lamination in the cm-scale. They are interpreted as sediment structures formed when the capillary fringe was close to the surface or even by shallow subaqueous flows with velocities of a few cm/s in an interdune/playa facies. Evidence for lacustrine sedimentation like mudstones or bottom-grown evaporites have not been found. The formation also contains hematite concretions with diameters typically between 4 and 6 mm, which make up a few percent of the rock (McLennan *et al.*, 2005, Squyres *et al.*, 2004). They form lag deposits upon decomposition of the hosting sulfate-sandstones. The "Burns Formation" is exposed over a thickness of 7 m, but is likely much thicker. The extent of the formation is difficult to determine due to a cover of basaltic sands and dust, but the lag deposit of hematite spherules covers approximately 150.000 km^2 (Christensen and Ruff, 2004).

The deposition of the sulfates of the "Burns Formation" in Meridiani Planum in a playa environment as reconstructed from sedimentological investigations is supported by the mineralogy of the sediments. According to combined data from the Alpha Particle X-Ray Spectrometer (APXS) and the Mössbauer Spectrometer, they consist of 40±10% (by mass) of basaltic siliciclastic components and 60±10% of chemical sediments, including sulfates, hematite, possibly chlorides and silica. The sulfates are Mg-, Fe- and Ca-sulfates, including ~10% of jarosite (McLennan *et al.*, 2005). Jarosite is of particular interest because it is stable only at low pH-conditions and forms on Earth during acid-sulfate alteration of volcanic rocks or during alteration of sulfides (primary pyrrhotite or hydrothermal pyrite), for example in mining waste as at the Rio Tinto (Fernández-Remolar *et al.*, 2005, Sánchez España *et al.*, 2005, Triantafyllidis and Skarpelis, 2006).

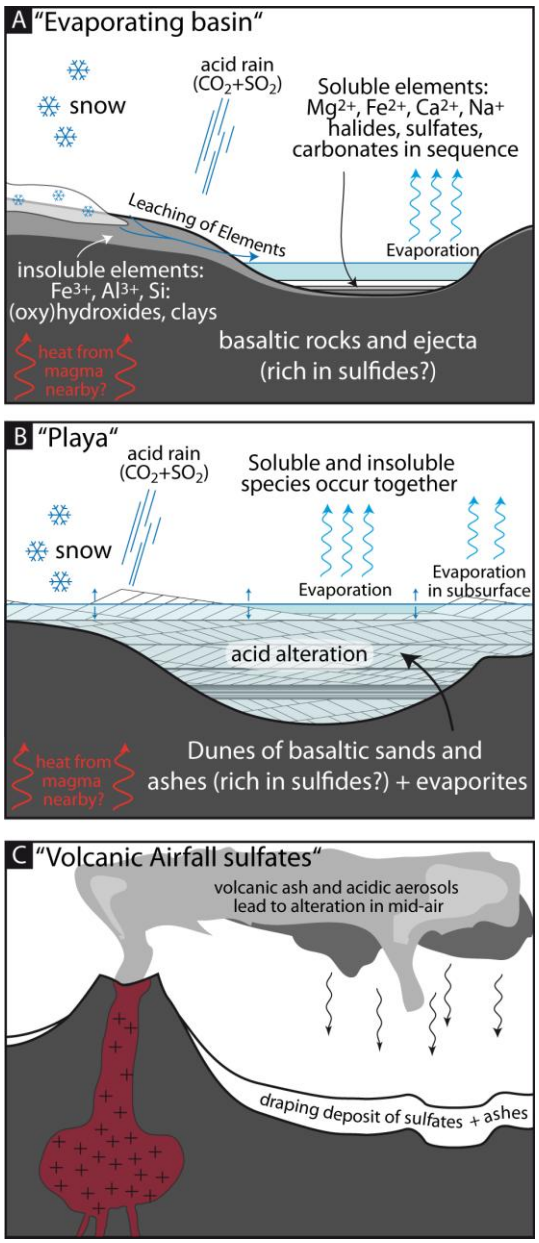

Fig. 2.9: Models for sulfate formation.

A: Evaporation of a standing body of water, leading to a separation of soluble and insoluble species. The source for the acidity is either atmospheric SO2 or the weathering of sulfides in the subsoil. Water may be provided by snow, rain, or groundwater upwelling. Nearby magmatic intrusions provide heat to melt ground ice. B: The "playa" model, similar to the deposits in Meridiani Planum. A fluctuating groundwater table leads to acid alteration of basalts and precipitation of sulfates in the subsurface. Soluble and insoluble species are not separated. C: Formation by alteration of volcanic ashes due to acidic aerosols and direct deposition of sulfates. Modified after Chevrier and Mathé, 2007.

As the primary Martian rocks also have a basaltic composition and likely contain sulfides, jarosite is a plausible mineral forming at acidic conditions on Mars. The "Burns Formation" informally received its name in honor of Roger Burns, who was first to propose the presence of jarosites on Mars (Burns, 1987, Burns and Fisher, 1990a, b). The coexistence of residual amorphous silica, insoluble jarosite and highly soluble Mg- and Fe-sulfates points to a low water-rock ratio, rapid evaporation and high brine concentrations (Chevrier and Mathé, 2007, King *et al.*, 2004, Tosca *et al.*, 2005): conditions best explained by alteration in situ in a playa environment rather than in an open water body. The hematite spherules (informally named "blueberries") contain 50-60% hematite and 40-50% basaltic material (McLennan *et al.*, 2005). It required a chemically distinct groundwater recharge, which led either to the dissolution of jarosite, or the oxidation of a ferrous sulfate such as melanterite to form hematite. Vugs at mm-scale observed in the "Burns Formation" are evidence for dissolution processes possibly leading to the formation of the hematite spherules, but the survival of sulfates indicates that the groundwater was still saturated with respect to all but the most soluble minerals. This is a further evidence for a highly concentrated brine expected in a playa/interdune lake.

The formation of the chemical sediments in Meridiani Planum is consistent with global hydrological modeling (Andrews-Hanna and Lewis, 2011, Andrews-Hanna *et al.*, 2007, Andrews-Hanna *et al.*, 2010). They indicate this area as a region of groundwater upwelling in the Hesperian. Similar groundwater models also indicate groundwater upwelling in the troughs of Valles Marineris, suggesting that the sulfates of the ILDs are playa deposits as well (Murchie *et al.*, 2009a). However, without in-situ measurements of the sedimentary structures in the ILDs, for example by a rover, the reconstruction of the depositional environment in Valles Marineris is difficult, and alterative formation models are still on the table. They include lacustrine deposition (Lucchitta *et al.*, 1992, Nedell *et al.*, 1987), volcanic (Chapman and Smellie, 2007, Chapman and Tanaka, 2002, Lucchitta *et al.*, 1992) or eolian processes (Nedell *et al.*, 1987, Peterson, 1981) or mass-wasting (Lucchitta *et al.*, 1994). A review of the investigations on Valles Marineris and the invoked formation processes is provided by Lucchitta, 2009a, b. The composition, morphology and stratigraphy of the ILD in Ophir Chasma, the northernmost basin in the central part of Valles Marineris, has been investigated in detail during this study. Results are presented in chapter 6 of this thesis.

An alternative source of the sulfur in found in the Martian rock record to primary pyrrhotite or hydrothermal pyrite is volcanic outgassing of SO_2. In the presence of water it can form an acidic fog rich in H_2SO_4, which can alter volcanic ashes on the surface or already during the eruption (Banin *et al.*, 1997, Settle, 1979, Tosca *et al.*, 2004).

2.2.2.6 Iron oxides

Iron oxides and oxyhydroxides were the first minerals proposed to be present on Mars due to the red color of the planet, because they usually form in alteration systems on Earth. The main phases observed by orbiters, telescopic measurements, and surface investigations by rovers and landers are microcrystalline red hematite (e.g., Bell *et al.*, 1990, Singer *et al.*, 1979), grey and crystalline hematite (Fig. 2.7B; Christensen *et al.*, 2000), and goethite. Hematite can be formed by hydrothermal processes (Catling

and Moore, 2003), palagonitization of volcanic ashes and glass (Bishop *et al.*, 1998), and weathering in tropical lateritic environments (Schwertmann, 1985) or polar environments (Bender Koch *et al.*, 1995), and is the only iron oxide that is thermodynamically stable under present-day Martian conditions (Chevrier and Mathé, 2007, Gooding, 1978).

The nanocrystalline red hematite is the main constituent of the red dust on Mars and is found almost everywhere, with the highest concentrations in the high albedo regions (Fig. 2.7A and B). In the outcrops investigated by the MERs, hematite forms a thin alteration rind of a few mm thickness at most, and the underlying basaltic rocks are unaltered. At the same time, the investigated soil is rich in olivine, which is prone to rapid weathering upon contact with liquid water. This suggests that the nanophase hematite is not formed by aqueous alteration, but by anhydrous solid-atmosphere or possibly solid-frost interaction. This very slow process would have been active during most of the Martian history, but became the dominant process in the Amazonian, when the formation of clays and sulfates ceased (Bibring *et al.*, 2005).

The hematite concretions in Terra Meridiani represent the largest outcrop of the grey and crystalline variety of hematite on Mars and cover approximately 150.000 km² (Christensen *et al.*, 2000), but grey hematite is also observed in Aram Chaos, Candor Chasma and Ophir Chasma (Christensen *et al.*, 2001b, Weitz *et al.*, 2008). As in Meridiani Planum, these outcrops are associated with layered deposits of possible sedimentary origin, suggesting a similar formation from the dissolution of ferric sulfates (e.g., jarosite) or oxidation of ferrous sulfates (e.g., melanterite; McLennan *et al.*, 2005). Grey hematite is spectrally unremarkable in the wavelength range used by OMEGA and CRISM, but the crystalline red variety is detectable, although a distinction from other (crystalline) ferric oxides can be difficult. Ferric oxides and hematite in particular have been detected in several chasms of Valles Marineris in association with sulfates. These locations partly coincide with detections of grey hematite with TES (Bibring *et al.*, 2007, Gendrin *et al.*, 2005a, Le Deit *et al.*, 2007, Mangold *et al.*, 2008, Murchie *et al.*, 2009a, Roach *et al.*, 2010a).

The presence of goethite on the surface of Mars was suggested by spectroscopic data gathered by Mariner, Mars 7 and the Phobos-2 mission (Kirkland and Herr, 2000, Morris and Golden, 1998). Goethite on Earth is often associated with hematite and forms in various alteration pathways (Schwertmann, 1985). Goethite-bearing outcrops have been found in the Columbia Hills (Clovis Rock) in Gusev crater using the Mössbauer spectrometer on MER Spirit (Klingelhöfer *et al.*, 2007). The formation of goethite in an atmosphere rich in water and CO_2 is probable (e.g., Burns and Fisher, 1990b). It is not stable under present day conditions but very slow transformation kinetics make it a metastable phase, explaining its presence on Mars (Burns and Fisher, 1990b, Chevrier and Mathé, 2007, Gooding, 1978).

Ferrihydrite ($5Fe_2O_3 * 9H_2O$) is a further iron oxyhydroxide possibly present on Mars. It is frequently found in terrestrial analogs of Martian soil, especially in palagonitized tephras (Bishop *et al.*, 1998), and is a usual precursor to crystalline phases such as hematite and goethite, depending on pH, temperature and water activity (Chevrier and Mathé, 2007, Schwertmann, 1985). Mössbauer measurements at both landing sites are consistent with ferrihydrite (Klingelhöfer *et al.*, 2004).

The Martian soil also contains magnetite and titanomagnetite ($Fe_{3-x}Ti_xO_4$). These minerals are the main carriers of natural magnetization in primary rocks and therefore this mineral is believed to be the main magnetic phase in the Martian regolith inherited from the parent rock and possibly altered to (titano)maghemite (Chevrier and Mathé, 2007).

2.2.2.7 Hydrated Silica

On Mars, hydrated silica is found in Mawrth Vallis as part of the layered phyllosilicate sequence in Mawrth Vallis, where it occurs together with kaolinite group minerals (Bishop *et al.*, 2008a). It also occurs in layered deposits on the plateaus above Valles Marineris, and in Melas Chasma and Noctis Labyrinthus. It shows as layers 1-10 m thick, and is partly associated with jarosite, indicating acidic formation conditions. West of Juventae Chasma, these deposits form inverted channels, and are thus evidence for fluvial activity in the Hesperian or Amazonian (Bishop *et al.*, 2009, Le Deit *et al.*, 2010, Milliken *et al.*, 2008a, Weitz *et al.*, 2010). Hydrated silicate outcrops are also reported from the MER/Spirit site at Gusev Crater (Squyres *et al.*, 2008). Alteration of basaltic lava, ash or glass, or hydrothermalism, possibly combined with fluvial transport, are discussed as formation mechanisms (Bishop *et al.*, 2009, Le Deit *et al.*, 2010, Milliken *et al.*, 2008a, Weitz *et al.*, 2010).

On Earth, opal mostly forms by diagenetic alteration or (partial) dissolution of sponge skeleton needles and planktic siliceous microfossils like radiolaria and diatoms in marine sediments deposited below the carbonate-compensation depth (~3500 m below sea level) in deep ocean basins, and also in freshwater lakes (Tucker, 1985).

Perhaps more relevant to Martian applications are abiotic forms of opaline silica formation during chemical weathering of silicate minerals. During leaching (incongruent dissolution), mono- and divalent cations (Na^+, K^+, Ca^{2+}, Mg^{2+}) are depleted from the primary minerals such as olivine, feldspars, amphiboles, pyroxenes and glass, leaving a residual coating enriched in Fe^{3+}, Al^{3+} and Si^{4+}, as mono- and divalent cations are easier exchanged (Minitti *et al.*, 2007, White, 1984). The solubility of SiO_2*nH_2O depends on the pH of the solution and is relatively low at pH < 9 and strongly increases at higher values. Aluminum forms several different Al-hydroxyl complexes upon dissolution in water. Their overall solubility is also controlled by the pH, but displays a behavior different to amorphous silica: it is relatively low at pH values between 4 and 9. Therefore, opaline silica alone forms at highly acidic conditions, and all other ions are flushed away. At circum-neutral conditions, Al-dominated phases like montmorillonite, kaolinite or gibbsite form, as both amorphous silica and Al-OH-species are relatively insoluble. The source rocks of opaline silica are not necessarily igneous rocks, but may also be phyllosilicates.

Opaline silica can also occur in hydrothermal systems, where a decrease of temperature at the spring or by mixing of waters decreases the solubility of amorphous silica, as at the Old Faithful geyser in the Yellowstone Park (Matthes, 1993).

2.3 Climate history and driving forces

The relative timing of morphological evidence for liquid water on the surface of Mars and the mineralogical record is intriguing. It is shown in Fig. 2.10. Phyllosilicate formation appears to be constrained to the Noachian era, indicating the

persistent presence of liquid water at moderate pH conditions at that time in the subsurface and/or at the surface (Bibring *et al.*, 2006, Ehlmann *et al.*, 2011). Sulfates are formed mainly during the Hesperian era, whereas the Amazonian era appears to be dominated by anhydrous formation of ferric oxides, which led Bibring et al., 2006, to invoke a new classification of the Martian geological history into the "phyllosian", "theiikian" and "siderikian" eras.

Valley networks are abundant in the Noachian-aged highlands. A peak of valley network formation is observed for the late Noachian, younger valley networks are rare (Carr, 1995, Hynek *et al.*, 2010). In contrast, outflow channels occur as early as in the Noachian, e.g., the Ma'adim Vallis (Irwin et al., 2004 and chapter 4 of this thesis), but their majority was formed in the Hesperian period and episodically reactivated during the Amazonian (Neukum et al., 2010).

Clay formation and valley networks together are strong indicators for a "warmer and wetter" climate in the Noachian (e.g., Squyres and Kasting, 1994), and a major change of surface conditions afterwards, yet exactly "how warm and how wet" is still an open debate (Squyres and Kasting, 1994). Stellar evolution models suggest that the Sun's luminosity near the end of the Noachian (3.8 Ga b. p.) was only 75% of its present value (Gough, 1981, Newman and Rood, 1977). With this luminosity, the Martian atmosphere would have to intercept 85% of the radiation from the surface to raise the temperature to 273 K, which a substantially higher greenhouse effect than the 56% of surface radiation that is intercepted by the atmosphere of Earth (Haberle, 1998). This, in turn, would require a Martian atmosphere with pressures between 0.5 and 10 bar (Haberle, 1998 and references therein), which is hard to reconcile with the high impact flux in the Noachian, which would prevent the formation of a thick atmosphere. In the Hesperian and Amazonian, water was available on the surface

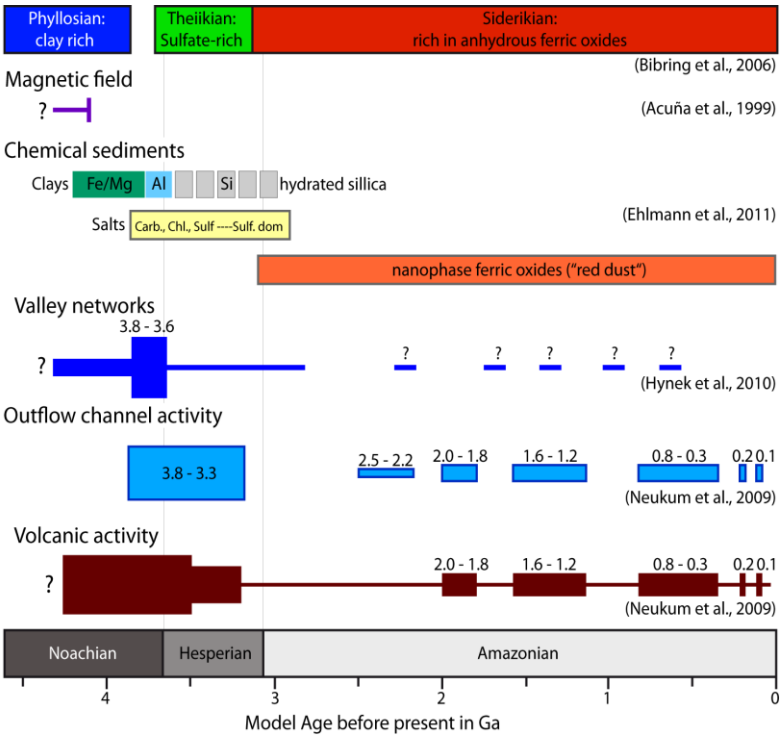

Fig. 2.10: Timing of volcanic and outflow channel activity and the formation of aqueous sediments.

only for short-lived periods, which appear to show remarkable peaks (Fig. 2.10; Neukum et al., 2010).

The reason for the different climate in the Noachian and the climate change afterwards still remains elusive, despite decades of spaceborne observations and theoretical modeling. A concise overview to this problem is provided by Haberle, 1998 and Carr, 2006, from which most of the following discussion has been abstracted.

One possibility for a warmer climate are the greenhouse gases CH_4, NH_3, H_2S and H_2O, if the early atmosphere was reducing. However, isotopic data from Xenon in Martian meteorites indicate a fractionation of Xe and retention of heavier Xe isotopes compared to C1 carbonaceous chondrules. As Xe is too heavy to be lost by thermal escape in the upper atmosphere, the mechanism proposed for its removal is a strong EUV flux from the early sun, which stripped away the lighter Xe isotopes into space (Pepin, 1991). This process would also have removed all lighter gases, including the proposed greenhouse gases. These gases are also destroyed relatively rapidly at timescales of tens to hundreds of years by ultraviolet photolysis, requiring a permanent source for them. Mars would then have acquired a second atmosphere by outgassing after the strong EUV flux was over.

Alternative atmospheric models require a dense atmosphere of 0.5 to 10 bars of CO_2 to raise the equatorial temperature above 273 K (Haberle, 1998), as already mentioned in chapters 2.2.2.2 and 2.2.2.4., yet high pressures of CO_2 would cause a condensation of CO_2 ice at the poles and/or formation of CO_2 clouds, limiting the atmospheric pressure to 2.5 to 3 bars, which would in turn allow equatorial temperatures of only 220 K.

Even if a thick atmosphere once existed, it would have been difficult to maintain against losses by impact erosion and weathering (Carr, 2006). The removal of the atmosphere by impacts depends on the impactor size, which must be large enough to accelerate the impact-created vapor plume to escape velocity, and the density of the atmosphere, with a denser atmosphere being more resistant to impact erosion. This implies that a dense atmosphere could be retained for some time and then rapidly recline, even at a constant impactor flux (Carr, 1999). The crater population observed in Noachian terrains is estimated to be sufficient to remove 50 to 90% of the atmosphere, demonstrating the effectiveness of this mechanism (Brain and Jakosky, 1998). However, impact erosion would be most effective during the time of the strong impactor flux at the beginning of the Noachian and not at the end, where the densest valley networks are observed. A way out of this dilemma could be the proposed peak of impactor flux around between 4.1 and 3.8 Ga, known as the Late Heavy Bombardment (LHB). The main argument for the occurrence of the LHB are radiometric ages from rock samples collected on the Moon, which peak around this age (Tera et al., 1974). It has been cited as the reason for the transition from the "phyllosian" to the "theiikian" era by Bibring et al., 2006. However, the occurrence of the LHB has been debated more than three decades and is still not resolved (e.g., Chapman *et al.*, 2007, Cohen *et al.*, 2000, Hartmann, 1975, 2003, Hartmann *et al.*, 2007, Stöffler and Ryder, 2001).

The second problem with a thick CO_2 atmosphere is that massive carbonate deposits would form and rapidly reduce the atmospheric pressure, which are not found, as mentioned in chapter 2.2.2.4. One mechanism to explain the scarcity of carbonates at the surface would be the formation

carbonates, which would have been flushed into the subsurface by acidic waters, but this process would be more difficult when the temperatures dropped and the soil became frozen and impermeable (Carr, 2006).

A further process leading to a reduction of the atmospheric pressure is sputtering. In this process, ionized atoms in the upper atmosphere are accelerated by the solar wind, collide with each other and are ejected into space. This would be effective after the phase of strong impact erosion (e.g., Kass and Yung, 1995). Both processes together might have removed 95 to 99% of the initial atmosphere (Brain and Jakosky, 1998), resulting in the negligible magnitude of the carbonate deposits found on the surface of Mars.

Thus, while phyllosilicates and valley networks in the Noachian indicate the presence of liquid water, the reasons for these climatic conditions are not resolved. After the Noachian, the surface conditions quickly became hyperarid, not very much different from the modern Martian climate. This is shown by a drop in the erosion rate and large volcanic plains dated to a lower Hesperian age, undissected by any fluvial features. It is also supported by the observation of the MERs that basaltic rocks of Mars contain olivine despite their Hesperian age, which would have been dissolved rapidly under more humid conditions. A further hint towards dry and cold conditions already in the Hesperian are the outflow channels, which require the presence of a thick cryosphere (Carr, 2006).

Age determinations in outflow channels and in volcanic provinces show remarkably similar results, with episodes of activity at 3.8 to 3.3 Ga, 2.5 to 2.2, 2.0 to 1.8, 1.6 to 1.2, 0.8 to 0.3, 0.2 and 0.1 Ga, as shown in Fig. 2.10 and Neukum et al., 2010. This could imply that ouflow events might be related, and possibly triggered, by intrusive or effusive volcanic events, which help breaking up the cryosphere. The ages of the peaks of volcanic and outflow channel activity based on crater counts are in good agreement with peaks of radiometric ages measured in Martian meteorites. This suggests that the episodic behavior might be related to the cooling of the planet interior in a "stagnant lid regime" rather than directly to atmospheric conditions (Neukum et al., 2010).

However, locally Hesperian and Amazonian valley networks are observed, which indicate not only the flow of water on the surface (as outflow channels) but also suggest precipitation and run-off, for example around Valles Marineris (Mangold et al., 2004), in the Newton and Gorgonum basins (this thesis, chapter 4; Howard and Moore, 2011) and elsewhere (Fig. 2.7; Hynek et al., 2010). This requires at least short, local excursions to a warmer climate, which cannot be explained directly by the emplacement of lava.

Further evidence for variations of the climate in the post-Noachian era are glacial and periglacial morphological features. They include debris aprons, lineated valley fill, viscous flow features, pingoes, patterned ground like polygons, and gullies at slopes and crater walls. An extensive overview of periglacial features on Mars is provided by van Gasselt, 2007. The gullies are among the youngest morphological features and show ages in the order of a few millions of years (Malin and Edgett, 2000a), but might have been active even within the last 300.000 years (Reiss et al., 2004). There is a broad consensus that gullies are formed by mass-wasting processes lubricated by water (e.g., Malin and Edgett, 2000a, Mangold *et al.*, 2003, Miyamoto *et al.*, 2004, Reiss and Jaumann, 2003, Védie *et al.*, 2008), although other lubricating agents like CO_2 or CO_2 hydrates

have been put forward as well (e.g., Hoffman, 2000, 2002, Jöns, 2002).

Water may have been provided by melting of subsurface ice by geothermal heat, possibly releasing liquid water held back behind an ice dam (e.g., Gilmore and Phillips, 2002, Malin and Edgett, 2000a) or by melting of snow or ice derived from precipitation (e.g., Christensen, 2003, Costard *et al.*, 2002). Some of the gullies cluster at similar elevations along slopes, which might be taken as evidence for permeable layers exposed at that elevation, and thus for the theory of groundwater-derived gullies, while others are located directly below the top of central peaks of craters and other isolated mounds, where the accumulation of groundwater is hard to conceive, and thus point to a meteoric origin of the water (Kneissl et al., 2009).

Gullies are friable features, which are unlikely to be conserved over long geological time scales, but other features possibly related to the accumulation of surface ice like debris aprons show crater retention ages of up to 1.3 Ga (van Gasselt, 2007).

The required climate excursions to allow the temporal presence of liquid water or even precipitation have been explained by several mechanisms. Baker et al., 1991 and Baker, 2001, proposed that the large floods in the Hesperian, which carved the outflow channels mostly around Chryse Planitia created temporary oceans lasting for up to 10.000 years. This released large amounts of CO_2 previously dissolved in the groundwater and stored as ice in the subsurface into the atmosphere, creating the warmer climate episodes, but this would again have resulted in the formation of carbonates, which are not found.

Alternatively, Segura et al., 2002, proposed that large impacts could have released large amounts of water and hot ejecta into the atmosphere, which would have led to global warming. This process is conceivable for the Noachian, when large impact basins of the required size of 600 km in diameter and larger were formed, but post-Noachian impacts of this size did not occur. The largest crater formed after the Noachian is Lyot. It has a diameter of 220 km and shows no sign of water erosion (Carr, 2006).

Large volcanic eruptions might have released large amounts of CO_2 into the atmosphere to create a greenhouse effect, and abundant volcanic SO_2 might have prevented the formation of carbonates, and episodic volcanic activity is indeed indicated from crater retention ages collected globally by Neukum et al., 2010, as stated above. However, at least locally, there appears to be a misalignment of these events and morphological features for liquid water and/or precipitation at the surface. The youngest gullies formed during the last few millions of years, and although evidence for volcanic eruptions as young as two million years have been found (Neukum et al., 2004), they appear too small and localized to explain a global climate change to form gullies in such large extent as they are observed.

Processes operating in this time scale are changes in the obliquity of the Martian spin axis and the eccentricity of the orbit of Mars around the sun. The calculation of these parameters backward in time is limited by the chaotic nature of this process, and therefore only possible for the last few millions of years. Results of such calculations by Laskar et al., 2002 and Laskar et al., 2004 are shown inFig. 2.11. It shows that the obliquity ranged between 15 and 35° during the last 5 Myr. Before that, the obliquity was higher, with values between 25 and 45°. Together with the eccentricity, ranging from almost zero to 0.12, this resulted in variations in the insolations of the polar caps by a factor of ~3. These variations

would have lead to a redeposition of polar ice towards lower latitudes during episodes of high obliquity in the form of snow or frost, resulting in Martian "ice ages" and periglacial surface features (Head *et al.*, 2003, Head *et al.*, 2005).

The exact timing of variations of orbital parameters prior to a few millions of years is impossible to calculate, but based on the calculations by Laskar et al., 2002, they certainly occurred during the entire history of Mars.

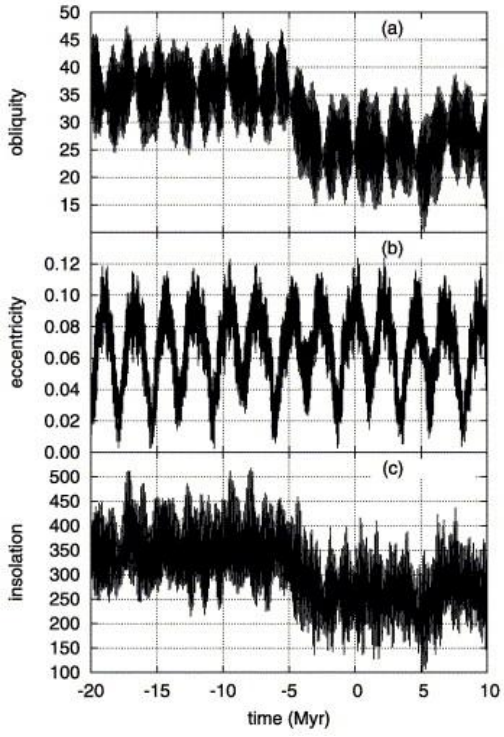

Fig. 2.11: Development of obliquity (a), eccentricity (b) and resulting insolation of the north pole (c) at summer solstice during the last 20 million years and modeled for the coming 10 million years. From Laskar et al., 2004).

Therefore, they are conceivable explanations also for older morphological features, especially those showing rhythmic layering, including the polar caps (Head *et al.*, 2005, Milkovich and Head, 2005, Schorghofer, 2007, Tanaka, 2005, Tanaka *et al.*, 2008), buried ice deposits in the southern mid-latitudes (Holt et al., 2008), gullies, polygons and mantling deposits (e.g., Levy *et al.*, 2011, Madeleine *et al.*, 2009) and valleys on Martian volcanoes, which would have formed by snow accumulation that was later melted by volcanic heat (Fassett and Head III, 2007).

Thus, the emerging picture arising from the erosion rate, valley networks and deltas, and the widespread presence of phyllosilicates in the Noachian aged terrains is that Mars was warmer and wetter during that period of its history. "Warmer and wetter" in this context still refers to a conditions comparable to arid, desertic regions of Earth, but at least during the late Noachian, connected channels existed, and clay formation occurred at the surface. In the early and middle Noachian, the formation of phyllosilicates might have been constrained to the subsurface. The mechanism(s) to explain these climatic conditions are poorly constrained. The lack of large carbonate deposits argues against a strong greenhouse effect due to CO_2 alone.

By the beginning of the Hesperian, the climatic conditions were probably cold and dry, similar to those observed today. Large floods, indicated by the outflow channels, volcanic eruptions, and variations of the orbital parameters of Mars might have been responsible for short-lived climatic excursions, which allowed the presence of liquid water on the surface to create sulfate and hematite deposits and locally valley networks.

Glacial and periglacial features point to variations in the location and extent of ice-rich surficial deposits during the last millions of years as well as in earlier times. Apparently, the recent glacial and periglacial activity left no deposits behind which are detectable in hyperspectral data of OMEGA and CRISM. One exception might be the gypsum-rich dune field near the north pole. In this location, the gypsum is released from

sublimating polar ice, and might have been formed prior to being trapped in the ice cap, or might have formed by the weathering of dust within the ice cap (Massé et al., 2010). This suggests that the liquid water, which is evidenced by gullies, does not remain at the surface long enough to dissolve, transport and accumulate the sulfate in the Martian soil in local lows, as these deposits would be visible in the high-resolution hyperspectral data of CRISM.

3 Theory of reflectance spectroscopy

3.1 The origin of absorption bands

Remote sensing reflectance spectroscopy utilizes the intensity of sunlight, reflected from a planetary body and measured in several hundreds of contiguous wavelength segments to analyze the composition of the observed body's surface and/or its atmosphere. This chapter will introduce the physical principles behind these measurements and clarify the necessary calibration steps before a signal measured at a sensor can be interpreted in terms of surface composition.

The absorptive and transmissive properties of a medium can be described by the complex index of refraction m:

$$m=n-i*k$$

where n indicates the phase speed, k is the extinction coefficient, quantifying the loss of amplitude an electromagnetic wave experiences as it propagates through a material. The absorption within a medium is described by the Beer law:

$$I=I_o*e^{-ax}$$

where I is the observed intensity in the medium, I_o is the initial intensity, a is the absorption coefficient, and x is the length of the transmitted path through the medium. The law is valid, if dispersion and thermal emission of the medium can be neglected, which is the case for the wavelength range of 0.4 to 2.6 µm observed here, under Martian conditions.

The absorption coefficient a is related to the extinction coefficient k and the wavelength by

$$a=4*\pi*k/\lambda$$

The reflectance, often denoted I/F, is defined as the wavelength-dependent reflected energy relative to the irradiation. Thus, the reflectance depends on the absorption coefficient a of the material (which depends of the extinction coefficient and the wavelength), and the mean path of the photons, which in granular media is the grain size.

Absorptions in the wavelength range of 0.4-2.6 µm are caused by three effects: crystal field transitions, charge transfers and molecular vibrational features.

3.1.1 Crystal field transitions

Crystal field transitions occur in minerals containing transition metal ions, which have unfilled inner electron orbitals. The electrons can absorb energy and jump to an excited state. This causes an absorption feature at the wavelength corresponding to the required energy (Burns,

1993). The required energy, and thus the wavelength of the absorption feature, depends on the metal ion and the mineral's crystal symmetry and ligand coordination (Burns, 1993). Among the transition metals (Sc, Ti, V, Cr, Mn, Fe, Co, Ni, Cu and Zn in the first period), iron is the most important constituent of terrestrial and extraterrestrial rocks (Mason, 1966).

3.1.2 Charge transfers

Charge transfers occur when an electron is excited by a photon and moves between neighboring ions (Clark, 1999). Charge transfers between oxygen and ligand occur in the ultraviolet region of the spectrum, the resulting absorption bands are much stronger than those caused by crystal field transitions (Bell *et al.*, 1975). In the case of the abundant iron oxides on Mars, the long wavelength part of these absorption band extend into the visible range, resulting in a red color. These large bands are superimposed by crystal field transitions and weaker charge transfers (Hunt *et al.*, 1971, Morris *et al.*, 1985).

3.1.3 Vibrational features

Vibrational features are caused by vibrations of the atoms in a molecule, excited by an incoming photon. These vibrations are composed from a limited number of simple motions, called fundamentals, which in turn depend on the number of atoms in a particle: for N atoms, 3N-6 fundamentals exist. The position and magnitude of the resulting absorption features depends on the masses of the involved atoms, the strength of the bonds between them, and the vibronic coupling (Hunt, 1977). Excitement of the fundamental vibrations can produce overtones at approximately twice (or 4 times, 8 times, etc) the fundamental frequency, and several overtones or fundamentals can form a combination feature at or near the sum of the involved fundamental or overtone frequencies (Hunt, 1977). The frequencies of the fundamentals of most of the geologically relevant materials are located in the mid and far infrared regions: The fundamentals of Si, Al or Mg associated with O all occur at 10 µm or at longer wavelengths. Their first overtones, which should occur at 5 µm, are not observed. Therefore, in the VNIR, no absorption features of these vibrations are observed.

Only a few molecular groups have high fundamentals or overtones in the VNIR. These are CO_3, SO_4, and, most important, H_2O and OH (Clark, 1999, Hunt, 1977). Water has three fundamentals, which appear at 3.106 µm, 6.08 µm and 2.903 µm, and overtones and combinations at 0.942, 1.135, 1.38, 1.454 and 1.875 µm (Hunt, 1977). The location and strength of the absorption bands caused by water in minerals such as hydrates vary depending on the locations and sites the water molecule occupies, but the bands near 1.4 µm and 1.9 µm always appear and are diagnostic for the presence of water. The hydroxyl group has one fundamental mode near 2.75 µm, with the exact location depending on the sites in the mineral the hydroxyl group is found at. This fundamental has an overtone near 1.4 µm, combination bands occur together with metal-OH stretching vibrations around 2.2 to 2.4 µm (Hunt, 1977).

3.2 Spectral features of minerals on Mars

In the following section, the spectral characteristics of the most important mineral classes that have been identified on Mars will be introduced.

3.2.1 Olivine

Olivine $(Fe,Mg)_2SiO_4$ is a nesosilicate. It forms a solid solution of the iron endmember fayalite and the magnesium endmember forsterite. It is an important rock-forming mineral in mafic and ultramafic rocks. In reflectance spectra, olivine shows a characteristic absorption band between 1 and 1.07 µm (Burns, 1970) caused by crystal field transitions of the contained iron. The shape of the absorption band therefore depends on the Mg/Fe ratio of the solid solution: pure forsterite contains no Fe and therefore shows no absorption band around 1°µm.

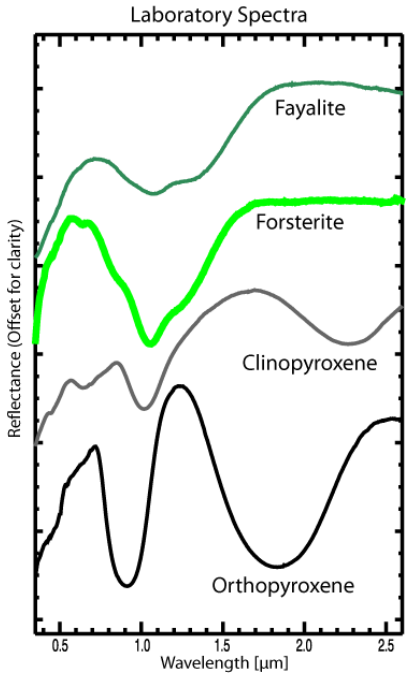

Fig. 3.1: Laboratory spectra of mafic minerals.

3.2.2 Pyroxenes

Pyroxenes are rock-forming minerals in many igneous rocks on Earth and Mars. They are inosilicate minerals, built up by chains of SiO_4-tetraeders and mostly Fe^{2+}, Mg^{2+}, Ca^{2+} and Mn^{2+} cations. Si^{4+} in the tetrahedrons can also be replaced by Al^{3+} and Fe^{3+}. Pyroxenes are grouped into low-calcium, orthorhombic pyroxenes (LCP/Opx) - and high-calcium, monoclinic pyroxenes (HCP/Cpx). Low calcium, orthorhombic pyroxenes form a solid solution of enstatite ($MgSiO_3$), ferrosilite ($FeSiO_3$) and minor modal amounts of the Ca-endmember wollastonite ($CaSiO_3$). Reflectance spectra of these minerals show a strong absorption band at 0.89 to 0.95 µm and a broad band at 1.82-2.09 µm (Adams, 1974). With increasing Fe and Ca content, the location of these absorption bands shifts to longer wavelengths. Weak bands are observed at 0.44 µm and 0.65 µm in the visible spectrum (Burns *et al.*, 1972).

Clinopyroxenes (Cpx, HCP) are richer in Ca and can be spectrally distinguished from orthopyroxenes. They show a strong absorption band around 1 µm, superimposed by absorption features at 0.75 to 0.8 µm (Adams, 1974, Jaumann, 1989). Their second broad absorption band is shifted to longer wavelengths compared to orthopyroxenes and is centered around 2.3 µm (Adams, 1974).

Spectrally, olivine and pyroxenes are distinguished by a much broader absorption band around 1 µm for olivines, which extends towards 1.5 µm. Olivines also lack the typical broad absorption band of pyroxenes around 2 µm.

3.2.3 Ferric oxides

Ferric oxides like magnetite, hematite, goethite and lepidocrocite and ferrihydrite show strong absorption bands around 0.9 µm due to crystal field transitions (Morris *et al.*, 1985). They also show various absorptions close to 0.5 µm, which are partly similar in position and shape, making a distinction among the ferric oxides difficult. On Mars, the situation is complicated by the ubiquitous red dust, which contains ferric oxides with grain sizes smaller than 0.1 µm, called nanophase ferric oxides, minor amounts of crystalline ferric oxide and ferrous constituents (Bell *et al.*, 2000, McCord *et al.*, 1977, Pinet and Chevrel, 1990). The dust shows a broad, shallow absorption band around 0.9 µm, a maximum near 0.75 µm and an absorptional edge shortward of 0.5 µm (Bell *et al.*, 2000). Therefore, occurrences of crystalline ferric oxides are distinguished from nanophase ferric oxides in dust by calculating spectral ratios to dusty regions and the removal of the continuum (Clark *et al.*, 1987): These data reduction methods will be introduced in detail in section 3.4.2.

Hematite (Fe_2O_3) occurs naturally in two forms, red hematite and grey hematite. Red hematite is fine-grained (0.1 to 10 µm) and can be distinguished from other ferric minerals by an absorption band at 0.53 µm, at a distinctly longer wavelength than the remaining ferric phases, and bands at 0.63 µm and 0.86 µm (Morris *et al.*, 1985, Roach *et al.*, 2010a). Grey hematite, with particle diameters >10 µm is coarser-grained than red hematite and spectrally not detectable in the visible and near infrared, but has been identified in the thermal infrared region by the Thermal Emission Spectrometer TES in Meridiani Planum, Aram Chaos and some chasmata of Valles Marineris (Christensen *et al.*, 1992, Christensen *et al.*, 2001b, Weitz *et al.*, 2008) and confirmed by the Mini-TES instrument on the Mars Exploration Rover Opportunity in Meridiani Planum (Christensen *et al.*, 2004b).

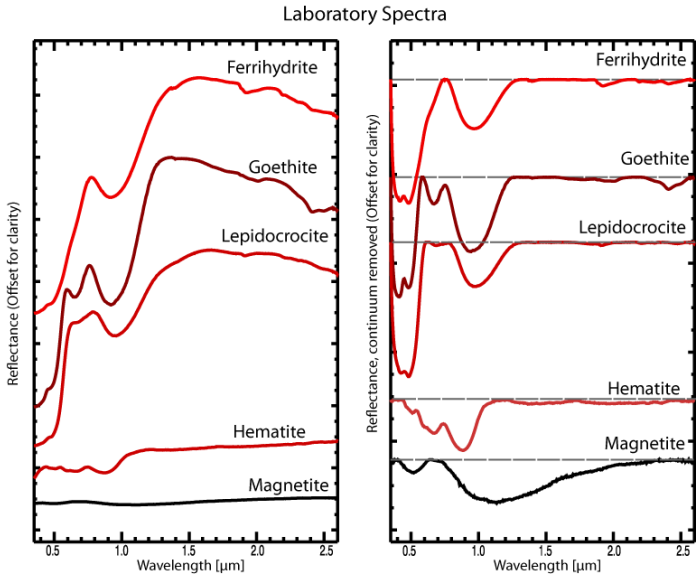

Fig. 3.2: Laboratory spectra of iron oxides.

Left: reflectance spectra. Right: continuum-removed reflectance spectra.

3.2.4 Sulfates

Sulfates are salts of sulfuric acid and are an important mineral group for the exploration of Mars, as many of them form only under restricted conditions and remain stable under narrow environmental conditions (Cloutis *et al.*, 2006).

There are over 350 natural sulfate minerals (Hawthorne *et al.*, 2000). They are generally built up by metal cations (M), SO_4^{2-} tetrahedra and possibly octahedra in the form MO_6 or $M(H_2O)_6$ (Hawthorne *et al.*, 2000). These complexes can appear unconnected, bound only by hydrogen bonds, as in hexahydrite and melanterite, as clusters (romerite, rozenite, etc.), they can form infinite chains (copiapite, ferricopiapite, etc), sheets, as in jarosite, anhydrite and gypsum etc. , or infinite frameworks, as in kieserite or szomolnokite (Cloutis *et al.*, 2006).

Generally, sulfates have spectral features in the VNIR range due to transition elements, H_2O and/or OH, provided they are present, and the SO_4 complexes. An overview of the position of absorption features in the visible and near infrared is shown in the appendix.

Selected corresponding laboratory spectra are shown in Fig. 3.3. Monohydrated (kieserite, szomolnokite), show a broad absorption feature around 2 µm. For szomolnokite, it stretches from 1.98 µm to approx. 2.10 µm, whereas for kieserite, this band extends up to 2.13 µm (Cloutis *et al.*, 2006). Both minerals show a diagnostic absorption band at 2.4 µm. Gypsum has a characteristic spectrum and is easily identified by its multiple absorption bands.

Polyhydrated sulfate have absorption bands around 1.4 µm and 1.9 µm and a drop-off near 2.4 µm caused by the H_2O in the mineral structure. This makes a distinction between the various sulfate minerals difficult, as the hydration state and the involved cation cannot be resolved with standard data analysis approaches, as the differences between the band positions are faint. Therefore, the potential of a more sophisticated spectral analysis method, which exploits not only the band positions, but also the shape of the reflectance spectra (Combe *et al.*, 2008b), is assessed in chapter 5.

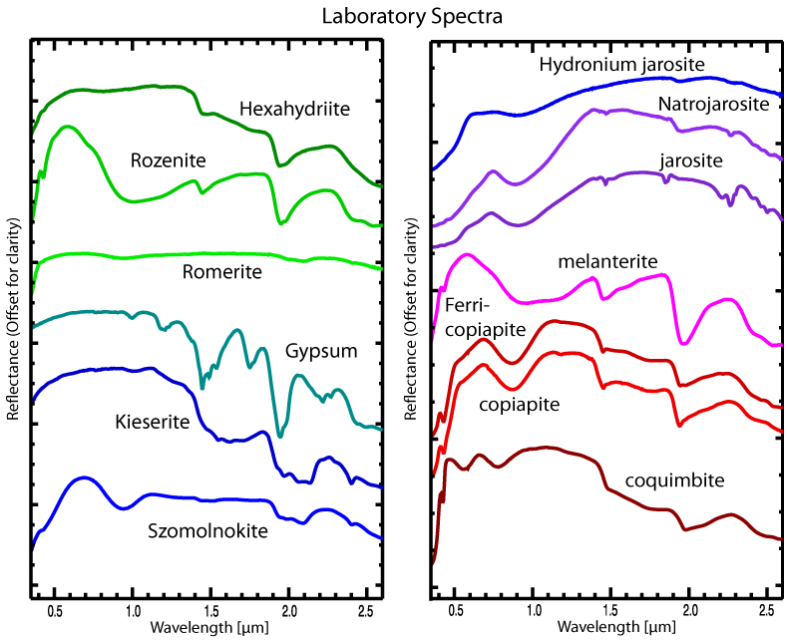

Fig. 3.3: Laboratory spectra of sulfate minerals.

Jarosites show characteristic reflectance spectra with absorption bands at ~1.47, ~1.85 and ~2.27 µm (plus several less prominent bands between ~2.06 and ~2.6 µm). They contain OH, but not H_2O and therefore lack an absorption band around 1.9 µm. Jarosites form under acidic conditions (pH <3, e. g., Höller, 1967) and are found in weathering products of sulfide-containing mine waste on Earth (e. g., Triantafyllidis and Skarpelis, 2006), where oxidation of pyrite, pyrrhotite and other sulfides provides the sulfuric acid (H_2SO_4) required for jarosite formation. Sulfides are common accessory minerals in igneous rocks (e. g., Matthes, 1993) and have also been found in Martian meteorites (e. g. Yanai, 1997). Therefore, similar sulfate formation mechanisms on Mars have been proposed by Burns, 1987, and later by Arvidson *et al.*, 2003, Christensen *et al.*, 2000, Tosca *et al.*, 2005, Tosca *et al.*, 2008a for the sulfates, including jarosite that have been identified in Meridiani Planum (e. g., Klingelhöfer *et al.*, 2004).

3.2.5 Carbonates

Carbonates display absorption bands caused by overtones and combination tones of C-O stretching and bending vibrational modes around 2.3 and 2.5 µm (Hunt and Salisbury, 1971). Example spectra of carbonates are shown in Fig.Fig. 3.4. The exact position of these bands depends on the major cation in the mineral and is found at shorter wavelengths (2.30 and 2.50 µm) for Mg-rich carbonates than for Ca (2.34 and 2.54 µm) or Fe-dominated carbonates (2.33 and 2.53 µm; Gaffey, 1987, Ehlmann *et al.*, 2008c). This points towards Mg-dominated carbonates (magnesite, $MgCO_3$). Carbonates typically also display strong absorption bands at 3.4 and 3.9 µm. These bands are only weakly expressed in CRISM data. Possible reasons are strong absorption features of water around 3 µm from hydrous minerals such as clays or hydrous carbonates found in the same region, a contribution of thermal emission in this wavelength range (Wagner and Schade, 1996) and the lower signal-to-noise ratio of the detector compared to wavelengths <2.7 µm (Murchie *et al.*, 2007a), which all contribute to obscuring these bands

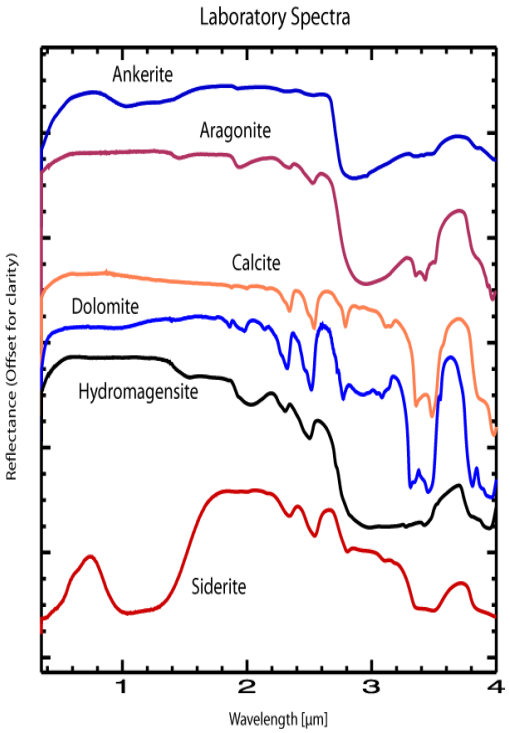

Fig. 3.4: Laboratory spectra of carbonate minerals.

(Ehlmann *et al.*, 2008c).

3.2.6 Phyllosilicates

Phyllosilicates form under a variety of alteration conditions and are important indicators of aqueous weathering processes (e.g., Bishop *et al.*, 2008b, Matthes, 1993).

The structure of phyllosilicates is well known and has been summarized e. g., by Matthes, 1993. They are build up from one or two sheets of tetrahedra, one sheet of octahedra, and one

interlayer. Tetrahedra are usually composed of a Si^{4+}, Al^{3+} or Fe^{3+} cations and O^{2-} anions, the edge-sharing octahedra are built up by 2 to 3 cations (often Fe^{2+}, Mg^{2+}, Li^{2+}, Al^{3+}) and OH^- anions. Trioctahedral phyllosilicates contain octahedra with three predominantly divalent cations, whereas dioctahedral phyllosilicates contain two predominantly trivalent cations and one vacancy. The interlayer can be occupied by a cation (K^+, Na^+, Ca^{2+}, H_3O^+), a vacancy or an octahedral interlayer as in chlorites. Thus, phyllosilicates are classified by the ratio of tetrahedral to octahedral sheets, the charge at the interlayer site between sets of tetrahedra and octahedra layers, and the occupancy of the interlayer space (Bishop *et al.*, 2008b). Examples for structures of the resulting classes of phyllosilicate are shown in Fig. 3.5.

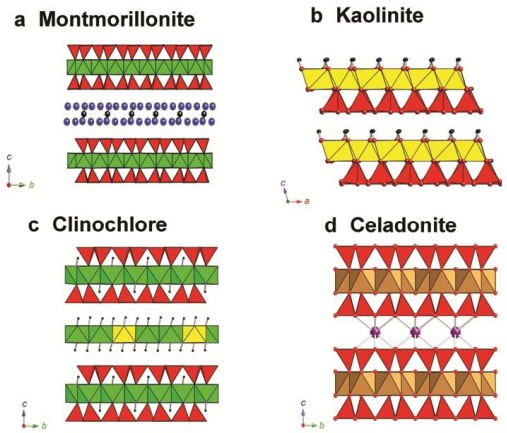

Fig. 3.5: structures of phyllosilicates. From Dyar *et al.*, 2007.

Minerals of the kaolinite-serpentinite group consist of one octahedral and one tetrahedral sheet (1:1). kaolinite is a dioctahedral phyllosilicate with two Al^{3+} per octahedron, serpentines are trioctahedral and contain 3 Mg^{2+} or Fe^{2+} per octahedron. Tetrahedral and octahedral layers are charge-balanced; they do not need interlayer cations and the interlayer site is empty.

Smectites have a ratio of 2:1 between tetrahedral and octahedral layers, and most of the octahedral sites are occupied by trivalent cations (Al^{3+}, Fe^{3+}): they are dioctahedral. Substitution of some these cations by divalent ions results in a slight negative charge (0.2-0.6), which is equilibrated by a small number of cations in the interlayer. This relatively weak bond at the interlayer allows smectites to take in variable amounts of water and swell.

The structure of micas is likewise built up by 2 tetrahedron layers and 1 octahedron layer, but ~25% of the tetrahedral Si^{4+} is replaced by Al^{3+}, resulting in a strong negative charge at the interlayer, which is compensated by K^+, Na^+ or Ca^{2+}. This bond is stronger than in smectites and prevents interlayer water and swelling. Chlorite minerals contain an interlayer of edge-sharing octahedra of Mg^{2+} or Fe^{2+} and 6 OH^-.

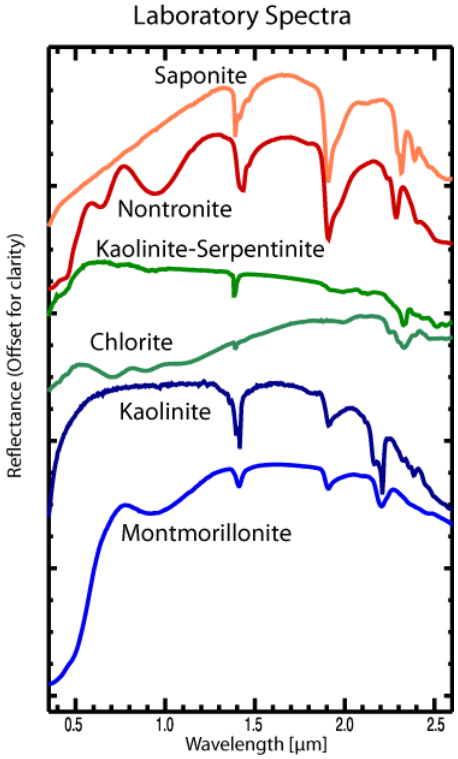

Fig. 3.6: Selected phyllosilicate spectra.

The spectral properties of phyllosilicates in the VNIR differ depending on the presence of transition elements (Fe), structural water, and the metal cations influencing the vibrational energies of the O-H bonds of the OH^- groups they are

coordinated with. Example spectra are shown in Fig. 3.6. Nontronite ($Na_{0.3}Fe^{3+}{}_2(Si,Al)_4O_{10}(OH)_2$•n($H_2O$)), an iron-rich smectite shows absorption bands at 0.5 and 0.95 µm due to electronic transitions in the Fe, and the chlorite spectrum shows a broad band around 1 µm due to the high Fe content. smectites and kaolinite-serpentine type clays show strong absorption bands around 1.4 µm due to OH overtones. Strong absorption bands at 1.9 µm are caused by H_2O in the interlayer space, and are therefore typical for smectite clays like montmorillonite and nontronite. Overtones of this water also produce stronger absorption features around 1.4 µm for smectites compared to the kaolinite-serpentine group. Both groups display strong OH combination bands in the region of 2.2-2.5 µm. The exact position of these bands depends on the cations in the octahedral sites. Generally, Al-dominated clays, with two Al^{3+} cations in the octahedra (dioctahedral clays, e.g., montmorillonite, $(Na,Ca)_{0.3}(Al,Mg)_2Si_4O_{10}(OH)_2$•n($H_2O$), kaolinite, $Al_2Si_2O_5(OH)_4$) have a band near 2.21 µm. This shifts to 2.29 µm for clays with Fe cations (nontronite) and 2.32 µm for Mg-dominated octahedral sites (Bishop *et al.*, 2002a, Bishop *et al.*, 2002b).

More specifically, montmorillonite shows single bands at 1.41 and 2.217 µm and an additional band at 2.44 µm due to Al_2-OH stretching overtones, plus water-related bands near 1.9 µm. Kaolinite shows a triplet at 1.395, 1.405 and 1.415 µm and a doublet at 2.17 and 2.21 µm, and no water band. Nontronite shows Fe_2-OH bands at 1.38-1.39, 2.24 and 2.29 µm plus H-O-H stretching overtones at 1.46 and 1.92 µm. Mg_3-OH tones in serpentines are observed at 1.41, 2.32 and 2.34 µm plus weak bands at 1.46 and 2 µm if water is adsorbed to the surface, as it is not part of the mineral structure. The Mg_3-OH bands are found at 2.33-2.36 µm for chlorites. They show additional features at ~2.25 µm (Bishop *et al.*, 2008b).

3.2.7 Hydrated silica

Another important mineral detectable with VNIR data is opaline silica (SiO_2*nH_2O). It displays spectral characteristics depending on its water content. Fully dehydrated amorphous silica (opal-A) containing only Si-OH groups has spectral bands at 1.37 and 2.20 µm (Anderson jr and Wickersheim, 1964, Bishop *et al.*, 2009). Hydration broadens these bands towards longer wavelengths, resulting in bands near 1.39 and

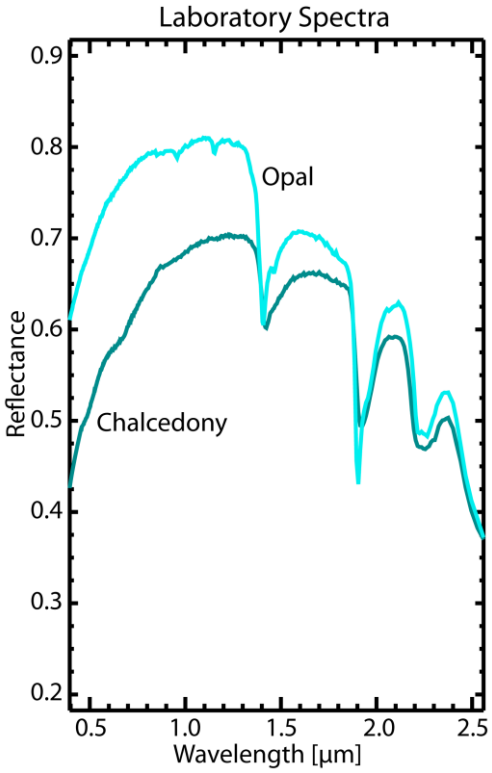

Fig. 3.7: VNIR-SWIR spectra of hydrated silica. The opal sample is a mixture of opal-A and opal-CT. From Clark *et al.*, 2007.

2.21-2.26 µm produced by the Si-OH-vibrations and a band near 1.9 µm due to H_2O (Anderson jr and Wickersheim, 1964; see Fig. 3.7).

Another variety is Opal-CT. It is microcrystalline and consists of very fine blades of Crystobalite and tridymite (e. g., Matthes, 1993). Crystobalite and tridymite are two crystalline forms of SiO_2; other forms are quartz and chalcedony. Spectra of opal-CT show a band near 1.41 µm, a stronger band at 1.9 µm than opal-A and a broader band from 2.21 to 2.26 µm (Bishop *et al.*, 2009, Milliken *et al.*, 2008b). Hyalite is another variety of opaline silica and occurs as a glassy veneer or crust on altered basaltic rocks. It is also named opal-AN and consists of water-containing silica-glass. The band positions of amorphous silica are similar to those of phyllosilicates, but the bands are much broader, allowing a distinction between the two mineral groups.

3.2.8 Spectrally bland minerals

Several important minerals are spectrally bland in the wavelength range used in this study. Whereas mafic minerals like olivine and pyroxenes can be detected, felsic minerals like feldspars, the most important rock forming mineral on Earth, and quartz do not display useful absorption features in the VNIR but can be detected in the thermal infrared. The minerals that are spectrally bland in VNIR data also comprise important anhydrous evaporites such as anhydrite and halite, although the latter appears to exist on Mars, as suggested by THEMIS-IR data (Osterloo *et al.*, 2008).

3.3 Reflectance spectroscopy in remote sensing

The laboratory spectra shown in the previous sections have been acquired under ideal, standardized conditions in a laboratory - reflectance spectra of natural materials in remote sensing data can differ considerably. The reasons for this are manifold. As a consequence, only the detection, not an estimation of the abundance of specific minerals is attempted in this work.

A typical remote sensing scenario is depicted in Fig. 3.8. The sun illuminates a surface element, which is at the same time observed by a sensor through its instantaneous field of view (IFOV). The angles θ_0, Φ_0, and θ_S, Φ_S denote the illumination and observation direction with respect to the surface normal n.

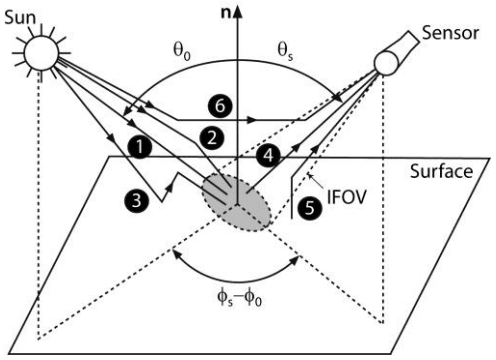

Fig. 3.8: Schematic diagram of a typical observation geometry. Modified from Nascimento and Dias, 2007.

The total radiance at the surface is the sum of direct solar radiation (ray 1), indirect solar radiation scattered by the atmosphere on the ground (ray 2) and radiation from nearby surface regions outside the sensor's field of view scattered onto the observed ground element (ray 3). These three components interact with the observed ground material and get reflected into the sensor (ray 4). The sensor also receives radiation that is scattered by the surface and the atmosphere (ray 5) and by only by the atmosphere (ray 6). A further component of the signal measured at the sensor is the radiation emitted by the surface itself (not shown in Fig.). Thus, the measured signal depends not only on the composition of the observed material, but also on the source of illumination (the sun), the light's paths through the atmosphere, the reflective properties of the

surface, and sensor characteristics. The various effects will be discussed in the following sections, roughly following the path of the light from the source to the sensor.

3.3.1 The Radiation Source: the Sun

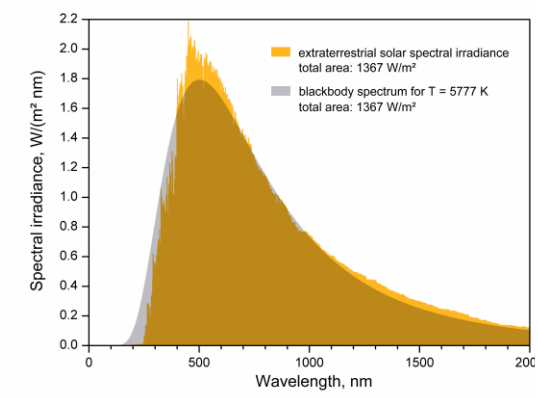

Fig. 3.9: The solar radiation spectrum. It can be approximated by a blackbody radiation of 5777 K.

To compare the radiance measured in the laboratory to the radiance measured by remote sensing, both are divided by the incident radiation on the target to obtain the reflectance (I/F).

The sun emits electromagnetic radiation over a wide range of wavelengths. The relative intensity of this radiation can be approximated by the radiation of a blackbody with a surface temperature of 5777°K (Fig. 3.9). The peak radiation is in the range of the visible light (or better: the sensibility of the human eye is adapted to the solar wavelength range with the highest irradiance).

The emitted solar radiation can be considered time-invariant for reflectance spectroscopy. Its variation with wavelength is controlled by the blackbody radiation and several absorption features of chemical elements in the solar photosphere. The emitted solar spectrum has to be scaled to the distance between sun and Mars at the time of the observation to derive the incident solar radiation (flux) at the top of the Martian atmosphere:

$$F_{Mars}(\lambda) = \left[\frac{F_{Earth}(\lambda)}{\left(\frac{r_{Sun-Mars}}{r_{Sun-Earth}}\right)^2}\right]\cos(z)$$

where

$F_{Mars}(\lambda)$ is incident radiation at top of Martian surface,

$F_{Earth}(\lambda)$ is the solar radiation at semimajor axis of Earth's orbit (1 AU),

$r_{Sun\text{-}Mars}$ is the distance between Sun and Mars at time of observation,

$r_{Sun\text{-}Earth}$ is the semimajor axis of the Earth's orbit (1 AU),

z is the zenith angle of the incident radiation (Levine *et al.*, 1977).

3.3.2 The atmosphere

The solar radiation is affected by the constituents of the atmosphere around the planetary body under investigation (Mars in this study). The constituents of the atmosphere are gases, suspended solid particles and liquid droplets (aerosols) and clouds. The physics of the interaction between radiation and atmosphere is described in textbooks on remote sensing, e.g., Asrar, 1989, Hapke, 1993, Rees, 2001, and are introduced here for completeness.

The most rigorous approach to take atmospheric effects into account are digital models, which reconstruct the physics of electromagnetic radiation interacting with the atmosphere and its constituents. This requires meteorological, seasonal and geographical information (Rees, 2001), which are not always available for Mars at the required spatial or temporal resolution. An example for a radiative transfer model is

MODTRAN (Berk *et al.*, 1987) but several others exist. A similar approach for CRISM data has been implemented by McGuire *et al.*, 2008, but a simpler method for atmospheric correction is generally used for OMEGA and CRISM data, which is described below.

The gases in the atmosphere cause absorption and molecular scattering. The ways by which gases absorb radiation are principally the same as for solids (chapter 3.1), and include electronic transitions and vibrations. They depend on the gaseous composition of the atmosphere. The Martian atmosphere contains 95% CO_2 (Owen *et al.*, 1977), which produces a triplet of absorption features around 2 µm and another feature at 2.7 µm. These absorption bands are not saturated, meaning that the atmosphere is not opaque in these wavelengths, and minerals on the surface of Mars can be unambiguously detected, even if they have absorption bands in the same spectral regions, such as sulfates. In order to estimate and remove the contribution of atmospheric absorptions from the data, the commonly used method is to calculate a transmission spectrum for the atmosphere by comparing spectra from spectrally bland regions at the base of Olympus Mons, where the atmosphere is dense, and at the summit of Olympus Mons (Erard and Calvin, 1997, Langevin *et al.*, 2005, McGuire *et al.*, 2009). A ratio of these two spectra is then the transmission spectrum of two passes through the atmosphere. This reference spectrum is then scaled to the spectrum of interest so that after division by the scaled reference spectrum, the "remaining" surface reflectance is forced to be equal at two wavelengths, one within the CO_2 absorption bands, and one outside (McGuire *et al.*, 2009). The scaling of the reference spectrum is required to adapt it to the surface pressure (and thus CO_2 band depth) at the location of interest, because it varies in a wide range, approximately between 1 and 10 mbars. In mathematical terms, this calculation is stated as follows:

$$I/F(\lambda) = A_L \cos(\theta)\,((T(\lambda))^{\beta}$$

Where:

$I/F(\lambda)$ is the radiance measured by OMEGA or CRISM at wavelength λ, divided by the solar irradiance at Mars distance,

$A_L \cos(\theta)$ is the surface albedo at a solar incidence angle of θ,

$T(\lambda)$ is the amospheric transmission spectrum derived from Olympus Mons, at the same wavelength, and

β is the scalable exponent to force equal reflectances inside and outside the CO_2 bands, so that

$$A_L(\lambda_1) = A_L(\lambda_2)$$

for a constant angle θ, this implies that

$$I/F(\lambda_1))/(\lambda_1)^{\beta}) = (I/F(\lambda_2))/T(\lambda_2)^{\beta})$$

and thus:

$$\beta = \ln\left(\frac{I/F(\lambda_1)}{I/F(\lambda_2)}\right) / \ln(\frac{T(\lambda_1)}{T(\lambda_2)})$$

The β is determined for every spectrum independently, and therefore allows for temporal and spatial variations of CO_2 pressure.

The second important attenuation in the atmosphere is scattering. For particles very much smaller than the wavelength, it can be quantified using the theory of Rayleigh scattering. According to this, the optical thickness of the atmosphere due to molecular Rayleigh scattering can be approximated as

$$\tau \approx \frac{N_A \rho_0}{M_m g} * \frac{128\pi^5 a^6}{3\lambda^4}$$

with

τ being the optical density,

N_A Avogadro's Number,

ρ_0 the atmospheric pressure at the level of reference,

M_m as the molar mass of CO_2,

λ as the wavelength, and

a as the particle /molecular diameter (Rees, 2001). The optical thickness is defined here as the attenuation of the radiation by the entire atmosphere. The above equation shows that due to the dependency on the 1/wavelength with the power of four, this effect is only significant for short wavelengths, approximately < 250 nm. This is the ultraviolet region and the blue part of the visible spectrum. This effect can therefore be neglected for SWIR data of Mars.

The Martian atmosphere also contains larger suspended particles. They consist of dust lifted up from the surface and have a diameter of a few nanometers. During dust storms, the dust load can be so high that the atmosphere becomes opaque, and observations taken at that time are useless. The scattering of electromagnetic waves by these particles is described by the Mie theory, which provides an exact solution for scattering at spherical bodies regardless of their diameter and its relationship to the wavelength, whereas Rayleigh scattering describes an approximation to the Mie theory for the case that the particles are much smaller than the wavelength. "The solution to the Mie problem is lengthy and complicated, and its details are not particularly instructive nor insightful" (Hapke, 1993), but it is interesting to address a few properties of the Mie solution. The Mie solution depends on the (complex) refractive index of the particle and the ratio of its diameter to the wavelength. In the case that the particles have about the same size as the wavelength, the effects are complicated, because interferences occur between waves propagating through the particles and waves passing near its surface. The behavior is therefore dependent of the exact values of the extinction coefficient and the diameter/wavelength ratio. Interestingly, particles can effect a larger part of a wave front than their cross-section, and the scattering can occur to a large part in a forward direction with respect to the propagation of the wave.

The atmosphere may also contain clouds of small ice crystals. These clouds can be easily visible in the data, but can also be very thin, so that their effect is only apparent in the spectra. The scattering properties are also described by Mie theory and approximate those of diffraction at a hole or slit, and the effects are solely dependent on the interference of the waves along the boundary.

In practice, the effects of scattering of aerosols have been treated within this thesis by calculating ratios between spectra from specific outcrops and averaged spectra over spectrally bland regions in the same observation, in order to remove spectral features common to both spectra, and to amplify those of the outcrops of interest.

3.3.3 Effects at the surface

3.3.3.1 Surface illumination conditions

The spectrum of radiation reflected from the surface depends on the composition of the observed material, but also on the observation geometry and the grain size, structure and temperature of the material.

As the radiation hits a surface, a part of it is reflected back, and another part is refracted into the solid matter, where it is either transmitted or absorbed. That is:

$$I_\lambda = R_\lambda + T_\lambda + A_\lambda$$

where I= (solar) irradiation

R=reflected energy

T=transmitted energy

A=absorbed energy

λ=wavelength

The reflective properties of a surface can be described by two endmembers, a specular reflector like a mirror, and a diffuse reflector, like an ideal, rough surface (Fig. 3.10). In the case of specular reflection, the incoming radiation is in part reflected back from the surface at the same angle as the incoming ray, and in part it is refracted inside the material, where it can be absorbed. In the case of a rough surface, the radiation is scattered towards all directions, and the intensity is dependent on the cosine of the angle of the incident ray to the normal. This surface is called a Lambertian scatterer. Whether a surface appears perfectly smooth and thus reflects specular, or is perfectly rough and acts as a Lambertian scatterer depends on the relationship between the degree of surface roughness and the wavelength. A surface can be considered effectively smooth at normal incidence, if the irregularities in surface height, as a measure for the roughness, are smaller than λ/8, which is called the Rayleigh roughness criterion. At higher incidence angles, rougher surfaces can appear effectively smooth, because the criterion is proportional to 1 over the cosine of the incidence angle (Rees, 2001).

Natural surfaces mostly behave like a mixture of the ideal reflector and scatterer at visible and near infrared wavelengths, as shown in Fig. 3.10c and d. The reflective behavior of natural surfaces with

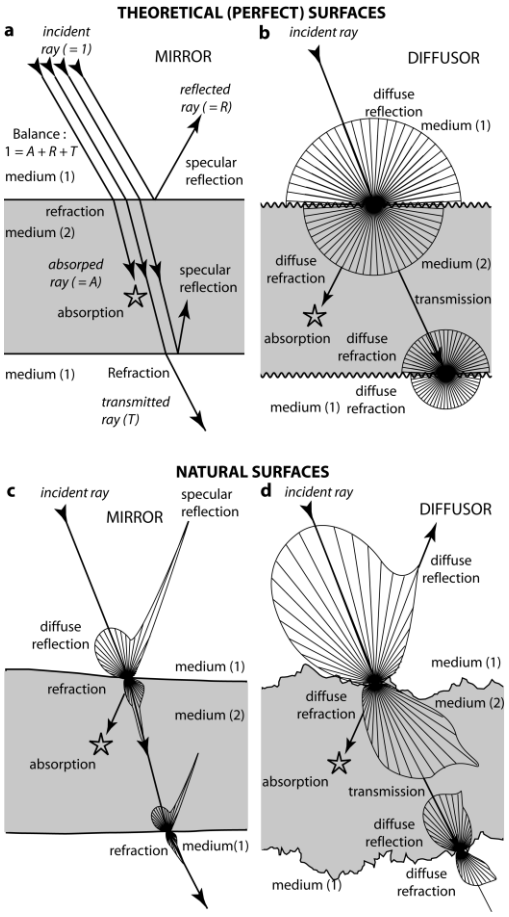

Fig. 3.10: Reflective properties of ideal and natural surfaces.

A: Ideal specular reflection, B: Ideal diffuse (Lambertian) reflection. C: Specular reflection on a natural medium, D, diffuse reflection on natural medium. Modified from Combe, 2005.

respect to the illumination and observation angle is described by the bidirectional reflectance function of that surface (BRDF). It is not known for most surfaces. Its determination requires multiple measurements at various observation conditions, which is difficult to realize outside a laboratory. The HRSC camera is equipped with five panchromatic line scanners, which observe the surface at different observation angles between -18.9° and +18.9° with respect to nadir (Jaumann *et al.*, 2007, Neukum and Jaumann, 2004). Their purpose is to calculate digital elevation models from the multiple stereo data, but also to determine the dependency of the

reflectance of the Martian surface on the observation angle. Despite the five-quasi-simultaneous measurements, several flyovers over the same target region are necessary to determine the BRDF, which makes it an elaborate task that been undertaken only for selected regions of Mars, for example Gusev Crater (Cord *et al.*, 2007). The task is further complicated by the fact that the transmission through the atmosphere is also dependent on the observation angle.

Thus, although the BRDF of the observed surface is in most cases unknown and not Lambertian, as a first approximation it is often considered Lambertian, when a surface reflectance model is needed, as, for example, for the atmospheric correction described above.

Several alternative models to the Lambert model have been proposed, but are used less frequently. A modification of the Lambert model is the Minnaert model, in which the BRDF is given by

$$R \propto (\cos\theta_0 \cos\theta_1)^{\kappa-1}$$

In this case, the reflection in the direction of the surface normal is increased or decreased by the value of κ. For κ=1 the Minnaert model is the same as the Lambert model. Other, more complex models include those proposed by Kubelka and Munk (Kubelka, 1948), and the Lommel-Seeliger law (e.g., Hapke, 1993). This law is widely used in planetary photometry, for example for the calculation of the shape of asteroids from their light curves (Fairbairn, 2005). A model, which also takes the observed increase in reflectivity at a phase angle of zero (illumination source, observer and target are lined up), known as the opposition effect, is proposed by Hapke, 1993. The increase in reflectance is caused by two effects. One is named coherent backscatter opposition effect (CBOE) which describes the constructive interference of backscattered light. It is strongest, when wavelength and surface material grain size are the same. The second is named Shadow hiding opposition effect (SHOE). Illumination of a rough surface always creates small shadows behind the surface irregularities, but these shadows are invisible from the point of view of the light source, explaining the increase in reflectivity.

3.3.3.2 The surface granulometry

A further effect on the observed spectra in reflectance spectroscopy is exerted by grain size. A fine-grained medium will contain more grain interfaces per unit area observed by one pixel of the instrument (the IFOV). Therefore, a finer grain leads to stronger scattering of the light at the surfaces of the grains, and a smaller fraction of radiation, which is refracted into the grain, where it may be absorbed. Inversely, the albedo decreases with increasing grain size. The depth of absorption bands increases with the average size of the grain. The absorption bands reach maximum (saturation) at grain sizes above 250 µm for most materials, because larger grains will become effectively opaque. In mixtures of grain sizes, as in natural materials, the reflective properties are dominated by the smallest grains, even if they make up only a minor fraction, making a deduction of modal compositions or grain size measurements from reflectance spectra difficult (Pieters, 1983). The grain size also effects the angular dependence of the reflectance, as noted above.

3.3.3.3 The surface composition

The entire purpose of hyperspectral reflectance measurements is the determination of the surface composition, and it has been shown in chapter 3.2 that specific minerals display characteristic absorption bands. However, the footprint of one pixel of CRISM has a minimum size of approximately 18 by 18 meters, and for OMEGA,

one pixel can cover an area of several square kilometers. Even if the spatial resolution of the instrument was as high as that of the highest resolved multispectral imager (HiRISE; 25 cm/pixel), it is evident that the surface material might be composed by not only one mineral type, but several different minerals. In the case of basaltic rocks, the individual pyroxene, feldspar and other minerals (e.g., olivine) can be only discerned under a microscope. Therefore, the spectra measured from a remote sensing platform will always be mixtures of minerals, which may or may not display spectral absorption bands. In the thermal infrared region of the electromagnetic spectrum, the measured spectrum can be regarded as a linear combination of the spectra of the individual minerals observed in one pixel of the instrument. Thus, an "unmixing" of the observed spectrum can be calculated, in which the areal fraction of each mineral type present on the ground is estimated, providing a kind of modal composition.

Unfortunately, for the visible to short wave infrared, this is only possible under several assumptions, which are not necessarily valid. In this wavelength range, mixtures of minerals have to be separated into areal mixtures and intimate mixtures. An areal mixture is present when two macroscopic outcrops, which both are composed of only one type of mineral, are observed in the same pixel of the instrument. An example may be a sand dune, composed of pyroxene-rich (basaltic) sand, next to a pure sulfate deposit. In this case, the observed spectrum is a linear mixture of the composition of the two outcrops. The "pure" spectra are then named endmember, and their fraction in the observed mixed spectrum represents the areal coverage of the outcrops in the pixel.

On the other hand, in an intimate mixture, grains of two or more minerals are mixed together, so that electromagnetic radiation interacts with different types of minerals consecutively. The observed mixed spectra will then be a non-linear combination of the endmember spectra, and an estimation of the modal composition is complicated. An example for this case might be a very thin sheet of basaltic sand on a sulfate outcrop. These examples show that both types of mixtures can occur naturally very close to each other, and a decision, whether the assumption areal mixtures is valid or not, can be problematic.

3.3.3.4 The effect of temperature

The spectral signal measured at the sensor is composed of two components, the sunlight reflected from the surface, and the radiation emitted by the surface itself. Like any other object with a temperature above absolute zero, the surface of Mars emits radiation, which is the blackbody radiation. Similar to the radiation of the sun, its wavelength spectrum is temperature dependent. The wavelength where the blackbody radiation is at its maximum is described by Wien's displacement law:

$$\lambda_{max} = \frac{A}{T}$$

where A is a constant with the value $2.898*10^{-3}$ [K*m], and T is the absolute temperature in Kelvin (Rees, 2001). For the average surface temperature of Mars of 210 K (Kieffer *et al.*, 1992), this yields a wavelength of 13.8 µm. The intensity of emitted radiation drops quickly towards wavelengths shorter than the location of the maximum, but it becomes noticeable within the detector ranges of OMEGA and CRISM. A model of the thermal emission of Mars compared to the incident solar radiation by Erard, 1998, shows that at wavelengths longer than 3.5 µm, the

thermal emission reaches 1% of the incident solar radiation, and should be taken into account. In the following case studies of this thesis, only the wavelength range up to 2.6 µm has been used, because this is the range were the characteristic absorption bands occur. Therefore, the thermal emission of the surface could be neglected.

An increase in temperature of the observed material increases the vibrations within its molecules. This, in turn, leads to wider and deeper absorption bands (Moroz *et al.*, 2000). It is therefore important to notice that reflectance spectra are influenced by the temperature even outside the range of thermally emitted radiation. A further, indirect effect of variations of temperature of the target material can be the inclusion and removal of water molecules into and out of the crystal lattice, which would also effect the reflectance spectra.

3.3.3.5 The Adjacency effect

The adjacency effect is related to both the composition of the target material at a large, macroscopic scale, and to the atmospheric conditions. Light scattered by material out of the IFOV of the sensor can be directed by atmospheric scattering into the sensor, or light may be reflected from the ground outside the IFOV into the observed region, before it is reflected back to the sensor (paths 3 and 5 in Fig. 3.8). These rays contribute to the at-sensor-radiance, and therefore alter the observed spectrum. This is called the adjacency effect, and depends on the radiance contrast between the material within the IFOV and around it, and also on the wavelength. Models have been developed to take this effect into account (e.g., Sanders *et al.*, 2001), but they have not been applied in this study.

3.3.4 Instrumental effects

Finally, instrumental effects of the sensor itself can influence the measured spectra. Ideally, the instrument has been thoroughly calibrated before the mission, and a check of the stability of the calibration is possible during the mission. The calibration of OMEGA and CRISM allow a calculation of measured digital numbers (DN) into physical units of radiance, but certain effects are not accounted for in the calibration. For example, spectra of the CRISM instrument contain artifacts near 1.65 µm, which are caused by a filter boundary at that location. Another effect common for hyperspectral line scanners like CRISM is the "spectral smile". In line scanners, the instrument observes a single line on the ground, oriented perpendicular to the direction of flight of the sensor. For each element of the line, it is split into a spectrum by a prism or grating, and the resulting spectra are observed in the long-direction of a CCD array, while the across-direction of the array represents the spatial dimension on the ground. In the case that the spectra are not perfectly aligned with the sensor array, the location of a specific wavelength on the sensor array can describe a curved line, the so-called "spectral smile". This effect leads to an apparent shift of wavelengths of spectral features across the sensor/image, which can cause misinterpretations. This effect does not occur at the OMEGA instrument, because its near-shortwave infrared data is collected in the whiskbroom mode, so that every spectrum is measured by the very same sensor line.

While some of these effects can be quantified in order to remove them during preprocessing, others, like atmospheric effects, are transient and therefore more difficult to handle. This is the reason why automatic data interpretation algorithms still require human interaction and

often fail completely to identify specific minerals present in the observed ground element. To mitigate this problem in Earth observing remote sensing, reference measurements are taken in the field, ideally at the same time as the remote sensing data is gathered: Data, which are not available for Mars, as none of the landed instrument carried a similar spectrometer as the two instruments used in this study

3.4 Data Processing and Data Analysis

3.4.1 Data preprocessing

The various effects that alter the spectra of minerals when measured from a remote platform like an airplane, satellite or spacecraft compared to laboratory spectra measured under standardized conditions have been described in the previous chapter, and the concepts to mitigate them have been introduced. This section will contain a technical description of the software implementation of these processing steps for the data from the OMEGA and CRISM instruments, respectively. The reader not interested in these technical details of the internet access points to the data, the file naming conventions and the step-by-step description of the preprocessing may jump directly to the next section.

3.4.1.1 OMEGA data preprocessing

The released OMEGA data is stored in ESA's Planetary Science Archive (ESA PSA) as well as NASA's Planetary Data System (NASA PDS). The entire data, including observations not yet released to the general public, is also stored on internal servers at the Freie Universität Berlin, where this thesis has been written.

The data organization is documented in the OMEGA Experiment Archive Interface Control Document (OMEGA EAICD, Poulleau *et al.*, 2005) and further metadata files provided at ESA PSA. The data corresponds to a processing level of 1B, indicating that it has been formatted to PDS standards. The science data has been sorted by orbit number, decompressed and separated from housekeeping and geometry data, but is still uncalibrated. Science data is stored in the "cube" format (.qub). In every observation sequence of OMEGA, the observation mode is changed normally from the 128 pixel wide mode to the 64, 32 and finally 16 pixel mode and back, as the spacecraft approaches and retreats from the Martian surface due to the elliptic orbit of Mars Express. The resulting observational data is stored separately according to the change of observational mode in the observation sequence. The files are named following this convention: ORBnnnn_x.QUB, where nnnn is the orbit number and x is the sequence number, starting with 0. Housekeeping and geometry data is stored in a separate file named ORBnnnn_x.NAV. The physical meaning and units of the individual bands in the geometry data files is documented in the OMEGA EAICD (Poulleau *et al.*, 2005).

Shapefiles of the footprints of the OMEGA data have been used here to identify OMEGA observations over the study areas in this thesis. They were extracted from the geometry files and provided for internal use at the Freie Universität Berlin planetary science group by Walter *et al.*, 2006.

The science data were extracted from the archived files and calibrated using the software scripts provided with the data at ESA PSA. For this study, the version SOFT04 was used, released in October 2006. The software consists of several scripts for specific processing steps and is written in Interactive Data Language (IDL).

A complete calibration (as used in this study) consists of the following steps. First, the data is extracted from the PDS/PSA file using *readomega.pro* provided in PSA as part of SOFT04. This routine converts the digital numbers in the original files into irradiance data with physically meaningful units (radiometric calibration). It also removes various instrumental effects such as bit errors and implements a smear correction. The data is returned as IDL variables (not files), named *jdat* for the calibrated data and *geocube* for the housekeeping data and geometry, together with further variables.

The OMEGA sensors degrade over time, and some elements of the CCD, corresponding to individual wavelength bands, become unreliable. The software provided in PSA therefore contains a file showing the number of the first orbit in which problems with a specific wavelength have been observed. This file is used to identify the "unusual" data according to the orbit number of the observation. Data in the "unusual" bands is multiplied by $1*10^{30}$. This creates strong spikes in spectra at the locations of the bands that should be used with caution, which are visually easily recognizable, yet the data can still be used for spectral ratios.

The next step is the atmospheric correction using the "volcano scan technique" as in Langevin *et al.*, 2005. The IDL software routine for this step (*atmocor_050517.pro* and *atmocor_120905.pro*) was written by Yves Langevin and was released only within the OMEGA science team, in which Prof. Neukum is a member. This routine reads in the calibrated science data (variable *jdat*) together with geometric information (variable *geocube*) and returns the variable *kdat*, which contains the irradiance corrected for the CO_2 bands caused by the Martian atmosphere, as described in the previous section. The irradiance has to be converted to reflectance (I/F) data using the incident solar spectrum and the distance between Sun and Mars at the time of the observation. This is also included in the atmospheric correction routine.

The data in the variables created by the software provided with the OMEGA data is organized as a three-dimensional cube with the dimensions ordered as *row-spectral dimension (spectel)-column*, whereas the ENVI software, which is used later for data analysis, requires the data to be ordered in *row-line-spectel*. Also, the output data arrays still contain the data of all three sensors of OMEGA, in a somewhat counterintuitive ordering. The first data is from the IR "C", channel (0.93-2.73 µm), then comes the data from the IR "L"-channel (2.55-5.1 µm), and finally the data from the visible spectrum (0.38-1.05 µm). While the visible channel is a push broom scanner, the IR channels are measured with a common whiskbroom mirror. Therefore, visible and IR channels do not necessarily coalign perfectly, and a separate geometric correction (projection on the planetary body) is advisable. Accordingly, the geographic coordinates of every pixel in the observation are provided separately in the .NAV file and the geocube variable. Thus, the final preprocessing steps are a conversion of the data ordering to that required by ENVI, the separation of the data of the three OMEGA channels, and the saving of the science and geometric data on the hard disk in a file readable by ENVI.

After this calibration, the data is imported into the commercial imagery data analysis software ENVI. It is likewise written in IDL. IDL and ENVI are commercial products available from Exelis Visual information Systems (www.exelisvis.com). ENVI is used for the analysis of the data and its geometric registration. Finally, the hyperspectral

data is overlain with further mostly higher resolving data from HRSC, CTX, MOC and HiRISE in the geographic information system ArcGIS from ESRI (www.esri.com).

3.4.1.2 CRISM preprocessing

The CRISM preprocessing is very similar to that of OMEGA. The main difference is that a plug-in for ENVI named CRISM Analysis Toolkit (CAT) is provided by the Planetary Sciences Group at the Brown University. It is available at the PDS Geosciences Node (http://geo.pds.nasa.gov/missions/mro/CAT_v6_7.zip). This tool provides a user-friendly graphical interface to similar processing steps as required for the OMEGA data, without the need for a console input.

The CRISM data are released regularly via the NASA PDS. The data is collected in several modes, with the most important being the "full resolution targeted" (FRT) mode with the full spectral and spatial resolution, the "half resolution long" mode (HRL), having a spatial resolution reduced by a factor of 2, but a footprint of roughly twice the size of a FRT observation, and the "multispectral mode" with spatial resolutions of 100 or 200 m/pixel and only selected spectral channels. The naming convention is as follows:
(ClassType)(ObsID)_(Counter)_
(Activity)(SensorID)_(Filetype)(version).(Ext),
where ClassType stands for the observation mode (FRT, HRL, MSP or other, less frequent type), ObsID is a hexadecimal ID number of the observation, Counter is the number of the data record within that observational sequence, taken as the gimbaled sensor approaches to and departs from the target, Activity is the type of data (e.g., IF for I/F, RA for radiance, and several codes for calibration measurements), SensorID is S or L for the visible or the infrared sensor of the instrument, and Filetype describes the processing level (EDR for experimental (raw) data, TRR for targeted reduced data. The full description of the naming scheme is provided in the CRISM Data Product Software Interface Specification (Murchie *et al.*, 2007b).

A convenient access point to find CRISM data in a for a specific geographic region is the CRISM map website (http://crism-map.jhuapl.edu/), where the location of every targeted CRISM footprint is displayed on a MOLA map of Mars. The map also provides a preview of the most important spectral indices for every observation, so that an easy visual assessment of the data quality is possible. The CRISM maps links to the PDS archive, where the data is stored and may be downloaded for further investigation.

The data from one observation consist of two files, one for the visible-near infrared (VNIR) data, and one for the infrared (IR) data, which are collected by two different sensors. A file with housekeeping and geometric information with the Filetype DDR corresponds to each of these to observation files, and a label file (extension .lbl), describing the content of the main file according to the PDS standards is provided with each data file. This makes a total of eight files (two observations, two geometry/housekeeping files, four label files), which have to be downloaded.

Unlike the OMEGA data, the released CRISM is already calibrated to radiance (Activity: RA) or reflectance (Activity: IF). The first step after download is therefore a simple conversion from the PDS data ordering scheme to the CAT ordering scheme, which is based on the requirements of the ENVI software. The next step is an atmospheric correction of the data. the CAT interface provides several options for this. The same "volcano scan technique" can be used as for the OMEGA data (Langevin *et al.*, 2005), but an

improved algorithm using different wavelengths is also implemented (McGuire *et al.*, 2009). The user has also the choice between different measurements of the atmospheric transmission spectrum measured at Olympus Mons at different dates. The idea is that some instrumental artifacts of the CRISM instrument may not have been accounted for in the calibration of the data, and may change over time. Therefore, an atmospheric transmission spectrum measured at the same time or close to the same time as the surface observation of interest might contain the same time-dependent artifacts, so that they cancel out during the atmospheric correction. In practice, ice clouds have been present over Olympus Mons when some of the reference atmospheric transmission spectra were taken, so that using these spectra introduces unwanted absorption bands into the observation, which were not present in the raw data. Therefore, using this option rather than the default volcano scan 61C4, which is cloud-free, requires a further control step by the operator.

The CRISM CAT also contains several filtering options to reduce spatially and spectrally distributed noise (Parente, 2008). Using these filters requires the operator to check visually, if the filtering is successful or if it removes actual information from the data. CAT can also calculate specific spectral parameters and project the data for comparison with other imagery.

3.4.2 Data Analysis

After removal of the most severe instrumental effects, a correction for the atmospheric contribution to the spectra and a suppression of random noise, the actual data analysis can take place. The high dimensionality of the data, having hundreds of bands in the case of OMEGA and CRISM means that the dimensionality of the information present in the data is usually higher than that of the data itself. This has two main consequences: Even in complex image scenes, with many different types of minerals (or man-made objects) present, spectra can be found, which are unique to these objects. This is a major advantage over multispectral data, as it allows a comparison of spectra measured from a remote sensing platform and laboratory spectra. On the other hand, the data is more difficult to analyze visually. Only up to three different bands can be visualized as a false color image by selecting them as the red, green and blue channel of an image, respectively. Therefore, for multispectral images with only a few channels, it is still feasible to find the most interesting band combinations by trial and error, and the usually higher spatial resolution as compared to hyperspectral imagery allows for the exploitation of the spatial continuity of features of a specific hue to identify and map the heterogeneity of the surface. For hyperspectral data, this is more complicated. The large number of spectral bands means that most of the bands are highly correlated so that selecting and visually inspecting all possible combinations of three channels out of the hundred channels is not a feasible strategy. Instead, other methods are required to reduce the data dimensionality. The case is further complicated by the various effects introduced in chapter 3.3 that influence the measured spectra. As a result, measured spectra often look very similar to laboratory spectra to the human eye, but subtle differences can cause important difficulties for automatic detection and identification algorithms.

The methodology of the exploitation of hyperspectral data is an active field of science, and hundreds of scientific articles have been published to introduce hyperspectral data analysis techniques. A recent overview is provided in

Kaufmann *et al.*, 2009. The methods may be grouped into statistical methods and model-based methods. Statistical methods aim to describe the internal variation of the remote sensing dataset, in order to identify clusters of data or to identify a limited set of spectral endmembers, which in the ideal case represent pure surface materials. These endmembers may then be mathematically combined to reconstruct the remaining image spectra. On the other hand, model based approaches use a priori information of materials possibly present in a scene to identify and map them in the data. Possibly the simplest method in this sense is the calculation of spectral parameters which describe the presence and depth of absorption bands at known wavelengths, which can be attributed to specific minerals or groups of minerals.

3.4.2.1 Spectral parameters

The calculation of spectral parameters is straightforward and intuitive, and is therefore the by far most commonly used method in the hyperspectral investigation of Mars using OMEGA and CRISM data. It is also the method used in the case studies on the knob fields in Terra Cimmeria (chapter 4) and Ophir Chasma (chapter 6) in this thesis.

The spectral parameters used in this thesis are those described in Pelkey *et al.*, 2007, Murchie *et al.*, 2007b and Murchie *et al.*, 2009b. They are shown in the appendix. These parameters were defined for wavelengths of the CRISM instrument, and were adapted to the closest band/wavelength of OMEGA, when required. At locations indicated by an increased spectral parameter, spectra were selected and visually compared to laboratory spectra.

To enhance the spectral contrast and to suppress instrumental artifacts not removed by the preprocessing, band ratios between regions of interest and spectrally bland regions were calculated. Spectra were averaged over at least three by three pixels and selected in the same column of the unprojected CRISM data, or were averaged over larger "regions of interest" (ROI) containing several dozens to hundreds of spectra.

The disadvantage of using "spectral summary parameters" is that they are not always unique for a specific mineral or even class of mineral. For example, many phyllosilicates and polyhydrated sulfates display an absorption band near 1.9 µm, making a decision between many matching candidate minerals based on this parameter alone ambiguous. Spectral parameters are only sensitive to the shape of the spectra at specific wavelengths, usually where absorption bands are located, but they do not take the overall shape of the spectra into account, which might provide a useful hint on the type of the observed mineral as well.

3.4.2.2 Spectral mixture analysis with the Multiple-Endmember Linear Unmixing Model MELSUM

Several different strategies have been proposed for more advanced data analysis techniques. They include expert systems like Tetracorder (Clark *et al.*, 2003), which uses a customized spectral fit to reference spectra stored in a library. The Modified Gaussian Model (Sunshine *et al.*, 1990) uses combinations of Gaussian curves to model the absorption bands of mafic minerals in order to estimate the composition of these solid solutions. It has also been applied to data from Mars (Bibring *et al.*, 2005, Combe *et al.*, 2008b, Mustard *et al.*, 2005).

A method specifically designed to account for mixtures of minerals, (which are expected at the spatial resolution of OMEGA and CRISM data),

is the spectral mixture analysis (SMA, Adams *et al.*, 1986). This method requires a set of reference spectra of "pure" materials, which may either come from a laboratory or from the image itself. If the reference spectra are derived from the image itself, they can be selected by the operator from regions which are known or expected to contain only one type of material, and thus provides spectra relatively pure and unaffected by other materials present in the scene. Statistical methods like the Principal Component Analysis (PCA) or the Minimum Noise Fraction transform (MNF; Green *et al.*, 1988), which is based on PCA, may be used to reduce the dimensionality of the data prior to the selection of the endmembers, and processing schemes like the Pixel Purity Index (PPI; Boardman *et al.*, 1995) or N-FINDR (Winter and Shen, 1999) may be used to extract the endmembers automatically.

The spectral mixture analysis usually assumes a linear mixture of spectra of pure endmember materials, although this assumption is only valid for areal mixtures, but not intimate mixtures or layers of translucent materials, and it is often not evident which type of mixture dominates in the given scene (Rencz, 1999). Despite this uncertainty, SMA has been demonstrated its value in analyzing the variability of remote sensing data (e.g., Adams *et al.*, 1986, Ramsey and Christensen, 1998, Adams and Gillespie, 2006, Combe *et al.*, 2008a, Combe *et al.*, 2008b).

In this thesis, the spectra mixture analysis scheme MELSUM (Combe *et al.*, 2008b) is used to investigate CRISM data of Juventae Chasma (chapter 5). Unlike in the original SMA of Adams *et al.*, 1986, this analysis scheme returns no negative endmember coefficients, which would not be meaningful, and allows the user to constrain the number of endmember spectra used in the mixture. Details of MELSUM are introduced in chapter 5.

4 Knob Fields in the Terra Cimmeria/Terra Sirenum Region of Mars: Stratigraphy, Mineralogy and Morphology

The following section has been submitted as

Wendt, L., Bishop, J. L. and Neukum, "**Knob Fields in the Terra Cimmeria/Terra Sirenum Region of Mars: Stratigraphy, Mineralogy and Morphology**" to ICARUS.

4.1 Abstract

We investigate the stratigraphy, morphology and mineralogy of five major knob fields in the region between Terra Cimmeria and Terra Sirenum on Mars based on HRSC, CTX, MOC and HiRISE imagery together with hyperspectral data from CRISM. The knob fields comprise Ariadnes Colles, Atlantis Chaos and Gorgonum Chaos and further, unnamed fields of mounds. They have been mapped in previous studies as Hesperian or Amazonian units and are located within the shoreline of the proposed "Eridania lake", the putative source of Ma'adim Vallis. The mounds contain Mg/Fe-bearing phyllosilicates and locally Al-rich phyllosilicates. Our geological mapping shows that the knob fields have a late Noachian age, which indicates later phyllosilicate formation than typically observed on Mars. The knob fields formed by alteration of the "Electris deposit", an airfall deposit possibly rich in basaltic glass (Grant and Schultz, 1990, Gradational epochs on Mars, - Evidence from west-northwest of Isidis Basin and Electris, Icarus 84, 166-195), in local depressions, possibly in the Eridania lake. The spectroscopic detection of phyllosilicates here may indicate that liquid water persisted longer in this region than elsewhere on Mars. The knob fields are embayed by the Hesperian ridged plains. Numerous valleys carve into the ridged plains and document that the aqueous history of this region continued into the Hesperian and Amazonian. The study area is traversed by the Sirenum Fossae. These graben appear to post-date the aqueous activity in the study area except in the Gorgonum basin, where a lake develeoped after their formation.

4.2 Regional Context and Scope

The region between Terra Cimmeria and Terra Sirenum between 164°E and 196°E and -27°N and -39°N on Mars features five major enigmatic fields of mounds, including Ariadnes Colles, Gorgonum Chaos and Atlantis Chaos, and several smaller, unnamed groups of knobs and individual mounds with a similar surface morphology, albedo, and texture.

The knob fields are found within local depressions between 70 and 240 km wide. These basins show rounded, but not circular outlines and display a concave, “bowl-shaped” internal relief of up to 1.5 km. This is unusual for impact basins of this size on Mars, which are usually circular or oval, and flat-floored (Irwin *et al.*, 2004). Thus, if these basins are indeed degraded impact basins, they must have formed by the erosional

integration of several sub-basins, as suggested for the Gorgonum basin by Howard and Moore, 2004. Some of the basins are outlined by concentric ridges that resemble wrinkle ridges (Baker and Head, 2009) and appear to be part of a regional ridge system induced by compressional stresses exerted from the Tharsis rise (Capitan and Van De Wiel, 2010). This is a further indication for tectonic formation or modification of the basins rather than an origin directly related to impact excavation.

The knob fields have been mapped based on Viking imagery as Hesperian or Amazonian chaotic terrain (Greeley and Guest, 1987, Scott and Tanaka, 1986), but have no direct link to outflow channels and show other differences to chaotic terrains in the Circum-Chryse Region (Capitan and Van De Wiel, 2010, Grant and Schultz, 1990, Howard and Moore, 2004, Moore *et al.*, 2003). Therefore, we use the terms "knob field" or "knobby terrain" rather than chaotic terrain to discern them from those regions formed by water release and collapse. Greeley and Guest, 1987, and Scott and Tanaka, 1986, interpreted the uplands surrounding the basins as Noachian cratered unit (Npl_1) or subdued cratered unit (Npl_2), and also noted a "cratered unit deeply furrowed by sinuous, intersecting, curved to flat-bottomed grooves, producing an etched or sculptured surface", named Nple (Greeley and Guest, 1987). The maps also showed three volcanic edifices of unknown age. Our investigations of these locations show no evidence for volcanic edifices, we therefore interpret them as Noachian cratered units as well. The undulating plains and depressions between the Noachian uplands are covered with smooth, featureless deposits dissected by wrinkle ridges. They have been mostly mapped as the Hesperian ridged plains unit (Hr) and interpreted as low viscosity lava flows (figure 1).

A slightly different stratigraphic interpretation is provided by Grant and Schultz, 1990. They describe a fine-grained, possibly loess-like deposit with a thickness of 150 to 300 m, they informally name "Electris deposit". It corresponds approximately to Nple (Noachian etched unit) of Greeley and Guest, 1987. The knob fields are interpreted by Grant and Schultz, 1990, as one of four different surface textures of the "Electris deposit". Grant *et al.*, 2010, suggest that the knob fields, formerly surface type four, are a separate unit overlaying the "Electris deposit", but possibly represent reworked Electris material. In both interpretations, the knob fields postdate the Hesperian ridged plains unit Hr. An even different stratigraphy is suggested by Baker and Head, 2009, Baker and Head, 2012. These studies place the knob fields stratigraphically below the Hr unit, and the "Electris deposit" above them.

Irwin *et al.*, 2004 suggested, that the overflow of a giant lake in this area, the Eridania lake, caused the formation of Ma'adim Vallis. Following the stratigraphic interpretation of Grant and Schultz, 1990, these authors placed the deposition of the "Electris deposit" after the outflow event, and concluded, that the knob fields are not related to the Eridania lake. The region also features abundant fluvial valleys in the Gorgonum and Newton basins (Howard and Moore, 2011), flat benches on the floor of Gorgonum basin (Howard and Moore, 2004), local deposits interpreted as chlorides (Osterloo *et al.*, 2010) and gullies, some of which originate from flanks of the knob mounds (Márquez *et al.*, 2005), which are evidence for a complex aqueous history in these basins.

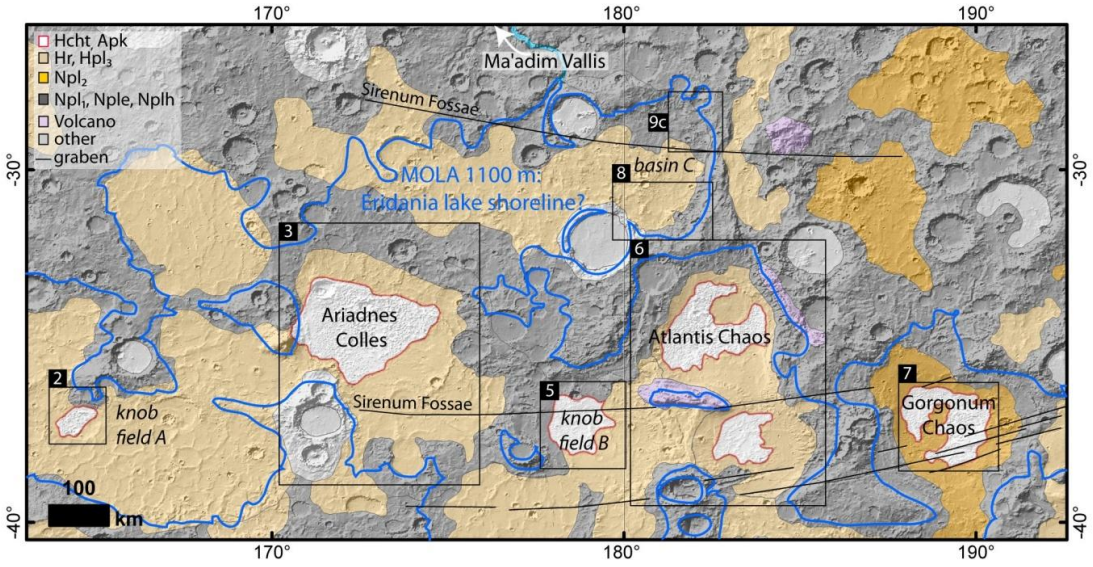

Fig. 4.1: Geologic overview map of the study area, modified after Greeley and Guest, 1987, Scott and Tanaka, 1986, on MOLA shaded relief map.

The blue line marks the MOLA 1100 m contour, the approximate shoreline of the suggested Eridania lake (Irwin et al., 2004).

The knob fields contain phyllosilicates (Annex and Howard, 2011, Noe Dobrea, 2007, Noe Dobrea *et al.*, 2008). Phyllosilicates on Mars are believed to be generally constrained to Noachian, "phyllosian" units (Bibring *et al.*, 2006). Phyllosilicates have also been identified in in younger, Hesperian deposits, e.g., in the Eberswalde and Holden craters, but it is not clear if the phyllosilicates formed in situ or were transported from a different location, where they might have formed in during the Noachian (Milliken and Bish, 2010). If the stratigraphic interpretation of Greeley and Guest, 1987, Scott and Tanaka, 1986 or Grant and Schultz, 1990, Grant *et al.*, 2010 is correct and the knob fields indeed postdate the Hesperian-aged ridged plains unit, they would indicate climatic conditions allowing the formation of phyllosilicates after the Noachian/Hesperian boundary, if these deposits formed in situ.

The region is cross-cut by Sirenum Fossae, a set of grabens similar to Mangala, Memnonia, Icaria, Thaumasia and Claritas Fossae that radially extend from the Tharsis rise. These structures have been described as the surface expression of volcanic dikes in the subsurface (Wilson and Head, 2002), which is supported by lava flows originating from Mangala Fossa (Basilevsky *et al.*, 2009). In the area of this study, no lava flows associated with Sirenum Fossae have been observed.

The purpose of this study is threefold: (1) To determine the regional stratigraphy of the clay-bearing units, as the suggested Hesperian and Amazonian ages of the deposits are at odds with observations of phyllosilicate-bearing units elsewhere on Mars, (2) to investigate the relationship between the clay bearing deposits and the proposed Eridania lake, and (3) to survey the aqueous history of this region of Mars with respect to the possible relationships between clay-

bearing units, valley networks, chloride deposits and the tectonic activity at Sirenum Fossae.

4.3 Methods and Datasets

In this study, we use panchromatic and color imagery from the High Resolution Stereo Camera (HRSC, Neukum and Jaumann, 2004), Context Camera (CTX, Malin *et al.*, 2007), Mars Orbiter Camera (MOC, Malin *et al.*, 1992) and the High Resolution Imaging Science Experiment (HiRISE, McEwen *et al.*, 2007) to define and map regions of similar texture, albedo or hue as geological/geomorphological units and to investigate their relative stratigraphy based on their cross-cutting or embayment relationship. All imagery was combined in the commercial geographical information system ArcGIS. Hyperspectral data from the Compact Reconnaissance Imaging Spectrometer for Mars (CRISM) is used to study the mineralogy of the light-toned deposits.

The HRSC is a pushbroom imager onboard ESAs Mars Express with nine CCD line scanners mounted behind a common optic system, which allow the systematic acquisition of multispectral and stereo data during a single overpass (Neukum and Jaumann, 2004). Mars Express is in a highly elliptical orbit with a pericenter altitude of ~290 km and an apocenter altitude of ~12,000 km. This results in variations of the ground resolution and swath width of the HRSC images. Orthoimages are usually produced at resolutions of 12.5 m/pixel or 25 m/pixel from the panchromatic nadir channel. Data from the color channels is usually binned with a 2-by-2 or 4-by-4 binning scheme. The orbit of Mars Express is not sun-synchronous, which leads to different illumination conditions in adjacent image strips, which can make the production of mosaics difficult. CTX is the panchromatic imager onboard Mars Reconnaissance Orbiter (MRO). It provides context imagery for the HiRISE and CRISM data products. Images of CTX have a swath width of 30 km and a resolution of approx. 6 m/pixel. Most of the study region is covered by this data. MOC is the camera on Mars Global Surveyor. Its narrow-angle camera produced tens of thousands of images at resolutions between 1.5 and 12 m/pixel. HiRISE is the high-resolution camera onboard MRO. It produces images in the red part of the spectrum (550-850 nm) in a swath 6 km wide, and images the central, 1.2 km wide part of the swath also in the blue-green region (400-600 nm) and infrared region (800-1000 nm) to produce nested color images. The images have a ground resolution as good as 25 cm/pixel.

We also used crater counts to estimate absolute ages. Craters were counted on CTX imagery in several counting areas around Ariadnes Colles, using the ArcGIS (trademark) extension developed by Kneissl *et al.*, 2011, which ensures a distortion-free measurement of crater diameters independently from the map projection used. The resulting crater size-frequency curves were analyzed based on the chronology function of Hartmann and Neukum, 2001 and the production function of Ivanov, 2001.

The topography of the study area was investigated based on data from the Mars Orbiter Laser Altimeter MOLA (Smith *et al.*, 2001). We used the data gridded to a 128 pixel/degree elevation model (MEGDR, Smith *et al.*, 2003).

To constrain the composition of the light toned knobs and layers, we used orbital near infrared hyperspectral data from CRISM (Murchie *et al.*, 2007a) onboard MRO. CRISM observations are acquired either in multispectral mapping mode or in hyperspectral targeted mode (Murchie *et al.*,

2007a). In the targeted mode, most observations have a ground resolution of 18 m (full resolution targeted mode FRT) or 36 m (half resolution targeted mode HRL) per pixel and data are acquired for 544 channels from 0.38-4 µm. Due to the relatively small size of the light-toned outcrops, we used only targeted observations in this study. The entire study area shown in figure 1 is covered by more than 160 targeted observations released to the public. We inspected the spectral summary products indicative of hydrated minerals for all of these observations on the CRISM website (http://crism-map.jhuapl.edu/) and selected the observations with the strongest spectral parameters for detailed analyses (table 4-1).

table 4-1: CRISM targeted observations analyzed in detail

CRISM Observation	Lat°/ Lon°	Year_day	Location
FRT00007DCD	-35.91 / 172.48	2007_267	Ariadnes Colles
FRT00008C90	-35.35 / 173.18	2007_350	Ariadnes Colles
FRT00009DD2	-35.64 / 172.85	2008_041	Ariadnes Colles
FRT00011D69	-35.23 / 173.39	2009_091	Ariadnes Colles
FRT00008377	-37.02 / 164.46	2007_288	Knob field A
FRT000096FE	-28.35 / 181.56	2008_015	Basin C
FRT0000951C	-37.59 / 184.69	2008_010	s. Atlantis basin

The CRISM I/F data was processed as described in Murchie *et al.*, 2009c. The data was divided by the cosine of the solar incidence angle, and spectral contributions from atmospheric CO_2 and other components were minimized by dividing by a scaled transmission spectrum (McGuire *et al.*, 2009). Spatial and spectral noise was filtered out using the routines described in Parente, 2008. The resulting spectra were averaged over at least 5 by 5 pixels to improve the signal-to-noise ratio, and divided by spectra from nearby, spectrally neutral regions in the same CRISM scene and in the same detector columns to remove remaining artifacts not due to the surface materials. We constrained our study to data in the range of 1 to 2.6 µm, as this is the range where overtones and vibrations of H_2O and hydroxyl groups in sulfates and clay minerals are observed.

4.4 Results

4.4.1 Morphology and stratigraphy of the knob fields

In the following sections, we document our observations made in the most prominent knob fields of the study area. The individual knob fields will be introduced from West to East, starting with knob field A.

4.4.1.1 Knob field A (westernmost field)

The westernmost knob field, hereafter named "knobfield A", partly covers a circular depression ~ 65 km in diameter (Fig. 4.2). Its lowest point is located at ~600 m above the Martian datum, while the rim is at ~800 m. The knobs are found at all elevations, but are constrained in the north-western side of the depression. They show angular or rounded outlines and form two size populations. The group of smaller knobs have a maximum extension on the order of a few hundred meters to ~1.5 km and cliff-like tops, whereas the larger knobs reach maximum lengths of ~12 km and form mesas. These mesas show a constant height above the surrounding terrain of ~300 m, irrespective of their absolute elevation above the Martian datum. The smaller, pointy-topped knobs are always lower than the mesas, suggesting that they represent degraded mesas

formed from a layer about 300 m thick. The elevation and extension of the knobs is lower towards the rim of the circular depression. Only small knobs are found close to the rim, whereas mesas are located at least ~10 km from the rim. At the SE-boundary, large mesas are found directly up to the limit of the knob field.

All knobs are light-toned, mesas appear to consist of the same light-toned material covered by a darker cover. The base of the knobs is locally exposed in impact craters (Fig. 4.2D), showing that the knobs consist of individual rock units and not a contiguous layer partly covered at its top. The knobs are covered by a thin (~10 m) very

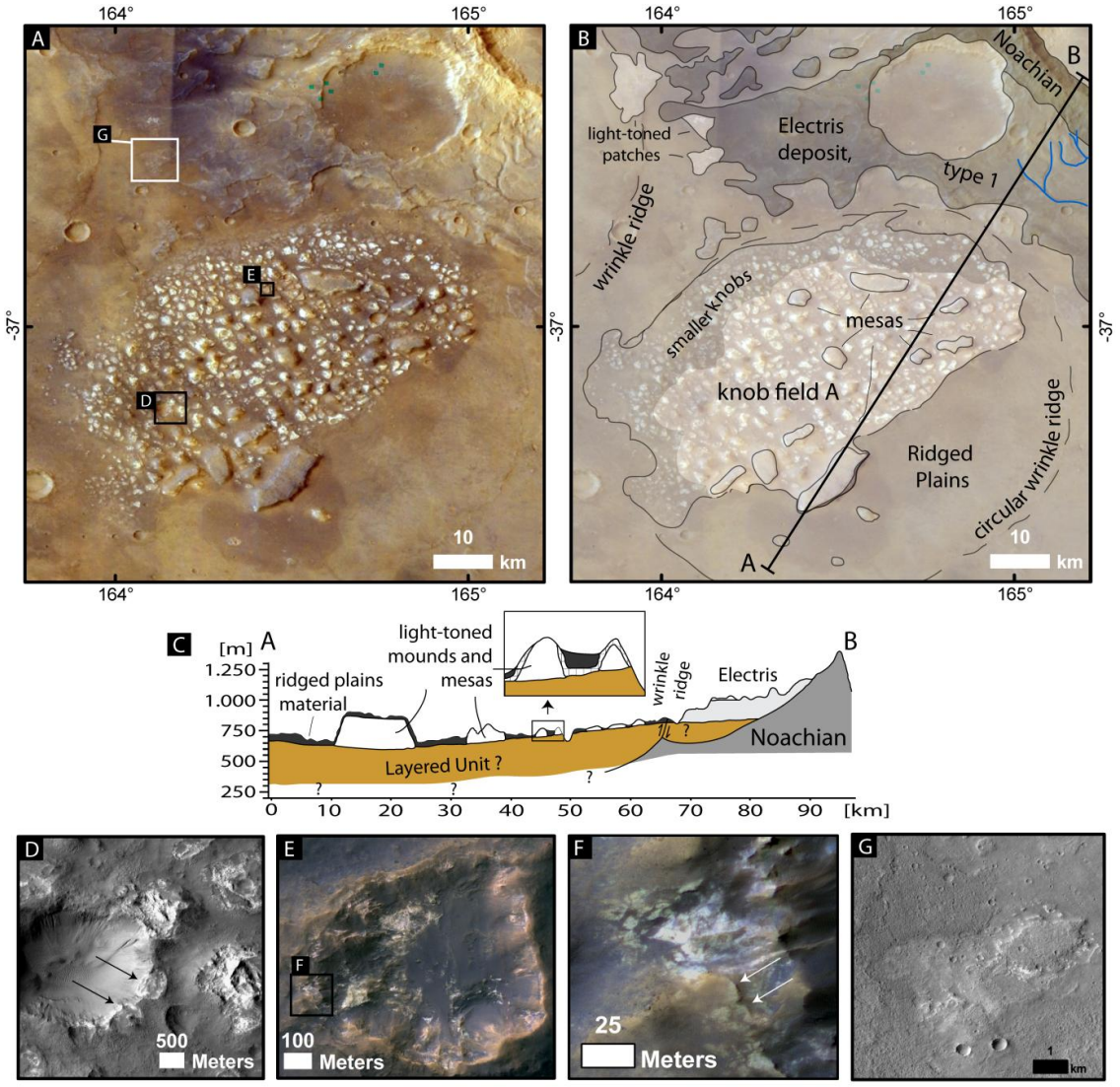

Fig. 4.2: Geological map of knob field A

See Fig 4.1 for overview map. A: HRSC color image from orbits 4286 and 4297. B: Geologic map. The knob field consists of mounds and mesas, and are embayed by the ridged plains unit. C: Interpretative cross-section. D: The light-toned material of the knobs forms only a thin layer, its lower boundary is visible in this crater (CTX image P04_002661-1426_XI37S196W). E: Detail of an eroded light-toned mound, which is covered by a more erosion-resistant bright crust, and a dark mantling (F, arrows; HiRISE image PSP_005707_1425_COLOR). G: Material with a similar texture and albedo is also exposed at the top of the Electris deposit and embayed by ridged plains.

light-toned, highly jointed layer. This layer appears to be more resistant to erosion than the inner parts of the mounds. In locations where this outer layer is breached, the underlying rock is strongly eroded (Fig. 4.2E and F). The protective, highly jointed crust covers not only the tops, but also the flanks of the mounds.

Directly north of the knob field is a scarp approximately 200 m high. It marks the boundary to the bench-forming outcrops described as "Electris deposit", type 1 (Grant and Schultz, 1990, Grant *et al.*, 2010). It is mostly covered by a thin dark mantling material, but locally, a light-toned, and indurated layer is observed at the top of the benches (Fig. 4.2G) that is similar in texture and albedo to the material found in the knobs. The mounds and the "Electris deposit" are surrounded by a smooth, undulating, plains-forming unit dissected by wrinkle ridges. This unit corresponds to the "ridged plains" unit Hr of Scott and Tanaka, 1986.

4.4.1.2 Ariadnes Colles

The Ariadnes Colles knob field is located in an oval, bowl-shaped depression with a maximum diameter of 240 km, centered at 173° E, 35°S (Fig. 4.3). Its lowest point is at an elevation of -250 m, the rim is at +500 m. The basin is surrounded by uplands with an even or slightly undulating topography that forms cliffs ~200 to 300 m high along its edges, mapped as "Electris deposit" by Grant *et al.*, 2010 (Fig. 2B therein). A smooth surface with wrinkle ridges, mapped as ridged plains unit (Hr), covers the area between the knobs and the "Electris deposit". Near 174°E, -38°N (arrow in Fig. 4.3B), three interconnected circular structures with diameters up to 50 km are visible. They are filled with the ridged plains unit and surrounded by the "Electris" deposit.

The knobs in this basin show a very similar morphology and distribution as those in knob field A. Mounds with up to ~1.5 km in diameter show heavily eroded, cliff-like tops, whereas larger mounds form flat-topped mesas with an elevation of ~270 m. Mounds near the outer boundary of the basin are smaller and lower than those in the center. The knob field ends abruptly towards the South-East. A few, singular mounds are found within the smooth plain in the South-East of the basin. Some mounds show a pattern of linear features on its surface (Fig. 4.3C). These linear features are more erosion-resistant than the surrounding rocks, and form a positive relief. They have been interpreted by de Pablo *et al.*, 2004, as volcanic or hydrothermal dikes, but could also be filled joints. They partly form parallel patterns that can be traced from one mound to the next. A light-toned, erosion-resistant crust covers many of the mounds, and is also found in the valleys between them (Fig. 4.3D). In the North of Fig. 4.3A and B, a light-toned material is found. It has a similar hue and texture as the light-toned material in the mounds, but forms patches rather than knobs. It is shown in higher detail in Fig. 4.4.

Many prominent dendritic valleys carve into the Electris deposit near the rims of the basin and run towards its center, for example near 173°E, -38°N. Some valley networks also carve into the light-toned material exposed in the North-East of Ariadnes Colles, shown in figure 4. These channels appear to be filled by the darker, ridged-plains material. The channel fill has locally been eroded to form inverted channels. Wrinkle ridges cross-cut the light-toned material and displace a channel (arrow).

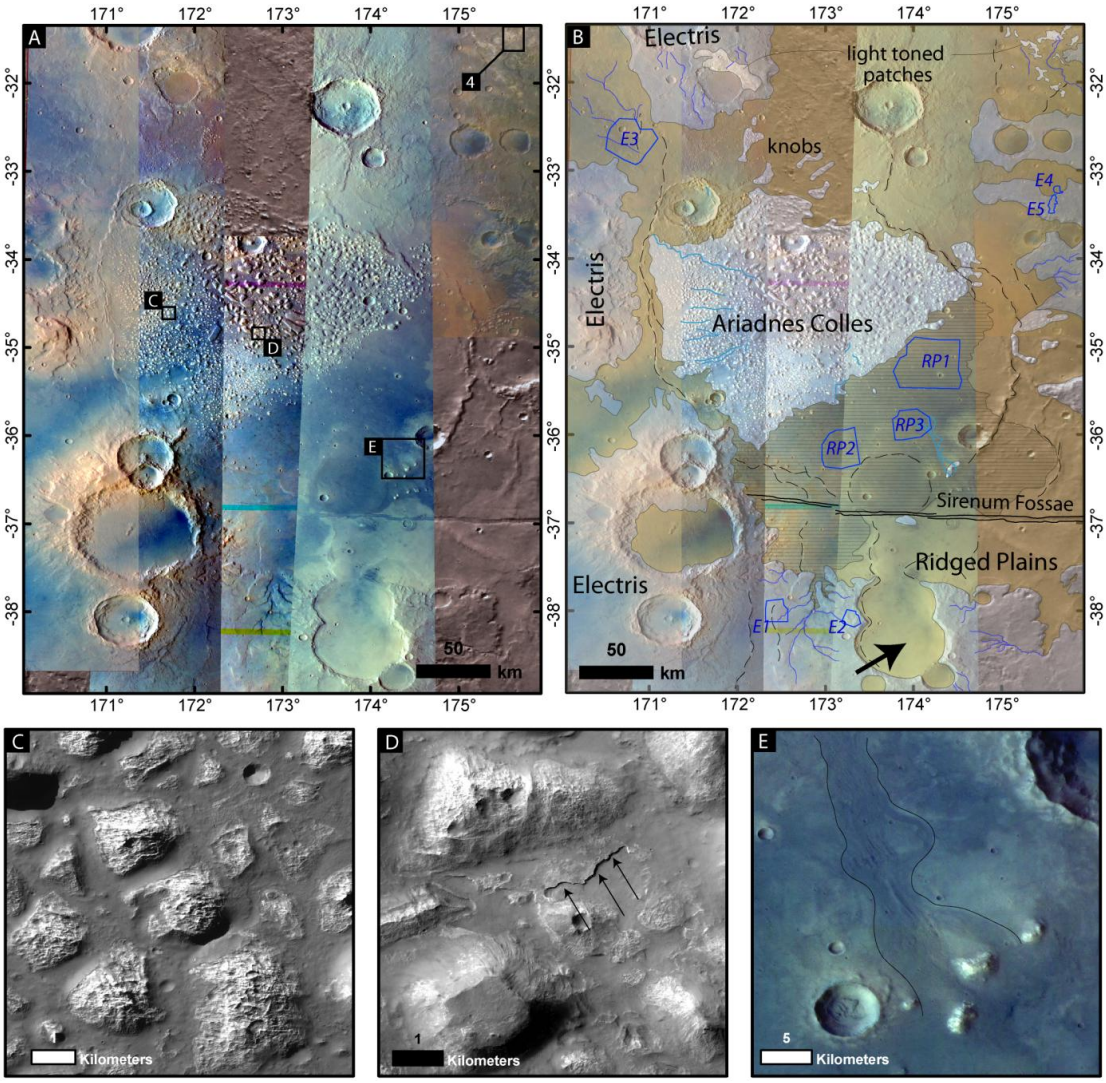

Fig. 4.3. Overview of Ariadnes Colles.

A: HRSC color images from orbits 0024, 4187, 4198 and 4231. B Geologic map as transparent overlay on same image data as in A. Both the Electris deposit and the knob fields are embayed or covered by the ridged plains unit. Blue polygons are crater counting areas on CTX imagery. Results are shown in fig 11. C: The knobs show a parallel pattern of joints, indicating no relative movement. Flow features run between the knobs (CTX B20_017442_1433_XN36S188W). D: The knobs are covered by a light-toned crust (arrows). It is found on and between the mounds, and therefore formed after the break-up into individual knobs (CTX P16_007223_145_XN_35S187W). E: Flow feature on top of ridged plains unit, postdating knobs, outlined in black (HRSC Orbit 4187).

Locally, valleys carve into the ridged plains unit. This is shown in Fig. 4.3E. Here, shallow channels run around light-toned mounds towards the basin center. The flow cuts into a dark, smooth deposit covering the south-eastern part of the Ariadnes basin. It appears to be the youngest deposit in this area and might be basaltic lava (hatched area in Fig. 4.3B).

A branch of the Sirenum Fossae cuts through the southern part of Fig. 4.3A and B. It forms a typical graben structure, locally displaced along ramps. We observe no sign of aqueous or volcanic

activity clearly related to the formation of the graben.

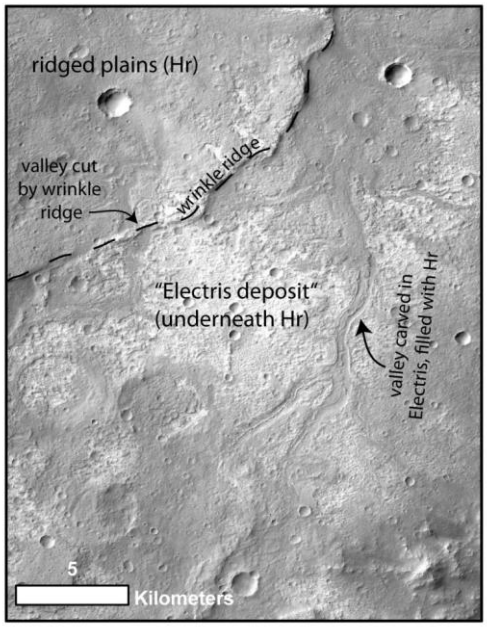

Fig. 4.4: Flow feature cutting into the light-toned material north-east of Ariadnes Colles.
Flows were later filled with ridged plains material, and wrinkle ridges formed (CTX P14_006590_1474_XN 32S184W).

4.4.1.3 Knob field B

As Ariadnes Colles, the basin of knob field B has a bowl-like shape (Fig. 4.5). Its lowest point is at an elevation of approx. -250 m. The mounds are found at elevations up to +150 m. The knob field ends abruptly towards the southeast. The limit of the knobs forms an almost straight line, which is not parallel to contour lines. The knob field is surrounded by a smooth plain dissected by wrinkle ridges. Some of the wrinkle ridges also displace the knob field. Light-toned ejecta of impact craters in the smooth, southeastern part of the basin suggest that a light-toned material is present here underneath a dark-toned, possibly basaltic cover (arrows in Fig. 4.5A).

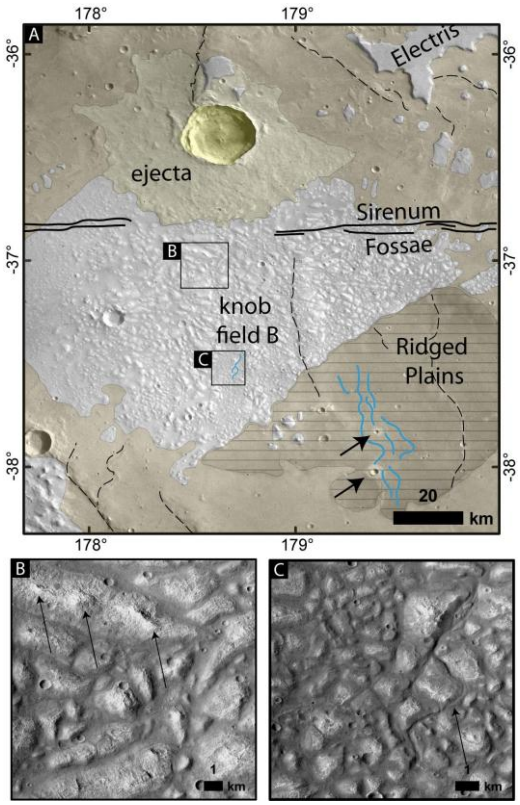

Fig. 4.5: Knob field B.
A: Geologic map of knob field B on HRSC image 2663_0001. The knob field is embayed by the ridged plains unit, wrinkle ridges formed after its deposition. Arrows indicate light-toned material exposed by impact cratering from underneath the Ridged Plains. B: The mounds in this field have elongated shapes and rounded tops, only the topmost sections are cliffy (arrows). C: Flow features run between the mounds (B and C: CTX P05_002911_1418_XN_38S181W).

Interestingly, some of the light-toned mounds have an elongated shape and are oriented preferentially in a ESE-WNW direction. Most of the mounds have a rounded upper surface, but the largest mounds show edged hilltops above rounded flanks (Fig. 4.5B). This morphology resembles nunataks, which are rocky peaks not covered with ice or snow within glaciers or ice-fields. Flow features are found both on top of the ridged plains and between the light-toned mounds (Fig. 4.5C).

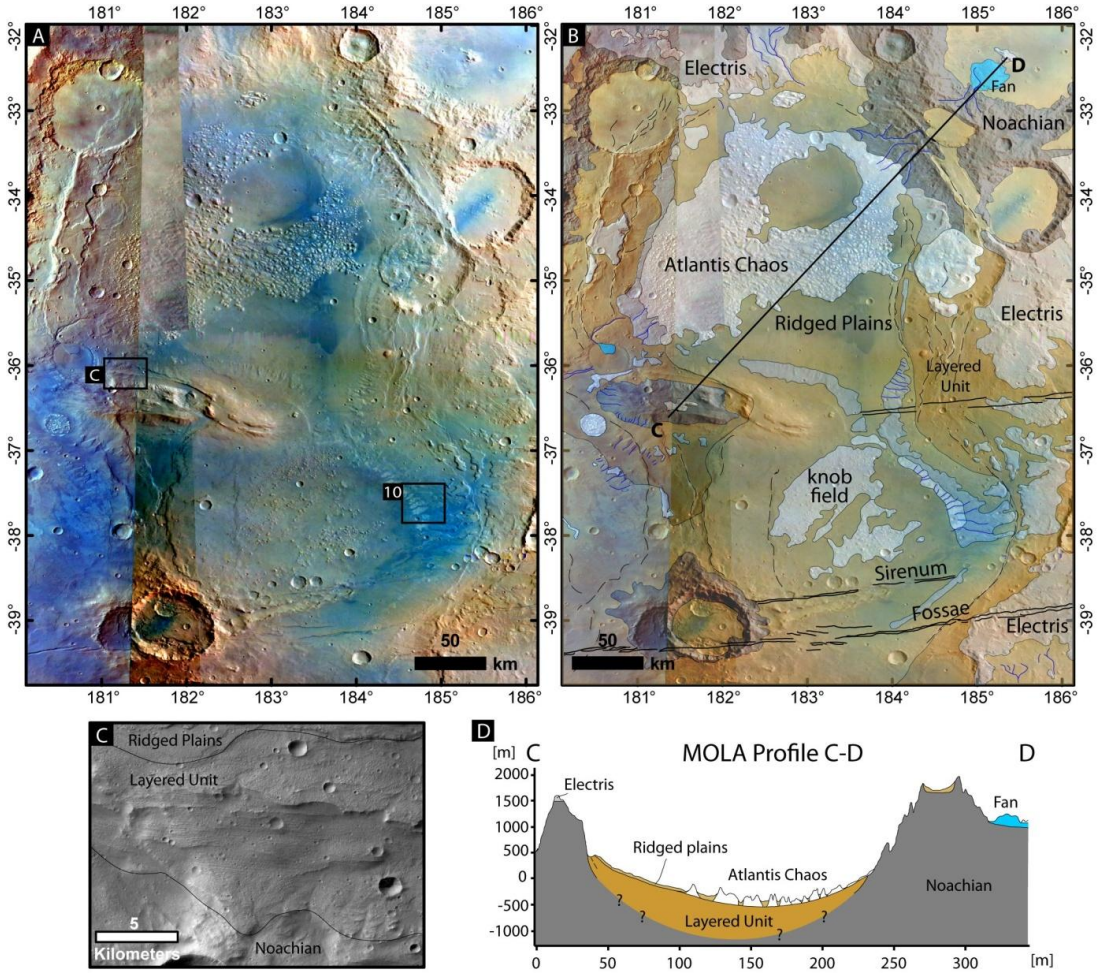

Fig. 4.6: Atlantis Basin.

A: HRSC color images from orbits 6411, 6393, 2183, 2630 and 2663. B: Geologic map. A layered unit with wrinkle ridges is found underneath the Electris deposit and the knob fields. Electris deposit and knob fields are covered/embayed by the ridged plains. C: Details of the layered unit at the contact to the underlying Noachian basement and the ridged plains on top (CTX P17_007605_1449_XI_35S179W). D: MOLA profile C-D and interpretative cross-section.

4.4.1.4 Atlantis Chaos

The light-toned knobs in Atlantis Chaos are located in a basin near 183°E 34°S. It is approximately 200 km in diameter, its lowest point is at -590 m, the surrounding Noachian mountains rise up to +2700 m (Fig. 4.6). An elongated rise in the south-west of the Atlantis basin (181°E 36°S) has been interpreted as a volcano (Greeley and Guest, 1987). We studied this structure based on higher resolved imagery, and found no evidence for volcanic features, such as a crater or lava flows. We therefore interpret it as Noachian material surrounded by wrinkle ridges. The Atlantis basin is connected in the south with a second, smaller (~175 km in diameter) basin ~890 m higher in elevation. Its lowest point is at ~+300 m. Light-toned, "chaotic" knobs are found both in Atlantis basin and in the southern basin, hereafter named "southern Atlantis basin". The light-toned material is found at all elevations, including a large (60 km) impact crater on the eastern rim of Atlantis (184.5°E 35°S), where the light-toned material is found at elevations up to +700 m.

Wrinkle ridges are found near the rim of the basin between eroded mesas of the Electris deposit. Smooth material displaying wrinkle ridges is also found embaying and onlapping the Electris deposit mesas around the basin. Around the mountain previously interpreted as a volcano, a rock unit is exposed underneath the ridged plains. It is shown in Fig. 4.6C and shows linear features, which are possibly exposed layers. The layers are on the order of tens of meters thick, and form packets on the order of hundreds of meters in thickness.

Wide flow features crosscutting the Electris deposits are abundant. Locally, a second generation of smaller flows can be observed cutting into the overlaying ridged plains material, as in the other basins of this study and Newton basin (Howard and Moore, 2011).

4.4.1.5 Gorgonum Chaos

The Gorgonum basin is approximately 240 km in diameter, its lowest point is at ~-400 m. As observed for the other basins, the Gorgonum basin is surrounded by a flat, cliff-forming unit, mapped as Electris deposit unit that is dissected by flow features into mesas. Light-toned material is observed both at the top of the Electris Deposit as a light-toned cover, as contiguous light-toned patches on the slopes of the basin, where the overlaying ridged plains material has been eroded away, and as light-toned mounds with similar sizes and textures as in the other knob fields towards the basin center (Fig 4.7A).

The eastern part of the Gorgonum basin floor is dissected into a chaotic terrain with a similar texture as the chaotic terrains in the circum-Chryse region. While most of the smaller faults in this dissected terrain appear to have a random orientation, the biggest faults are oriented parallel to Sirenum Fossae. The dissected terrain and the light-toned knobs in the center of the basin approximately below the 0 m contour line are covered by darker-toned deposit (Fig. 4.7; Howard and Moore, 2004, 2011). The cover is mostly very thin, so that the shape of the underlying mounds is still clearly observable. This blanket has been interpreted as a lake sediment, and the sharp boundary near 0 m as the shoreline (blue line in Fg. 4.7B; Howard and Moore, 2004, 2011). The northern and western slope of the Gorgonum basin above the 0-m-contour line are cut by numerous valleys, the so-called Mid-Latitude Valleys (MLV) of Howard and Moore, 2011.

A close inspection of the valleys on the western side of the basin (Fig4.7C) shows that the valleys do not end at the suggested shoreline but continue further down the slope to approx. -150 m. At this elevation, a dissected, "chaotic" terrain is observed, which shows a distinct texture. The individual mounds are a few hundred meters in diameter, which is much smaller than the chaotic mesas on the eastern side of the basin. Near the -300 m contour line, flat-topped benches cover parts of the basin center. They show steep scarps towards the lowest parts of the basin at an elevation of ~-400 m (Howard and Moore, 2004, 2011).

The flat-topped benches embay the dissected terrain in the eastern part of Gorgonum (Fig 4.7D), and some of the valleys used the Sirenum Fossae as a flow path (Fig 4.7C). The valleys on the slopes of Gorgonum start somewhere near the rim of the basin.

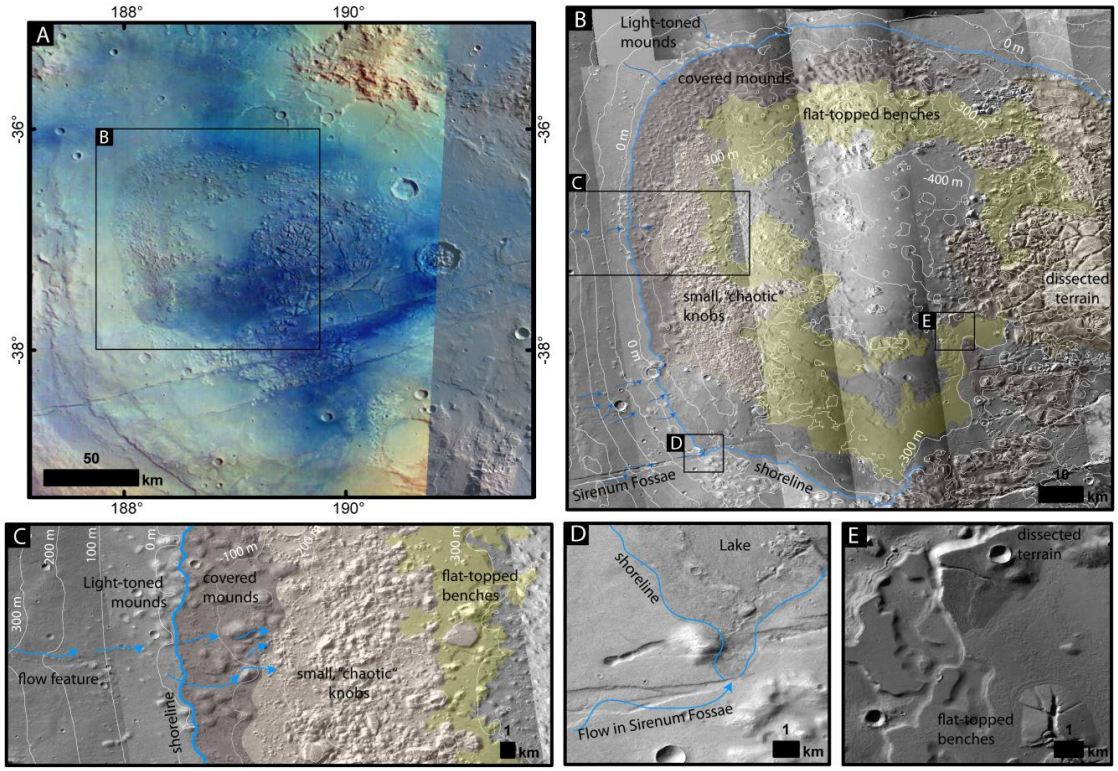

Fig. 4.7: Gorgonum Basin.

A: Overview to the Gorgonum Basin; HRSC image 2575. B: Mosaic of CTX images of the central part of Gorgonum basin, overlain with colored geologic interpretation. The light-toned mounds are found at all elevations. Below a putative shoreline of a lake near 0 m elevation, they are covered by a thin veneer. Flat-topped mesas are found near -300 m. The eastern boundary of the basin is covered by dissected terrain possibly related to Sirenum Fossae. Near the western shore, "chaotic" knobs with diameters around 100 m are located at elevations near 200 m. The presence of a lake here has also been suggested by Howard and Moore, 2011, figure 4. C: CTX image of the western rim of the putative lake. A valley cuts into the slope of Gorgonum down to the putative shoreline near 0 m. As the lake level drops, the valley continues further down the slope until ~-150 m. The small "chaotic" knobs found here might be dessicated lake sediments, that released water, forming a lower lake level at -300 m, where flat benches formed. D: In this basin, water flowed in a branch of Sirenum Fossae, showing that here, the graben formation predated or was contemporaneous with the aqueous activity. E: The flat-topped benches show small flow features and overlay the dissected terrain in the east of the basin.

4.4.2 Basin C

We named the depression north of Atlantis at 181°E, 30°S basin C (Fig. 4.8). It has an oval shape ~240 km by 150 km, its floor is at approximately +400 m. In this basin, the layer-forming light-toned material (LTM) and the knob fields can be observed in direct vicinity. The light-toned material is found both on the rim of the basin and in the basin center. A few mesas and mounds in the center of the basin display a higher elevation than the surrounding light-toned mounds.

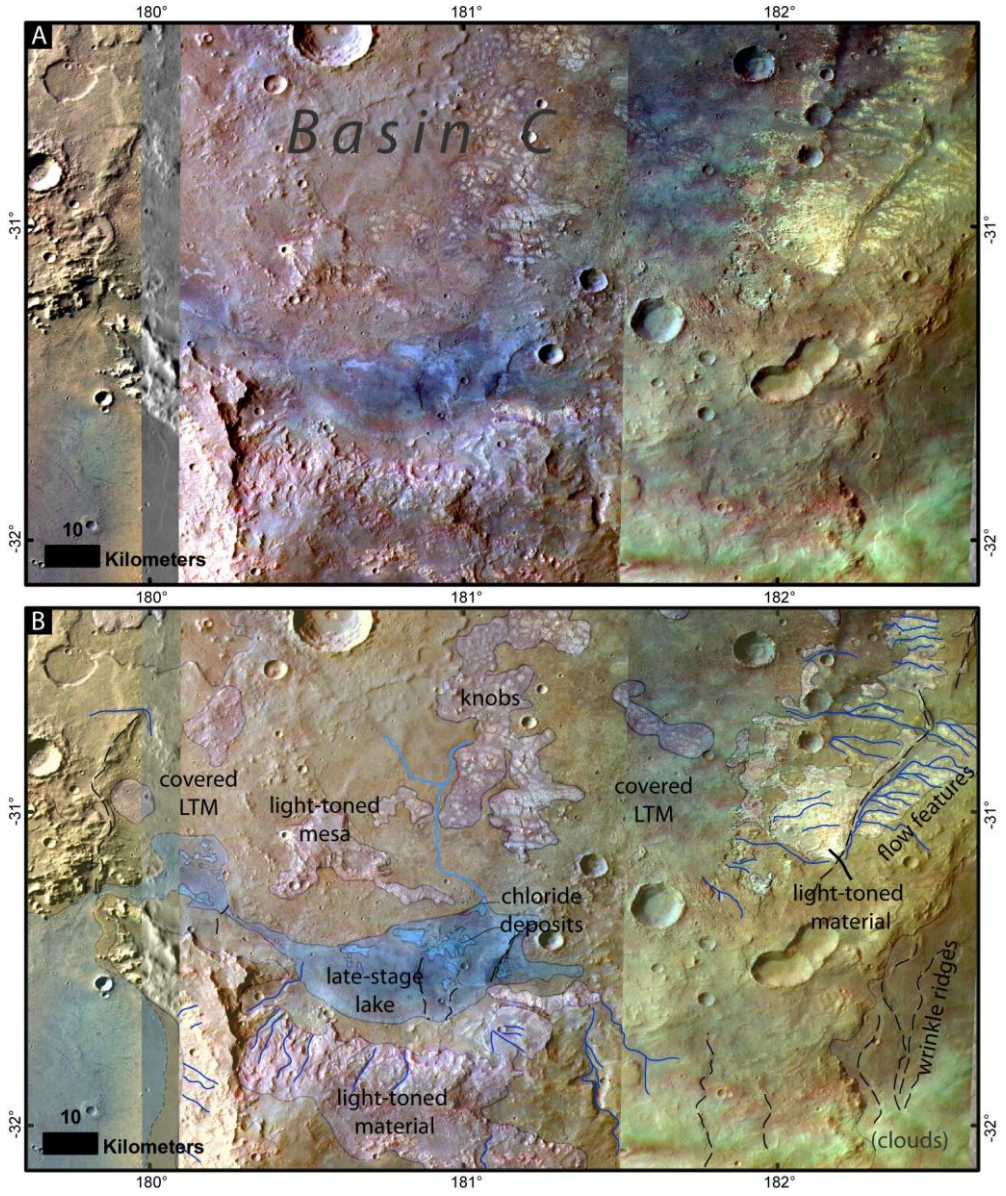

Fig. 4.8: Southern part of basin C.

A: HRSC color images 8474, 6411, 6393, B: Geological map on color images. The basin is filled with light-toned material(LTM), which is partly eroded to knobs. The light-toned material is covered with a dark, likely basaltic cap. Numerous flow features eroded into the light-toned material and formed a lake in the south of the basin. The lake contains a distinct sediment with a bright blue color in HRSC, which consists of chlorides (Osterloo et al., 2010).

Locally the mesas are dissected into polygonal mounds with similar extensions of a few km as the mounds in the other basins. Dark, possibly basaltic material covers the light-toned material. It is also found in the fissures separating the mounds from each other. A few wrinkle ridges and several valleys crosscut the light-toned deposits. The valleys are partly inverted. The flow features continue across the dark-toned cover material, partly through gaps between higher mounds of light-toned material. In the south of this basin, deposits interpreted as chlorides by Osterloo *et al.*, 2010 show a distinct light blue hue in the stretched HRSC color data (Fig. 4.8). They are located in the deepest part of the basin.

4.4.3 Mineralogy

Most of the CRISM observations of the light-toned mounds show relatively weak or absent conclusive absorption features, either due to unfavorable atmospheric conditions or spectrally neutral coatings, but in some observations, clear absorption features appear, which suggest a relatively uniform composition of the light-toned material in the study area. Exemplary CRISM spectra of the light-toned material are shown in Fig. 4.9 toFig. 4.11. Spectral data from the North of basin C is shown in Fig. 4.9. Fig. 4.9A shows the spectral parameters OLINDEX, BD2210 and BD2300 (Pelkey *et al.*, 2007) as the red, green and blue channels overlain on a CTX image. Many spectra of the light-toned material show an increasing upward slope between 1 and 2.2 µm, which can be indicative of a ferrous component. An alternative interpretation for this spectral

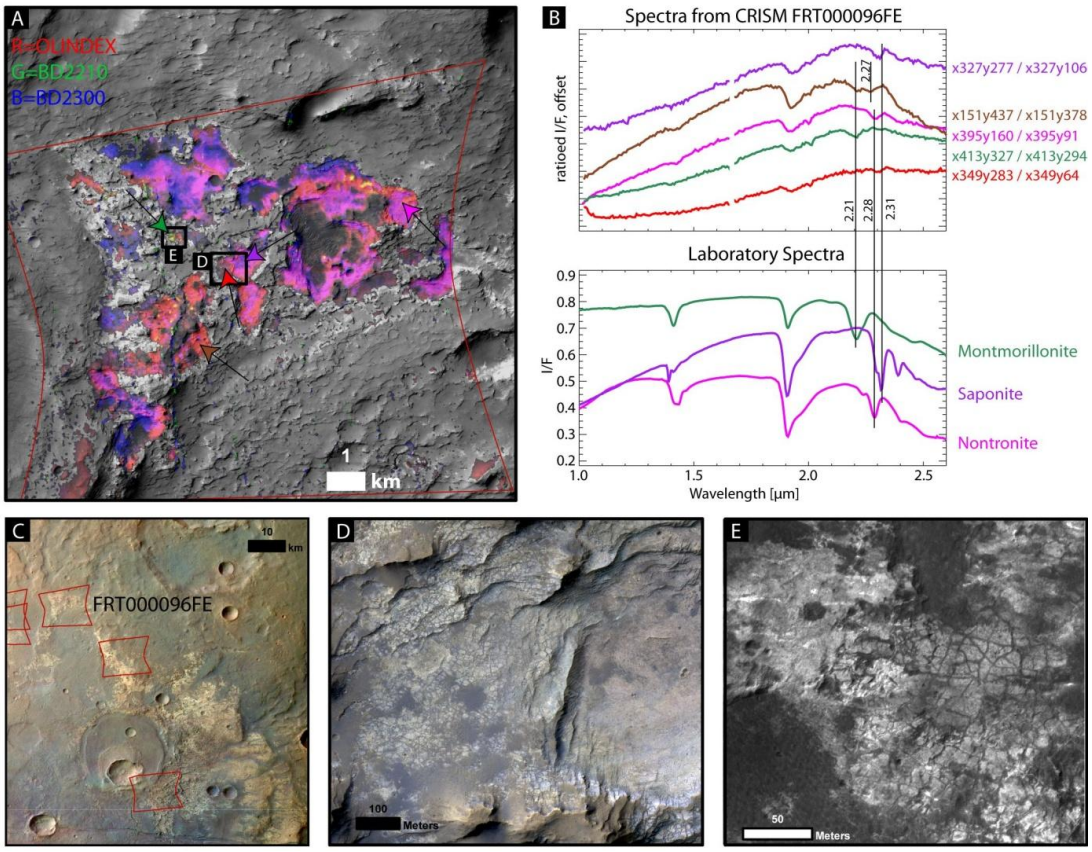

Fig. 4.9: The mineralogy of the light-toned material.

A: CRISM parameter map of FRT 000096FE on CTX image P15_006893_1510_XN_29S178W. Red: OLINDEX, green: BD2210, blue BD2300. B selected ratioed spectra from A, and matching laboratory spectra. Coordinates correspond to the unprojected file, spectra were averaged over 5 by 5 pixels. The spectra show an upward slope from 1 to 2.2 µm, indicative for a ferrous component. The most common material identified is the Mg-rich phyllosilicate saponite, Fe -rich nontronite also occurs. Locally, montmorillonite is detected, and some spectra resemble acid-leached clays (brown spectrum; Madejová et al., 2009). Locally, the light-toned material has only a very weak 1.9 µm band and is almost featureless near 2.3 µm, indicating a further, non-identified hydrated phase. C: HRSC color image 6411 as overview to A. See Fig. 4.1 for location. D: Detail of Mg-clay-rich material (right) and weakly hydrated material (left). Note the different joint spacing. The joints in the weakly hydrated material are wider spaced and filled with a light-toned joint fill. It partly covers horizontal sections as well. HiRISE image PSP_006893_1515 _COLOR. E: Detail of Al-rich clay in HiRISE PSP_006893_1515_RED. The Al-rich clay is found as a top layer on the Mg/Fe-rich phyllosilicates.

feature is an admixture of olivine. Olivine is present in the basaltic cover, as suggested by a spectra shown in Fig. 4.9 and Fig. 4.10. The material mostly displays absorption bands near 1.4, 1.93, 2.31 and 2.4 µm, indicative for Mg-rich phyllosilicates like saponite. The band near 2.3 µm shows some variation between 2.28 and 2.31 µm, which shows that more iron-rich phyllosilicates such as nontronite are also present.

The H_2O combination band is observed here at 1.93 µm, but usually occurs at 1.91 µm for smectites (Bishop *et al.*, 2008b). A similar phenomenon is also observed in Mawrth Vallis (Bishop *et al.*, 2012) and could indicate the presence of ferrihydrite, whose band at 1.93 µm might contribute to the shift in the H_2O combination band.

Locally, a doublet of absorption bands at 2.21 and

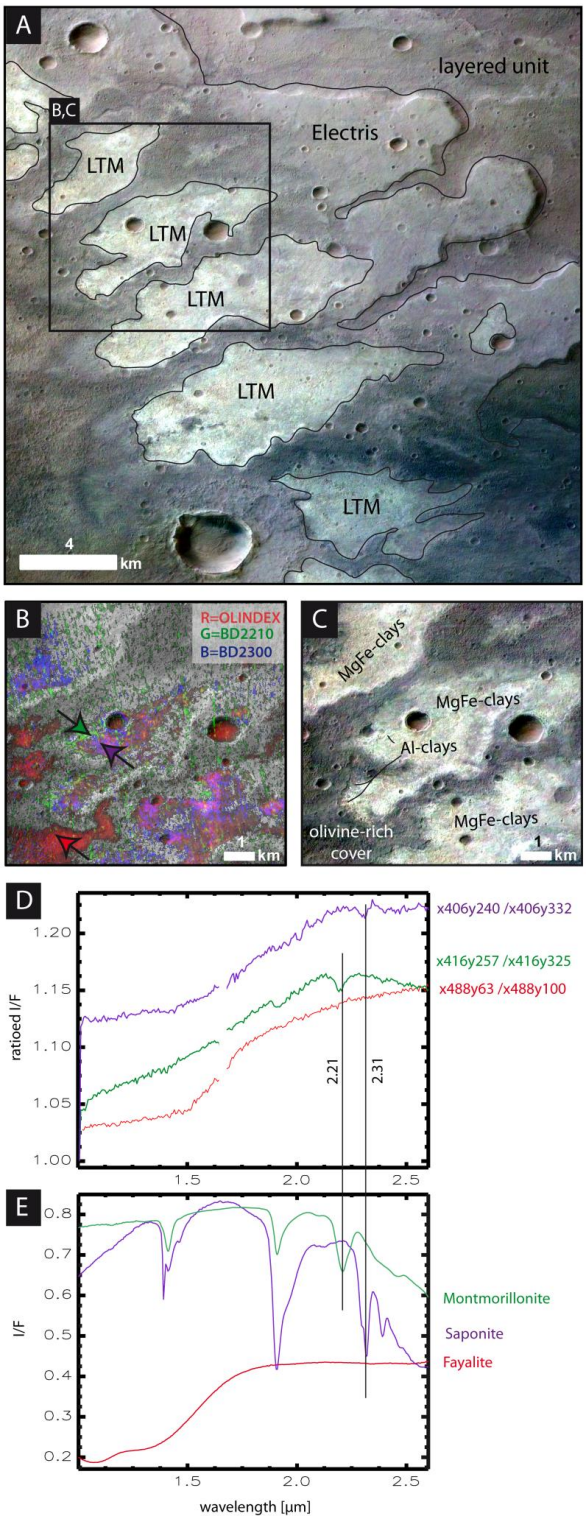

Fig. 4.10: Detail of light-toned deposits in southern Atlantis basin. See Fig. 4.6 A for location.
A: HRSC color false composite of orbit 6547, pansharpened with CTX P13_005970_1426XI_38S175W. The light-toned material (LTM) is found at the top of the Electris deposit, which itself overlays the layered unit. B:Same CTX image as in A, overlain with spectral parameters OLINDEX, BD2210 and BD2300 from CRISM FRT0000951C. The light-toned material is dominated by MgFe-rich smectites. Their spectra (D) show a strong increase of reflectance between 1 and 2 µm. The dark capping rock is olivine bearing. C: Same as a with spectral interpretation. Al-rich smectites form only small outcrops on top of the FeMg smectites. D: Selected CRISM spectra (location indicated by arrows in B), ratioed to neutral spectrum in same detector column. Spectra are averaged over 5 by 5 pixels, numbers indicate coordinates in unprojected image. E: Comparable laboratory spectra.

2.27 µm is observed. Similar spectral features have been measured in leaching experiments, during where Mg-rich clays were exposed to hydrochloric acid (Madejová *et al.*, 2009), and have also been observed in Martian rocks in Ius Chasma (Roach *et al.*, 2010b). Minor amounts of aluminum rich clays such as montmorillonite are also observed (Fig. 4.9B), as well as hydrated silicate. Locally, spectra are observed that are consistent with a mixture of smectites and a further hydrated component. They show weak absorption features around 2.2 µm and might correspond to amorphous Al/Si-OH phases, but an exact identification is difficult. These spectral observations are consistent with results from Annex and Howard, 2011, Noe Dobrea *et al.*, 2008 and Grant *et al.*, 2010. Gilmore *et al.*, 2011 used a superpixel segmentation method to analyze CRISM spectra from Ariadnes Colles and report the presence of Mg-Fe rich smectites and Al-smectites and interpreted some spectra as mixtures of smectites and polyhydrated sulfates.

The relationship between mineralogy and texture is not always evident. HiRISE images of locations of the Al-phyllosilicate rich spots show the presence of joint fills and color changes of Mg-clay rich rocks. The outcrop in Fig. 4.10D shows an irregular surface covered with a dark mantling. The Mg-rich clay shows a fractured texture observed on phyllosilicate surfaces elsewhere on Mars, such as in Mawrth Vallis (Loizeau *et al.*, 2010, McKeown *et al.*, 2009). Near the surface, the Mg-rich clay appears more bluish, and shows a wider joint spacing, and joints are filled with a light-toned precipitate. CRISM spectra of these areas show weaker absorption bands, but spectral features that can be attributed to the light toned joint fills were not observed.

The spatial relationship between the dominating MgFe-smectites and the much less observed Al-

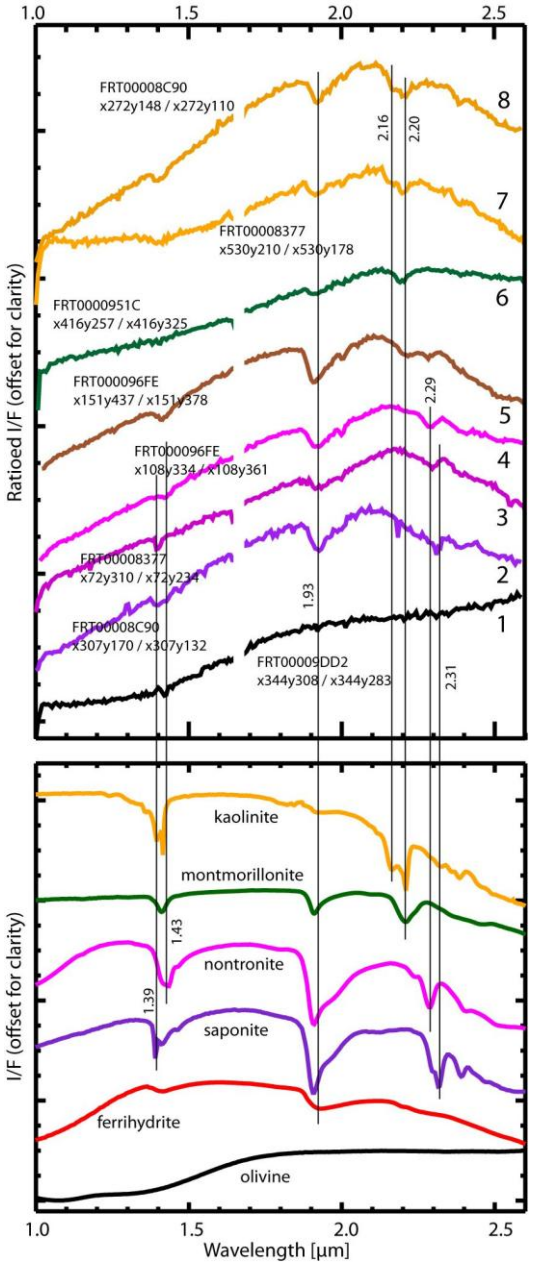

Fig. 4.11: Compilation of ratioed spectra from CRISM observations

Spectra indicate the variation of minerals detected, and laboratory spectra. The light-toned material is dominated by Mg-rich smectites like saponite and Fe-rich nontronite. Locally spectra resembling acid-leached smectites (Madejová et al., 2009) and small outcrops of Al-rich spectra resembling montmorillonite and kaolinite are observed. Spectra are averaged over 5x5 pixels, and ratioed. Names of spectra indicate the CRISM observation and the unprojected coordinates therein.

rich smectites is difficult to assess. Because the outcrops of the Al-smectites are small, textural differences are minor. An exception is shown in Fig. 4.10 of light-toned material in the southern Atlantis basin. Here, the Electris deposit forms a flat-topped bench inclined towards the center of the basin south-west of Fig. 4.10. The Electris deposit shows patches of light-toned material at its top. Electris and light-toned material are covered by a thin, dark mantle, and are incised by fluvial rills running towards the South-West. The overlain CRISM parameter map (Fig. 4.10B) indicates the presence of Mg-smectite with a strong increase in reflection from 1 to 2 µm, caused either by a ferrous component, or by olivine mixed into the spectra, which is present in the dark capping rock on top of the light-toned material. The Al-rich smectite is found only in small outcrops on the top of the Mg/Fe smectite near the dark cover. This indicates that (1) the Al-rich smectites overlay the Mg/Fe smectites, (2) they may have formed by alteration of the underlying material, and (3) they are possibly less erosion-resistant, because they are found only in small quantities in at least partly secluded locations.

The spectral variability of the light-toned material is summarized in Fig. 4.11, showing spectra from further CRISM observations in this area. The dominating clay minerals are Mg- and Fe-rich varieties (spectra 2,3,4). Locally, spectra resembling montmorillonite and kaolinite are observed (spectra 6,7,8). The presence of spectra similar to spectra observed in acid leaching experiments on clays by Madejová *et al.*, 2009 (spectrum 5) suggests that the Mg- and Fe-rich clays may have been altered after their formation to form the more Al-rich varieties. The clay-rich deposits are locally covered by basaltic material showing spectral characteristics of olivine (spectrum 1).

4.4.4 Age determinations

We counted craters in several (crater-count) areas around Ariadnes Colles (Fig. 4.12). Although the ridged plains and the Electris deposit are units with a regional extent, the selection of appropriate crater counting areas was difficult. Due to the low thickness of the Electris deposit of only 200 m, crater counting was performed at the scale of CTX imagery, at which the surface of the Electris deposit is very rugged and mostly inappropriate for crater counting. The resulting crater size-frequency curves were analyzed individually for each counting area, and data curves providing

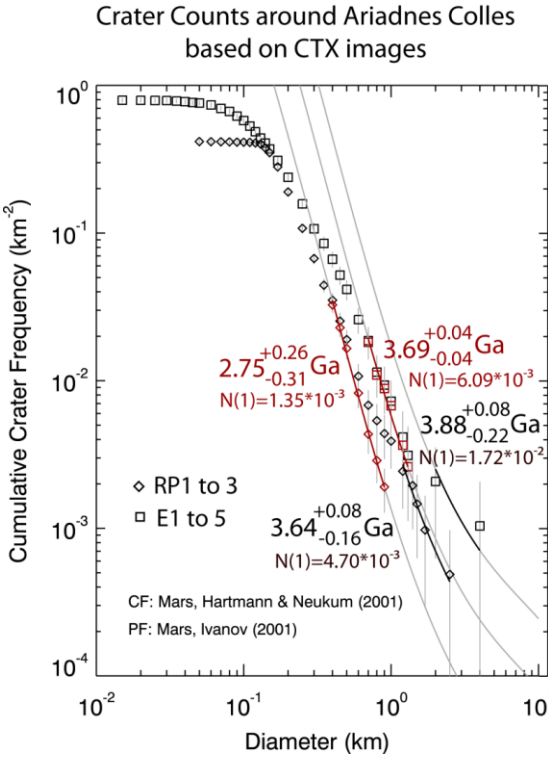

Fig. 4.12: Cumulative crater size-frequency curves. Curves measured on CTX imagery around Ariadnes Colles. Squares indicate summarized curve from counting areas on the Electris deposit, diamonds refer to combined curve of counting areas in ridged plains (Fig. 4.3). Red data points have been corrected for resurfacing (Michael and Neukum, 2010).

reliable retention ages were combined based on the geological mapping to improve the statistics. The resulting crater size-frequency curves were analyzed individually for each counting area, and data curves providing reliable retention ages were combined based on the geological mapping to improve the statistics. The resulting crater size-frequency curves are shown in Fig. 4.12. It shows the crater records of the combined counting areas E1 through E5 on the "Electris" unit and RP1 through RP3 on the ridged plains unit, respectively. The counts on the "Electris deposit" results in an age of 3.88 Ga, near the Noachian-Hesperian boundary. The resurfacing age estimated on this unit is 3.69 Ga. This is similar to the base age of 3.64 Ga measured for the ridged plains unit. This age indicates that the ridged plains unit is younger than the Electris deposit, consistent with crosscutting/embayment relationships that the ridged plains unit was emplaced in the Early Hesperian around 3.7 Ga, and that this event apparently also erased some of the smaller craters in the "Electris deposit". The ridged plains display a somewhat less clear resurfacing age of 2.75 Ga. The geological process or event that led to the resurfacing is uncertain. It could be related to a late emplacement of lava, to the younger fluvial events observed in this area, or to a further process that has not been identified yet.

4.5 Discussion

One of the main objectives of this study is the investigation of the relative stratigraphy of the individual units. In knob field A (Fig. 4.2), the light-toned mounds show a maximum height of 300 m. The largest mounds show mesa-like tops, whereas mounds lower than 300 m systematically form rugged tops. The base of the knobs has locally been exposed by impacts. These two observations suggest that the mounds are erosional remnants of a layer once up to 300 m thick, unlike the chaotic terrains in the circum-Chryse region, which do not show a layer structure.

The circular wrinkle ridge around the knob field suggests that the light-toned material accumulated in an impact crater. This would also explain why the knobs are smaller towards the outer rim of the knob field, as in these areas close to the rim of the impact basin, a thinner light-toned layer would have been deposited. The scarp of the Electris deposit in the NE of the basin has approximately the same height as the light-toned mounds. Light-toned patches are observed on top of the scarp. They have a similar texture and hue as the light-toned material in the knobs. Therefore, they might consist of the same material, yet with different thicknesses. The ridged plains were interpreted by Grant and Schultz, 1990, Grant *et al.*, 2010, Scott and Tanaka, 1986 as underlying the Electris deposit and the knob fields. Our inspection of the surface of the ridged plains along the scarp revealed no evidence for the removal of an overlaying unit. We therefore interpret the ridged plains as overlaying and embaying the Electris deposit. This is supported by the observation of a wrinkle ridge apparently cross-cutting the Electris deposit near the upper left of Fig. 4.2A and B. If the ridged plains indeed overlay the Electris deposit and the knob field, it is unclear which unit is exposed underneath the light-toned material, as in Fig. 4.2D. One possibility is the "layered unit", a unit susceptible to wrinkle ridge formation underlying the knob fields in the Atlantis basin. The light-toned mounds are covered by a thin, light-toned, jointed and apparently more erosion-resistant cap. This cap is observed both at the top and at the flanks of mesas. It must therefore have formed after the break-up of the once contiguous

layer into individual mounds. The resulting stratigraphic interpretation is shown in the cross-section in Fig. 4.2C.

Further evidence for the stratigraphic position of the ridged plains on top of the knob fields and the Electris deposit is found in the Ariadnes basin. The three interconnected circular structures near 174°E, -38°N are most likely impact basins (Fig. 4.3A,B). They are surrounded by the Electris deposit and filled with the ridged plains. Therefore, the Electris deposit must have already been in place at the time of the impacts, but the deposition of the ridged plains material occurred later.

The mounds in Ariadnes Colles partly display a pattern of parallel lineaments, possibly dikes or joints. This pattern can be traced from one mound to the next, indicating that they once formed a contiguous layer, and that the mounds were not translocated relative to each other. The light-toned patches in the North and North-East of Ariadnes are probably remnants of this contiguous layer. They are dissected by valleys which are filled with ridged-plains material (Fig. 4.4). This shows again, that the ridged plains are younger than the light-toned material. The valleys observed on top of the ridged plains (Fig. 4.3) must have formed in a later aqueous phase than the valleys in the light-toned material.

Similar observations can be made in knob field B (Fig. 4.5). Here, a wrinkle ridge is found within the knob field, showing that the light-toned material must have been in place at the time of the wrinkle ridge formation. The mounds in this basin mostly show a rounded upper surface, but the uppermost parts of the largest mounds have rugged, uneven tops. One possible explanation would be the presence of an ice sheet eroding the lower parts of the mounds, and leaving only the uppermost sections of the highest mounds sharp.

In the Atlantis basin (Fig. 4.6), the stratigraphic relationship between the light-toned mounds, the Electris deposit and the ridged plains is not as straight-forward as in the other basins in this study. Although the smooth plains dissected by wrinkle ridges and mapped as ridged plains appears to embay and thus onlap on the light-toned mounds and the material mapped as Electris deposit, wrinkle ridges are also observed between mesas of the Electris deposit. This is evident at the western rim of the northern part of the Atlantis basin and at the eastern side of the southern Atlantis basin. Our interpretation is that one unit susceptible to wrinkle ridge formation is found below the Electris deposit, and a second one covers the Electris deposit. It is this latter one, which is mapped as "ridged plains" in this study, whereas the first is mapped as a "layered unit". It is also exposed at the structure formerly interpreted as a volcano (Greeley and Guest, 1987) shown in Fig. 4.6C, where it displays layering planes. The layered unit is also found on the eastern side of the southern Atlantis basin and shows a similar layering texture.

The knob fields in basin A, Ariadnes Colles, basin B and in part in the Atlantis basins show sharp boundaries towards the southeast. They have a parallel orientation, suggesting a common origin. They are possibly formed by wind erosion, degrading the knob fields, with wind directions predominantly coming from the South-East.

The deposits in basin C show the light-toned material within the process of breaking up into individual knobs. Some mounds stand up higher over the surrounding light-toned material, suggesting that its thickness has been reduced by erosion. In most places, the light-toned material is

covered by dark, possibly basaltic material. In places, this basaltic material is found in fissures between mounds. After the complete removal of the mounds by erosion, these features stand out as walls and show the location of the previous mounds. Locally, valleys debouch into flat areas where water has ponded. This is evidenced by the deposits appearing light blue in HRSC false color data, which have been interpreted as chlorides by Osterloo *et al.*, 2010. Upon close inspection, linear features become apparent, which might be shoreline deposits. They suggest that the chloride-forming lake dewatered into the impact basin in the southwest corner of Fig. 4.8.

The deposits in the Gorgonum basin show the most diverse evidence for aqueous processes occurring after the deposition and degradation of the light-toned material. The eastern part of the basin shows a dissected terrain, resembling the chaotic terrains around the Chryse region in its pattern. The largest of the faults in the dissected terrain are parallel to the Sirenum Fossae, indicating that these faults might have contributed to the formation of the dissected terrain. Some of the valleys running down the slope of Gorgonum basin use branches of the Sirenum Fossae as flow paths, as shown in Fig. 4.7C. Therefore, the valleys must have formed after the formation of the grabens, unlike in the other basins of this study, where the Sirenum Fossae appear to post-date all other events. The valleys were probably sourced by melting ice accumulated on the basin slope and rim (Howard and Moore, 2011). Alternatively, magmatic dikes underneath the Sirenum Fossae might have contributed to the melting of accumulated ice or snow in the basin slopes and rim. Note that the light-toned mounds formed prior to Sirenum Fossae and the lake in the lowest parts of the Gorgonum basin.

The valleys, the thin dark deposits below the 0-m-contour line and the flat-topped benches at -300 m have been interpreted by Howard and Moore, 2004, 2011 as evidence for a lake. The suggested lake would have been covered with a 300-m-thick ice sheet between 0 m and -300 m elevation, which resulted in the compression of soft sediments in the liquid water underneath the ice cover, forming the flat-topped benches (Howard and Moore, 2004, 2011). Our observations suggest a slightly different evolution, including an open lake with little or no ice cover and a dropping water level. The lake probably had its high-stand near 0 m, but the water level dropped quickly to approx. -150 m. This is shown by the valleys running into the lake, which have continuity below the 0-m-contour down to the -150-m-contour, and the relatively thin cover of sediments, which preserved the shape of the underlying light-toned mounds. The water level stabilized near -150 m, and sediments were deposited near the shore. Later, the lake level dropped further to -300 m. This exposed the water-rich sediments above this level, they collapsed into the small "chaotic" knobs, and new, flat-topped benches formed below -300 m.

Taking these observations and interpretations together the knob fields of the Terra Cimmeria/Terra Sirenum region of Mars display many characteristics in common. All knob fields are constrained to local basins, but occur at variable elevations. The albedo, texture and morphometry of the mounds suggest that they are erosional remnants of a once contiguous layer of light-toned material draping the entire region of this study, as similar material is found as patches elsewhere in the region, and various stages of break-up into knobs from contiguous layers to narrow fractures as in basin C to mounds and mesas have been found.

A thin (few m thick) layer of the light-toned material exposed at the top of the fine-grained, cliff-forming benches has been mapped as part of the "Electris deposit" (Grant and Schultz, 1990, Grant *et al.*, 2010). The Electris material underneath the light-toned cover sometimes shows layering, but mostly appears featureless and displays an intermediate albedo. In a few places, impact craters in the knob fields expose the lower boundary of the light toned material. Here, we observe no evidence for a fine-grained, featureless layer with intermediate albedo resembling the "Electris deposit" at the basin rims. This suggests that the light-toned material does not simply superpose the "Electris deposit" material, but replaces it or was formed by alteration of it.

Both the "Electris deposit" and the light-toned mounds and patches are located stratigraphically on top of a layered material showing wrinkle ridges, which we called layered unit (Npl_2 in Greeley and Guest, 1987). They are also covered by a relatively thin layer of basaltic material usually mapped as ridged plains (Hr). This implies that the Electris deposit and the light-toned material formed before the Hr unit, as also observed by Golder and Gilmore, 2012a, b. Despite the large extent of the region showing light-toned mounds and patches, their mineralogy appears to be relatively uniform. The outermost parts of the mounds and light-toned patches often show a light-toned, hardened crust. It is spectrally neutral or shows very weak absorption bands of Fe/Mg-clays. Strong absorption bands are only observed where this outer crust has been breached by erosion. This might explain why most of the CRISM observations in this area show no clear absorption features. The dominating constituents observed with CRISM are Fe- and Mg-rich clays with a ferrous component, together with minor amounts of possibly acid-leached clays and Al-rich clays. Noe Dobrea *et al.*, 2008, reported, that the mineralogy changes from mound to mound. We interpret these changes to be due to local variations of the alteration processes affecting the deposits. This is suggested by the presence of joint fills as well as color changes in the Mg-rich rocks seen in HiRISE imagery. They provide evidence for the circulation of water within the joints after the deposition of the rocks.

These observations allow a reconstruction of the geologic events in this area (Fig. 4.13):

(1) Deposition of the Electris deposit on top of the Noachian basement and the layered unit. The concave-up geometry of the layered unit has been seen as evidence for the existence of the Eridania lake, which would have inhibited an efficient transport of sediments towards the basin center. This would have prevented the development of a horizontal, flat crater floor typical for craters of this size (Irwin *et al.*, 2004). Our observations suggest that the Electris deposit is stratigraphically below the ridged plains unit (Hr; Greeley and Guest, 1987, Scott and Tanaka, 1986). It is found both inside the suggested shoreline of the Eridania lake at 1100 m and outside, and is not constrained to the study area investigated here. Outcrops of this material are found in the entire region between 160°E and 210°E and -30°N and -50°N (Grant *et al.*, 2010). If our stratigraphic interpretation is correct, the Electris deposit would have been formed prior to the Eridania lake, and an alternative explanation is required for the unusual shape of the basins. However, the non-circular outline of the basins, and the presence of many wrinkle ridges and Sirenum Fossae faults show that tectonic forces played an important role in the shaping of these basins - they might therefore also be responsible

for the bowl-like relief of the basins, although the exact mechanism remains unclear.

The valleys cross-cutting the Electris deposit were interpreted by Irwin *et al.*, 2004, as fluvial features post-dating the Eridania lake. With the new stratigraphic position of the Electris deposit established in this work, they would dewater directly into the Eridania lake or local basins in the same location. Grant *et al.*, 2010, investigated several possible depositional modes for the Electris deposit, and concluded that the relatively constant thickness despite variable absolute elevations, observed bedding thicknesses and other characteristics are best explained by formation by airfall, possibly similar to loess.

(2) Valleys carved into the Electris deposit and dewater into the Eridania lake or into local basins. As discussed before, the Eridania lake would have existed after deposition of the Electris deposit. Irwin *et al.*, 2004 noted that most of the largest valleys end near the 1100-m-contour, which would have been the approximate shoreline of the Eridania lake. This lake is required to allow outflow activity in Ma'adim Vallis, because the head of this outflow channel is at a higher elevation than the putative source region of it. The lake eventually breached a mountain barrier West of basin C , and deepened Ma'adim Vallis. The formation of Ma'adim Vallis by a catastrophic outflow event is not consistent with results from Cabrol *et al.*, 1998, who reconstructed a sustained activity of Ma'adim Vallis between 2 Ga and 700 Ma based on crater counts. Capitan and Van De Wiel, 2010, noted that other morphologic features expected for a lake at this level, including deltas and clear indicators of shorelines are missing, yet these morphological features might have been eroded before or covered by the emplacement of the younger ridged plains unit.

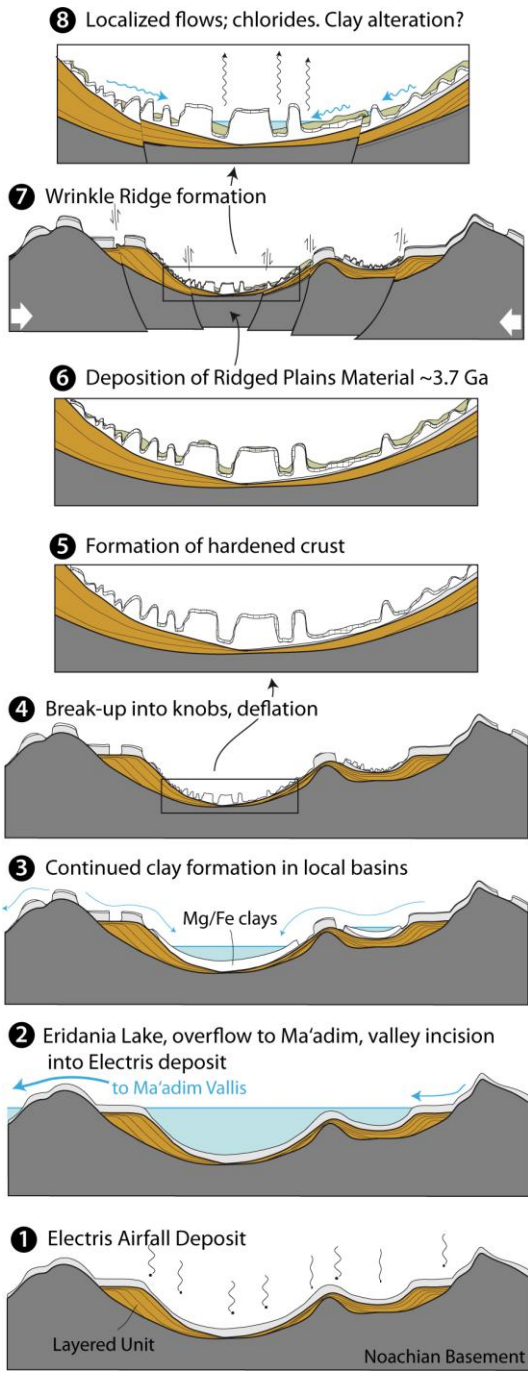

Fig. 4.13: Interpretative geologic history of the basins in the study area (schematic).

(3) The water level dropped and individual lakes at different absolute elevations formed, in which the Electris deposit was altered into Mg/Fe-phyllosilicates. The Electris deposit outcrops near the rims of the basins are locally covered with a thin, light-toned layer. It displays a similar texture as the light-toned material towards the basin

centers, and also has the same mineralogy dominated by Mg/Fe-clays (Grant *et al.*, 2010). Consequently, the light-toned mounds and mesas might overlay the Electris deposit (Noe Dobrea *et al.*, 2008). On the other hand, the mounds and mesas in the basin centers have the same thickness as the Electris deposit, and a layer resembling the Electris deposit underneath the light-toned mounds and mesas is not found, even if the lower boundary of the light-toned material is exposed by impact craters. Therefore, we suggest that the light-toned material consists of Electris material that has been aqueously altered into phyllosilicates. This is consistent with the presence of phyllosilicates in local lows at variable elevations, and valleys running into these lows. Clay minerals have been detected in several hundreds to thousands of individual outcrops in Noachian-aged regions of Mars (Bibring *et al.*, 2006, Mustard *et al.*, 2008). In most cases, it is unclear if the clays are authigenic, detrital or diagenetic (Ehlmann *et al.*, 2011, Grotzinger and Milliken, 2011). On Earth, clay minerals are often deposited, eroded and redeposited in a different location. The sedimentological indicators for these processes are difficult to observe from orbit on Mars, and rover investigations are necessary. The lack of plate tectonics on Mars suggests, however, that the clay minerals on Mars might have experienced a simpler recycling history than the same minerals on Earth, despite their higher age (Milliken and Bish, 2010). Indicators for detrital phyllosilicate deposits are found, for example, in Eberswalde crater, where clays with similar mineralogy are found in the source region of the delta-forming channels and in the delta deposits in that crater, suggesting that they were transported from the former to the latter (Milliken and Bish, 2010). The clays in this study are found at or near the surface, excluding a diagenetic origin. The dendritic valleys on the Electris deposit and the locally observed thin layer of clay minerals at its top (Grant *et al.*, 2010) suggest that water was provided at least in part by precipitation, as groundwater would have caused clay formation at depth, but not at the surface. Therefore, we suggest that the clays in the light-toned deposits studied here were formed by top-down alteration of the possibly glass-rich Electris deposit (Grant *et al.*, 2010, Noe Dobrea and Swayze, 2010) in situ, or transported from the slopes of the basins towards the centers. This formation mechanism would make these deposits "sedimentary clays" of Ehlmann *et al.*, 2011, which is consistent with their late-Noachian age.

(4) The clay-rich, light-toned layer broke up into individual knobs, and large parts of the deposit were eroded by deflation. Most of the knobs analyzed show no preferential orientation and are on the order of a few 100 m to a few km in size, and the comparison to basin C (Fig. 4.8) suggests that they are formed by break-up along a polygonal fault pattern. The fault spacing is on the same order as giant polygons described in Utopia Planitia and elsewhere on Mars (e.g., Carr *et al.*, 1976). Patterns with polygon diameters on the order of cm to tens of meters can originate in several different ways on Earth, including desiccation shrinkage of wet sediments to produce mud cracks, cooling of lava, and complex freeze-thaw cycles to produce ice-wedge polygons or thermal contraction polygons (Hiesinger and Head, 2000, and references therein). Polygonal patterns in the same scale order on Mars have been attributed to similar formation processes, but it has become clear that these mechanisms cannot readily account for the giant polygons in the km scale (Hiesinger and Head, 2000, van Gasselt, 2007). The theories put forward for the formation of giant polygons include uplift and extension

after removal of a standing body of water in Utopia Planitia (Hiesinger and Head, 2000), contraction over a rough-surfaced buried topography (Cooke *et al.*, 2011), or regional tectonic stress (Pechmann, 1980).

The circular knob-free plain near the center of Atlantis Chaos might have been caused by an ice lens, as suggested by de Pablo and Fairén, 2004. This lens was possibly the remains of the Eridania lake, that inhibited the transport of altered Electris material to the center of the Atlantis basin. The knob free area is slightly offset from the lowest part of the basin, where a remaining ice lens would be expected. Therefore, the floor of Atlantis would have to have been tilted in a later stage (7). This would be consistent with sloped crater floors on the rims of Ariadnes basin (Irwin *et al.*, 2004). When the knob fields were eroded by wind, the predominant wind direction must have been SE, resulting in the abrupt boundaries of Ariadnes and Atlantis Chaos and knob field A, which all trend in a SW-NE-direction.

(5) A hardened crust formed at the outward-facing parts of the clay-rich mounds. Strong absorption features of clays are observed only when the outer crust is breached; otherwise, only very faint absorption bands occur, suggesting that the outer crust consists of desiccated, clay-rich material.

(6) The knob fields were covered or embayed by basaltic material forming the Hesperian ridged plains unit Hr (Greeley and Guest, 1987, Scott and Tanaka, 1986). The source of the material is unknown. A direct link to the Sirenum Fossae is not observed.

(7) Compressional stress exerted from the Tharsis Rise produced reverse faults in the subsurface and wrinkle ridges in the layered deposits (ridged plains, layered unit) near the surface. The wrinkle ridges, including those in the layered unit underneath the Electris deposit, cannot have formed earlier, because otherwise the overlaying units would not be faulted/folded as well.

(8) Numerous valleys on top of the uppermost basaltic ridged plains and between the individual knobs as well as on the slopes of the basins developped (Howard and Moore, 2011). They are evidence for further water related events in this area after the clay forming activity. The valleys were deflected by the wrinkle ridges and formed local lakes. Locally, these lakes might have been frozen, resulting in morphologies resembling Nunataks (Fig. 4.8B).

In basin C, a lake formed and evaporated, leaving a deposit rich in chloride behind (Fig. 4.8; Osterloo *et al.*, 2010). The light-toned deposits have filled joints and display spectra indicative of acid leaching (e.g. Madejová et al., 2009; Bishop et al., 2012). Locally, aluminum-rich phyllosilicates such as montmorillonite, are found, which can form by acid alteration of Mg/Fe-smectites (Bishop *et al.*, 2008a). It is unclear if this alteration occurred at the same time as the formation of the chloride deposits, or if it took place at another point in time.

Faults of the Sirenum Fossae cross-cut the entire study area (not shown in Fig. 4.13). They postdate the clay formation, and in most parts of the study area the relationship to later aqueous events is unclear. An exception is the Gorgonum basin, where a lake formed in the basin center below the 0-m-contour. Valleys feeding this lake ran through branches of Sirenum Fossae, and sediments of the lake superposed parts of the grabens and the dissected terrain connected to Sirenum Fossae (Howard and Moore, 2011).

The absolute timing of most of the steps forming the basins described above is difficult to constrain. The main activity of Ma'adim Vallis is

estimated to have occurred at the N/H boundary (Irwin *et al.*, 2004), which fits better with our observations than the long-lasting channel activity from 2 Ga to 700 Ma proposed by Cabrol *et al.*, 1998. Crater counts on the ridged plains unit in the Ariadnes Colles area yield an age of ~3.6 Ga. The incision of the small valleys into this unit occurred in the late Hesperian and Early Amazonian (Howard and Moore, 2011).

4.6 Conclusions

Fields of light-toned knobs in the Terra Cimmeria/Terra Sirenum region of Mars are interpreted as erosional remnants of a once contiguous layer of light-toned material, which is exposed in many small outcrops from underneath its basaltic cover. They are not regions of collapse and outflow of water as in the Circum-Chryse region. Knobs only occur in local basins, where deposits were thickest, and where aqueous alteration of the material was the most efficient. In high-standing areas, the same material forms only a thin, light-toned cap rock, which led to the formation of flat mesas and steep cliffs. The light-toned material contains Mg- and Fe-rich phyllosilicates, which appear to have been locally altered to Al-rich phyllosilicates by acid leaching. The clays possibly formed by subaqueous alteration of the Electris Deposit, a fine-grained sedimentary unit described as airfall deposit (loess) by Grant *et al.*, 2010. The stratigraphic position of the phyllosilicate-rich deposit is consistent with clay formation within a network of local lakes that possibly once formed the Eridania lake (Irwin *et al.*, 2004) in the late Noachian. Further research is necessary to map the exact flow relationships between the individual basins. The knob fields were later covered by the Hesperian ridged plains unit (Hr) modified by deflation, wrinkle ridge formation, Sirenum Fossae faults, and the incision of local valleys sourced from precipitation or melting snow/ice packs in the upper parts of the local basins (Howard and Moore, 2011). Locally, chlorides were deposited in evaporating lakes (Osterloo *et al.*, 2010). This study combines mineralogical, morphological and stratigraphical evidence on a regional scale to decipher a complex and long-lasting aqueous history. The aqueous activity continued after the main phase of clay formation near the N/H boundary, and features valley networks, localized lakes and possibly mineral alteration stages.

Acknowledgment

We thank two anonymous reviewers for their constructive remarks and comments, which helped improving the manuscript.The work has been financially supported by the German Space Agency (DLR Bonn) grant 50QM1001 "HRSC on Mars Express" on behalf of the German Federal Ministry of Economics and Technology. We thank S. Walter from the Freie Universität Berlin for the processing of several datasets and mosaics.

5 Regional Study of the light-toned mounds in Juventae Chasma by linear spectral unmixing of near infrared data from CRISM

The following section has been published as:

Wendt, L., Combe, J.-P., McGuire, P. C., Bishop, J. L. and Neukum, G., 2009, "**Linear spectral unmixing of near-infrared hyperspectral data from Juventae Chasma, Mars**" in *Image and Signal Processing for Remote Sensing XV*, edited by Bruzzone, L., Notarnicola, C., and Posa, F., Proceedings of SPIE Vol. 7477 (SPIE, Bellingham, WA), 7477 0M, (2009).

The article may be found using this link: http://dx.doi.org/10.1117/12.830095

5.1 Abstract

Juventae Chasma is a depression north of Valles Marineris on Mars, approximately 185 km wide and 270 km long. It contains several mounds of light-toned, layered deposits several tens of kilometers of maximum extension and up to 3300 m in elevation. Near infrared spectral data from the Observatoire pour l'Eau, la Minéralogie, les Glaces et l'Activité OMEGA onboard ESA's Mars Express indicated mono- and polyhydrated sulfates as main constituents of these deposits, including gypsum in one of the mounds (Gendrin *et al.*, 2005b). We analyze the light-toned outcrops based on data from NASA's Compact Reconnaissance Imaging Spectrometer for Mars (CRISM), featuring an increased spatial resolution of up to 18m/pixel and increased spectral resolution of 7 nm. We perform Spectral Mixture Analysis (SMA) in order to introduce physical modeling and to enhance some surface units. We use one type of SMA, the Multiple-Endmember Linear Unmixing Model MELSUM (Combe *et al.*, 2008b), which guarantees positive mixing coefficients and allows us to limit the number of spectral components used at a time. We use linear unmixing both as a similarity measure using spectra from the image itself as endmembers to assess the internal variability of the data, and to detect mineral spectra within the observations. We confirm the presence of the monohydrated sulfate szomolnokite (previously detected by Kuzmin *et al.*, 2008, Rossi *et al.*, 2008) in all of the four light-toned deposits observed. Based on our analysis, we reject the presence of gypsum on mound B (previously detected by Gendrin *et al.*, 2005b). A possible match for the polyhydrated sulfate present here could be rozenite, but other sulfate minerals also have to be considered. The implications of the possible presence of iron-bearing polyhydrated sulfates such as rozenite and the absence of calcium-bearing gypsum for the geological history of the outcrops are not yet fully understood. Our next step is the geochemical modeling of the weathering of Martian basaltic rocks, dominated by iron and magnesium silicates, to iron-bearing sulfates under acidic conditions.

5.2 Introduction

Juventae Chasma is a closed depression located around 4° S, 61°W on Mars (Fig. 5.1). It is located about 500 km north of the main canyons of Valles Marineris. The depression is about 185 km wide and 270 km long, its floor lies six to seven km below the surrounding, Hesperian-aged

lava plains. The chasm is located at the southern end of Maja Vallis, one of the Martian outflow channels debouching into the Chryse Region of Mars. While most of the floor of the depression is covered by dark, basaltic sand, it hosts four major light-toned layered deposits, labeled A-D (Catling *et al.*, 2006, Chapman *et al.*, 2003). These outcrops form mounds up to several tens of km in extension and up to 3.3 km in height. The mounds unconformably overlie chaotic terrain on the canyon floor. The mineralogy of these outcrops was studied by Gendrin *et al.*, 2005b based on data from the infrared spectrometer Observatoire pour l'Eau, la Minéralogie, les Glaces et l'Activité OMEGA (Bibring *et al.*, 2004) on board ESA's Mars Express, suggesting monohydrated sulfates (kieserite, szomolnokite) as major constituents. They also suggested that the upper part of mound B contained the polyhydrated sulfate gypsum. This was questioned by Kuzmin *et al.*, 2008, who remarked that a late-stage precipitation of gypsum after the formation of monohydrated sulfates, as suggested by the observed stratigraphy, is thermodynamically not favorable. This is confirmed by thermodynamic modeling and laboratory tests by Tosca *et al.*, 2005 of the acidic weathering and following sulfate precipitation of the basaltic source rock present on Mars, indicating that Mg- and Fe-bearing sulfates should predominate over Ca-bearing sulfate such as gypsum. A more recent study by Bishop *et al.*, 2009, using hyperspectral data from the Compact Reconnaissance Imaging Spectrometer for Mars (CRISM, Murchie *et al.*, 2007a) onboard NASA's Mars Reconnaissance Orbiter MRO confirms the presence of the monohydrated sulfate szomolnokite as well as the presence of polyhydrated sulfate in the upper layers of mound B, but left the exact identification of the polyhydrated sulfate open due to the high similarity among the spectra of this mineral group.

The formation of the light-toned deposits remains unsolved. Suggested scenarios include a volcanic emplacement by sub-ice volcanoes (Chapman *et al.*, 2003), which now appears less likely due to the presence of sulfates, a formation as a volcanic airfall deposit, or the precipitation from a standing body of water (Gendrin *et al.*, 2005b). The formation as spring deposits was suggested by Rossi *et al.*, 2008, which would explain the apparent morphological differences between the individual outcrops.

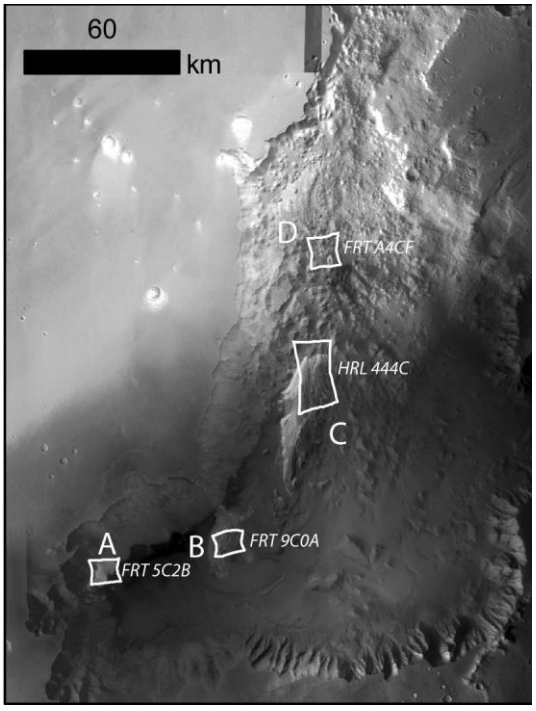

Fig. 5.1: Overview of Juventae Chasma.
Image mosaic of High Resolution Stereo Camera (HRSC) nadir images from Juventae Chasma on Mars acquired in orbit 243, 449, 1059, 1929, 1940 and 1984 with the location of the four light-toned deposits A-D (Chapman *et al.*, 2003, Scott and Tanaka, 1986) and the CRISM datasets used in this study.

In this study, we analyze CRISM hyperspectral data using the Spectral Mixture Analysis (SMA; Adams and Gillespie, 2006). The SMA is a generic name of methods that assume that remote-

sensing spectra of the surface are linear combinations of spectra of their constituents. This is a way to introduce physical modeling of areal mixtures as an a priori knowledge. The objective is essentially to separate the observed surface units for better geological interpretation. As a result, it is possible to map relative spatial variations. Evaluations of abundance by this method is only possible in rare cases where spectral mixtures within a pixel result patches of various surface components at macro-scale. We use one method of SMA, the Multiple Endmember Linear Spectral Unmixing Model (MELSUM; Combe *et al.*, 2008b). Specifically, MELSUM allows us to use a reference spectral library which can stem either from the spectral observation itself or from a spectral library. Furthermore, MELSUM returns linear mixture solutions with positive mixing coefficients only, and allows the user to constrain the maximum number of constituents that contribute to the linear mixture of each observed spectrum, avoiding a combination of a high number of reference spectra at amplitude levels in the order instrument noise, which would return a mathematically better, but in a practical sense worse result. Our objective is also to determine the type of polyhydrated sulfate present at mound B by taking advantage of the entire shape of the observed spectrum rather than only a few selected spectral regions.

For this purpose, we analyzed four CRISM observations, one from each of the four light-toned deposits (Fig. 5.1). We first determined the spectral variability present in the dataset by using MELSUM with image endmember spectra selected visually from the datasets. In a second step, we assessed the composition of the individual regions identified in the first step using MELSUM with a set of endmembers from laboratory measurements. The following section provides an overview to the dataset used for this study and the pre-processing applied to it, followed by a detailed description of MELSUM. Section 4 documents the results for the individual outcrops/datasets, and section 5 concludes the paper.

5.3 The CRISM Dataset

CRISM is an imaging spectrometer collecting spectra by two detectors in the range of 0.36-1.05 and 1.00-3.92 µm with a spectral resolution of 6.5 nm (Murchie *et al.*, 2007a). In the full resolution targeted (FRT) mode, CRISM acquires images in all the available 544 channels with a spatial resolution of approx. 18 m/pixel from selected targets approx. 10 by 10 km in width and length. In half resolution long targeted mode (HRL), the pixels are spatially binned, resulting in a spatial resolution of roughly 40 m/pixel over an area of approx. 10 by 20 km. These types of observation are possible due to the gimbaled mounting to the spacecraft, which allows tracking of a target during the fly-over of the spacecraft. This results in the hour-glass shape of the observations in Fig. 5.1. CRISM also features multispectral modes that allow a continuous acquisition over longer image stripes at 72 selected channels and a spatial resolution of 100 or 200 m/pixel. In this study, only FRT and HRL were used.

The data is converted from digital numbers to I/F values using the steps described and implemented in the CRISM Analysis Tool (CAT). The instrument background is removed and the raw data is divided by internal calibration standards. It is then divided by the solar irradiance to obtain reflectance data. Illumination variations across a scene are alleviated by dividing by the cosine of the incidence angle, thereby assuming a Lambertian behavior. The most important

processing step is the correction of atmospheric effects. The CO_2 atmosphere of Mars results in a triplet of strong absorption bands near 2 µm - a correct removal of these bands is critical to a spectral mixture analysis, as many sulfate minerals show absorption features in the same spectral region. The CO_2 absorption bands are removed by dividing by a scaled transmission spectrum acquired from observations from the base and top of Olympus Mons using the wavelengths proposed by McGuire *et al.*, 2009. We generally had the atmospheric correction algorithm select the ideal transmission spectrum to remove time-dependent wavelength shifts observed with the CRISM sensors. Although generally not remarkable, these shifts can cause strong artifacts in the spectral region of the CO_2 bands. However, some of the transmission spectra contain features of water vapor and thus introduce a water signature to the corrected data. Therefore, the data was checked visually, and in the case of an observed water-related absorption features near 1.5 and 1.9 µm, the default transmission spectrum was selected. Finally, large spikes and bands in the data were removed using a cleaning algorithm (Parente, 2008). We used data only from CRISM's long wavelength sensor in the spectral range of 1.0 -2.5 µm. For selected regions, average spectra over at least 3 by 3 pixels were analyzed.

5.4 Methodology

5.4.1 The Multiple-Endmember Linear Spectral Unmixing Model (MELSUM)

Analysis of HRSC color data at a spatial resolution of 50 m/pixel (Wendt *et al.*, 2008) and imagery from the High Resolution Imaging Science Experiment HiRISE with a spatial resolution of up to 25 cm/pixel (Wendt *et al.*, 2009) indicate that even when using CRISM data with a spatial resolution of 18 m /pixel, no pure mineral spectra can be expected, but mixtures of several minerals. Mixtures of minerals can be generally grouped into areal mixtures, where the individual components are spatially separated from each other, and intimate mixtures, where the individual types of mineral grains are mixed with each other. In the (ideal) first case, observed spectra can be modeled by a linear combination of endmember spectra from the image itself or from a spectral library (Singer *et al.*, 1979). In the latter case, the light interacts with more than one endmember, leading to a complicated non-linear behavior (e.g., Hapke, 1981), which usually requires more knowledge on the atmospheric conditions at the time of the observation and the minerals involved than available. MELSUM therefore uses linear unmixing as the strategy to model the observed spectra. However, as both areal and intimate mixtures occur on natural surfaces, and thus intimate mixing effects have to be accommodated by linear combinations, a link between the resulting mixing coefficients and the actual proportion of materials on the surface is not straight forward and is not attempted in this study.

MELSUM has been successfully applied to data from a range of planetary bodies acquired with different sensors, including AVIRIS data from Cuprite, Nevada, OMEGA data from Mars (Combe *et al.*, 2008b) and Clementine UVVIS data from the Moon (Combe *et al.*, 2008a). As other SMA algorithms, MELSUM is based on the well-known least-square system

$$Y = AX \qquad (1)$$

where Y is the observed remote sensing spectrum, A is a matrix of the input spectra and X is a vector containing the coefficients for each of the library

spectra that make up the observed spectrum Y. The solution to this equation is

$$X = (A^tA)^{-1} A^t Y \quad (2)$$

with the constraint that negative coefficients have no physical meaning and are therefore not allowed. One algorithm that supports this non-negativity constraint is the one suggested by Lawson and Hanson, 1974. This algorithm can return solutions that require a high number of laboratory spectra at abundance levels in the order of the instrument noise, which is hard to interpret in a geological sense. Therefore, MELSUM uses a different strategy to obtain non-negative coefficients and to give the user the option to constrain the maximum number of endmembers in the solution. First, MELSUM explores all possible combinations of less or equal the number of allowed endmember spectra in the final solution and stores the X^2 residual. It then returns the solution with the lowest residual and only non-negative coefficients, at the expense of a considerably longer computation time. A maximum number of three to four endmembers allowed in the mixture was used, which proved to be sufficient, as the addition of a fifth endmember did not result in significantly lower residuals.

5.4.2 The choice of the spectral library

We analyzed the CRISM scenes in the first step using manually chosen spectra from selected areas in the scene itself to determine the variability of spectra present in the scene. We started with only a low number of image spectra and analyzed the resulting residual image. We then iteratively added further image spectra to the endmember library until the observed residuals were in the order of the instrument noise and spatially not coherent. In a second step, we analyzed spectra averaged over typically 3 by 3 pixels using MELSUM against a set of laboratory spectra. Finally, we modeled every spectrum of the CRISM scenes in an automatic way using a set of laboratory spectra to produce coefficient maps.

Our library of laboratory spectra is derived from the CRISM spectral library available with the CRISM Analysis Tool CAT. It contains a spectrum for clinopyroxene, orthopyroxene, the Mg-rich olivine forsterite and the Fe-rich olivine fayalite to account for the mafic minerals present on Mars. It also contains hematite and goethite as representatives of the Martian iron oxides. The sulfates are represented by szomolnokite and kieserite as monohydrated sulfates, gypsum and a range of polyhydrated sulfates. We also included a spectrum for water ice to account for thin Martian ice clouds. The final library contained a total of 24 spectra when an entire scene was processed, and up to 60 spectra when spectra from selected spots were modeled, including borates and other evaporites known from Earth. However, those more "exotic" minerals never matched the observed spectra, and were therefore left aside in the following calculations. Note, however that not for all sulfate minerals possibly stable under Martian conditions a spectrum was available.

5.4.3 The photometric library

The shape of a spectrum is not only determined by the type of mineral observed, but also by the grain size and texture variations, but reference spectra for different grain sizes are not available for all minerals. In fact, smaller grain sizes lead to lower absorption band depths, but a higher surface scattering, and thus a higher signal. Featureless material present in the scene influences the overall brightness of the scene, and the surface phase function and the atmospheric backscattering can lead to an observed spectral slope, which cannot be accommodated by the spectra in the

reference library alone. Therefore, the MELSUM library contains a flat spectrum, a positive and a negative slope as "photometric" library to compensate these effects. These spectra are included into the inversion process in addition to the user-defined number of allowed endmembers in the solution. The reflectance level of these spectra is purely arbitrary, and was chosen to a maximum of 0.1.

5.4.4 Sum of coefficients is not constrained to 1

In a strict case of an areal mixture of perfectly known minerals, the coefficients of the spectra in the linear mixture in equation (1) sum up to 1, and the coefficients correspond to areal fractions of the observed pixel. The same is the case when the endmember library contains spectra from the scene itself. However, when modeling the observed spectra with a library of laboratory spectra of pure minerals, the linear combinations have to accommodate at the same time areal mixtures, intimate mixtures, grain size effects and illumination/scattering effects, which are represented by artificial spectra in the photometric library. Consequently, the coefficients cannot be considered image fractions, and their sum is not expected to be 1.

5.5 Results

5.5.1 MELSUM unmixing results for mound A

Mound A is the southernmost sulfate deposit in Juventae Chasma. It is located at the foot of the rim surrounding the depression. It rises approximately two km above the chasm floor and has a spatial extension of 15 by 7 km. We used the CRISM observation FRT00005C2B and applied an atmospheric correction with the time-dependent atmospheric transmission spectrum (CDR420862848019_AT000 0000L_5.IMG) and removed stripes and noise from the data using the CIRRUS module of CAT with the default settings. The results of the linear mixture analysis are shown in Fig. 5.2.

We first selected two image spectra, one for the light-toned material, and one for the dark dunes material on the floor of the chasm (Fig. 5.2 B). The spectrum of the sulfate deposit features a deep absorption band near 2 µm, a narrow absorption band near 2.4 µm and a drop-off beyond 2.4 µm. The spectrum of the dark material also displays an absorption band around 2 µm, and a broad feature between 1.8 and 2.3 µm, centered approximately at 2.1µm. We used these two spectra to characterize the spatial distribution of these materials to the first order. The resulting coefficient images and the residual (Fig. 5.2 C-E) show that these spectra are a fair first-order representation of the spectral variability present in this dataset.

We then used MELSUM to model the selected image spectra with up to 3 endmembers from a library of laboratory spectra containing 24 sulfates, iron oxides and mafic minerals. As all CRISM spectra seem to display an absorption band near 1.2 µm, we decided to exclude the channels below 1.3 µm. The mixture analysis shows that the sulfate spectrum can be very well modeled by a combination of the szomolnokite ($FeSO_4*H_2O$) and a mix of the two pyroxene endmembers in the spectral library. On the contrary, the dark dunes image spectrum is well modeled by a high coefficient for pyroxenes, and a minor admixture of szomolnokite. This indicates that material from each of the two regions is transported into the other region by wind, which is in agreement with the findings of Bishop *et al.*,

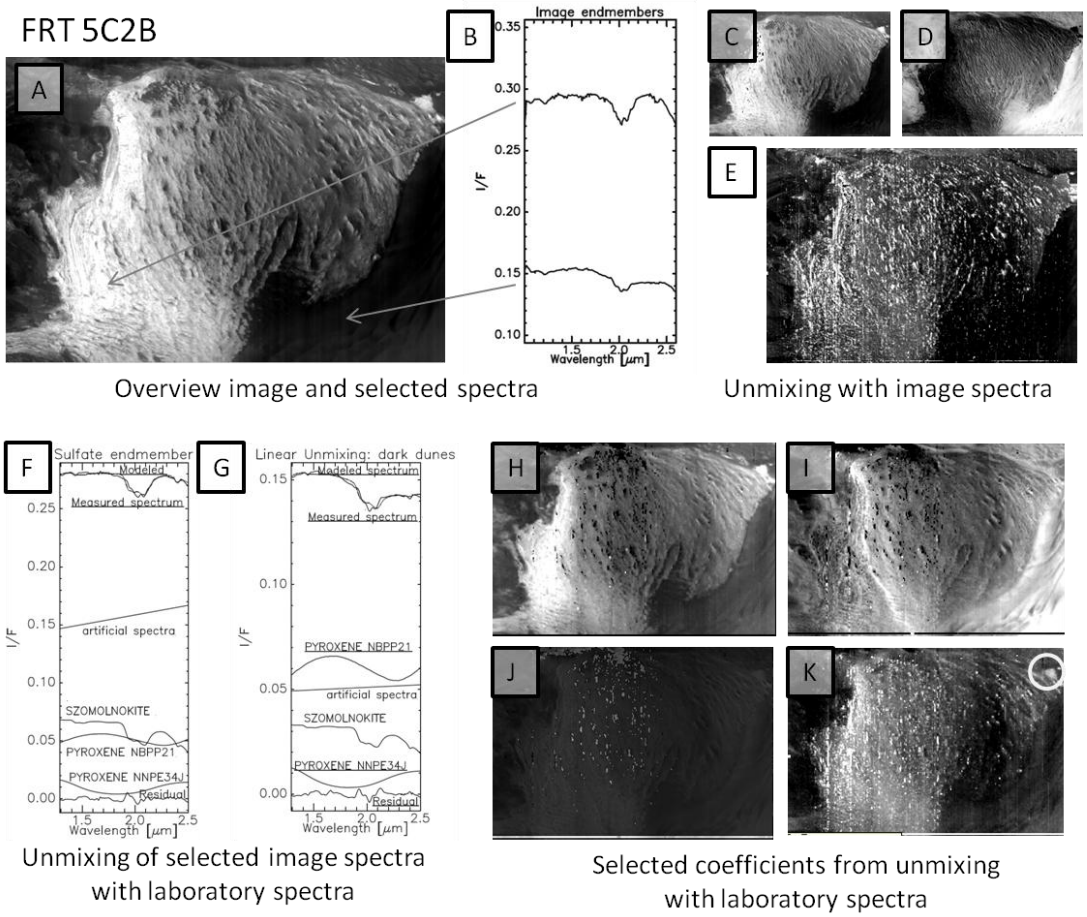

Fig. 5.2: Linear unmixing results for mound A, CRISM observation 5C2B.

A: Channel 4 (1.021 µm), unprojected. North is approx. 10° to the right. B: Manually selected spectra for sulfate-rich region (top) and dunes region (bottom). C-E: Unmixing results with image endmembers: C: sulfate endmember coefficient, D: dunes coefficient E: residual. F: Unmixing of sulfate endmember. G: Unmixing of dunes endmember. H-K: Unmixing results with laboratory spectra: H: szomolnokite coefficient I: clinopyroxene coefficient (NBPP21). J: orthopyroxene coefficient (NNPE34J), K residual.

2009 and Wendt *et al.*, 2008. The highest residual between modeled and measured spectra occur around 2µm absorption band. This suggests that the absorption features caused by the Martian CO_2 atmosphere have not been removed completely, and demonstrates the importance of a thorough correction before a linear spectral mixture analysis can be attempted.

Fig. 5.2 H-K show the result of the MELSUM unmixing of the entire scene, using the same spectral library of 24 laboratory spectra and constraining the solution to 3 endmembers. As expected, the light-toned deposit is dominated by szomolnokite, whereas the dark material is modeled by clinopyroxene and a minor contribution of orthopyroxene and szomolnokite. The residual image displays some image defects present in the raw data, but also shows some correlation to the albedo (Fig. 5.2A and K). Apparently, the surface spectra are modified by illumination effects that cannot be addressed by MELSUM's photometric spectra alone. The residual also displays a spot at the right side of the image (Fig. 5.2K, white circle), which is not well modeled by the spectral library used. This spot is interpreted by Bishop *et al.*, 2009 as a mixture of

szomolnokite and polyhydrated sulfate. Although our SMA has not revealed the type of polyhydrated sulfate in this mixture, it was able to identify it as distinct from the remaining sulfate material.

Bishop *et al.*, 2009 also report the presence of the monohydrated mineral kieserite ($MgSO_4*H_2O$) at a few spots of this outcrop. The spectra of szomolnokite and kieserite both display an absorption band near 2.4 µm, but are distinguished by an absorption maximum near 2.08 for szomolnokite and 2.13 for kieserite. Kieserite also displays a broad absorption near 1.7 and a shoulder near 1.8. These features have not been observed or detected in this study.

5.5.2 Unmixing results for mound B

Mound B has an extension of approximately 30 by 15 km and rises about 2800 m above the chasm floor. The lower part of the mound displays layering in the order of 10 m per layer, whereas in the upper part, layers are about 100 m thick. OMEGA near infrared hyperspectral data suggested kieserite in the lower, thinly layered part, and gypsum in the upper part of the mound Gendrin *et al.*, 2005b. We used CRISM observation FRT 9C0A and applied a non time-dependent atmospheric correction with the transmission spectrum ADR_VS_061C4_0000000L_5.IMG, as it produced better results than the time-dependently selected transmission spectrum proposed by CAT. We removed stripes and spikes using the CIRRUS function of CAT with default parameters.

Based on the a-priori information from the OMEGA study (Gendrin *et al.*, 2005b), we selected three regions of interest and calculated mean spectra over a few hundred spectra as input library for the SMA with image endmembers (Fig. 5.3). The lower part shows an asymmetric absorption around 2 µm, with a minimum at 2.08 µm and a smaller band at 2.4, both diagnostic for szomolnokite. The upper sulfate unit's spectrum has an asymmetric absorption with a minimum near 1.9 and a drop-off at 2.3, indicative for polyhydrated sulfates. The spectrum of the dark material resembles that of the dark dunes at mound A, but has a lesser pronounced absorption band near around 2 µm.

The results of the unmixing using these image spectra as input and allowing mixtures of all three endmembers in the solution nicely show that linear unmixing with MELSUM is an appropriate method to identify similar spectra in a scene. As expected, the lower part of the mound is modeled by mixtures of the lower sulfate unit spectrum and the dark dunes spectrum, while in the upper part of the mound, only the spectrum from that region is chosen as the sulfate endmember. The residual image displays high values at locations that can be attributed to image defects.

The spectral mixture analysis allowing a choice of three endmembers out of a library of 24 spectra of the upper sulfate unit returned a combination of romerite ($Fe_3(SO_4)_4*14\ H_2O$) and rozenite ($FeSO_4*4\ H_2O$), plus a minor contribution of pyroxene. The lower sulfate unit can be well explained by szomolnokite and pyroxene, whereas the dark material is best modeled by a combination of pyroxene plus some romerite and some hematite.

The unmixing coefficient images give a somewhat less clear impression. The coefficient of romerite is found almost everywhere in the scene, in both the upper and the lower sulfate unit, and displays a vertical striping, with elevated values towards the sides of the image. The reason for this is that the shape of the romerite spectrum is rather

unspecific and fits very well to the absorption band near 2 µm. Thus, an admixture of romerite into the spectrum mathematically helps to accommodate the spectra measured, when the 2 µm micron feature is too deep to be modeled by a single sulfate spectrum from the library alone. We therefore do not interpret the occurrence of a romerite spectrum in the best solution presented by MELSUM as an indicator that romerite is present at mound B. The striping, which is also seen in the data for hematite, and the fact that the rozenite occurrence appears to be correlated with the illumination suggests that the CRISM data contains some cross-track illumination variations that are not removed by artificial linear spectra in the MELSUM library.

Consequently, we conclude that the lower part of the mound shows spectra of szomolnokite mixed with basaltic, pyroxene-rich sand, whereas the upper part is modeled by a combination of romerite, natrojarosite and rozenite. This does not necessarily indicate that these minerals are present, but could suggest that their mixture resembles a mineral that was not included in the

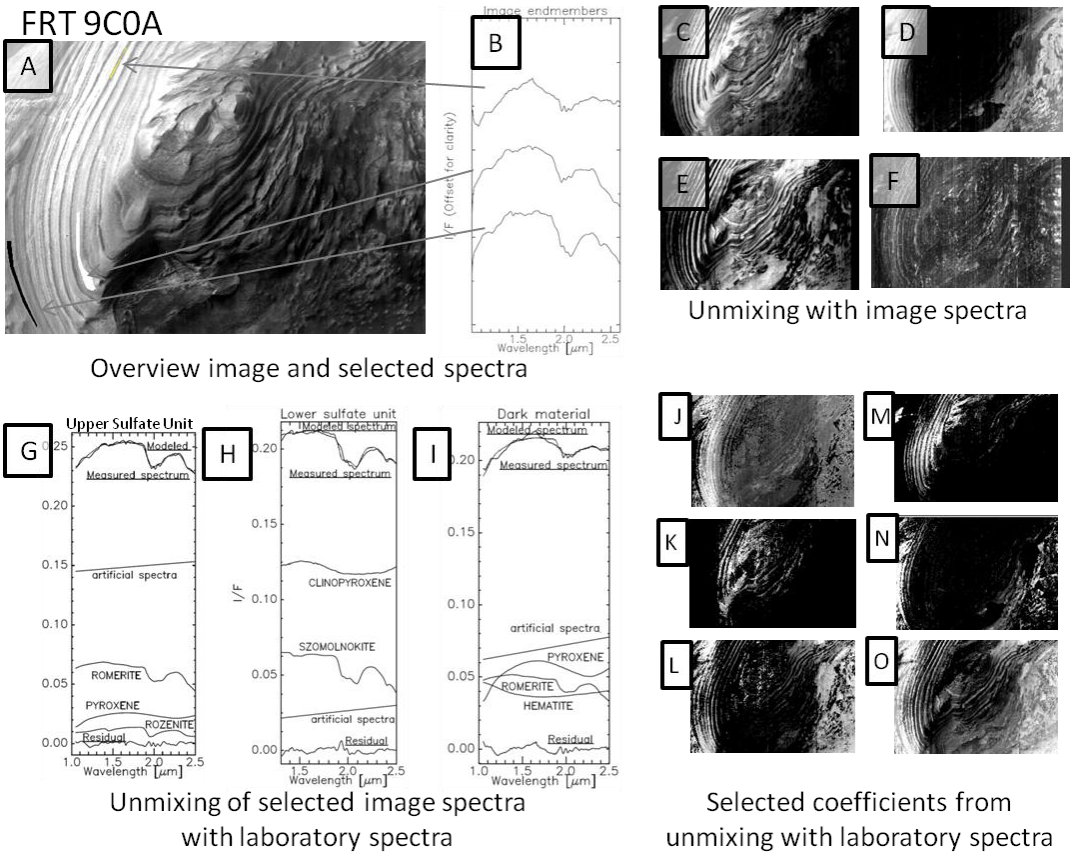

Fig. 5.3: Linear unmixing results for mound B, CRISM observation 9C0A.

A: Channel 4 (1.021 µm), unprojected. North is approx. 10° to the right. B: Spectra for manually chosen regions of interest: dark layers (top), upper sulfate unit (center) and lower sulfate unit (bottom). C-F: Unmixing results with image endmembers: C: upper sulfate endmember coefficient, D: lower sulfate coefficient E: dark material coefficient. F: residual. G: Unmixing of upper sulfate spectrum. H: Unmixing of lower sulfate unit spectrum. I: Unmixing of dark material. J-O: Unmixing results with laboratory spectra: J: Romerite coefficient K: Natrojarosite coefficient. L: Hematite coefficient M: Rozenite coefficient, N: Szomolnokite coefficient, O: Pyroxene.

spectral library, as we did not have access to spectra from all possible minerals. It does, however show that MELSUM is capable of discriminating mono- and polyhydrated sulfates, and that gypsum is not present, which is in agreement to Bishop *et al.*, 2009. As for mound A, the presence of kieserite, reported by Bishop *et al.*, 2009 for isolated spots, could not be confirmed with this method.

5.5.3 Unmixing results for mound C

In the CRISM observation HRL 444C we started again by selecting two image endmembers from the scene itself and used MELSUM for the spectral mixture analysis after an atmospheric correction with the transmission spectrum from ADR_VS_061C4_0100000L_5.IMG and destriping/despiking with CIRRUS. The image endmembers were averaged spectra over 3 by 3 pixels. Our first test using one spectrum for the light-toned material and one for the dark dunes material showed high residuals in certain regions. We therefore iteratively added spectra from those areas to the image endmember library until the residuals appeared to be controlled by data defects only. The image endmembers sufficient to describe the data to first order are shown in Fig. 4B. The endmember for the light-toned material shows the 2.4 band of szomolnokite. The second image spectrum shows characteristics of olivine, while the third one is dominated by pyroxene. All three spectra show a very deep, symmetric absorption band around 2µm and a weaker band at 1.5 µm, indicating the presence of water ice clouds above the target.

The SMA using these three image endmembers are shown in Fig. 5.4 C-F. They show that the light-toned mound itself is dominated by the sulfate-rich image endmember, while the dark material is modeled by the olivine- or pyroxene-rich endmember plus the sulfate endmember. While most of the dark material at the foot of the mound is spectrally unremarkable, the pyroxene or olivine endmember is correctly detected, in agreement to Bishop *et al.*, 2009. Although we included a spectral slope into the spectral library, MELSUM failed to model the spectra of the very bright areas on the upper left side of the mound.

The unmixing of the sulfate-rich endmember is shown in Fig. 5.4G. Note that due to the very deep, symmetrically shaped absorption band near 2 µm, MELSUM returned romerite as the best matching sulfate together with pyroxene. This did not reproduce the 2.4 µm band observed in the data, and was therefore wrong. We therefore removed romerite from the spectral library, which made MELSUM return the shown solution containing szomolnokite, which is considered correct despite the higher residuals around the 2 µm band. The olivine-rich spectrum was modeled by szomolnokite and forsterite. The solution with the lowest residual for the pyroxene-rich endmember was a combination of coquimbite and pyroxene (Fig. 5.4I). However, the residuals are high, and the spectral shape is not well reproduced. We therefore removed all sulfate spectra from the library except szomolnokite, which returned the solution shown in Fig. 5.3J, a combination of szomolnokite, pyroxenes and hematite. Despite the higher residuals this solution appears more plausible. Note, however that the water ice spectrum is not included into the solution, although water absorption features are clearly observable at 1.5 and 2 µm.

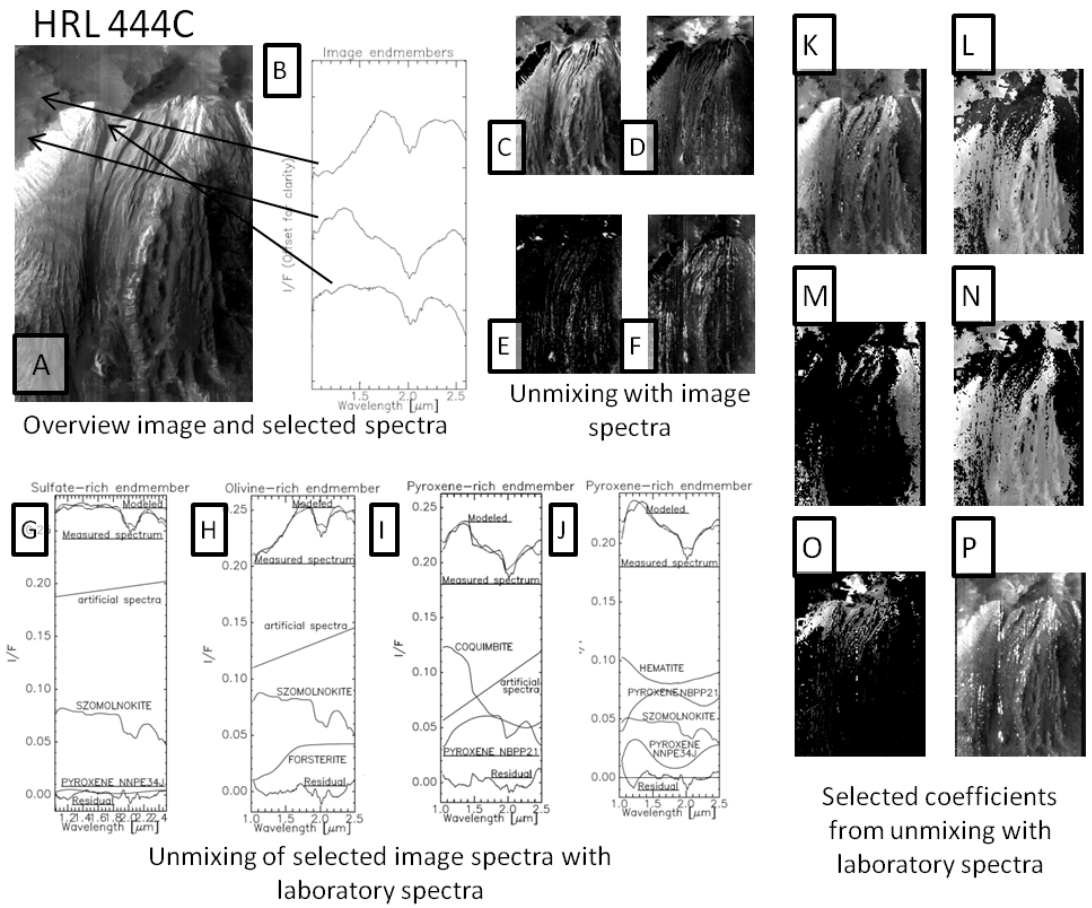

Fig. 5.4: Linear unmixing results for mound C, CRISM observation 444C.

A: Channel 4 (1.021 µm), unprojected. North is approx. 10° to the right. B: Interactively chosen image spectra: olivine-rich material (top), pyroxene-rich material (center) sulfate-rich material (bottom). C-F: Unmixing results with image endmembers: C: sulfate image endmember coefficient, D: pyroxene-rich endmember E: olivine-rich endmember F: residual. G: Unmixing of sulfate spectrum. H: Unmixing of olivine-rich spectrum. I: Unmixing of pyroxene-rich spectrum: note the very bad fit. J: Unmixing of pyroxene-rich spectrum with szomolnokite as sulfate spectrum. K-P: Unmixing results with laboratory spectra: K: Szomolnokite coefficient L: hematite coefficient. M: Coquimbite coefficient N: Pyroxene NBPP21 coefficient O: Pyroxene NNPE34J coefficient P: residual.

The unmixing results using the library of laboratory spectra (without romerite) and constraining the number of endmembers to three are shown in Fig. 5.4K-P. Only the szomolnokite endmember coefficient image seems to be consistent with the unmixing results using image endmembers (Fig. 5.4C), while the other endmember coefficients do not correspond well with those results, and the residuals are comparatively high. Note that the forsterite endmember was nowhere included into the unmixing solution (and is therefore not shown), despite the clear olivine-rich spectrum in Fig. 5.4B. Apparently, the higher level of noise in the original spectra compared to the spectra averaged over 3 by 3 pixels shown in Fig. 5.4B caused MELSUM to return solutions containing other combinations of spectra.

5.5.4 Unmixing results for mound D

Fig. 5.5 shows the results for CRISM observation FRT A4CF south of mound D. We applied the atmospheric correction with the transmission spectrum CDR430887634919_AT0000000L_5.IMG and used CIRRUS to remove spikes and stripes. The observation contains several smaller sized light-toned deposits. Fig. 5.5B-D show the MELSUM results using a spectral library of 24 laboratory spectra, and constraining the solution to 3. The light-toned material (Fig. 5.5B) can be well modeled by a linear combination of szomolnokite and pyroxenes. Most of the scene is dominated by spectra similar to Fig. 5.5C. It has a lower albedo compared toFig. 5.5B and the 2.4 µm band is less pronounced, but it can nevertheless be modeled by the same endmember spectra, szomolnokite and pyroxenes, with coefficients in the same order of magnitude. This is interesting, as due to the lower albedo we would expect higher coefficients for the mafic minerals, and demonstrates that coefficient values cannot be transformed directly into abundance values.

A few isolated regions display spectra dominated by pyroxene (Fig. 5.5D). Their locations at hillsides suggest that here, fresh, unaltered basaltic material has recently been brought to the surface by landslides. The MELSUM unmixing of

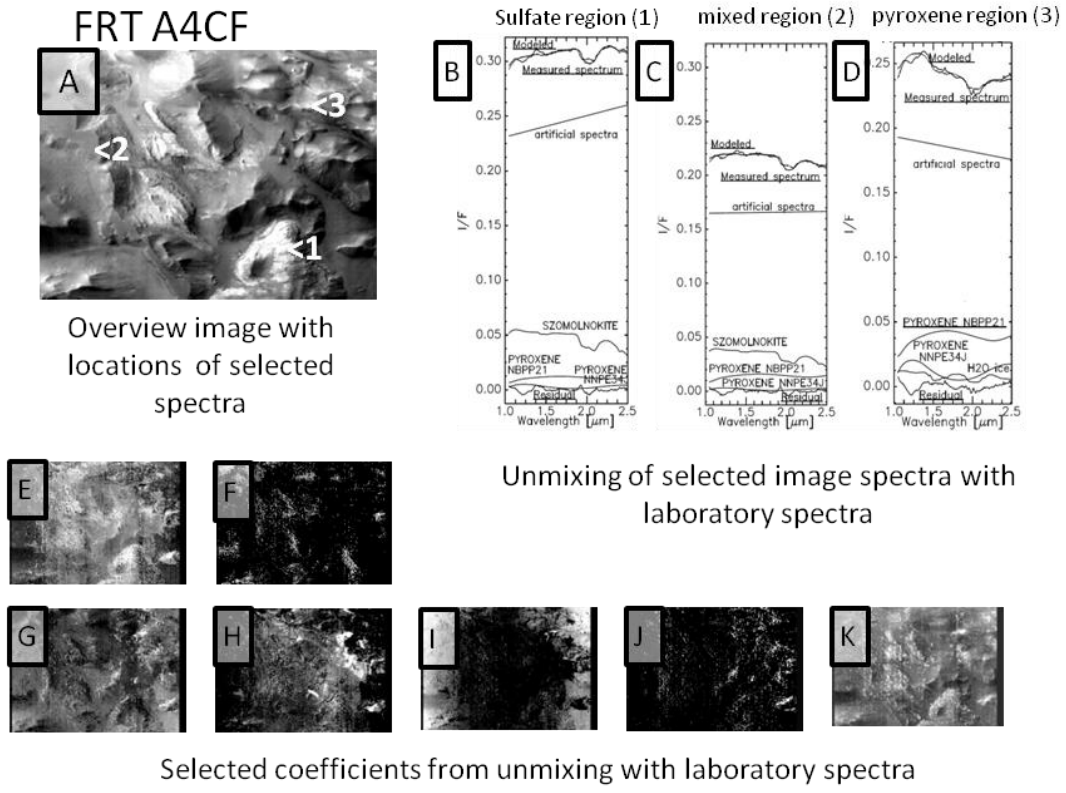

Fig. 5.5: Linear unmixing results for mound D. CRISM observation FRT A4CF.

A: Channel 4 (1.021 µm), unprojected. North is approx. 10° to the right. B-D: Unmixing results of iteratively chosen image endmembers. B: sulfate image endmember coefficient (spot 1) , C: mixed image endmember unmixing result (spot 2). D: pyroxene-rich spectrum unmixing results (spot 3). E-K: Unmixing of entire scene with laboratory spectra. E: Szomolnokite coefficient F: Natrojarosite coefficient. G: Pyroxene NBPP21 coefficient. H: Pyroxene NNPE34J coefficient. I: H2O ice coefficient. J hematite coefficient . K: residual.

the entire scene is shown in Fig. 5.5E-K. The szomolnokite coefficient is correlated to the light-toned outcrops, indicating that this mineral is the most important sulfate mineral in these outcrops. There are, however, a few spots where natrojarosite is also returned by MELSUM. We do not interpret this as an indicator for the existence of natrojarosite in this region. As in observation HRL 444C, spectral features of water ice clouds are present, which are not uniformly modeled by an admixture of the water ice library spectrum (Fig. 5.5I). A mixture of szomolnokite and natrojarosite could therefore be a solution with the lowest residual, although the correct solution would be szomolnokite plus water ice. The same is the case for the hematite coefficient, which we do not consider a proof for hematite, as the most important diagnostic spectral features of hematite are outside the spectral range considered in this study. A visual control and comparison to Bishop *et al.*, 2009 suggests that the coefficient images of the pyroxene endmembers (Fig. 5.5 G and H) are a fair representation of the pyroxene occurrence in this scene. As for the other mounds, we were not able to confirm the presence of kieserite, as reported by Bishop *et al.*, 2009.

5.6 Conclusions

The results show that mounds A, C, D and the lower part of mound B contain szomolnokite, which is contaminated by wind-blown basaltic, pyroxene- and sometimes olivine-rich sand, which is in general agreement with Bishop *et al.*, 2009. The upper part of mound B contains polyhydrated sulfates, which are clearly distinguished by MELSUM from the monohydrated szomolnokite. The observed spectra match best combinations of romerite and rozenite and/or natrojarosite, and windblown, pyroxene-rich material. We can therefore exclude the presence of gypsum proposed by Gendrin *et al.*, 2005b. The correct type of polyhydrated mineral actually present at mound B is still open, as our spectral library did not contain all sulfate species possible. MELSUM has, however, proved its potential in solving this problem once the spectral library is completed.

The linear spectral mixture analysis algorithm MELSUM is capable of modeling spectra from CRISM in a convincing way. The detection of szomolnokite, pyroxenes and olivine correspond to the results found by Bishop *et al.*, 2009 using spectral indices. MELSUM worked especially well when spectra taken from the observation itself were used. The results show, however that a correct removal of the CO_2-gas bands is a prerequisite for a successful linear unmixing. The presence of ice clouds also caused problems for the unmixing algorithm. This had the effect that MELSUM returned solutions containing the wrong sulfate mineral, because it better matched the combined water ice and sulfate band around 2µm, but did not reproduce the characteristic absorption band of monohydrated sulfates at 2.4 µm. MELSUM worked best on averaged spectra, but was vulnerable to noisy data: in this case, small absorption bands like the 2.4 µm feature are often missed by the linear unmixing method.

Our next step to improve MELSUM is to give the user more control on the library spectra in the solution. When the user identifies the presence of water ice in the spectrum, only solutions that contain this spectrum should be considered. Likewise, one could allow MELSUM to select only one sulfate spectrum from the spectral library plus a combination of pyroxenes and olivine to model the mafic sand present here.

The implications of the presence of mostly szomolnokite as a monohydrated sulfate in all outcrops and possibly rozenite or other iron

bearing sulfates in mound B, as also reported by Bishop *et al.*, 2009, are not yet fully understood and require further analysis. The absence of the Ca-bearing gypsum detected by Gendrin *et al.*, 2005b, however, fits much better to the predominantly Fe and Mg bearing mafic mineralogy of the putative basaltic source rock of the Martian sulfates. Our next step is a geochemical modeling of the weathering of basaltic rock under acidic conditions to bridge the gap between (ambiguous) spectral information and the suggested formation processes of the sulfatic outcrops.

5.7 Acknowledgements

The work of Lorenz Wendt was supported by the German Space Agency (DLR Bonn) under the project Mars Express. The work by Patrick McGuire has been funded by a Humboldt Research Fellowship. PCM has also been supported by NASA funds through the Applied Physics Laboratory, under subcontract from the Jet Propulsion Laboratory through JPL Contract #1277793.

6 The Light-Toned Deposits in Ophir Chasma

The following section has been published as:

Wendt. L., Gross, C., Kneissl, T, Sowe, M., Combe, J.-P., Le Deit, L., McGuire, P. C., and Neukum, G., 2011, "**Sulfates and Iron Oxides in Ophir Chasma, based on OMEGA and CRISM observations**" in *Icarus*, Vol. 213, Issue 1, p 86-103.

The article may be found using this link: http://dx.doi.org/10.1016/j.icarus.2011.02.013

6.1 Abstract

We investigate the sulfate and iron oxide deposits in Ophir Chasma, Mars, based on short-wave infrared data from the Compact Reconnaissance Imaging Spectrometer for Mars - CRISM and from the Observatoire pour la Minéralogie, l'Eau, les Glaces et l'Activité - OMEGA. Sulfates are detected mainly in two locations. In the valley between Ophir Mensa and the southern wall of Ophir Chasma, kieserite is found both within the slope of Ophir Mensa, and superposed on the basaltic wall of the chasm. Here, kieserite is inconformably overlain by polyhydrated sulfate deposits and iron oxides. Locally, jarosite and unidentified phases with absorptions at 2.21 μm or 2.23 μm are detected, which could be mixtures of jarosite and amorphous silica or other poorly crystalline phases. The second large sulfate-rich outcrop is found on the floor of the central valley. Although the same minerals are found here, polyhydrated sulfates, kieserite, iron oxides, and locally a possibly jarosite-bearing phase, this deposit is very distinct. It is not layered, almost horizontal, and located at a much lower elevation of below -4250 m. Kieserite superposes polyhydrated sulfate-rich deposits, and iron oxides form lags. The facies of sulfate formation remains unclear, and could be different for the two locations. A formation in a lake, playa or under a glacier is consistent with the mineralogy of the central valley and its flat, low-lying topography. This is not conceivable for the kieserite deposits observed south of Ophir Mensa. These deposits are observed over several thousands of meters of elevation, which would require a standing body of water several thousands of meters deep. This would have led to much more pervasive sulfate deposits than observed. These deposits are therefore more consistent with evaporation of groundwater infiltrating into previously sulfate-free light-toned deposits. The overlying polyhydrated sulfates and other mineral phases are observed in outcrops on ridges along the slopes of the southern chasm wall, which are too exposed to be reached by groundwater. Here, a water supply from the atmosphere by rain, snow, fog or frost is more conceivable.

6.2 Introduction

The Light-Toned Deposits [LTD] or Interior Layered Deposits [ILD] (Lucchitta *et al.*, 1992) within the chasmata of Valles Marineris are some of the most intensely studied geological features on Mars. Many theories for their formation have been put forward, including subaerial fluvial deposition or volcanism (Lucchitta *et al.*, 1992), accumulation of eolian dust or sand (Peterson, 1981), evaporite precipitation in lakes (McKay and Nedell, 1988) or from groundwater (Murchie *et al.*, 2009a), subaqueous (Nedell *et al.*, 1987) or sub-ice volcanism (Chapman and Tanaka, 2001), or the formation as spring deposits (Rossi *et al.*, 2008), but a conclusive theory combining all

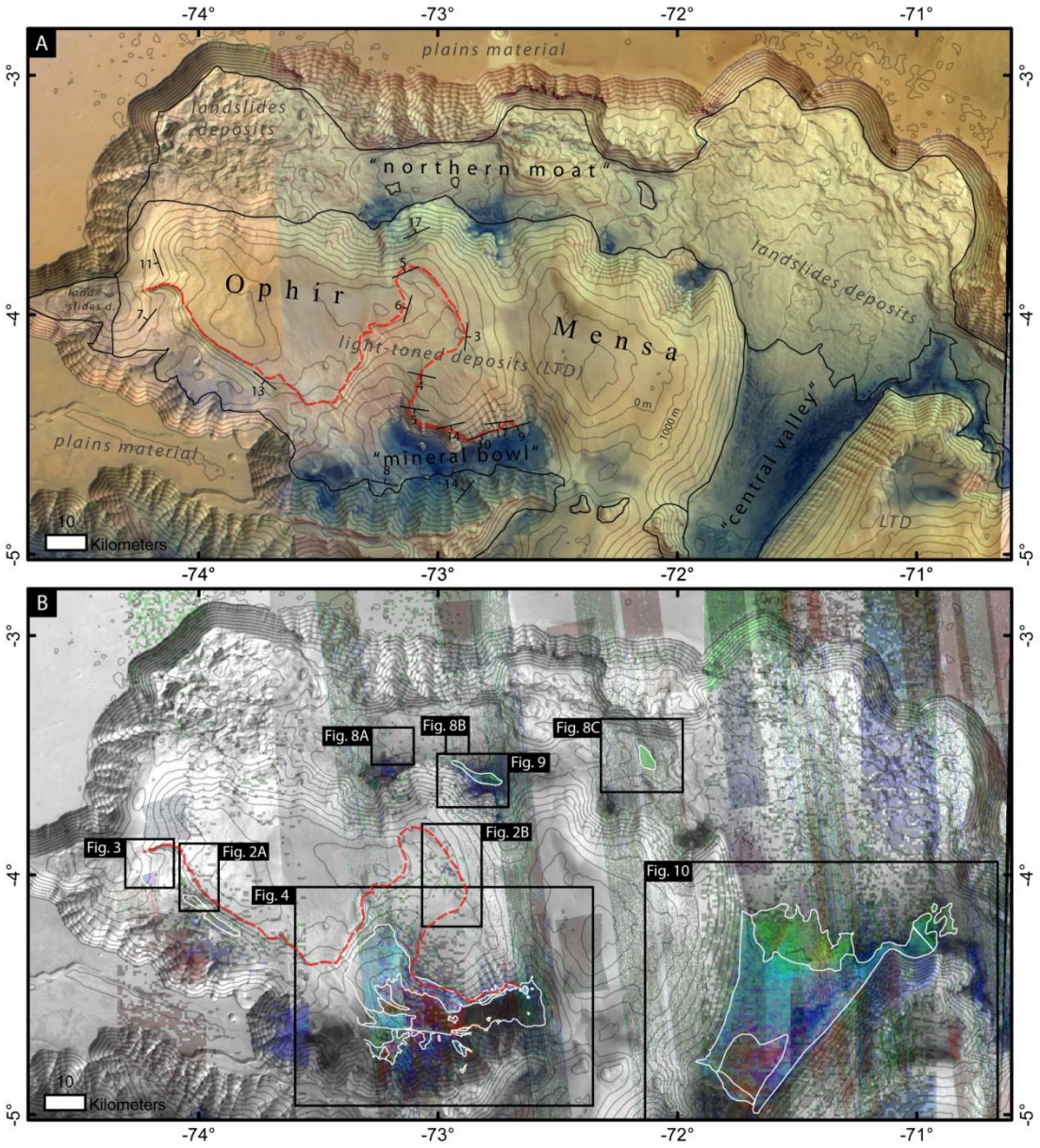

Fig. 6.1: Overview to Ophir Chasma.

A: Color mosaic of HRSC orbits 334 and 3127 of Ophir Chasma with location names and simplified geologic units. Contour lines every 500 m from HRSC DTM with 150 m post spacing. Dashed red line: Prominent marker horizon in Ophir Mensa, separating it in a lower and upper unit. Local layer strike and dip measurements. Compare to Zegers et al., 2006.

B: HRSC nadir mosaic with contour lines for orientation, overlain with 'ratio of reflectance at 1 and 1.3 µm', SINDEX and BD2100 as RGB image from OMEGA and CRISM multispectral and targeted observations, and resulting mineralogical units (white lines). Iron oxides appear red, polyhydrated sulfates green, monohydrated sulfates blue.

implications suggested by the composition, structure and stratigraphic position of these deposits is still missing. A detailed discussion of the shortcomings of each of the formation theories is provided by Lucchitta, 2009a, 2009b. One major constraint on these theories is the role of liquid water, evidenced by the presence of ferric oxides and sulfates, which are the subject of this study.

The mineralogy of the LTD's has been studied on a regional scale by Gendrin *et al.*, 2005b and Mangold *et al.*, 2007a, based on short-wave infrared (SWIR) data from the Observatoire pour la Minéralogie, l'Eau, les Glaces et l'Activité OMEGA (Bibring *et al.*, 2004), and by Weitz *et al.*, 2008, based on thermal infrared data from the Thermal Emission Spectrometer TES (Christensen *et al.*, 1992). A comparative study on the geological context of the individual outcrops of aqueous minerals in Valles Marineris by Chojnacki and Hynek, 2008, showed that the LTDs are much more diverse than previously thought, which makes a single formation process explaining all depositions by the same mechanism less likely, and which raises the need for individual, detailed mineralogical and geologic studies for each of the basins of Valles Marineris. In this paper, we analyze SWIR data from OMEGA and the Compact Reconnaissance Imaging Spectrometer for Mars CRISM (Murchie *et al.*, 2007a) in combination with multispectral imagery, digital elevation models and stereo images from the High Resolution Stereo Camera HRSC (Neukum and Jaumann, 2004), and panchromatic images from HRSC, the Context Imager CTX (Malin *et al.*, 2007) and the High Resolution Imaging Science Experiment HiRISE (McEwen *et al.*, 2007) acquired over Ophir Chasma in order to understand the mineralogy and local stratigraphy and layering characteristics of the water-related minerals found here, mainly sulfates and iron oxides. Similar studies on neighboring chasmata include the work of Mangold *et al.*, 2008, and Murchie *et al.*, 2009a, on West Candor Chasma, Le Deit *et al.*, 2008, on East Candor Chasma, and Roach *et al.*, 2010b, on Ius Chasma.

Ophir Chasma is the northernmost depression of central Valles Marineris. It extends approximately 270 km in East-West direction and 90 km in North-South direction (Fig. 6.1). The floor of the chasma lies at elevations between 4200 and 4800 m below datum, its rim is at elevations between 3400 and 4500 m above datum. Most of the western part of Ophir Chasma is covered by a mound of LTDs, Ophir Mensa, which rises up to an elevation of 3200 m above datum. This results in a total thickness of (at least) 7-8 km of deposits, assuming that the floor below Ophir Mensa is approximately horizontal at an elevation close to the deepest points of the chasm. Ophir Mensa is surrounded on all sides by depressions, which separate these deposits from the chasm walls. For convenience, we informally named the depression to the north as the "northern moat", the depression to the south as "mineral bowl", following Chojnacki and Hynek, 2008, and the depression to the east as the "central valley" (Fig. 1A). A second mound of light-toned deposits is located between the central valley and the south-eastern rim of Ophir Chasma.

The geology of the LTDs was investigated by Nedell *et al.*, 1987 and Komatsu *et al.*, 1993, and a geological map based on Viking imagery was provided by Lucchitta, 1999. According to these authors, the chasmata of Valles Marineris probably formed as collapse structures along faults that later widened to grabens into the surrounding Noachian to Hesperian aged plains, which are built up by Tharsis-derived lava. By the time of the deposition of the LTDs, the chasm walls were already eroded to the spur-and-gully morphology observable today, which indicates that the deposition was clearly post-tectonic. Subsequently, the LTDs were heavily eroded by wind and/or water action. The walls of the chasmata receded from the remaining LTD platforms, and the resulting "moat" surrounding them was partly covered by landslides.

6.3 Datasets and Methods

6.3.1 Hyperspectral data

OMEGA and CRISM are both visible-short wave infrared imaging spectrometers. OMEGA (Bibring *et al.*, 2004) is the mapping infrared spectrometer onboard ESA's Mars Express spacecraft. It covers the wavelength range from 0.38 µm to 5.1 µm in 352 contiguous bands. The data is acquired by three different channels, one for the visible to near infrared spectrum (0.38-1.05 µm), a second for the spectral range from 0.93 to 2.73 µm and a third covering the range from 2.55 to 5.1 µm. We used mostly data from 0.93 to 2.73 µm, as this range covers electronic transition absorptions due to olivine and pyroxene (Adams, 1974, Cloutis and Gaffey, 1991, Sherman *et al.*, 1982, Sunshine and Pieters, 1990), and vibrational absorptions in H_2O and/or hydroxyl-bearing minerals such as phyllosilicates, hydrated sulfates and oxyhydroxides (Burns, 1993, Clark *et al.*, 1990). The spectral resolution of OMEGA is 20 nm in this wavelength range. Due to Mars Express' highly elliptical orbit, the spatial resolution of OMEGA varies between 300 m and 3-4 km per ground element. Most of the OMEGA data used in this study have a spatial resolution in the order of 600 to 700 m per ground element.

CRISM (Murchie *et al.*, 2007a, 2009c) onboard NASA's Mars Reconnaissance Orbiter (MRO) features a similar spectral range from 0.4 to 3.9 µm in 544 bands at a spectral resolution of 6.55 nm, recorded by two distinct detectors, the "S"-detector in the range of 0.39 to 1.02 µm, and the "L" detector in the range of 1.02 to 3.92 µm wavelength. The data are acquired in several modes, including the targeted mode at a spatial resolution of 18 m (FRT mode) or 36 m/pixel (HRL mode) using all bands, or in multispectral mapping (MSP) mode at a spatial resolution of 200 m per pixel using a subset of 72 selected spectral bands. We mostly used the data in the range of 1 to 2.6 µm, as this is the range where absorption bands of sulfates occur, but included the visible range for the confirmation of the

table 6-1: List of CRISM and OMEGA observations used in this study

CRISM targeted observations[a]	CRISM Multispectral Mapping Strips[a]	OMEGA observations[b]
FRT000082C5_07	MSP000031C3_05	0548_3
FRT000096E6_07	MSP000032FE_05	1180_5
FRT0000A86A_07	MSP000033F3_07	1202_1
FRT0000AD8D_07	MSP000034E0_05	1213_2
FRT0000B27B_07	MSP00003899_01	3228_3
FRT0000B994_07	MSP00003A47_01	4358_3
FRT0000BB63_07	MSP00003EA9_05	4380_3
FRT000109E5_07	MSP00004044_07	
HRL0000508A_07	MSP0000416B_05	
HRL00005B82_07	MSP000046F2_07	
HRL00007468_07	MSP00004825_01	
HRL000075E7_07	MSP00004AA1_01	
HRL00007E21_07	MSP00005575_03	
HRL0000A432_07	MSP000059A0_05	
HRL0000B7D4_07	MSP00006CCB_01	
HRL0000BF5E_07	MSP0000CB50_01	
HRL0000C30D_07		
HRL0000C59C_07		

[a] The first three characters of the CRISM file names designate the type of observation: full(FRT) or half resolution targeted (HRL) observation or multispectral mapping strip (MSP). The next characters are unique hexadecimal identifiers for each observation. The last two Fig.s indicate the component image used from that observation.

[b] OMEGA observations are identified by the four-digit orbit number followed by the sequence number within that orbit.

presence of ferric oxides. Table 1 provides the observation numbers used here.

The OMEGA and CRISM data were converted to I/F, divided by the cosine of the solar incidence angle, and the CO_2 absorption features around 2 µm caused by the Martian atmosphere were removed using the improved volcano-scan technique provided by McGuire *et al.*, 2009. Noise in CRISM data was reduced using various filtering procedures (Parente, 2008). We used the spectral indices or "summary products" (Bishop *et al.*, 2009, Murchie *et al.*, 2009b, Pelkey *et al.*, 2007) on OMEGA and CRISM data to identify spectral features characteristic for specific minerals or groups of minerals. Out of these, the index for a band at 1.9 µm due to combinations of H_2O bending and stretching vibrations (BD1900), the 2.1 µm band depth (BD2100) the band depth at 2.21-2.26 µm due to Si-OH vibrations (BD2210) and the index quantifying the spectral convexity around 2.3 µm caused by H_2O absorptions (SINDEX) were particularly useful to identify regions that required detailed spectral analysis.

Ferric oxide was identified by its strong increase in reflection between 1 and 1.3 µm, which we calculated as the ratio between the reflectance at 1.2767 µm and the reflectance at 1.080 µm for CRISM data and the ratio between reflectance at 1.2705 µm and 1.0837 µm for OMEGA data, similar to Le Deit *et al.*, 2008, Mangold *et al.*, 2008. This index is sensitive to ferric oxides or oxyhydroxides like hematite and goethite or mixtures containing these minerals, but also to iron bearing sulfates, like, for example, copiapite. We therefore corroborated the presence of ferric oxides using the spectral data in the visible-near infrared range from the CRISM S detector. To this end, we excluded the spectral data shortward of 0.41 µm and longward of 0.97 µm as well as the range between 0.64 and 0.69 µm due to known calibration problems in these regions of the detector (Murchie *et al.*, 2009c). Spectra of Mars in the visible wavelength range are dominated by the presence of nanophase ferric oxides. The detection of coarse-grained red hematite, goethite or other ferric phase therefore requires the calculation of spectral ratios to a reference spectrum in the same observation, which is spectrally inconspicuous and dominated only by dust. These reference spectra were calculated as average spectra over a few hundreds or thousands of pixels. The spectral bands of ferric oxides, ~0.53 and 0.86 µm for red hematite and ~0.5 and 0.9 µm for other ferric phases, were then made visible by removing the continuum separately in the range of 0.41 to 0.64 µm and 0.69 to 0.97 µm (Clark *et al.*, 1987). Further evidence for the presence of ferric oxides in Ophir Chasma is the independent identification of grey hematite in the thermal infrared by TES (Weitz *et al.*, 2008). Spectra in the range of 1 to 2.6 µm were averaged over regions of interest and either compared directly to laboratory spectra or likewise ratioed to spectrally bland (dusty) regions. We used laboratory spectra of pure minerals from the RELAB spectral library provided with the CRISM Analysis Tool (CAT).

An absorption band near 1.9 µm is found in various types of minerals: Hydrated silica, hydrated sulfates, phyllosilicates and also carbonates show this spectral feature, which makes further absorptions necessary to distinguish between these groups of minerals. Monohydrated sulfates show an absorption near 2.1 µm, which is detected by the BD2100 index. The exact location of this absorption band is at 2.13 µm for the magnesium-rich kieserite ($MgSO_4*H_2O$) and at 2.09 µm for the iron-rich szomolnokite ($FeSO_4*H_2O$). Both minerals also show an

absorption at 2.4 µm (Cloutis *et al.*, 2006). A distinction between these two minerals was only attempted for OMEGA and CRISM data at full spectral resolution. and not the multispectral data from CRISM, as the generally higher noise level prevented an analysis to this detail.

Polyhydrated sulfates are identified by absorption bands at 1.45 and 1.95 µm and a drop-off in reflectance near 2.4 µm. Absorptions in the 2.2-2.3-µm-region are indicative for hydrated silica, phyllosilicates, or jarosite, and are attributed to OH-stretching and Si-OH bending. Hydrated silica such as opal show a broad absorption band between 2.20 and 2.26 µm due to overlapping bands caused by hydroxyl-groups and water molecules in the hydrate sphere. Jarosite is identified by absorptions at 1.47, 1.85 and a doublet at 2.21 and 2.26 µm. Phyllosilicates show a narrow absorption band in the wavelength region between 2.2 and 2.31 µm. Its exact position allows a distinction between aluminum-rich clays like montmorillonite (2.20 µm), iron-rich nontronite (2.28 µm), and magnesium-rich saponite (2.31 µm).

6.3.2 Panchromatic and multispectral imagery

The High Resolution Stereo Camera HRSC (Neukum and Jaumann, 2004) combines nine CCD line detectors behind a common optics. The viewing directions of the detectors are oriented at angles between -18.9 and +18.9° with respect to the nadir view, and four of the sensors are equipped with broadband color filters for the red, green, blue and near infrared sections of the spectrum. This design allows for the simultaneous acquisition of panchromatic images with a map-projected ground resolution of up to 12.5 m per pixel, multispectral/color images and panchromatic multiple stereo ground coverage to produce digital terrain models (DTM). The resolutions of the color channels and the off-nadir panchromatic channels is usually reduced onboard by a factor of two or four with respect to the nadir channel to reduce the amount of data to be transferred to Earth (McCord *et al.*, 2007).

The HRSC color images have been beneficial for the mapping of the dark, basaltic sand dunes and deposits (McCord *et al.*, 2007, Williams *et al.*, 2009),which have a bluish hue in color-stretched RGB representations of the red, green and blue HRSC channels, and for the distinction between Al- and Mg/Fe-rich clay minerals in Mawrth Vallis (Loizeau *et al.*, 2007). Although a direct correlation between HRSC color spectra and specific minerals or rock types in other cases is difficult, the subtle color variations in HRSC images can and should be used to distinguish geologic units visually. We therefore used HRSC RGB representations of the red, green and blue HRSC channel, pansharpened with the higher resolved panchromatic, nadir-viewing HRSC channel or with CTX (Malin *et al.*, 2007) images in several occasions in this study.

We investigated the geometry of the LTDs based on digital elevation models (DTM) with spatial resolutions of 50 or 100 m cell size, which were derived from individual HRSC orbits (Gwinner *et al.*, 2000).We also used a regional DTM of the entire Valles Marineris at a resolution of 150 m cell size, which was produced from several bundle-block-adjusted HRSC orbits (Dumke *et al.*, 2010). We estimated the attitude of observed layers by fitting a plane through three or more points selected in the HRSC DTMs along the outcrop of the layering observed in the co-registered imagery (similar to Zegers *et al.*, 2006) using the software tool developed by Kneissl *et al.*, 2010. In addition to this, anaglyphs were produced directly from the HRSC nadir channel

and one of the stereo channels, as these products provide more topographical detail than a DTM produced from the same data.

We also used panchromatic imagery from the Context Imager CTX (Malin *et al.*, 2007) with a spatial resolution of approx. 6 m per pixel, and panchromatic and color images from the HiRISE experiment (McEwen *et al.*, 2007) with a spatial resolution of up to 25 cm per pixel.

6.4 Results

6.4.1 Overview

Fig. 6.1A shows Ophir Chasma as a false color mosaic of the red, green and blue channel of HRSC. Fig. 6.1B shows the mineral indices for iron oxides, sulfates (SINDEX) and monohydrated sulfates (BD2100) calculated from OMEGA and CRISM data as a RGB image overlain on a panchromatic HRSC mosaic. In this visualization, monohydrated sulfates appear in a blue-green hue, polyhydrated sulfates have a green hue, and iron oxides are shown in red.

In the HRSC color image, dark, basaltic material appears with a bluish hue. It is found as a dune-forming aeolian deposit in the central valley, the "mineral bowl", in wind traps along the northern of Ophir Mensa and on top of the ILD east of the central valley. The basaltic sand covers ILDs and landslides, its deposition therefore occurred after sulfate formation. The dark material shows a spectral signature of pyroxenes and in the central valley of pyroxenes and monohydrated (kieserite) deposits. Possible sources of the basaltic material are the eroding chasm walls and landslide material, and a possible late-stage volcanism (Lucchitta, 2002). In nearby western Candor Chasma, dark, basaltic material shows a spectral signature of monohydrated sulfates, and HiRISE images show distinct, friable layers within the ILDs, from which the basaltic sands are released by erosion (Murchie *et al.*, 2009a). Similar layers are not found in Ophir Chasma. The ILDs appear to be mostly massive, without showing a layering structure. Locally, dark bands are observed, e. g., east of the central valley. At close inspection, these bands appear to be superficial, aeolian deposits on terraces caused by differential erosion along layering in the ILDs, but not basalt-bearing layers *within* the ILDs. The fact that the basaltic sand in the central valley shows spectral features of monohydrated sulfates does not imply an origin of the basalts from within the ILDs, as suggested for western Candor Chasma, as the sulfate signature is likely caused by the light toned kieserite deposits peeking through the loose, dark sand cover. On the other hand, erosion of the chasm walls inevitably continued during deposition of the ILDs independent of the depositional environment in the basin: therefore, an incorporation of basaltic material into the ILDs most likely took place, but the lack of distinct, dark layers suggests that this process played only a minor role. Consequently, the co-occurrence of pyroxenes and sulfates does not imply a genetic relationship between the two groups of minerals, which would allow a reconstruction of a common deposition.

Spectral signatures of iron oxides and sulfates are found only on a small fraction of the deposits in Ophir Chasma, while most of the deposits are spectrally bland. Mangold *et al.*, 2008, Chojnacki and Hynek, 2008, and LeDeit, 2008, observed that sulfates are found only in consolidated rocks with an elevated thermal inertia in TES data, and concluded that sulfates might be much more pervasive within the LTDs, but undetectable due to a cover of unconsolidated dust. This general trend is correct, but many locations are spectrally

bland despite relatively high thermal inertia values (Chojnacki *et al.*, 2006). This is the case for the ILD material on the northern flank of Ophir Mensa, which shows an elevated thermal inertia, but is nevertheless spectrally featureless in CRISM and OMEGA data. Although optically thick dust deposits could mask spectral features in the visible and near infrared region and at the same time hardly affect the thermal radiation, these locations are on steep flanks with deep erosional rills and free of dunes in high-resolution imagery, which does not suggest a dust cover.

The locations of sulfate and ferric oxide detections can be divided into three groups based on their stratigraphy with respect to Ophir Mensa. The observations in the west of Ophir Mensa (Fig. 6.3) and on the northern side of the "mineral bowl" suggest the presence of sulfates within the deposits of Ophir Mensa. On the southern wall of the "mineral bowl" (and Ophir Chasma), the stratigraphic relationship to Ophir Mensa is not completely clear. The outcrops in the "moat" north of Ophir Mensa and in the central valley form the third group of deposits, as they appear to overlay, and thus postdate the formation and erosion of the bulk of the light-toned deposits making up Ophir Mensa. All outcrops will be discussed in detail in the following text.

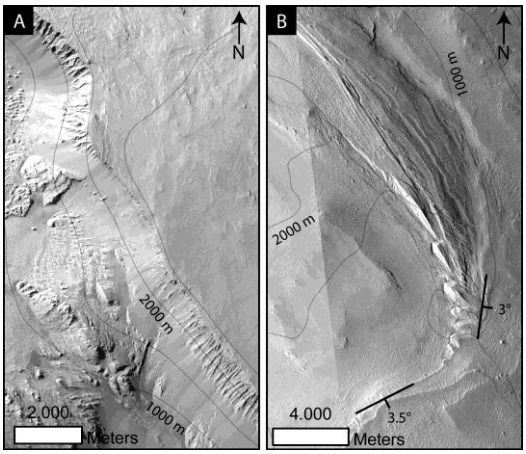

Fig. 6.2: Details of the horizon marked red in Fig. 6.1. In the west of Ophir Mensa, it forms a steep cliff near the top of the mound (A). In the center of Ophir Mensa, it plunges at angles around 4° under the overlying LTDs further east and north (B). CTX images P02_002208_1748, P12_005676_1746, P15_006955_1746.

Fig. 6.1A also shows the location of a prominent marker horizon within Ophir Mensa as a dashed, red line. This horizon shows several curves and can be traced from the western end of Ophir Mensa up to its base at the eastern end of the "mineral bowl" valley. It mostly forms a steep cliff approx. 500 m high (Fig. 6.2). Layer attitude measurements along this horizon indicate that the layering generally dips outward, following the topography of Ophir Mensa (compare to Zegers *et al.*, 2006). In the west of Ophir Mensa, the horizon is located stratigraphically near the top of the mound and dips approximately horizontally. In the center of Ophir Mensa, the horizon appears to plunge at angles in the order of 5° underneath the stratigraphically higher deposits of the eastern Ophir Mensa. Towards the flanks, dip angles increase to around 20°. A kink in the slope is observed in the "mineral bowl", changing from 17° directly above the marker horizon to values around 10° below it. Interestingly, the sulfate deposits within Ophir Mensa are only found in the section beneath this horizon.

6.4.2 Western Ophir Mensa

Fig. 6.3 shows a subset of the CRISM targeted observation FRT0000B27B in the western part of Ophir Mensa. In this location, the LTDs show layering in the order of a few tens of meters in thickness, which dip westward at moderate angles around 7°. Absorption bands near 1.6 µm, 2.1 µm and at 2.4 µm suggest the presence of monohydrated sulfates such as kieserite. The slightly lower albedo and the presence of small dunes in the region showing a presence of

polyhydrated sulfates (green) in the HiRISE image PSP_008458_1760 (Fig. 6.3B) suggests that the boundary of kieserite detection, which does not coincide with the layering, is caused by the thin dust coverage, and not by a change of the mineralogy of the rocks in these layers. This suggests that the ILDs of Ophir Mensa above the marker horizon are sulfate-free, whereas the detection below this horizon is controlled by the presence or absence of a masking dust cover. Thus, in the lower part sulfates might be much more abundant, despite only limited detections in orbital data.

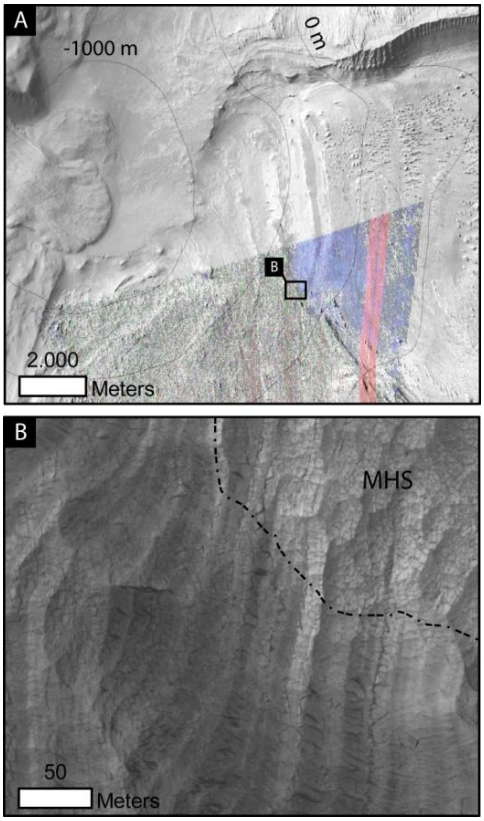

Fig. 6.3: Detail from western Ophir Mensa.
A: CTX observation P20_008893_1762 overlain with spectral indices from CRISM FRT0000B27B as inFig. 6.1, showing presence of kieserite (blue) and a weak presence of polyhydrated sulfates (green). The red stripe is an artifact.
B: Detail of HiRISE observation PSP_008458_1760. MHS: monohydrated sulfates. The kieserite detection boundary is controlled by dust cover and oblique to layering, suggesting that kieserite is abundant in this part of Ophir Mensa despite spatially limited detections, whereas the area showing the PHS signature is stronger affected by dust.

6.4.3 The "mineral bowl"

The "mineral bowl" is the depression between Ophir Mensa and the southern wall of Ophir Chasma. It extends approximately 70 km in East-West-direction and is up to 20 km wide (Fig. 6.4). It owns its informal name due to the complex relationship between spectrally bland ILDs of Ophir Mensa and sulfates and crystalline ferric oxide detections within Ophir Mensa, on the southern wall, and on the valley floor (Chojnacki and Hynek, 2008). The southern wall itself is built up from layers of basaltic rocks (Lucchitta, 1999). The spatial and spectral resolution of the CRISM and OMEGA data of this valley is very diverse. Therefore, the mineralogy of this complex outcrop region can only locally be assessed in detail. We will provide an overview of the mineral phases observed, before discussing the relationship between Ophir Mensa and the southern chasm wall (Fig. 6.5) and between the southern chasm wall and the overlying LTDs (Fig. 6.6).

Starting in the eastern part of the northern slope of the valley, CRISM detects absorption bands at 1.6, 2.13 and 2.4 µm consistent with kieserite at the base of Ophir Mensa and an erosional remnant of Ophir Mensa approx. one km towards the center of the valley. These outcrops show layering of tens of meters in thickness, and HiRISE imagery reveals even thinner internal layering in the meters scale. The layers were interpreted as the source of crystalline ferric oxides found in the dark material covering the floor of the valley (Weitz *et al.*, 2008).

The sulfate and hematite-bearing rocks form a bench, which is evidenced by a break in dip angles from approx. 17° in the sulfate-free ILDs above to 10° within the sulfate-bearing rocks. The floor of the "mineral bowl" drops towards the south and is covered by dark material, which appears to be a mixture of basaltic, pyroxene rich sand and crystalline ferric oxides, as evidenced by TES (Weitz et al., 2008) and CRISM data. Several light-toned patches with a spectral signature of monohydrated sulfates are found underneath this blanket. This suggests that the bench of sulfate-rich material extends further south underneath the dark cover to the opposite slope of the valley.

In the center of the northern slope of the "mineral bowl", the sulfate-bearing bench forms a cliff about 400 meters high. Polyhydrated sulfate deposits are observed near the top of the cliff, monohydrated sulfate-rich deposits are found at the base and on the valley floor below. In the western part of the "mineral bowl", the base of Ophir Mensa is heavily eroded and forms a deep embayment towards the north, bound by steep flanks. OMEGA and CRISM data show kieserite spectra on these walls up to an elevation of approximately +250 m. The observation of

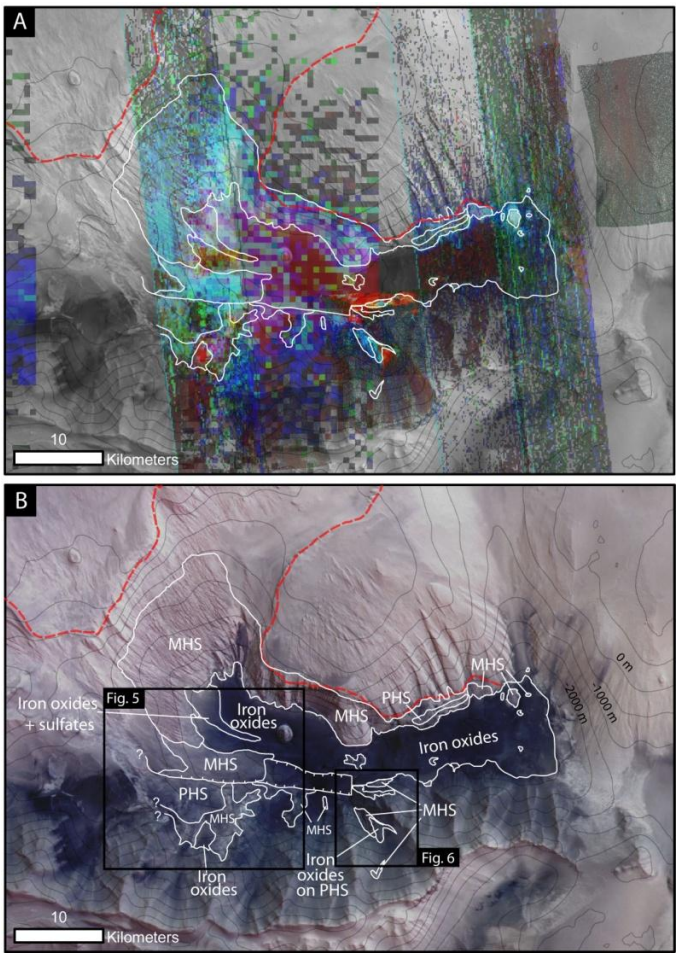

Fig. 6.4: Mineralogy of the "mineral bowl"

A: HRSC orbit 334 of the "mineral bowl" overlain with HRSC contours and spectral indices as in fig. 1. Red dashed line: Prominent horizon in Ophir Mensa. Sulfate detections are restricted to units below this horizon.

B: Interpreted mineralogical map of same region. MHS: monohydrated sulfates. PHS: Polyhydrated sulfates.

kieserite spectra despite the heavy erosion suggests that fresh sulfates from within Ophir Mensa are exposed, rather than being a thin surface coating on the Ophir Mensa slopes. On the valley floor, layering of smooth, dark-toned, basaltic material and lighter-toned material with intermixed sulfates and iron oxides can be observed. Locally, light-toned, sulfate-rich dunes are found.

The relationship between Ophir Mensa and the southern chasm wall is shown in Fig. 5. Monohydrated sulfates are observed within the eroded base of Ophir Mensa and overlying the spur-and-gully morphology of the southern chasm wall ("MHS in situ" in Fig. 6.5A), where they are found from the foot of the slope at an elevation of ~-2200 m up to ~+800 m. The thickness of the light-toned cover of the southern wall appears to increase from the top to the bottom of the southern slope, suggesting downslope movement of material. Several light-toned ridges are observed (white arrows in Fig. 6.5) covering the kieserite deposits, which have been described as "pasted on" the underlying basaltic basement (Chojnacki and Hynek, 2008, Weitz *et al.*, 2008) based on MOC imagery (Malin *et al.*, 1992). They are too small to be resolved in the CRISM MSP data available here, but are very similar in texture to light-toned ridges further to the east, (Fig. 6.6 and 6.7), showing a distinct mineralogy (see below). The kieserite on the southern slope of the "mineral bowl" is overlain by rough-textured polyhydrated sulfates and locally ferric oxides.

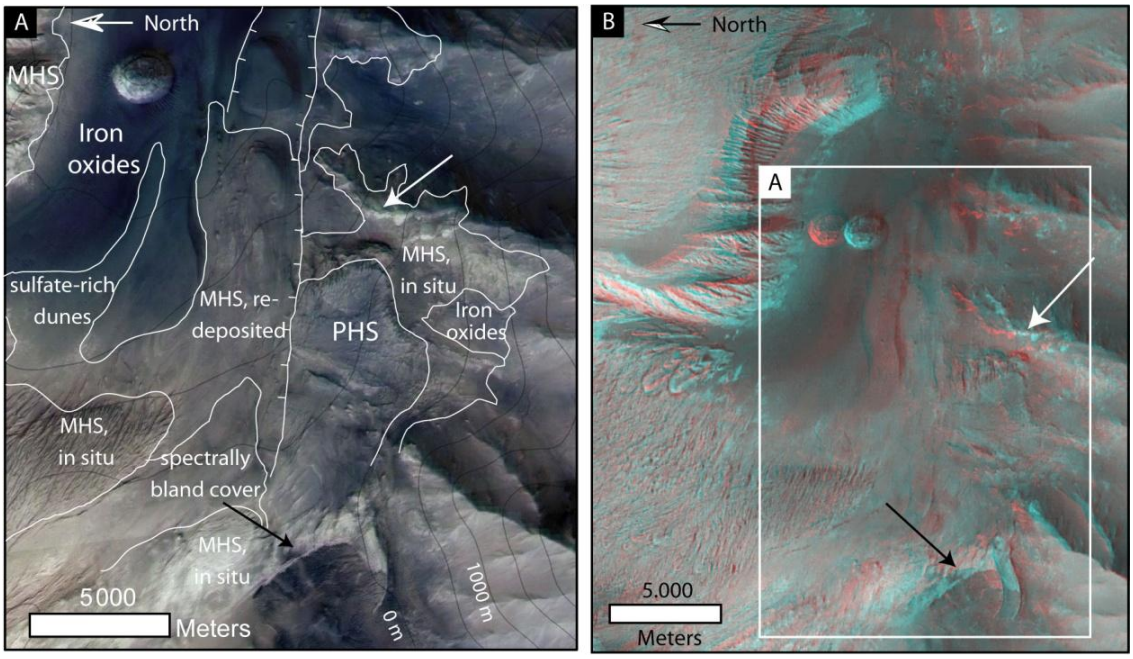

Fig. 6.5: Closeup on detail of Fig. 6.4

Fig. A shows the complex stratigraphic relationship between Ophir Mensa, LTDs on southern chasm wall and basaltic wall rock (CTX P12_005676_1746 and P13_006243_1746 overlain on HRSC color image orbit 3127) North is left. Mineralogy as in Fig. 6.4, combined with geomorphologic interpretation. MHS: monohydrated sulfates. PHS: polyhydrated sulfates. White arrow: Light-toned material on ridge of southern wall. Black arrow: "Tongue" of LTD bridging a valley between Ophir Mensa and southern wall. This implies that a depression already existed at this location at the time of sulfate deposition (see text). B: Anaglyph from HRSC orbit 3127 of the same area.

The sulfate deposits on the southern wall end abruptly along an east-west-trending lineament we interpret as a normal fault. Together with a parallel feature approx. two to three km northward it forms a graben in the floor of the "mineral bowl" (center of Fig. 6.5A). The graben can be traced further eastward as a depression with angular boundaries (top of Fig. 6.5B). The graben is filled with smooth layers of monohydrated sulfates eroded from Ophir Mensa and the southern chasm wall ("MHS, redeposited" in Fig. 6.5A). Partly, these monohydrated sulfate outcrops are covered by spectrally bland material from further up the slope of Ophir Mensa.

The black arrows in Fig. 6.5 mark a "tongue-shaped" deposit that bridges the gap between the southern slope of Ophir Chasma and Ophir Mensa. It starts below the top of Ophir Mensa at approx. 0 m elevation, stretches down the slope of Ophir Mensa to an elevation of ~-400 m, and rises again to ~0 m on the southern wall of Ophir Chasma. This outcrop is covered only by OMEGA data at a spatial resolution of 2.5 km/pixel and is partly overlain by smooth material, but the textural similarity to outcrops further to the east suggests that it consists of kieserite and is the westward prolongation of the kieserite deposits on the southern chasm wall ("MHS, in situ" Fig. 6.5). If this is the case, this suggests that (1) at the time when light-toned deposits of Ophir Mensa extended further to the south, as suggested by the monohydrated sulfates on the southern wall and the southward continuation of the light-toned deposits underneath a basaltic cover described in the eastern part of the "mineral bowl" (Fig. 6.5), these light-toned deposits never filled up the "mineral bowl" to the top of Ophir Mensa, but instead, a valley existed at the location of the "tongue-shaped" deposit between Ophir Mensa and the southern wall. It also suggests that (2) the polyhydrated sulfate deposits on the southern wall discordantly superpose the kieserite deposits ("MHS in situ",Fig. 6.5) on the southern chasm wall. Further high resolution HiRISE and CRISM observations of this part of the "mineral bowl" would help to solve this case.

The diverse mineralogy and complex depositional pattern of the LTDs on the southern wall are observed at the highest spectral and spatial resolution in the CRISM observation FRT0000A86A in Fig. 6.6. It shows ridges of kieserite in the valley cut into the chasm wall (center of Fig. 6.6A). These ridges, which could correspond to "MHS in situ" in Fig. 5, are overlain by a sequence of smooth layers corresponding to "MHS, redeposited" in Fig. 6.5. The smooth layers dip downslope at an angle of approx. 14°. Polyhydrated sulfates are found concordantly on the top of the smooth layers, but at the foot of the slope, they discordantly superpose and embay a massive outcrop of kieserite (Fig. 6.7A, C). Iron oxides are mostly associated with polyhydrated sulfates, but they also occur directly on top of kieserite. We analyzed the ferric oxides further using the CRISM data in the visible spectrum, as described in section 2. The regions appearing red in Fig. 6.5A show very similar spectral characteristics with a broad absorption band at 0.86 µm and two minor bands at 0.5 and 0.58 µm, resembling the spectrum of red hematite (Fig. 6.6G).

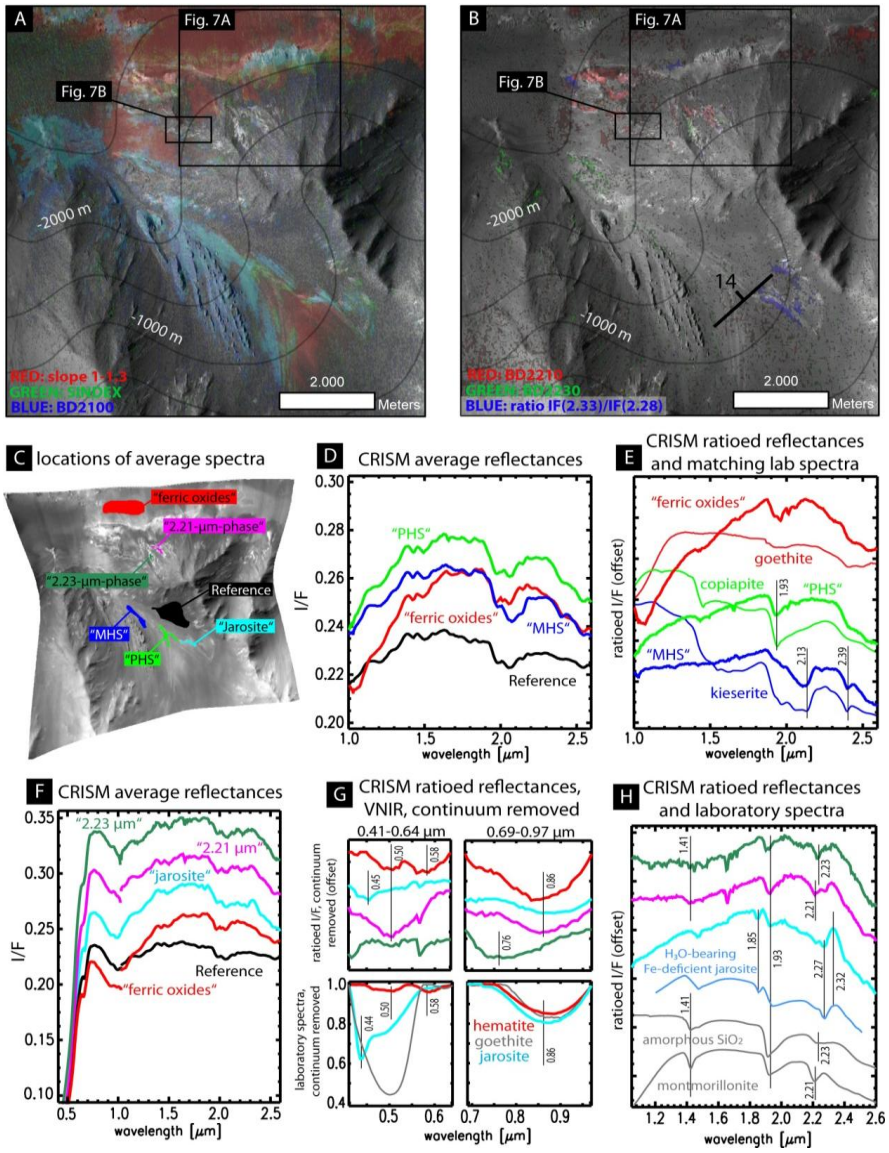

Fig. 6.6: Detailed view of southern slope of Ophir Chasma.

A: CTX observation P03_002208_1748 and P12_005676_1746 of LTDs on southern chasm wall overlain with spectral indices from FRT0000A86A as in fig. 6.1. Contours from HRSC DTM. LTDs form deposits on top of basaltic wall rock. Layered kieserite is superposed by polyhydrated sulfates and iron oxides. Layers dip downslope. At base of slope, polyhydrated sulfates embay kieserite, suggesting discordant deposition. B: Same as A, but spectral indices BD2210, BD2230 and ratio between reflectance at 2.33 µm and 2.28 µm as red, green and blue color planes. C: locations, where average spectra were taken. Spectra were averaged over tens to thousands of pixels to reduce noise, and divided by a spectrally inconspicuous reference region (black). D: Average reflectance spectra of monohydrated sulfates, polyhydrated sulfates, iron oxides and reference. E: Same spectra as D, ratioed to reflectance spectrum, and matching library spectra from RELAB. F: Average reflectance spectra of the three spectrally distinct regions in B, in the range of 0.41 µm to 2.6 µm, together with ferric oxide spectrum and reference for comparison. Three phases are observed: A phase with absorption band at 2.21 µm (magenta), one with a band at 2.23 µm (green) jarosite (cyan). G: Ratioed reflectance spectra in the range of 0.41 to 0.64 µm and 0.69 to 0.97 µm with separately removed continuum, and resembling laboratory spectra. H: Same spectra as in F and G (except ferric oxide), in the spectral range 1 - 2.6 µm, ratioed to reference region spectrum. Spectra resemble jarosite/H3O-jarosite mixed with amorphous silica or Al-rich clays (montmorillonite). Library spectra from RELAB, except H_3O-jarosite from Milliken et al., 2008.

Three other mineral phases are detected in this CRISM observation as well. Phase one displays spectral bands at 1.85 and 2.27 µm, diagnostic for jarosite, with the Fe-depleted H_3O-jarosite (Milliken *et al.*, 2008a) being the best match (blue in Fig. 6.6B). It is found in several locations close to polyhydrated sulfates, both in the narrow valley and near the base of the slope. In the visible spectral range, this material displays an asymmetric absorption band at 0.45 µm, which fits to an absorption feature of jarosite at 0.44 µm.

A second phase is characterized by absorptions near 1.93 and 2.21 µm and a shoulder near 2.32 µm (2.21-phase). Its spectrum does not match any of the laboratory spectra available from RELAB. Laboratory spectra with an absorption near 2.2 µm include amorphous SiO_2 and Al-rich phyllosilicates like montmorillonite (Fig. 5). However, amorphous SiO_2 shows a broad absorption band around 2.22 µm and no shoulder towards longer wavelengths, while montmorillonite has a narrow absorption band at 2.21 µm and shoulder near 2.27 µm, which makes both minerals unlikely matches. Similar spectra have been reported by Roach *et al.*, 2010b from Ius Chasma and elsewhere in Valles Marineris, and have been interpreted as hydrated silica phases or mixtures of phyllosilicates, amorphous silica and/or jarosite. A third phase has a very similar spectrum as the 2.21-µm-phase, but shows an absorption band at 2.23 µm. This spectrum is similar to spectra observed in Aram Chaos and interpreted as a ferric hydroxysulfate (Lichtenberg *et al.*, 2010), which was produced in the laboratory by desiccation of synthetic melanterite ($Fe^{2+}SO_4$•7(H_2O)). Unlike any other spectra in this observation, this material displays an absorption band at 0.76 µm (Fig. 6.5G). The polyhydrated ferric sulfate coquimbite ($Fe^{3+}{}_2(SO_4)_3$•9(H_2O), not shown) hasFig. 6.7 a

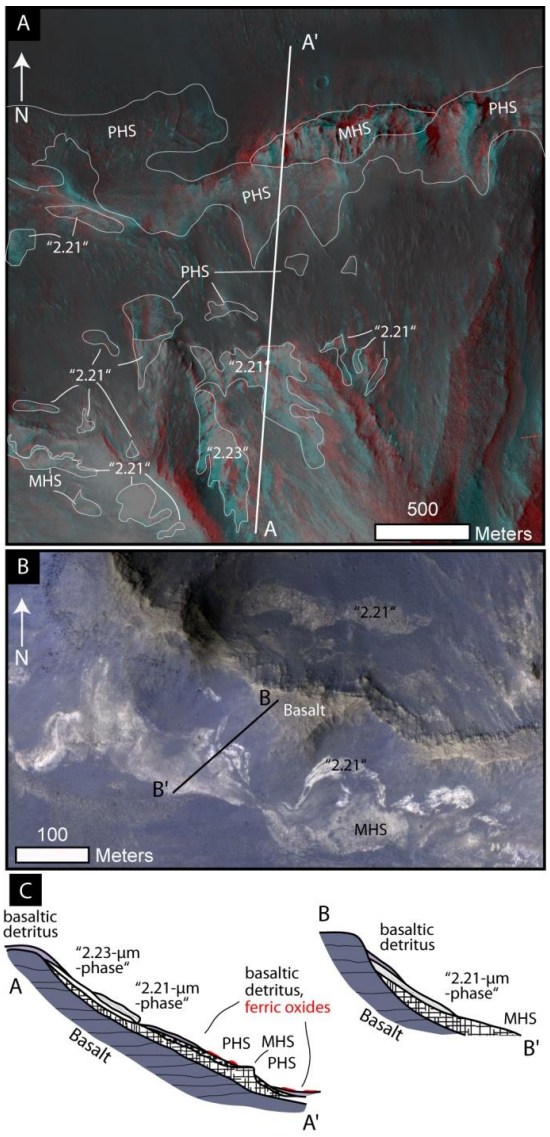

Fig. 6.7: HiRISE view and profiles from southern slope. A: Details of LTD at the foot of southern chasm wall (HiRISE anaglyph of ESP_011662_1750 and ESP_011807_1750). B: Detail of ridge in Fig. 6. The 2.21-micron-phase overlays kieserite as a thin, very bright coating. Its occurrence is restricted to the talus deposit underneath fresh basaltic ridge. A water supply to this location from groundwater or by a lake is inconsistent. Instead, water might have precipitated as rain, frost or snow from above. (HiRISE ESP_011807_1750_COLOR). C: Interpretative cross-sections to A and B (not to scale). The 2.21-µm-phase, the 2.23-µm-phase and the polyhydrated sulfates are found in similar positions discordantly superposing MHS. The relationship among these phases is unclear due to basaltic cover. Ferric oxides are found in association with PHS.

similar band near 0.76 µm, but its spectrum does not match in the short wave infrared range. The 2.21-µm-phase and the 2.23-µm-phase occur in similar stratigraphic positions. They superpose kieserite deposits as a thin, very light-toned coating, and are covered by basaltic debris , as shown in Fig. 6.7 and the schematic cross-sections therein. The outcrop of the 2.23-µm-phase in Fig. 6.7A appears to be more deeply eroded than the 2.21-phase. It therefore is interpreted as underlying the 2.21-µm-phase in the cross section in Fig. 7C. Polyhydrated sulfates are found in a similar stratigraphic position overlying kieserite units. The basalts at the top of the ridge in Fig. 7B appear blocky and layered, and thus resemble remnants of basaltic lava flows underlying the sulfates rather than aeolian deposits on top of them. This ridge is very similar to ridges in the west of the "mineral bowl" (white arrow in Fig. 5), suggesting that its mineralogy is present elsewhere in this part of Ophir Chasma, but not detected due to the lack of high-resolution spectral data.

6.4.4 The "northern moat"

The "northern moat" is the west-east-trending valley between Ophir Mensa and the northern rim of Ophir Chasma. Its floor is mostly covered by landslides eroding the chasm wall. In a few places, patches of light-toned material appear through windows in the landslide material cover (Fig. 6.8). The two outcrops in Fig. 6.8A and B have a texture similar to Ophir Mensa, which suggests that Ophir Mensa once extended further northward. The two patches show no spectral signature of sulfates, and are located at elevations of -3100 m and -3300 m, whereas a third patch of light-toned material is found at -4600 m. This third patch is similar in texture to the floor of the

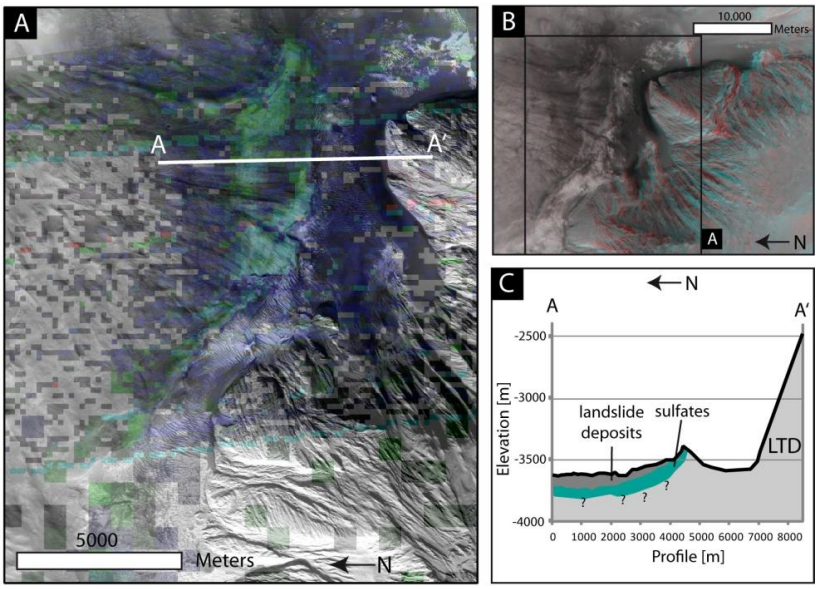

Fig. 6.8: Sulfate deposit north of Ophir Mensa.

A: Sulfate deposits in landslide superposed on now partly eroded LTD of Ophir Mensa (CTX P03_002208_1748; spectral indices as in fig. 1). B: Anaglyph from HRSC orbit 2083 visualizing the stratigraphy. C Interpretative cross-section of landslide based on HRSC DTM showing sulfates overlaying Ophir Mensa LTD.

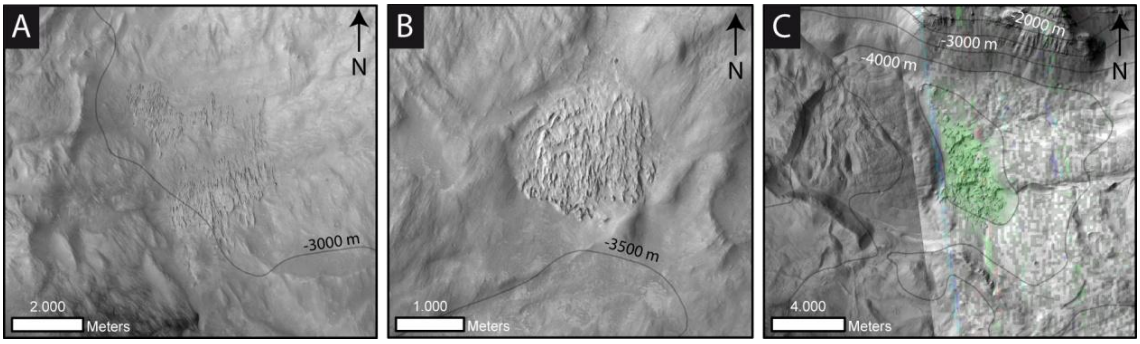

Fig. 6.9: Outcrops of light-toned material underneath landslide deposit cover in "northern moat".
A and B: Sulfate-free LTDs at elevations of 3100 and 3300 m below datum. C: Sulfate-bearing LTD at elevation -4600 m. Possible floor of "northern moat" prior to landslides. (CTX images P12_005676_1746, P03_002208_1748, P18_007891_1742; contours: HRSC).

central valley. Ratioed CRISM MSP and OMEGA spectra show an absorption band at 1.4 µm, a broad feature at 1.9 µm and a drop-off in reflectance longward of 2.3 µm, consistent with polyhydrated sulfate. The similar elevation, mineralogy and texture of this outcrop and the deposits in the central valley suggests that unlike the two outcrops in Fig. 6.8A and B, this outcrop is not a remnant of Ophir Mensa, but rather an infill of the basin between Ophir Mensa and the northern chasm wall, similar to the central valley fill.

Sulfates are also found within the deposits of a landslide in Fig. 6.9. It shows sulfate-rich material at the tip of a landslide fan that was deposited against the LTDs of Ophir Mensa. Since the time of deposition of this landslide, the slope of Ophir Mensa has been eroded backward 1.2 to 2.5 km by wind, leaving behind a flat, dune-covered plain between the landslide deposit and the slope of Ophir Mensa.

The HRSC anaglyph in Fig. 6.8B suggests that the landslide deposit and the sulfate material therein overlay the light-toned deposits of Ophir Mensa, as shown in the cross-section in Fig. 9C. Theoretically, the sulfates could have formed prior to the landslide event, or by water released by the landslide event itself. Lucchitta, 1987, argued that the landslides in the central valley of Ophir Chasma released large quantities of water, which caused the collapse of the mountain barrier between Ophir and Candor Chasmata, and deepened the central valley. However, Quantin *et al.*, 2004, observed that landslides in Valles Marineris occurred at all times between 3.5 Ga and 50 Ma before present, and that they always show the same characteristics. This suggests that no water was involved in the formation of the landslides, as the atmospheric conditions during this period did not allow a sustained existence of liquid water. The topographic elevation of the sulfates of -3450 m is also much higher than the -4500 m of the closest sulfate deposits in the "northern moat" (Fig. 6.9C). We therefore conclude that the sulfates in Fig. 6.8 were formed prior to the landslide events. The ages of the landslides in Ophir Chasma range between 80 Ma and 1 Ga (Quantin *et al.*, 2004) and provide no constraints on ILD formation and water-related activity, which ended at 3 to 3.5 Ga (Quantin *et al.*, 2010).

6.4.5 The central valley

The floor of the central valley is partly covered by sulfate-rich deposits, as shown in Fig. 6.10. Its surface gently drops from -4250 m in the south-west to -4900 m in the north-east, resulting in a

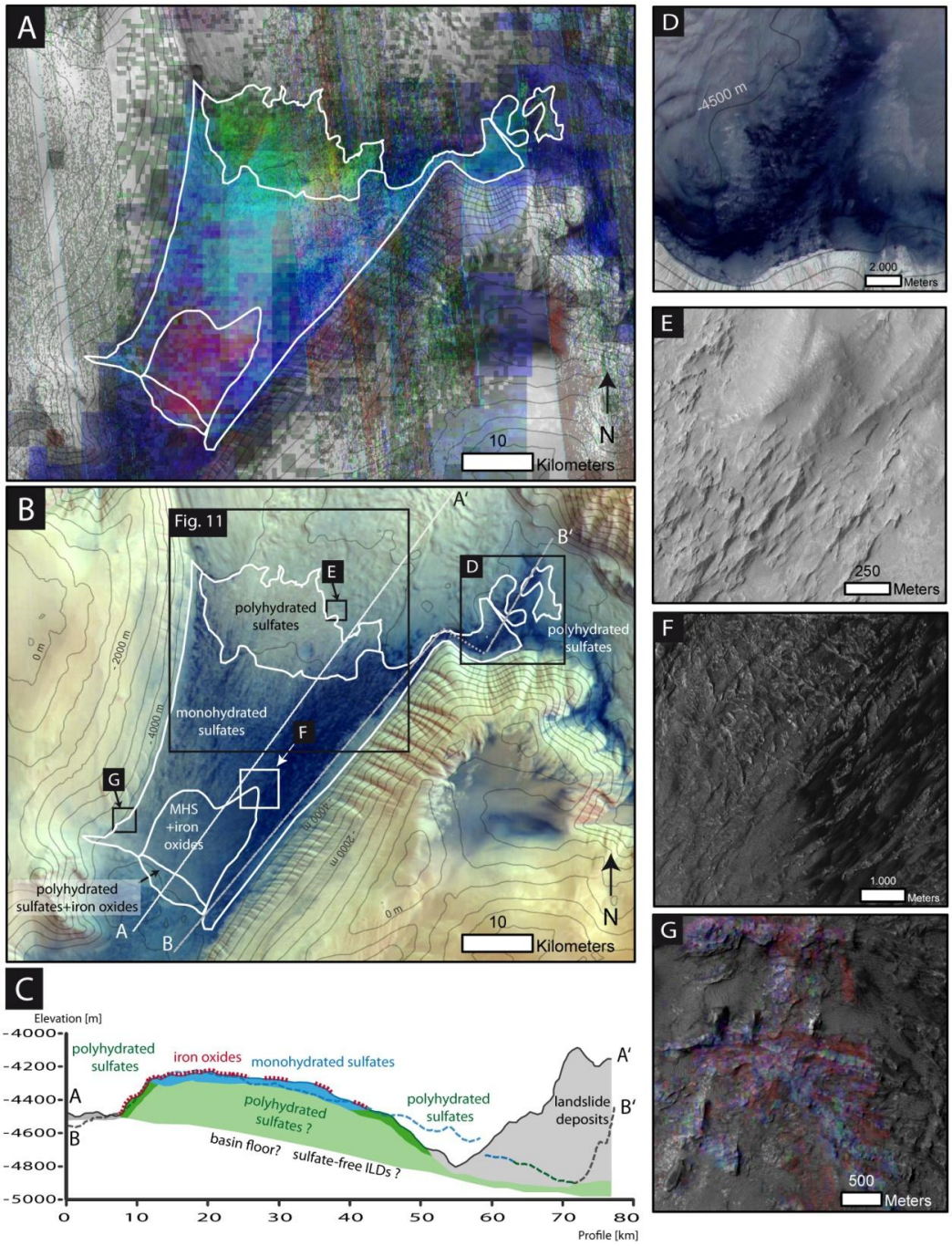

Fig. 6.10: The central valley of Ophir Chasma.

A: HRSC nadir (orbit 334) and contours of the central valley of Ophir Chasma overlain with spectral indices as in Fig. 6.1B: HRSC color image with interpreted mineralogy. MHS: Monohydrated sulfates. Polyhydrated sulfates are found in north of central valley. They are overlain by monohydrated sulfates (kieserite), iron oxides accumulating in the southern part of the valley, and basaltic dunes. C: Interpretative longitudinal profile of central valley. Monohydrated sulfates superpose polyhydrated sulfates. D: Sulfates are revealed in HRSC color data by their distinct hue. E: Fluted surface texture of polyhydrated sulfates. (HiRISE PSP_007535_1755_RED) F: Ridged surface texture of kieserite-bearing valley floor, covered by basaltic dunes (SE of Fig.) and iron-oxide rich deposits (SW of Fig.; CTX P20_008972_1756).G: Example of curvilinear, sulfate-bearing ridges. Spectral indices from CRISM HRL0000B7D4 as in Fig. 6.1 on HiRISE PSP_009183_1750

dip of approximately 1° (Chojnacki and Hynek, 2008, Gendrin *et al.*, 2005b, Mangold *et al.*, 2007a). The deposits are at least 270 m thick, and are easily recognized by a distinct hue in HRSC false color images (Fig. 6.10D). The CRISM observations of this area generally confirm the mineralogy derived from OMEGA data. The top of the deposit is dominated by the monohydrated sulfate kieserite that is partly covered by dunes of dark-toned, basaltic material. It has a rough, fluted texture with curved ridges trending approximately perpendicular to the valley axis (Fig. 6.10E, F and G). An increase of the spectral slope between 1 and 1.3 µm in CRISM and OMEGA spectra in the southern part of the valley indicates that the smooth material with an intermediate albedo found in this part of the valley is rich in ferric oxides (Fig. 6.10F).

Directly south of landslide deposits in the north of the central valley, the valley floor deposits display spectra of polyhydrated sulfates. They show a fluted, wind-eroded topography (Fig. 6.10E), but are devoid of the ridges found in the monohydrated sulfates (Fig. 6.10F) and are not covered by dark, basaltic dunes. The patch is topographically lower than the neighboring monohydrated-sulfate rich deposits. This suggests that monohydrated sulfates overlay polyhydrated sulfates, as shown in the cross-section in Fig. 6.10C. The superposition of monohydrated sulfates on top of polyhydrated sulfates is contrary to sulfates in the "mineral bowl" and other chasmata of Valles Marineris, such as Juventae Chasma (Bishop *et al.*, 2009, Gendrin *et*

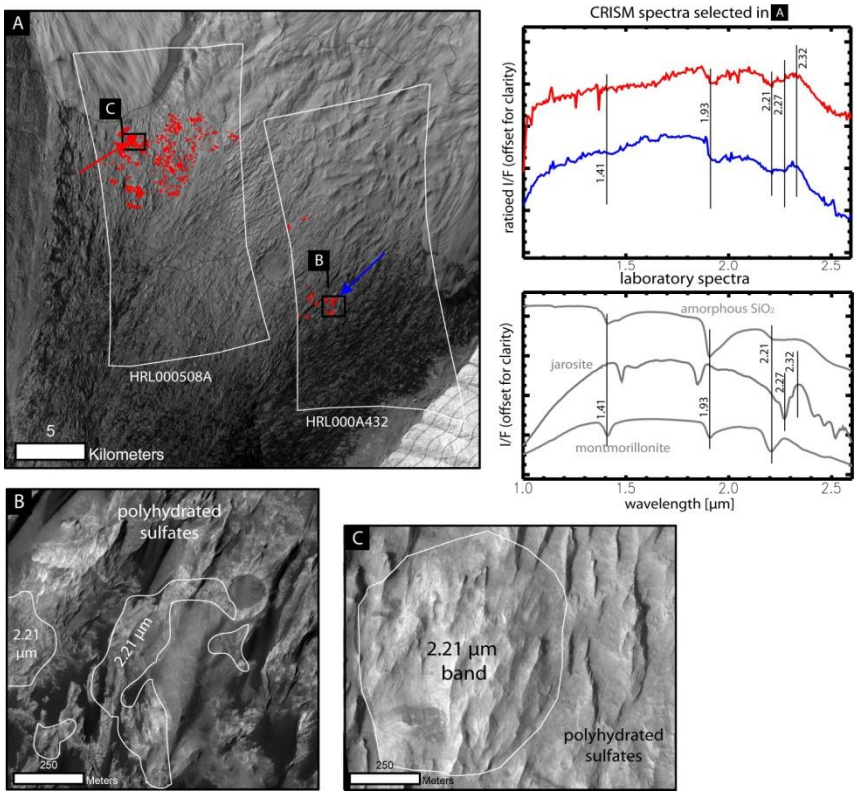

Fig. 6.11: Enigmatic spectra in central valley.

A: Spectral index BD2210 of two CRISM HRL observations overlain on CTX images of the northern central valley (CTX P05_003131_1747, P20_008972_1756), and exemplary spectra. Spectra resemble jarosite with additional phases mixed in (compare fig. 6). B and C: Outcrops of the 2.21 µm phase here are sub-circular and almost indistinguishable in texture from the surrounding sulfate-rich rock.

al., 2005b) and West Candor Chasma (Murchie *et al.*, 2009a). The boundary between poly- and monohydrated sulfates is gradational and coincides with a decrease in albedo from the brighter poly- to the slightly darker monohydrated sulfates. However, it also coincides with an increase in the abundance of dark dunes. Therefore, the albedo difference between the brighter polyhydrated sulfates and the darker monohydrated (kieserite-dominated) sulfates (Chojnacki and Hynek, 2008), might be caused by the presence of basaltic dunes and iron oxides in the area of the monohydrated sulfates, and not by a color variation between the two sulfate species. Both sulfate species are not layered. The deposit ends abruptly near the remains of the mountain barrier between Ophir and Candor Chasma at 72° E, 5° S.

Light-toned, often sub-circular patches with a diameter of a few hundred meters are observed in the northern part of the central valley, where polyhydrated minerals are found (Fig. 6.11). They show bands at 1.93 µm, 2.21 µm and 2.27 µm and shoulder at 2.32 µm in CRISM targeted observations, which is very similar to the 2.21-µm-phase observed in the "mineral bowl" (Fig. 6.6and Ius Chasma (Roach *et al.*, 2010b). Again, a mixture of jarosite (possibly H_3O-jarosite) and amorphous silica or montmorillonite is the best spectral match. A phase with a band at 2.23 µm is not observed here. Unlike the deposits in the "mineral bowl", the deposits in the central valley are not layered, and almost indistinguishable from the surrounding deposits by their texture alone.

6.5 Discussion

6.5.1 Mineral detections

Roach *et al.*, 2010b suggested four hypotheses for the minerals showing absorption bands at 2.21 µm observed in Ius Chasma, which are spectrally very similar to the 2.21-µm-phase observed in Ophir Chasma: (1) a sulfate mineral structurally similar to jarosite, (2) amorphous silica mixed with Fe-Mg-smectite, (3) a mixture of Al- and Fe-Mg-smectite, or (4) poorly crystalline mixed Al-Fe clay formed either by acid alteration of clay minerals or as a direct formation from dissolved basalt.

Library spectra of the three most common jarosite minerals, Na-jarosite, K-jarosite and H_3O-jarosite, are very similar to the 2.21-µm-phase, but no perfect spectral match. Like the unknown phase, they display absorptions at 1.93 µm and a shoulder near 2.32 µm, but the band at 1.85 µm, characteristic for jarosites, is not observed in the unknown phase. An absorption band at 2.21 µm is observed in K-jarosite, but this mineral shows a second, deeper absorption near 2.27 µm, which is absent or only weakly expressed in the unknown phases. Therefore, if a jarosite mineral is present in these phases, it is probably mixed with a different mineral.

Amorphous silica displays a broad spectral band at 2.21 µm, and a shoulder at 2.26 µm. In contrast, the absorption band at 2.21 µm of the unknown phase is narrow, and its right shoulder is located at longer wavelengths at 2.32 µm, which makes pure amorphous silica a bad spectral match. A mixture of Al-rich and Mg/Fe-rich clay minerals or of clay minerals and jarosite could reproduce the absorption bands observed here. However, clays form under circum-neutral pH- conditions, whereas the clear identification of jarosite in neighboring locations, and partly in similar stratigraphic positions, points towards acidic conditions (pH < 3-4, Papike *et al.*, 2006), which makes the presence of clay minerals unlikely. A theoretical alternative would be the formation of clay minerals at a different location than the

jarosite minerals and subsequent transport to this place, but the location of the 2.21-µm-phase high on the slopes just below the crests of fresh basaltic wall rock effectively rules out this option, as it suggests a formation of this phase *in situ*.

The last hypothesis is the formation as a poorly crystalline Fe-SiO_2-phase by acidic to neutral leaching of nontronite, which would produce Si-OH vibrations due to the formation of amorphous silica as in clay-rich material exposed to acidic vapors at Mauna Kea (Swayze, unpublished data in Roach *et al.*, 2010b). This mechanism would also explain the observed 2.23 µm band observed locally during this study due to FeAlOH vibrations. Alternatively, Tosca *et al.*, 2008b, report the formation of a poorly crystalline Fe-SiO_2-phase as a precipitate from dissolved basalt by addition of S and Cl under oxidizing conditions at a pH of 5-7 in laboratory tests, which would possibly display similar spectral bands between 2.21 and 2.26 µm.

Of the proposed mineralogies of the unknown 2.21-µm-phase, we favor a mixture of jarosite and amorphous silica or jarosite and a newly formed, poorly crystalline Fe-SiO_2- phase, and a mixture of jarosite and a poorly crystalline Fe-Al-SiO_2-phase for the locations showing a 2.23 µm absorption, rather than mixtures of different phyllosilicate minerals or phyllosilicate minerals and jarosite. In the "mineral bowl" (Fig. 6.6), the clear identification of H_3O-jarosite suggests acidic conditions, which are inconsistent with clay formation. Amorphous silica in combination with jarosite has also been identified by CRISM on the plateau above Juventae Chasma (Bishop *et al.*, 2009, Milliken *et al.*, 2008a) and in Melas Chasma (Metz *et al.*, 2009), where they are interpreted as the product of acidic alteration of basalts.

On Earth, jarosite and amorphous silica are known from acid mine drainage deposits, for example in Spain (i.e., Sánchez España *et al.*, 2005) and Greece (Triantafyllidis and Skarpelis, 2006), where the oxidation of sulfides produces sulfuric acid, which in turn dissolves olivines, pyroxenes and feldspars in the basaltic rocks to form jarosite, leaving behind amorphous silica and kaolinite as the least soluble minerals. A similar mechanism has been proposed for Mars (Burns, 1987, Burns and Fisher, 1990b, Poulet *et al.*, 2008). Investigations on a Martian meteorite show that a part of the jarosite and amorphous silica on Mars formed under hydrothermal conditions (McCubbin *et al.*, 2009), but the H_3O-jarosite best matching the spectra from Ophir, Melas and Juventae Chasma indicates temperatures below 100°C (Milliken *et al.*, 2008a). All jarosite species indicate a limited water supply and short time for the chemical alteration, as the acidity is not neutralized by the decomposition of feldspars (Höller, 1967, Madden *et al.*, 2004). H_3O-jarosite forms at even lower water/rock ratios, when sulfide minerals dissolve more rapidly than rock forming minerals, resulting in a lack of Na and K with respect to Fe in the solution, which prevents the formation of K- and Na-jarosite (Brophy and Sheridan, 1965). At rising pH, H_3O-jarosite becomes unstable, and goethite (FeOOH) forms, while the sulfate ions go back into solution (Burns and Fisher, 1990b). At the same time, poorly crystalline Fe-or FeAl-SiO_2-phases can form (Tosca *et al.*, 2008b), which can be considered precursors to clay minerals. Goethite can later transform into hematite, while the sulfate ions could precipitate as polyhydrated sulfates upon evaporation of the brine. An alternative source for the acidity required for the jarosite formation other than weathering of sulfides are volcanic, SO_2-rich exhalations as

observed at the Kilauea volcano (Schiffman *et al.*, 2006).

The mineral assemblage observed on the southern wall of Ophir Chasma (Fig. 6.6 and Fig. 6.7) is consistent with an acidic alteration of basaltic rock: jarosite and the unidentified, possibly jarosite-amorphous silica bearing phases are almost always observed at the top of the hillsides, just below the crest, locations that would have received very little water. They are covered by basaltic debris, which would be the source rock. They are topographically higher than iron oxide detections and polyhydrated sulfates, which would represent the more developed alteration products. On the northern side of the mineral bowl, where the slopes are lacking a basaltic cover, no 2.21-µm-phase or jarosite are found. In the central valley, the relationship between the abundant polyhydrated sulfates and the patchy outcrops of the 2.21-µm-phase is not clear and gives no hint on the formation history. A possible source rock for the sulfatic alteration products cannot be identified.

6.5.2 Stratigraphic relationships

Any hypothesis for the formation of the light-toned deposits and the role of water therein has to meet the constraints imposed by the stratigraphic relationships within the LTD units and between the LTDs and the wall rocks. They are visualized in Fig. 12 and summarized as follows:

(1) All light-toned deposits in Ophir Chasma superpose the spur-and-gully morphology of the canyon walls. Their deposition therefore postdates the formation of the chasm (Chojnacki and Hynek, 2008).

(2) The LTDs of Ophir Mensa can be divided into two units based on layer boundaries and mineralogy. A marker horizon (fig. 1) separates the two units. Its dip roughly follows the local topography, with steep (~20°) slopes at the flanks of Ophir Mensa and approx. horizontal layering in the center. This implies that the eastern part of Ophir Mensa is younger than the western part.

(3) The lower unit of Ophir Mensa is kieserite-bearing. The strong erosion of Ophir Mensa in the "mineral bowl" suggests that the kieserite signature is not a superficial deposit draped over a sulfate-free rock, but that the entire lower unit contains kieserite sulfate.

(4) The monohydrated sulfates on the southern wall of the "mineral bowl" are connected to Ophir Mensa by a "tongue" of light-toned, sulfate-rich material. This suggests that these deposits are of the same age. The monohydrated sulfates in the "mineral bowl" therefore formed, when Ophir Mensa extended further southward up to the southern wall of the chasm. The top of the LTDs along the southern wall of Ophir Chasma dropped from west to east, as shown by remnants of light-toned material on the chasm wall.

(5) However, at the time of sulfate formation, a precursor valley of the "mineral bowl" already existed, which formed a depression between the center of Ophir Mensa and the southern wall. This is shown by the (likely) sulfate-bearing "tongue" between the southern wall and Ophir Mensa: It starts near the top of Ophir Mensa, drops down at its center and raises again towards the southern wall (Fig. 6.5B).

(6) Polyhydrated sulfates in the "mineral bowl" are found near the top of the light-toned material. The transition between kieserite and polyhydrated sulfates appears concordant on the upper slope of the southern wall (Fig. 6.6 and Fig. 6.7), but discordant in the lower parts, where polyhydrated sulfates embay an eroded remnant of kieserite-rich rock. Further westward, the polyhydrated

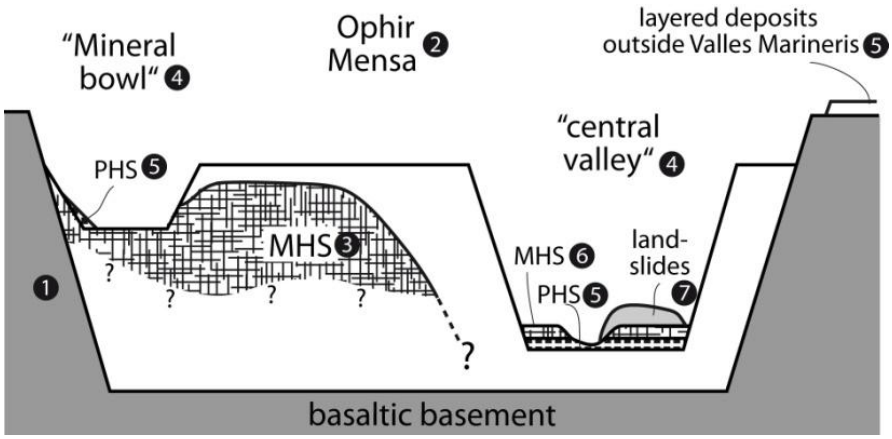

Fig. 6.12: Suggested succession of events in Ophir Chasma.
1: Opening of Valles Marineris. 2: Deposition of the LTDs such as Ophir Mensa, possibly as airfall deposits or ash. 3: Formation of kieserite in Ophir Mensa by intruding groundwater. 4: Excavation of the "mineral bowl", "central valley" and "northern moat". 5: Deposition and/or alteration to form polyhydrated sulfates and other phases in "mineral bowl", possibly by precipitation water. Deposition of PHS and MHS (6) in "central valley", possibly in lake or underneath a glacier. The relative timing of these events is not constrained and could coincide with deposition of layered deposits with similar mineralogy on the plateau above Valles Marineris. 7: Landslides enlarge the chasm and partly cover the floor.

sulfates appear to discordantly overlay parts of the "tongue" between Ophir Mensa and the southern wall. This implies that polyhydrated sulfates formed after the deposition and partial erosion of the kieserite-rich rocks.

(7) It is not clear if the polyhydrated sulfates precipitated directly in their current form, or if they formed by hydration of the underlying kieserite-rich material. The presence of jarosite and poorly constrained, probably amorphous silica-rich material underneath a cover of basaltic debris is consistent with an acid alteration of the basaltic cover caused by the decomposition of sulfides, as suggested by Burns, 1987. This would require the presence of water, which could also have transformed monohydrated kieserite to polyhydrated sulfates. An alteration from kieserite to polyhydrated sulfates has also been suggested for Ius Chasma (Roach *et al.*, 2010b), whereas the variation in sulfate mineralogy in Candor and Juventae Chasma has been interpreted to be caused by changes of the composition of the evaporating brine (Murchie *et al.*, 2009a, Bishop *et al.*, 2009).

(8) Ferric oxides contained within the sulfate-rich deposits in Ophir Mensa (Bibring *et al.*, 2007) accumulate on the floor of the "mineral bowl", where they form a partly indurated lag deposit together with sulfates and basaltic debris from the south wall.

(9) The sulfates of the central valley and the "northern moat" show distinct characteristics. They formed after the incision of the central valley, and therefore post-date Ophir Mensa.

(10) All sulfate deposits in the central valley are found below -4250 m, approx. 1450 m below the lowest sulfate detections in the "mineral bowl". Only the sulfates underneath a landslide in the "northern moat" are found at higher elevations (Fig. 6.8), but it is not clear if they formed *in situ*

or have been transported to this elevation by the landslide.

(11) In the central valley, monohydrated kieserite apparently stratigraphically superposes polyhydrated sulfates, unlike in Candor Chasma, Aram Chaos and Juventae Chasma, where monohydrated sulfates are stratigraphically below polyhydrated sulfates (Bishop *et al.*, 2009, Lichtenberg *et al.*, 2010, Murchie *et al.*, 2009a), but similar to Ius Chasma (Roach *et al.*, 2010b).

6.5.3 Implications for formation hypotheses

The presence of sulfates within the ILDs of Ophir Mensa indicate that water played a role in their formation. On the other hand, large parts of the ILDs are spectrally bland although they are likely not covered by dust, as indicated by elevated TI values around 500 thermal inertia units (Chojnacki and Hynek, 2008, Fig. 2a), steep slopes and no visible small dunes in HiRISE images. Therefore, these parts of the LTDs must either have formed under dry conditions that did not involve water, or they are cemented by minerals that are not detectable from orbit, such as halite (NaCl) or anhydrite ($CaSO_4$). In the following paragraphs, we will discuss the formation of the ILDs in the light of our observations before we investigate whether the sulfates in Ophir Chasma precipitated from evaporating groundwater (Roach *et al.*, 2010b, Rossi *et al.*, 2008), lakes (Lucchitta, 2009a, 2009b, McKay and Nedell, 1988), meteoric water, or a combination of these processes.

Some authors suggested that the LTDs were exhumed light-toned material from the chasm walls (Adams *et al.*, 2009, Malin and Edgett, 2000b). This idea can be rejected, as the light-toned material clearly overlies the spur-and-gully morphology of the chasm walls as elsewhere in Valles Marineris (Blasius *et al.*, 1977, Lucchitta *et al.*, 1992, Nedell *et al.*, 1987). The idea that the LTDs are sub-ice volcanoes was proposed by Chapman and Tanaka, 2001. This theory explains the outward-dipping layers of the LTDs and the fact that most LTDs form free-standing mounds, separated from the chasm walls by depressions. However, it implies that the LTDs are volcanic strata. This is contradictory to the lack of a basaltic spectral signature of these rocks and the missing of clear volcanic morphologies such as craters or lava flows.

If the LTDs were eolian or pyroclastic deposits (Chapman and Tanaka, 2001, Peterson, 1981), we would expect similar deposits outside Valles Marineris (Glotch and Rogers, 2007). Layered deposits are found on the plains surrounding Valles Marineris (Bishop *et al.*, 2009, Milliken *et al.*, 2008a, Le Deit *et al.*, 2010), which are interpreted as airfall deposits (Le Deit *et al.*, 2010). These deposits are much thinner (<100 m) than the deposits within the chasmata. Thus, an origin of the spectrally bland material in the LTDs by airfall, either as volcanic clasts or windblown dust, is conceivable, but an additional mechanism to trap and lithify these deposits is required to explain the observed thickness of the deposits (Lucchitta, 2009a, b).

Regardless of the origin of the spectrally bland LTDs, the sulfates within them are formed by water. The stratigraphic relationships described in section 4.2 require at least two phases of sulfate formation. In a first phase, sulfates formed within Ophir Mensa and in a second phase in the central valley. The monohydrated sulfates on the southern wall of Ophir Chasma appear to be remnants of the sulfates of Ophir Mensa, which once extended further southward. The polyhydrated sulfates possibly formed later, either by alteration of the

previous monohydrated sulfate, or by acid weathering of the overlaying basaltic debris. The timing of this alteration phase is poorly constrained. It can be contemporaneous with the sulfate formation in the central valley and the northern moat, or might also have taken place independently from that event. For nearby Capri Chasma, Roach *et al.*, 2010a, advocated the concept that the monohydrated kieserite was not the sulfate phase that initially precipitated, but was formed later during diagenesis from previously polyhydrated sulfates under the overburden of several kilometers of sediments on top. The LTDs of Ophir Mensa are several kilometers thick; therefore, diagenetic processes or intrusions of brines that altered an initial mineralogy to the mineralogy now observed is possible, but an assessment of their role is difficult and remains an open question.

The idea that the sulfates formed in lakes (Lucchitta, 2009a, 2009b, Peterson, 1981) implies that the lakes acted as a trap for clastic deposits. The sulfates therefore would have formed at the same time as the spectrally bland clasts hosting them. If this was the case, we would expect horizontal layering and a constant upper elevation of the sulfate detection, which would resemble the water level in the lake. The upper part of the LTDs, which is sulfate-free, would have been formed by a different process. Therefore, the elevation variations of the upper sulfate detection limit in the "mineral bowl" and the lack of sulfate detections in the LTDs at similar elevations on the northern and eastern flank of Ophir Mensa are better explained by a formation by groundwater (Murchie *et al.*, 2009a) that entered the LTD mound after its deposition. In this case, the variations in elevation of the sulfate detections and the coexistence of sulfate-bearing and sulfate-free LTDs at the same elevation would reflect the initial morphology of the hosting sediments in the chasm, or variations of their permeability.

The deposits in the central valley are almost horizontal, which is consistent with a formation in a lake as well as a playa, similar to the mechanism proposed for Meridiani Planum (Arvidson *et al.*, 2003). The slight dip towards the north would either imply a dip of the sediments after deposition, possibly by downfaulting of the entire chasm floor along the northern rim, or simply deposition on an inclined chasm floor. The remnants of the collapsed mountain ridge between Ophir and Candor Chasma could have acted as a barrier to form a lake behind it. The low elevation of the sulfate deposit, implied by sulfate detections restricted to elevations below -4250 m, is consistent with the proposed lake in central Valles Marineris/Coprates Chasma with a maximum ponding level at -3560 m proposed by Harrison and Chapman, 2008. The flanks of the central valley show rills on both sides. Similar structures in Candor have been interpreted by Murchie *et al.*, 2009a, as braided channels formed by flowing water. If this was the case in Ophir Chasma, they could have acted as pathways for water entering the suggested lake. The rills have also been interpreted to be formed by glacial scouring (Chapman and Smellie, 2007, Roach, 2009), which would also be consistent with a (frozen) lake in the central valley. However, the rills may also have formed by wind erosion: Many of them are not perfectly perpendicular to the slope of the hillsides they form in, but curve southward. This is a strong indication for wind erosion rather than flowing water or ice.

Like in the central valley, polyhydrated sulfates are found topographically below monohydrated sulfates in western Candor Chasma and Aram Chaos (Lichtenberg *et al.*, 2010, Murchie *et al.*, 2009a). In these locations, the polyhydrated

sulfates have been interpreted as late-stage sediments that were deposited discordantly in low-lying areas after erosion of the monohydrated sulfates, so they would be stratigraphically above the monohydrated sulfate-rich deposits. In the central valley, we do not see evidence for this interpretation. The boundary between mono- and polyhydrated sulfates is transitional, and no unconformity is observed. We therefore interpret that the topographically low polyhydrated sulfates are also stratigraphically below the monohydrated sulfates. This stratigraphy has also been inferred for mono- and polyhydrated sulfates in Ius Chasma (Roach *et al.*, 2010b).

The sulfates on the southern wall of the "mineral bowl" are spread over a wide range of elevations, and dip downslope. This, and the "tongue" between Ophir Mensa and the southern wall, implies that the "mineral bowl" depression existed already at the time of the deposition of these sulfates. Even if Ophir Mensa once extended further southward, it would already have been eroded away at least partly, as otherwise the layering of the deposits on the southern wall would be more horizontal. If the sulfates were formed in a lake, this lake would have to have been deep enough to form sulfates very high on the slope. In this case, other parts of this valley would have been submerged at the same time, and should therefore show sulfate deposits too, which have not been observed. The formation by evaporating groundwater would require that a groundwater discharge from the entire slope of the chasm wall: water leaking from the top of the wall would not have reached the debris deposits below the basaltic rocks on the "spurs" of the wall, where some of the sulfates are found (fig. 7). The presence of high water tables in the narrow mountain ridge between Ophir and Candor Chasma is also not likely. Therefore, if these deposits are indeed acid alteration products of basalt, which is consistent with the spectral observations of jarosite, amorphous silica, ferric oxides, polyhydrated sulfates and possibly poorly crystalline Fe-SiO_2- or Fe-Al-SiO_2-phases (the 2.21-µm-phase and the 2.23-µm-phase), the best way to explain the supply of water to the locations where these minerals are found, would be rain, snow or frost.

Glaciers in Valles Marineris, which could provide the required water, and could also explain the variable range of elevations where water has been present, have been proposed in previous studies (Chapman and Smellie, 2007, Chapman and Tanaka, 2001, Chapman and Tanaka, 2002, Mège and Bourgeois, 2010), but in this particular location, associated landforms such as U-shaped valleys are missing. A second source for water could be the fog clouds in Valles Marineris (i.e., Moehlmann *et al.*, 2009). If the Martian soil contains perchlorates, as suggested by results from the Phoenix lander (Zorzano *et al.*, 2009), these hygroscopic minerals would attract water from the fog clouds in Valles Marineris and allow liquid water at temperatures as low as 225°K. However, if this is indeed the process responsible for the alteration, it remains unclear why it would be constrained to this part of Ophir Chasma only, as other parts of the LTDs in the same chasm at similar elevations did not develop a spectral hydration signature.

6.6 Conclusions

Our study confirms and refines, based on OMEGA and CRISM data, previous studies based on OMEGA data alone (Chojnacki and Hynek, 2008, Gendrin *et al.*, 2005b, Mangold *et al.*, 2007a). Water-related minerals in Ophir Chasma are found mainly in two locations: In the "mineral bowl" valley between Ophir Mensa and the

southern wall, and on the central valley floor. The same minerals are observed in these two locations, kieserite, polyhydrated sulfates, iron oxides and newly discovered phases that are consistent with mixtures of jarosite and amorphous silica or other poorly crystalline phases, but the two deposits are very distinct (Chojnacki and Hynek, 2008). In the "mineral bowl", kieserite is found in the bulk material of Ophir Mensa and on the southern wall, where it could represent remnants of Ophir Mensa, which once extended further southward. The variations in elevation of these sulfates are best explained by a post-depositional alteration of clastic material of unknown origin, possibly airfall deposits, by ground water rather than an open water body. On the southern wall, kieserite is superposed by H_3O-jarosite, and/or possible jarosite-amorphous-silica mixtures with spectral bands at 2.21 µm or 2.23 µm, polyhydrated sulfates and iron oxides. This sulfate deposit is layered, dips downslope, is stretched over a wide range of elevations, and could be stratigraphically discordant to the underlying bulk LTDs. Its formation therefore possibly took place after the excavation of the "mineral bowl" valley. A similar succession of polyhydrated sulfates discordantly on top of monohydrated sulfates in local depositional traps has been observed in western Candor Chasma and Aram Chaos (Lichtenberg *et al.*, 2010, Murchie *et al.*, 2009a). In Candor Chasma, rills that show similarities to braided river beds on the slopes of LTD mounds have been interpreted as evidence of springs relatively high up the slopes of the chasm, which would have supplied the water that eventually deposited the polyhydrated sulfates. In Ophir Chasma, locations of the polyhydrated sulfates and the phases with absorptions at 2.21 or 2.23 µm on ridges of the underlying basaltic material is neither consistent with a water supply scenario nor with an open lake: therefore, meteoric water in the form of snow, frost or fog might have played a role. Debris from the LTDs, including iron oxides, are found as lag deposits on the floor of the valley, where they mix with basaltic material (Bibring *et al.*, 2007, Chojnacki and Hynek, 2008, Weitz *et al.*, 2008). On the northern side, the lack of CRISM targeted observations prevents a detailed spectral analysis.

The sulfates in the central valley form a flat deposit at low elevations (<-4250 m), but appear to be stratigraphically higher than Ophir Mensa's LTDs. These deposits are not layered, show ridges or joints, and kieserite superposes polyhydrated sulfates. The polyhydrated sulfates contain outcrops a few hundred meters in diameter of an unidentified mineral phase spectrally consistent with a jarosite-amorphous-silica mixture. A deposition of these deposits in a lake, possibly behind a mountain barrier that once separated Candor and Ophir Chasma, or in a playa-like environment as in Meridiani Planum is conceivable.

The proposed succession of events is very similar to the suggested history of western Candor Chasma, where the bulk of the sulfates in the LTDs is formed by intruding groundwater, and a lesser amount of sulfates is formed by fluvial processes after excavation of the valleys cross-cutting the ILDs by outflow events (Murchie *et al.*, 2009a, Fig. 9). However, in Ophir Chasma, the excavation of the central valley is not necessarily an outflow event, but possibly caused by glaciers. We do not observe convincing evidence for fluvial activity.

6.7 Acknowledgements

The authors like to thank Leah Roach and an anonymous reviewer for their comments, which

greatly helped to improve the manuscript. The study has been funded in part by the German Space Agency (DLR Bonn) grant 50QM301 (HRSC on Mars Express) financed by the German Federal Ministry of Economics and Technology and the Helmholtz Alliance “Planetary Evolution and Life”. L. W. and C. G. thank Giuseppe Marzo for fruitful discussions on the spectral data. P. C. M. would like to acknowledge support from the Alexander-von-Humboldt Foundation and from the CRISM Science Team.

7 Summary and Conclusions

In this thesis, outcrops of phyllosilicate-rich deposits in the Terra Cimmeria/Terra Sirenum region (chapter 4) and sulfate- and ferric oxide-bearing deposits in Juventae Chasma (chapter 5) and Ophir Chasma (chapter 6), both part of Valles Marineris, were investigated in detail based on hyperspectral data from OMEGA and CRISM together with multispectral and panchromatic imagery and topography data. The objective of the studies was to clarify the local morphology, stratigraphy and mineralogy in order to conclude on the processes or environments as well as the relative timing of their formation.

The phyllosilicates in the Terra Cimmeria/Terra Sirenum region are found in the light-toned knobs and in a regional layer mapped as Electris deposit by Grant and Schultz, 1990, Grant *et al.*, 2010. A consistent collection of different erosional states of the Electris deposit from a contiguous layer to a locally dissected layer to individual knobs separated from each other is observed. Therefore, the light-toned mounds in the central parts of the basins are interpreted as remnants of a once contiguous layer of Electris deposit material. Light-toned patches of the same material are exposed from underneath a basaltic cover in the entire region.

A correlation between the local topography and the thickness of the light-toned material is observed: Knobs up to 300 m high are observed only within local basins, whereas in high-standing areas, the same material forms only a thin light-toned cap, which led to the formation of flat mesas and steep cliffs. This distribution suggests that the phyllosilicates (mostly Mg- and Fe-rich smectites, but also montmorillonite and hydrated silica) were formed in situ by aqueous alteration of the primary Electris material, which is interpreted as a fine-grained, possibly loess-like eolian deposit rich in basaltic glass (Grant and Schultz, 1990, Grant *et al.*, 2010). The alteration would have been most effective in local topographic lows, where water ponded, leaving the thickest deposits in these locations behind. The local basins were possibly once connected to form the Eridania lake (Irwin *et al.*, 2004) in the late Noachian.

The knob fields were later covered by the Hesperian ridged plains unit (Hr), modified by deflation, wrinkle ridge formation, Sirenum Fossae faults, and the incision of local valleys sourced from precipitation or melting snow/ice packs in the upper parts of the local basins (Howard and Moore, 2011). Locally, chlorides were deposited in evaporating lakes (Osterloo *et al.*, 2010).

This study thus clarifies five important aspects:

1. The Timing. Our geological mapping indicates a late Noachian age for the light-toned knobs and layers in this area, in disagreement with the stratigraphic placement of Greeley and Guest, 1987, Scott and Tanaka, 1986 and Grant and Schultz, 1990, who interpret them to be younger than the Hesperian ridged plains unit (Hr). The stratigraphic placement is in agreement with the "phyllosian" period of Bibring *et al.*, 2006.

2. The relationship to Ma'adim Vallis. Our mapping suggests that the phyllosilicates formed in local basins, which might once have been connected. Thus, their formation in the Eridania lake or its sub-basins is conceivable.

3. The clay-formation environment. Our mapping of the clay-bearing deposits indicates that in this location, phyllosilicates appear to have formed at the surface or within local basins, but not in the

subsurface, as no thick overlaying deposits are found. This fits to their late Noachian age, as an elevated erosion rate and valley network density due to precipitation and run-off has been observed for this epoch (Hynek *et al.*, 2010).

4. The post-Noachian aqueous history. The study area displays a second generation of fluvial features and local lakes that left chlorides behind (Osterloo *et al.*, 2010), which formed after the knob fields and the ridged plains, as they incise into them. They are evidence for an aqueous history after the Noachian. The valley systems were likely fed by melting local precipitation (Howard and Moore, 2011).

5. No important role of Sirenum Fossae. The study area is dissected by branches of grabens of Sirenum Fossae. The formation of similar grabens elsewhere on Mars has been explained by the intrusion of volcanic dikes underneath them (Wilson and Head, 2002). Neukum *et al.*, 2010, noticed peaks of volcanic and outflow activity in the global Martian record at distinct times, suggesting that the volcanic activity might have played the major role as a drving force for outflow events. In this light, the magmatic dikes assumed underneath Sirenum Fossae could theoretically have provided the heat required to form the aqueous features in this area, but but this appears not to be the case here, as in all basins but the Gorgonum basin, the aqueous events are older than the Sirenum Fossae, and no volcanic features like lava flows are observed in a clear relationship to the grabens.

The study of the light-toned mounds in Juventae Chasma using linear spectral unmixing (chapter 5) mainly aimed on technical details of the unmixing methods. It shows that the four mounds informally known as mound A, B, C and D contain sulfate minerals, which are contaminated by wind-blown basaltic, pyroxene- and sometimes olivine-rich sand. This is in general agreement with Bishop *et al.*, 2009. The upper part of mound B contains polyhydrated sulfates, which are clearly distinguished by the linear unmixing method MELSUM from the underlying monohydrated sulfates szomolnokite ($FeSO_4*1H_2O$) and/or kieserite ($MgSO_4*1H_2O$). The best spectral match for the polyhydrated sulfates are combinations of romerite ($Fe_3(SO_4)_4*12H_2O$) and rozenite ($FeSO_4*4H_2O$) and/or natrojarosite ($NaFe_3(SO_4)_2(OH)_6$) with windblown, pyroxene-rich material. We can therefore exclude the presence of gypsum ($CaSO_4*2H_2O$) proposed by Gendrin *et al.*, 2005b. The exact type of polyhydrated sulfate in mound B is still not determined, because the similarity of the spectra of the polyhydrated sulfate makes a distinction between them difficult even with the method used here.

The study has shown that the linear spectral mixture analysis algorithm MELSUM (Combe *et al.*, 2008b) is capable of modeling spectra from CRISM in a convincing way. The detection of szomolnokite, pyroxenes and olivine correspond to the results found by Bishop *et al.*, 2009 using spectral indices. The study however also shows the vulnerability of this method to a correct calibration, noise removal and atmospheric correction. As the entire spectra are used and not only selected spectral bands, errors or artifacts in the spectra have a high impact on the quality of the result. For example, small absorption bands like the 2.4 µm feature are often missed by the linear unmixing method.

The implications of the presence of mostly szomolnokite as a monohydrated sulfate in all outcrops and possibly rozenite or other iron-bearing sulfates in mound B, as also reported by Bishop *et al.*, 2009 instead of kieserite as in most

other LTD in the Vallis Marineris region (e.g., in Ophir Chasma, chapter 6 of this thesis) are not yet fully understood and require further analysis. The absence of the Ca-bearing mineral gypsum detected by Gendrin *et al.*, 2005b, however, fits much better to the predominantly Fe- and Mg-bearing mafic mineralogy of the putative basaltic source rock of the Martian sulfates. A different, and possibly more fruitful method to decipher the mineralogy of the sulfate deposits is to reconstruct the sulfate formation process in a geochemical reaction computer model such as PHREEQC (Parkhurst and Appelo, 1999). The author of this thesis is co-author in a research project using this approach on the sulfate deposits in Juventae Chasma (Al-Samir *et al.*, 2012).

The study on the sulfate-bearing light-toned deposits in Ophir Chasma shows a remarkable variety of minerals and formation settings, and indicates at least two aqueous events in this area. It confirms and further elaborates upon previous studies by Chojnacki and Hynek, 2008, Gendrin *et al.*, 2005b, Mangold *et al.*, 2007a. Water-related minerals are found mainly in two locations of Ophir Chasma, in the valley informally named "mineral bowl" between Ophir Mensa and the southern chasm wall, and in the central, approximately N-S trending valley.

Although with kieserite, polyhydrated sulfates, ferric oxides and phases with an absorption band at 2.21 µm, consistent with mixtures of jarosite or poorly crystalline phases, the same minerals are observed at the two locations, the deposits are distinct from each other (Chojnacki and Hynek, 2008). The kieserite-bearing material in the "mineral bowl" is found in the bulk material of Ophir Mensa and on the (basaltic) southern wall of the chasm, suggesting that the light-toned deposits of Ophir Mensa once extended further southward across the "mineral bowl" valley. The topographic elevation of the highest sulfate detection varies in the order of several thousand meters, which is not consistent with a formation in an open water body, as it would have left more or less horizontal layers behind. A preferred explanation is that the sulfates formed by post-depositional aqueous alteration of older (sulfate-free) deposits of unknown, possibly eolian origin by groundwater intruding from the sides of the chasm. Hydrological models have shown shown that the canyons of Vallis Marinieris might indeed have been zones of groundwater upwelling, similar to the assumed situation in Meridiani Planum (Murchie *et al.*, 2009a).

On the southern wall of the chasm, kieserite-rich rocks are superposed by H_3O-jarosite, and/or possible jarosite-amorphous-silica mixtures with spectral bands at 2.21 µm or 2.23 µm, polyhydrated sulfates and iron oxides. The layering attitude of these deposits suggests that they discordantly overlie the underlying kieserite, and thus formed at a later time, when the "mineral bowl" valley had already been carved into the deposits of Ophir Mensa. Spectrally similar, discordant sulfate-bearing units have also been observed in western Candor Chasma and Aram Chaos (Lichtenberg *et al.*, 2010, Murchie *et al.*, 2009a). The water source for this second aqueous event is not clear. For Candor Chasma, rills in the slopes of the mounds of light-toned material were regarded as braided river beds, an interpretation that is not shared by the author of this thesis. These "rivers" are taken by Murchie *et al.*, 2009a as evidence for springs relatively high up the slopes of Candor Chasma, which would have supplied the required water. The sulfate deposits investigated in Ophir Chasma are found on local ridges, which would not have been reached by water running down the chasm walls, as it would be confined to local rills. Therefore, meteoric

water in the form of snow, frost or fog might have played a role.

Debris from the LTDs, including iron oxides, are found as lag deposits on the floor of the valley, where they mix with basaltic material (Bibring *et al.*, 2007, Chojnacki and Hynek, 2008, Weitz *et al.*, 2008).

The sulfates in the central valley form a flat deposit at low elevations (<-4250 m), but appear to be stratigraphically higher than Ophir Mensa's LTDs. In this location, kieserite-rich rocks overlay polyhydrated sulfates. The deposits show no internal layering structures, but display a distinct texture of ridges, which can be interpreted as filled joints. The polyhydrated sulfates contain outcrops a few hundred meters in diameter of an unidentified mineral phase spectrally consistent with a jarosite-amorphous-silica mixture.

As these deposits constitute an almost horizontal surface, they might have formed in a lake at a time when Ophir Chasma was a closed basin not yet connected to the central Candor Chasma. A playa-like environment in this area as in Meridiani Planum is conceivable for the origin of these deposits.

The overall picture that arices is that Mars experienced an era when phyllosilicates formed during the Noachian (the "phyllosian"), a sulfate-forming era in the Hesperian ("theiikian) and an era dominated by mostly anhydrous processes ("siderikian") during the Amazonian (Bibring *et al.*, 2006). The phyllosilicates investigated here date to the late Noachian, a time when evidence for the longlasting presence of liquid water on the surface of Mars is ample, suggesting that at this time, the climate of Mars was "warmer and wetter" than at present. This "warmer and wetter" period was comparable to modern day terrestrial conditions in Antarctic dry valleys, where melting of ice temporally occurs in local microenvironments (Fastook *et al.*, 2012). Later aqueous events in the Hesperian and Amazonian left valley networks and chemical sediments such as sulfates and chlorides behind and might have included precipitation and run-off, but these events did not last long enough to form phyllosilicates. What exactly happened at the Noachian-Hesperian boundary still remains elusive. The current mission of the Mars Science Laboratory "Curiosity", which is bound to land in Gale Crater 6. August, 2012 is set to shed light on this enigma, as it will investigate a stratigraphic sequence covering this important boundary.

This thesis has also shown that on a local to regional scale, deciphering the exact depositional environment requires complex studies that combine a multitude of spectral and imagery datasets at all scales.

8 Bibliography

Adams, J. B., 1974. Visible and near-infrared diffuse reflectance spectra of pyroxenes as applied to remote sensing of solid objects in the solar system. J. Geophys. Res. 79, 4829-4836.

Adams, J. B., Gillespie, A. R., 2006. Remote Sensing of Landscapes with Spectral Images - A Physical Model Approach, Cambridge University Press, Cambridge.

Adams, J. B., Gillespie, A. R., Jackson, M. P. A., Montgomery, D. R., Dooley, T. P., Combe, J. P., Schreiber, B. C., 2009. Salt tectonics and collapse of Hebes Chasma, Valles Marineris, Mars. Geology 37, 8, 691-694.

Adams, J. B., Smith, M. O., Johnson, P. E., 1986. Spectral mixture modeling - A new analysis of rock and soil types at the Viking Lander 1 site. J. Geophys. Res. 91, 8098-8112.

Al-Samir, M., van Berk, W., Kneissl, T., van Gasselt, S., Gross, C., Wendt, L., Jaumann, R., 2012. A Model Scenario for Kieserite-Dominated Evaporites in Juventae Chasma, Mars. 43rd Lunar and Planetary Institute Science Conference The Woodlands, TX, USA.

Altheide, T. S., Chevrier, V. F., Noe Dobrea, E., 2010. Mineralogical characterization of acid weathered phyllosilicates with implications for secondary martian deposits. Geochim. Cosmochim. Acta 74, 21, 6232-6248.

Anderson jr, J. H., Wickersheim, K. A., 1964. Near infrared characterization of water and hydroxyl groups on silica surfaces. Surf. Sci. 2, 252-260.

Andrews-Hanna, J. C., Lewis, K. W., 2011. Early Mars hydrology: 2. Hydrological evolution in the Noachian and Hesperian epochs. J. Geophys. Res. 116, E2, E02007.

Andrews-Hanna, J. C., Phillips, R. J., Zuber, M. T., 2007. Meridiani Planum and the global hydrology of Mars. Nature 446, 7132, 163-166.

Andrews-Hanna, J. C., Zuber, M. T., Arvidson, R. E., Wiseman, S. M., 2010. Early Mars hydrology: Meridiani playa deposits and the sedimentary record of Arabia Terra. J. Geophys. Res. 115, E6, E06002.

Annex, A. M., Howard, A. D., 2011. Phyllosilicates Related to Exposed Knobs in Sirenum Fossae, Ariadnes Colles. 42nd Lunar and Planetary Science Conference The Woodlands, TX, USA.

Arvidson, R. E., Seelos, F. P., Deal, K. S., Koeppen, W. C., Snider, N. O., Kieniewicz, J. M., Hynek, B. M., Mellon, M. T., Garvin, J. B., 2003. Mantled and exhumed terrains in Terra Meridiani, Mars. J. Geophys. Res. (Planets) 108, E12, 8073.

Arvidson, R. E., Squyres, S. W., Anderson, R. C., Bell, J. F., III, Blaney, D., Brückner, J., Cabrol, N. A., Calvin, W. M., Carr, M. H., Christensen, P. R., Clark, B. C., Crumpler, L., Des Marais, D. J., de Souza, P. A., Jr., d'Uston, C., Economou, T., Farmer, J., Farrand, W. H., Folkner, W., Golombek, M., Gorevan, S., Grant, J. A., Greeley, R., Grotzinger, J., Guinness, E., Hahn, B. C., Haskin, L., Herkenhoff, K. E., Hurowitz, J. A., Hviid, S., Johnson, J. R., Klingelhöfer, G., Knoll, A. H., Landis, G., Leff, C., Lemmon, M., Li, R., Madsen, M. B., Malin, M. C., McLennan, S. M., McSween, H. Y., Ming, D. W., Moersch, J., Morris, R. V., Parker, T., Rice, J. W., Jr., Richter, L., Rieder, R., Rodionov, D. S., Schröder, C., Sims, M., Smith, M., Smith, P., Soderblom, L. A., Sullivan, R., Thompson, S. D., Tosca, N. J., Wang, A., Wänke, H., Ward, J., Wdowiak, T., Wolff, M., Yen, A., 2006. Overview of the Spirit Mars Exploration Rover Mission to Gusev Crater: Landing site to Backstay Rock in the Columbia Hills. J. Geophys. Res. 111, E2, E02S01.

Asrar, G. (Ed.) 1989, Theory and applications of optical remote sensing. 734, Jon Wiley & Sons, New York, Chichester, Brisbane, Toronto, Singapore.

Baird, A. K., Toulmin, P., III, Rose, H. J., Jr., Christian, R. P., Clark, B. C., Keil, K., Gooding, J. L., 1976. Mineralogic and petrologic implications of Viking geochemical results from Mars - Interim report. Science 194, 1288-1293.

Baker, D. M., Head, J. W., 2009. The Origin of Eridania Lake and Ma'adim Vallis: An Investigation of Closed Chaos Basins, Hesperian Ridged Plains, and Tectonic Constructs on the Floor of a Large Hypothesized Paleolake on Mars. 40th Lunar and Planetary Science Conference, The Woodlands, TX, USA.

Baker, D. M. H., Head, J. W., 2012. Geology and Chronology of the Ma'adim Vallis-Eridania Basin Region, Mars: Implications for the Noachian-Hesperian Hydrologic Cycle. 43rd Lunar and

Planetary Science Conference, The Woodlands, TX, USA.

Baker, V. R., 2001. Water and the martian landscape. Nature 412, 6843, 228-236.

Baker, V. R., Strom, R. G., Gulick, V. C., Kargel, J. S., Komatsu, G., Kale, V. S., 1991. Ancient oceans, ice sheets and the hydrological cycle on Mars. Nature 352, 6336, 589-594.

Bandfield, J. L., 2002. Global mineral distributions on Mars. J. Geophys. Res. 107, E6, 5042.

Bandfield, J. L., 2006. Extended surface exposures of granitoid compositions in Syrtis Major, Mars. Geophys. Res. Lett. 33, 6, L06203.

Bandfield, J. L., Glotch, T. D., Christensen, P. R., 2003. Spectroscopic Identification of Carbonate Minerals in the Martian Dust. Science 301, 1084-1087.

Bandfield, J. L., Hamilton, V. E., Christensen, P. R., 2000. A Global View of Martian Surface Compositions from MGS-TES. Science 287, 1626-1630.

Bandfield, J. L., Hamilton, V. E., Christensen, P. R., McSween, H. Y., 2004. Identification of quartzofeldspathic materials on Mars. J. Geophys. Res. (Planets) 109, 10009.

Banin, A., Han, F. X., Kan, I., Cicelsky, A., 1997. Acidic volatiles and the Mars Soil. J. Geophys. Res. 102, E6, 13341-13356.

Barnhart, C. J., Howard, A. D., Moore, J. M., 2009. Long-term precipitation and late-stage valley network formation: Landform simulations of Parana Basin, Mars. J. Geophys. Res. 114, E1, E01003.

Basilevsky, A. T., Neukum, G., Kneissl, T., Dumke, A., 2009. Geologic Analysis of HRSC Images of the Area East of the Mangala Valles Head Graben, Mars. 40th Lunar and Planetary Science Conference The Woodlands, TX, USA.

Bell, J. F., III, McCord, T. B., Owensby, P. D., 1990. Observational Evidence of Crystalline Iron Oxides on Mars. J. Geophys. Res. 95, B9, 14447-14461.

Bell, J. F., McSween, H. Y., Crisp, J. A., Morris, R. V., Murchie, S. L., Bridges, N. T., Johnson, J. R., Britt, D. T., Golombek, M. P., Moore, H. J., Ghosh, A., Bishop, J. L., Anderson, R. C., Brückner, J., Economou, T., Greenwood, J. P., Gunnlaugsson, H. P., Hargraves, R. M., Hviid, S., Knudsen, J. M., Madsen, M. B., Reid, R., Rieder, R., Soderblom, L., 2000. Mineralogic and compositional properties of Martian soil and dust: Results from Mars Pathfinder. J. Geophys. Res. 105, 1721-1756.

Bell, P. M., Mao, H. K., Rossman, G. R., 1975. Absorption Spectroscopy of ionic and molecular units in crystals and glasses. in: C. Karr, Jr. , (Ed.), Infrared and Raman spectroscopy of lunar and terrestrial materials. Academic Press, New York, 1-38.

Bender Koch, C., Mörup, S., Madsen, M. B., Vistisen, L., 1995. Iron-containing weathering products of basalt in a cold, dry climate. Chem. Geol. 122, 1-4, 109-119.

Berk, A., Bernstein, L. S., Robertson, D. C., 1987, MODTRAN: A moderate resolution model for LOWTRAN. United States Airforce Geophysics Laboratory, Hanscom Air Force Base, 40.

Bibring, J.-P., Langevin, Y., Gendrin, A., Gondet, B., Poulet, F., Berthé, M., Soufflot, A., Arvidson, R., Mangold, N., Mustard, J., Drossart, P., 2005. Mars Surface Diversity as Revealed by the OMEGA/Mars Express Observations. Science 307, 1576-1581.

Bibring, J.-P., Langevin, Y., Mustard, J. F., Poulet, F. o., Arvidson, R., Gendrin, A., Gondet, B., Mangold, N., Pinet, P., Forget, F., 2006. Global Mineralogical and Aqueous Mars History Derived from OMEGA/Mars Express Data. Science 312, 400-404.

Bibring, J. P., Arvidson, R. E., Gendrin, A., Gondet, B., Langevin, Y., Le Mouelic, S., Mangold, N., Morris, R. V., Mustard, J. F., Poulet, F., Quantin, C., Sotin, C., 2007. Coupled Ferric Oxides and Sulfates on the Martian Surface. Science 317, 1206-1210.

Bibring, J. P., Soufflot, A., Berthé, M., Langevin, Y., Gondet, B., Drossart, P., Bouyé, M., Combes, M., Puget, P., Semery, A., Bellucci, G., Formisano, V., Moroz, V., Kottsov, V., Bonello, G., Erard, S., Forni, O., Gendrin, A., Manaud, N., Poulet, F., Poulleau, G., Encrenaz, T., Fouchet, T., Melchiori, R., Altieri, F., Ignatiev, N., Titov, D., Zasova, L., Coradini, A., Capacionni, F., Cerroni, P., Fonti, S., Mangold, N., Pinet, P., Schmitt, B., Sotin, C., Hauber, E., Hoffmann, H., Jaumann, R., Keller, U., Arvidson, R., Mustard, J., Forget, F., 2004, OMEGA: Observatoire pour la Minéralogie, l'Eau, les Glaces et l'Activité. Mars Express: the Scientific Payload, 37-49.

Bishop, J., Madejova, J., Komadel, P., Froschl, H., 2002a. The influence of structural Fe, Al and Mg on the infrared OH bands in

spectra of dioctahedral smectites. Clay Minerals 37, 4, 607-616.

Bishop, J., Murad, E., Dyar, M. D., 2002b. The influence of octahedral and tetrahedral cation substitution on the structure of smectites and serpentines as observed through infrared spectroscopy. Clay Minerals 37, 4, 617-628.

Bishop, J. L., Dobrea, E. Z. N., McKeown, N. K., Parente, M., Ehlmann, B. L., Michalski, J. R., Milliken, R. E., Poulet, F., Swayze, G. A., Mustard, J. F., Murchie, S. L., Bibring, J.-P., 2008a. Phyllosilicate Diversity and Past Aqueous Activity Revealed at Mawrth Vallis, Mars. Science 321, 830-833.

Bishop, J. L., Fröschl, H., Mancinelli, R. L., 1998. Alteration processes in volcanic soils and identification of exobiologically important weathering products on Mars using remote sensing. J. Geophys. Res. 103, E13, 31457-31476.

Bishop, J. L., Lane, M. D., Dyar, M. D., Brown, A. J., 2008b. Reflectance and emission spectroscopy study of four groups of phyllosilicates: smectites, kaolinite-serpentines, chlorites and micas. Clay Minerals 43, 1, 35-54.

Bishop, J. L., Loizeau, D., McKeown, N. K., Saper, L., Dyar, M. D., Des Marais, D., Parente, M., Murchie, S. L., 2012. What the ancient phyllosilicates at Mawrth Vallis can tell us about possible habitability on early Mars. Planet. Space Sci., submitted.

Bishop, J. L., Parente, M., Weitz, C. M., Noe Dobrea, E. Z., Roach, L. H., Murchie, S. L., McGuire, P. C., McKeown, N. K., Rossi, C. M., Brown, A. J., Calvin, W. M., Milliken, R., Mustard, J. F., 2009. Mineralogy of Juventae Chasma: Sulfates in the light-toned mounds, mafic minerals in the bedrock, and hydrated silica and hydroxylated ferric sulfate on the plateau. J. Geophys. Res. (Planets) 114.

Bishop, J. L., Pieters, C. M., Burns, R. G., Edwards, J. O., Mancinelli, R. L., Fröschl, H., 1995. Reflectance Spectroscopy of Ferric Sulfate-Bearing Montmorillonites as Mars Soil Analog Materials. Icarus 117, 1, 101-119.

Blasius, K. R., Cutts, J. A., Guest, J. E., Masursky, H., 1977. Geology of the Valles Marineris - First analysis of imaging from the Viking 1 orbiter primary mission. J. Geophys. Res. 82, 4067-4091.

Boardman, J. W., Kruse, F. A., Green, R. O., 1995, Mapping Target Signatures Via Partial Unmixing of Aviris Data. Fifth JPL Airborne Earth Science Workshop. Jet Propulsion Laboratory, Pasadena, 23-26.

Boynton, W. V., Ming, D. W., Kounaves, S. P., Young, S. M. M., Arvidson, R. E., Hecht, M. H., Hoffman, J., Niles, P. B., Hamara, D. K., Quinn, R. C., Smith, P. H., Sutter, B., Catling, D. C., Morris, R. V., 2009. Evidence for Calcium Carbonate at the Mars Phoenix Landing Site. Science 325, 5936, 61-64.

Brain, D. A., Jakosky, B. M., 1998. Atmospheric loss since the onset of the Martian geologic record: Combined role of impact erosion and sputtering. J. Geophys. Res. 103, E10, 22689-22694.

Bridges, J. C., Catling, D. C., Saxton, J. M., Swindle, T. D., Lyon, I. C., Grady, M. M., 2001. Alteration Assemblages in Martian Meteorites: Implications for Near-Surface Processes. Space Science Reviews 96, 1, 365-392.

Bridges, J. C., Grady, M. M., 2000. Evaporite mineral assemblages in the nakhlite (martian) meteorites. Earth Planet. Sci. Lett. 176, 3-4, 267-279.

Brophy, G. P., Sheridan, M. F., 1965. Sheridan, Sulfate studies IV: The jarosite-natrojarosite-hydronium jarosite solid solution series. Am. Mineral. 50, 1595-1607.

Brown, A. J., Hook, S. J., Baldridge, A. M., Crowley, J. K., Bridges, N. T., Thomson, B. J., Marion, G. M., de Souza Filho, C. R., Bishop, J. L., 2010. Hydrothermal formation of Clay-Carbonate alteration assemblages in the Nili Fossae region of Mars. Earth Planet. Sci. Lett. 297, 174-182.

Burns, R. G., 1970. Mineralogical Applications of Crystal Field Theory, Univ. Cambridge Press, Cambridge.

Burns, R. G., 1987. Ferric sulfates on Mars. J. Geophys. Res. 92, E570-E574.

Burns, R. G., 1993. Origin of electronic spectra of minerals in the visible to near-infrared region. in: C. M. Pieters, P. A. J. Englert, (Eds.), Remote Geochemical Analysis: Elemental and Mineralogical Composition. Cambridge University Press, New York, 3-29.

Burns, R. G., Abu-Eid, R. M., Huggins, F. E., Trombka, J. I., Peterson, L. E., Reedy, R. C., Arnold, J. R., 1972, Crystal field spectra of lunar pyroxenes. Lunar and Planetary Science Conference Proceedings.

Burns, R. G., Fisher, D. S., 1990a. Evolution of sulfide mineralization on Mars. J. Geophys. Res. 95, 14169-14173.

Burns, R. G., Fisher, D. S., 1990b. Iron-sulfur mineralogy of Mars - Magmatic evolution and chemical weathering products. J. Geophys. Res. 95, 14415-14421.

Cabrol, N. A., Grin, E. A., Landheim, R., Kuzmin, R. O., Greeley, R., 1998. Duration of the Ma'adim Vallis/Gusev Crater Hydrogeologic System, Mars. Icarus 133, 1, 98-108.

Cabrol, N. A., Grin, E. A., Newsom, H. E., Landheim, R., McKay, C. P., 1999. Hydrogeologic Evolution of Gale Crater and Its Relevance to the Exobiological Exploration of Mars. Icarus 139, 2, 235-245.

Capitan, R. D., Van De Wiel, M., 2010. Landform hierarchy and evolution in Gorgonum and Atlantis basins, Mars. Icarus 211, 1, 366-388.

Carr, M. H., 1983. Stability of streams and lakes on Mars. Icarus 56, 3, 476-495.

Carr, M. H., 1995. The Martain drainage system and the origin of valley networks and fretted channels. J. Geophys. Res. 100, E4, 7497-7507.

Carr, M. H., 1999. Retention of an atmosphere on early Mars. J. Geophys. Res. 104, E9, 21897-21909.

Carr, M. H., 2006. The Surface of Mars, Cambridge University Press, Cambridge, New York, Melbourne, Madrid, Cape Town, Singapore, Sao Paulo.

Carr, M. H., Masursky, H., Baum, W. A., Blasius, K. R., Briggs, G. A., Cutts, J. A., Duxbury, T., Greeley, R., Guest, J. E., Smith, B. A., Soderblom, L. A., Veverka, J., Wellman, J. B., 1976. Preliminary Results from the Viking Orbiter Imaging Experiment. Science 193, 4255, 766-776.

Carter, J., Poulet, F., Bibring, J. P., Murchie, S., 2010. Detection of Hydrated Silicates in Crustal Outcrops in the Northern Plains of Mars. Science 328, 1682-1686

Catling, D. C., 1999. A chemical model for evaporites on early Mars: Possible sedimentary tracers of the early climate and implications for exploration. J. Geophys. Res. 104, 16453-16470.

Catling, D. C., Moore, J. M., 2003. The nature of coarse-grained crystalline hematite and its implications for the early environment of Mars. Icarus 165, 2, 277-300.

Catling, D. C., Wood, S. E., Leovy, C., Montgomery, D. R., Greenberg, H. M., Glein, C. R., Moore, J. M., 2006. Light-toned layered deposits in Juventae Chasma, Mars. Icarus 181, 1, 26-51.

Chapman, C. R., Cohen, B. A., Grinspoon, D. H., 2007. What are the real constraints on the existence and magnitude of the late heavy bombardment? Icarus 189, 1, 233-245.

Chapman, M. G., Gudmundsson, M. T., Russell, A. J., Hare, T. M., 2003. Possible Juventae Chasma subice volcanic eruptions and Maja Valles ice outburst floods on Mars: Implications of Mars Global Surveyor crater densities, geomorphology, and topography. J. Geophys. Res. 108, E10, 2-1.

Chapman, M. G., Smellie, J. L., 2007. Mars Interior layered deposits and terrestrial sub-ice volcanoes compared: observations and interpretations of similar geomorphic characteristics. in: M. G. Chapman, (Ed.), The Geology of Mars. Cambridge University Press, Cambridge, 178-210.

Chapman, M. G., Tanaka, K. L., 2001. Interior trough deposits on Mars: Subice volcanoes? J. Geophys. Res. 106, E5, 10087-10100.

Chapman, M. G., Tanaka, K. L., 2002. Related Magma-Ice Interactions: Possible Origins of Chasmata, Chaos, and Surface Materials in Xanthe, Margaritifer, and Meridiani Terrae, Mars. Icarus 155, 324-339.

Chevrier, V., Mathé, P. E., 2007. Mineralogy and evolution of the surface of Mars: A review. Planet. Space Sci. 55, 289-314.

Chevrier, V., Poulet, F., Bibring, J.-P., 2007. Early geochemical environment of Mars as determined from thermodynamics of phyllosilicates. Nature 448, 60-63.

Chicarro, A., Martin, P., Trautner, R., 2004. The Mars Express Mission: An Overview. ESA Special Publication 1240, 3-13.

Chojnacki, M., Hynek, B. M., 2008. Geological context of water-altered minerals in Valles Marineris, Mars. J. Geophys. Res. (Planets) 113, E12, 12005.

Chojnacki, M., Jakosky, B. M., Hynek, B. M., 2006. Surficial properties of landslides and surrounding units in Ophir Chasma, Mars. J. Geophys. Res. (Planets) 111, E4, 04005.

Christensen, P. R., 2003. Formation of recent martian gullies through melting of extensive water-rich snow deposits. Nature 422, 6927, 45-48.

Christensen, P. R., Anderson, D. L., Chase, S. C., Clancy, R. T., Clark, R. N., Conrath, B. J., Kieffer, H. H., Kuzmin, R. O., Malin, M. C., Pearl, J. C., Roush, T. L., Smith,

M. D., 1998. Results from the Mars Global Surveyor Thermal Emission Spectrometer. Science 279, 5357, 1692-1698.

Christensen, P. R., Anderson, D. L., Chase, S. C., Clark, R. N., Kieffer, H. H., Malin, M. C., Pearl, J. C., Carpenter, J., Bandiera, N., Brown, F. G., 1992. Thermal emission spectrometer experiment - Mars Observer mission. J. Geophys. Res. 97, E5, 7719-7734.

Christensen, P. R., Bandfield, J. L., Clark, R. N., Edgett, K. S., Hamilton, V. E., Hoefen, T., Kieffer, H. H., Kuzmin, R. O., Lane, M. D., Malin, M. C., Morris, R. V., Pearl, J. C., Pearson, R., Roush, T. L., Ruff, S. W., Smith, M. D., 2000. Detection of crystalline hematite mineralization on Mars by the Thermal Emission Spectrometer: Evidence for near-surface water. J. Geophys. Res. 105, 9623-9642.

Christensen, P. R., Bandfield, J. L., Hamilton, V. E., Ruff, S. W., Kieffer, H. H., Titus, T. N., Malin, M. C., Morris, R. V., Lane, M. D., Clark, R. L., Jakosky, B. M., Mellon, M. T., Pearl, J. C., Conrath, B. J., Smith, M. D., Clancy, R. T., Kuzmin, R. O., Roush, T., Mehall, G. L., Gorelick, N., Bender, K., Murray, K., Dason, S., Greene, E., Silverman, S., Greenfield, M., 2001a. Mars Global Surveyor Thermal Emission Spectrometer experiment: Investigation description and surface science results. J. Geophys. Res. 106, 23823-23872.

Christensen, P. R., Jakosky, B. M., Kieffer, H. H., Malin, M. C., McSween, H. Y., Jr., Nealson, K., Mehall, G. L., Silverman, S. H., Ferry, S., Caplinger, M., Ravine, M., 2004a. The Thermal Emission Imaging System (THEMIS) for the Mars 2001 Odyssey Mission. Space Science Reviews 110, 85-130.

Christensen, P. R., Kieffer, H. H., 2003. Water on Mars: Evidence from Minerals and Morphology. Sixth International Conference on Mars, Pasadena, CA, USA.

Christensen, P. R., Morris, R. V., Lane, M. D., Bandfield, J. L., Malin, M. C., 2001b. Global mapping of Martian hematite mineral deposits: Remnants of water-driven processes on early Mars. J. Geophys. Res. 106, 23873-23886.

Christensen, P. R., Ruff, S. W., 2004. Formation of the hematite-bearing unit in Meridiani Planum: Evidence for deposition in standing water. J. Geophys. Res. 109, E8, E08003.

Christensen, P. R., Wyatt, M. B., Glotch, T. D., Rogers, A. D., Anwar, S., Arvidson, R. E., Bandfield, J. L., Blaney, D. L., Budney, C., Calvin, W. M., Fallacaro, A., Fergason, R. L., Gorelick, N., Graff, T. G., Hamilton, V. E., Hayes, A. G., Johnson, J. R., Knudson, A. T., McSween, H. Y., Mehall, G. L., Mehall, L. K., Moersch, J. E., Morris, R. V., Smith, M. D., Squyres, S. W., Ruff, S. W., Wolff, M. J., 2004b. Mineralogy at Meridiani Planum from the Mini-TES Experiment on the Opportunity Rover. Science 306, 1733-1739.

Clark, B. C., Castro, A. J., Rowe, C. D., Baird, A. K., Evans, P. H., Rose, H. J., Jr., Toulmin, P., III, Keil, K., Kelliher, W. C., 1976. Inorganic analyses of Martian surface samples at the Viking landing sites. Science 194, 1283-1288.

Clark, R., Swayze, G., Wise, R., Livo, K. E., Hoefen, T., Kokaly, R. F., Sutley, S. J., 2007, USGS digital spectral library splib06a, Digital Data Series 231. US Geological Survey.

Clark, R. N., 1999. Spectroscopy of rocks and minerals, and principles of spectroscopy in: A. N. Rencz, (Ed.), Remote Sensing for the Earth Sciences: Manual of Remote Sensing, 3rd edn. J. Wiley & Sons. , New York, 3-58.

Clark, R. N., King, T. V. V., Gorelick, N. S., 1987, Automatic continuum analysis of reflectance spectra. Third Airborne Imaging Spectrometer Data Analysis Workshop. JPL Publication, 138-142.

Clark, R. N., King, T. V. V., Klejwa, M., Swayze, G. A., Vergo, N., 1990. High spectral resolution reflectance spectroscopy of minerals. J. Geophys. Res. 95, 12653-12680.

Clark, R. N., Swayze, G. A., Livo, K. E., Kokaly, R. F., Sutley, S. J., Dalton, J. B., McDougal, R. R., Gent, C. A., 2003. Imaging spectroscopy: Earth and planetary remote sensing with the USGS Tetracorder and expert systems. J. Geophys. Res. 108, E12, 5131.

Cloutis, E. A., Gaffey, M. J., 1991. Pyroxene spectroscopy revisited - Spectral-compositional correlations and relationship to geothermometry. J. Geophys. Res. 96, 22809-22826.

Cloutis, E. A., Hawthorne, F. C., Mertzman, S. A., Krenn, K., Craig, M. A., Marcino, D., Methot, M., Strong, J., Mustard, J. F., Blaney, D. L., Bell, J. F., Vilas, F., 2006. Detection and discrimination of sulfate minerals using reflectance spectroscopy. Icarus 184, 121-157.

Cohen, B. A., Swindle, T. D., Kring, D. A., 2000. Support for the Lunar Cataclysm Hypothesis from Lunar Meteorite Impact Melt Ages. Science 290, 5497, 1754-1756.

Combe, J. P., 2005. Études des surfaces planétaires par télédétection visible-infrarouge hyperspectrale. 299, Université de Nantes, Nantes.

Combe, J. P., Le Mouélic, S., Kramer, G. Y., McCord, T. B., 2008a. Mapping of the Mineralogy of the Moon with Clementine UVVIS and NIR Data Analyzed by a Multiple-Endmember Linear Spectral Unmixing Model (MELSUM). 39th Lunar and Planetary Science Conference League City, TX, USA.

Combe, J. P., Le Mouélic, S., Sotin, C., Gendrin, A., Mustard, J. F., Le Deit, L., Launeau, P., Bibring, J. P., Gondet, B., Langevin, Y., Pinet, P., 2008b. Analysis of OMEGA/Mars Express data hyperspectral data using a Multiple-Endmember Linear Spectral Unmixing Model (MELSUM): Methodology and first results. Planet. Space Sci. 56, 7, 951-975.

Connerney, J. E. P., Acuña, M. H., Wasilewski, P. J., Ness, N. F., Rème, H., Mazelle, C., Vignes, D., Lin, R. P., Mitchell, D. L., Cloutier, P. A., 1999. Magnetic Lineations in the Ancient Crust of Mars. Science 284, 5415, 794-798.

Cooke, M., Islam, F., McGill, G., 2011. Basement controls on the scale of giant polygons in Utopia Planitia, Mars. J. Geophys. Res. 116, E9, E09003, 10.1029/2011JE003812.

Cord, A. l., Baratoux, D., Mangold, N., Martin, P., Pinet, P., Greeley, R., Costard, F., Masson, P., Foing, B., Neukum, G., 2007. Surface roughness and geological mapping at subhectometer scale from the High Resolution Stereo Camera onboard Mars Express. Icarus 191, 1, 38-51.

Costard, F., Forget, F., Mangold, N., Peulvast, J. P., 2002. Formation of Recent Martian Debris Flows by Melting of Near-Surface Ground Ice at High Obliquity. Science 295, 5552, 110-113.

Crisp, J. A., Adler, M., Matijevic, J. R., Squyres, S. W., Arvidson, R. E., Kass, D. M., 2003. Mars Exploration Rover mission. J. Geophys. Res. (Planets) 108, 8061.

Davila, A. F., Gross, C., Marzo, G. A., Fairén, A. G., Kneissl, T., McKay, C. P., Dohm, J. M., 2011. A large sedimentary basin in the Terra Sirenum region of the southern highlands of Mars. Icarus 212, 2, 579-589.

de Pablo, M. A., Fairén, A. G., 2004. Atlantis basin, Sirenum Terrae, Mars: geological setting and astrobiological implications. International Journal of Astrobiology 3, 03, 257-263.

de Pablo, M. A., Márquez, A., Stansbery, E., 2004. A Possible Dike System on Atlantis Basin Regin, Sirenum Terrae, Mars. 35th Lunar and Planetary Science Conference League City, TX, USA.

Delamere, A. W., Becker, I., Begstrom, J., Burkepile, J., Day, J. D., Dorn, D., Gallagher, D., Hamp, C., Lasco, J., Beies, B., Sievers, A., Streetman, S., Tarr, S., Tommeraasen, M., Volmer, P., 2003. MRO High Resolution Imaging Science Experiment (HiRISE): Instrument development. Sixth International Conference on Mars, Houston, TX. USA.

Dumke, A., Spiegel, M., van Gasselt, S., Neu, D., Neukum, G., 2010. Systematic Processing of High-Resolution Digital Terrain Model Quadrangles on the Basis of Mars-Express HRSC Data. 41st Lunar and Planetary Science Conference, The Woodlands, TX, USA.

Dyar, M. D., Gunter, M. E., D., T., 2007. Mineralogy and Optical Mineralogy, Mineralogical Society of America, Chantilly, Virginia, USA

Ehlmann, B. L., Mustard, J. F., Bishop, J. L., Swayze, G., Roach, L. H., Clark, R. N., Milliken, R. E., Poulet, F., Murchie, S. L., Mro Crism, T., 2008a. Distinct Provinces of Aqueous Alteration in the Western Isidis Region Identified with MRO-CRISM. 39th Lunar and Planetary Science Conference League City, TX, USA.

Ehlmann, B. L., Mustard, J. F., Fassett, C. I., Schon, S. C., Head Iii, J. W., Des Marais, D. J., Grant, J. A., Murchie, S. L., 2008b. Clay minerals in delta deposits and organic preservation potential on Mars. Nature Geosci 1, 6, 355-358.

Ehlmann, B. L., Mustard, J. F., Murchie, S. L., Bibring, J.-P., Meunier, A., Fraeman, A. A., Langevin, Y., 2011. Subsurface water and clay mineral formation during the early history of Mars. Nature 479, 7371, 53-60.

Ehlmann, B. L., Mustard, J. F., Murchie, S. L., Poulet, F., Bishop, J. L., Brown, A. J., Calvin, W. M., Clark, R. N., Des Marais, D. J., Milliken, R. E., Roach, L. H., Roush, T. L., Swayze, G. A., Wray, J. J., 2008c. Orbital Identification of

Carbonate-Bearing Rocks on Mars. Science 322, 5909, 1828-1832.

Ehlmann, B. L., Mustard, J. F., Swayze, G. A., Clark, R. N., Bishop, J. L., Poulet, F., Des Marais, D. J., Roach, L. H., Milliken, R. E., Wray, J. J., Barnouin-Jha, O., Murchie, S. L., 2009. Identification of hydrated silicate minerals on Mars using MRO-CRISM: Geologic context near Nili Fossae and implications for aqueous alteration. J. Geophys. Res. (Planets) 114.

Erard, S., 1998. A Spectrophotometric Model of Mars in the Near-Infrared. 29th Lunar and Planetary Science Conference, Houston, TX, USA.

Erard, S., Calvin, W., 1997. New Composite Spectra of Mars, 0.4-5.7 µm. Icarus 130, 2, 449-460.

Fairbairn, M. B., 2005. Planetary Photometry: The Lommel-Seeliger Law. Journal of the Royal Astronomical Society of Canada 99, 3, 92-93.

Fairén, A. G., 2010. A cold and wet Mars. Icarus 208, 1, 165-175.

Fairen, A. G., Fernandez-Remolar, D., Dohm, J. M., Baker, V. R., Amils, R., 2004. Inhibition of carbonate synthesis in acidic oceans on early Mars. Nature 431, 7007, 423-426.

Fassett, C. I., Head III, J. W., 2007. Valley formation on martian volcanoes in the Hesperian: Evidence for melting of summit snowpack, caldera lake formation, drainage and erosion on Ceraunius Tholus. Icarus 189, 1, 118-135.

Fassett, C. I., Head, J. W., 2008. Valley network-fed, open-basin lakes on Mars: Distribution and implications for Noachian surface and subsurface hydrology. Icarus 198, 1, 37-56.

Fassett, C. I., Head, J. W., III, 2005. Fluvial sedimentary deposits on Mars: Ancient deltas in a crater lake in the Nili Fossae region. Geophys. Res. Lett. 32, 14, L14201.

Fastook, J. L., Head, J. W., Marchant, D. R., Forget, F., Madeleine, J.-B., 2012. Early Mars climate near the Noachian-Hesperian boundary: Independent evidence for cold conditions from basal melting of the south polar ice sheet (Dorsa Argentea Formation) and implications for valley network formation. Icarus 219, 1, 25-40.

Fernández-Remolar, D. C., Morris, R. V., Gruener, J. E., Amils, R., Knoll, A. H., 2005. The Río Tinto Basin, Spain: Mineralogy, sedimentary geobiology, and implications for interpretation of outcrop rocks at Meridiani Planum, Mars. Earth Planet. Sci. Lett. 240, 1, 149-167.

Flinn, E. A., Reid, G. C., Csanady, G., 1977. Scientific results of the Viking Project, American Geophysical Union, Washington, DC, USA

Gaffey, S. J., 1987. Spectral reflectance of carbonate minerals in the visible and near infrared (0.35-2.55 um): Anhydrous carbonate minerals. J. Geophys. Res. 92, 1429-1440.

Gellert, R., Rieder, R., Anderson, R. C., Brückner, J., Clark, B. C., Dreibus, G., Economou, T., Klingelhöfer, G., Lugmair, G. W., Ming, D. W., Squyres, S. W., d'Uston, C., Wänke, H., Yen, A., Zipfel, J., 2004. Chemistry of Rocks and Soils in Gusev Crater from the Alpha Particle X-ray Spectrometer. Science 305, 5685, 829-832.

Gendrin, A., Bibring, J.-P., Mustard, J. F., Mangold, N., Quantin, C., Gondet, B., Langevin, Y., Poulet, F., Sotin, C., Le Mouélic, S., Combe, J.-P., Hutchison, L., Team, T. O., 2005a. Identification of Predominant Ferric Signatures in Association to the Martian Sulfate Deposits. 36th Lunar and Planetary Science Conference, League City, TX, USA.

Gendrin, A., Mangold, N., Bibring, J.-P., Langevin, Y., Gondet, B., Poulet, F., Bonello, G., Quantin, C., Mustard, J., Arvidson, R., LeMouélic, S., 2005b. Sulfates in Martian Layered Terrains: The OMEGA/Mars Express View. Science 307, 5715, 1587-1591.

Gilmore, M. S., Phillips, E. L., 2002. Role of aquicludes in formation of Martian gullies. Geology 30, 12, 1107-1110.

Gilmore, M. S., Thompson, D. R., Anderson, L. J., Karamzadeh, N., Mandrake, L., Castaño, R., 2011. Superpixel segmentation for analysis of hyperspectral data sets, with application to Compact Reconnaissance Imaging Spectrometer for Mars data, Moon Mineralogy Mapper data, and Ariadnes Chaos, Mars. J. Geophys. Res. 116, E7, E07001.

Glotch, T. D., Bandfield, J. L., Tornabene, L. L., Jensen, H. B., Seelos, F. P., 2010. Distribution and formation of chlorides and phyllosilicates in Terra Sirenum, Mars. Geophys. Res. Lett. 37, 16, L16202.

Glotch, T. D., Rogers, A. D., 2007. Evidence for aqueous deposition of hematite- and

sulfate-rich light-toned layered deposits in Aureum and Iani Chaos, Mars. J. Geophys. Res. (Planets) 112, E6, 06001.

Golder, K. B., Gilmore, M. S., 2012a. Evolution of Chaos Terrain in the Eridania Basin, Mars. 43rd Lunar and Planetary Science Conference, The Woodlands, TX, USA

Golder, K. B., Gilmore, M. S., 2012b. Geomorphological Mapping of Eastern Eridania Basin and Associated Subbasins, Mars. Lunar and Planetary Science Conference, The Woodlands, TX, USA.

Golombek, M. P., Cook, R. A., Economou, T., Folkner, W. M., Haldemann, A. F. C., Kallemeyn, P. H., Knudsen, J. M., Manning, R. M., Moore, H. J., Parker, T. J., Rieder, R., Schofield, J. T., Smith, P. H., Vaughan, R. M., 1997. Overview of the Mars Pathfinder Mission and Assessment of Landing Site Predictions. Science 278, 5344, 1743-1748.

Golombek, M. P., Grant, J. A., Parker, T. J., Kass, D. M., Crisp, J. A., Squyres, S. W., Haldemann, A. F. C., Adler, M., Lee, W. J., Bridges, N. T., Arvidson, R. E., Carr, M. H., Kirk, R. L., Knocke, P. C., Roncoli, R. B., Weitz, C. M., Schofield, J. T., Zurek, R. W., Christensen, P. R., Fergason, R. L., Anderson, F. S., Rice, J. W., 2003. Selection of the Mars Exploration Rover landing sites. J. Geophys. Res. (Planets) 108, 8072.

Gooding, J. L., 1978. Chemical weathering on Mars thermodynamic stabilities of primary minerals (and their alteration products) from mafic igneous rocks. Icarus 33, 3, 483-513.

Gough, D. O., 1981. Solar interior structure and luminosity variations. Sol. Phys. 74, 21-34.

Grant, J. A., Golombek, M. P., Grotzinger, J. P., Wilson, S. A., Watkins, M. M., Vasavada, A. R., Griffes, J. L., Parker, T. J., 2011. The science process for selecting the landing site for the 2011 Mars Science Laboratory. Planet. Space Sci. 59, 11-12, 1114-1127.

Grant, J. A., Irwin, R. P., III, Grotzinger, J. P., Milliken, R. E., Tornabene, L. L., McEwen, A. S., Weitz, C. M., Squyres, S. W., Glotch, T. D., Thomson, B. J., 2008. HiRISE imaging of impact megabreccia and sub-meter aqueous strata in Holden Crater, Mars. Geology 36, 3, 195-198.

Grant, J. A., Schultz, P. H., 1990. Gradational epochs on Mars - Evidence from west-northwest of Isidis Basin and Electris. Icarus 84, 166-195.

Grant, J. A., Wilson, S. A., Noe Dobrea, E., Fergason, R. L., Griffes, J. L., Moore, J. M., Howard, A. D., 2010. HiRISE views enigmatic deposits in the Sirenum Fossae region of Mars. Icarus 205, 1, 53-63.

Greeley, R., Guest, J. E., 1987. Geological Map of the eastern equatorial region of Mars I-1802-B. U.S. Geological Survey, Flagstaff, AZ, USA.

Green, A. A., Berman, M., Switzer, P., Craig, M. D., 1988. A transformation for ordering multispectral data in terms of image quality with implications for noise removal. IEEE Transactions on Geoscience and Remote Sensing 26, 65-74.

Gross, C., Wendt, L., Combe, J. P., Jodlowski, P., Marzo, G. A., Roush, T. L., McCord, T., Halbach, P., Neukum, G., 2011. Investigation on a Pyllosilicate-Bearing Crater in the Northern Plains of Mars. Lunar Planet. Sci.,

Grotzinger, J., Milliken, R., 2011. The Sedimentary Rock Record of Mars: Distribution, Origins, and Global Stratigraphy. in: J. Grotzinger, R. Milliken, (Eds.), Sedimentary Geology of Mars. SEPM

Grotzinger, J. P., Arvidson, R. E., Bell III, J. F., Calvin, W., Clark, B. C., Fike, D. A., Golombek, M., Greeley, R., Haldemann, A., Herkenhoff, K. E., Jolliff, B. L., Knoll, A. H., Malin, M., McLennan, S. M., Parker, T., Soderblom, L., Sohl-Dickstein, J. N., Squyres, S. W., Tosca, N. J., Watters, W. A., 2005. Stratigraphy and sedimentology of a dry to wet eolian depositional system, Burns formation, Meridiani Planum, Mars. Earth Planet. Sci. Lett. 240, 1, 11-72.

Gwinner, K., Hauber, E., Jaumann, R., Neukum, G., 2000. High-resolution, digital photogrammetric mapping: A tool for Earth science. EOS Transactions 81, 513-513.

Gwinner, K., Scholten, F., Preusker, F., Elgner, S., Roatsch, T., Spiegel, M., Schmidt, R., Oberst, J., Jaumann, R., Heipke, C., 2009. Topography of Mars from global mapping by HRSC high-resolution digital terrain models and orthoimages: Characteristics and performance. Earth Planet. Sci. Lett. 294, 3-4, 506-519.

Haberle, R. M., 1998. Early Mars Climate Models. J. Geophys. Res. 103, E12, 28467-28479.

Halevy, I., Schrag, D. P., 2009. Sulfur dioxide inhibits calcium carbonate precipitation: Implications for early Mars and Earth. Geophys. Res. Lett. 36, 23201.

Halevy, I., Zuber, M. T., Schrag, D. P., 2007. A Sulfur Dioxide Climate Feedback on Early Mars. Science 318, 5858, 1903-1907.

Hamilton, V. E., Christensen, P. R., 2005. Evidence for extensive, olivine-rich bedrock on Mars. Geology 33, 433-436.

Hamilton, V. E., Christensen, P. R., McSween, H. Y., Jr., Bandfield, J. L., 2003. Searching for the source regions of martian meteorites using MGS TES: Integrating martian meteorites into the global distribution of igneous materials on Mars. Meteoritics and Planetary Science 38, 871-885.

Hamilton, V. E., Wyatt, M. B., McSween, H. Y., Jr., Christensen, P. R., 2001. Analysis of terrestrial and Martian volcanic compositions using thermal emission spectroscopy 2. Application to Martian surface spectra from the Mars Global Surveyor Thermal Emission Spectrometer. J. Geophys. Res. 106, E7, 14733-14746.

Hapke, B., 1981. Bidirectional reflectance spectroscopy 1: Theory. J. Geophys. Res. 84, 4571-4586.

Hapke, B., 1993. Theory of Reflectance and Emittance Spectroscopy, Cambridge University Press, Cambridge, New York, Melbourne, Madrid, Cape Town

Harrison, K. P., Chapman, M. G., 2008. Evidence for ponding and catastrophic floods in central Valles Marineris, Mars. Icarus 198, 351-364.

Hartmann, W. K., 1975. Lunar "cataclysm": A misconception? Icarus 24, 2, 181-187.

Hartmann, W. K., 2003. Megaregolith evolution and cratering cataclysm models—Lunar cataclysm as a misconception (28 years later). Meteoritics & Planetary Science 38, 4, 579-593.

Hartmann, W. K., Neukum, G., 2001. Cratering chronology and the evolution of Mars. Space Science Reviews 96, 1, 165-194.

Hartmann, W. K., Quantin, C., Mangold, N., 2007. Possible long-term decline in impact rates: 2. Lunar impact-melt data regarding impact history. Icarus 186, 1, 11-23.

Hawthorne, F. C., Krivovichev, S. V., Burns, P. C., 2000. The crystal chemistry of sulfate minerals. in: C. N. Alpers, *et al.*, (Eds.), Sulfate Minerals: Crystallography, Geochemistry, and Environmental Significance. Mineralogical Society of America, Washington, DC, 1-112.

Head, J. W., Greeley, R., Golombek, M. P., Hartmann, W. K., Hauber, E., Jaumann, R., Masson, P., Neukum, G., Nyquist, L. E., Carr, M. H., 2001. Geological Processes and Evolution. Space Science Reviews 96, 1, 263-292.

Head, J. W., Mustard, J. F., Kreslavsky, M. A., Milliken, R. E., Marchant, D. R., 2003. Recent ice ages on Mars. Nature 426, 6968, 797-802.

Head, J. W., Neukum, G., Jaumann, R., Hiesinger, H., Hauber, E., Carr, M., Masson, P., Foing, B., Hoffmann, H., Kreslavsky, M., Werner, S., Milkovich, S., van Gasselt, S., HRSC Co-Investigator Team, 2005. Tropical to mid-latitude snow and ice accumulation, flow and glaciation on Mars. Nature 434, 7031, 346-351.

Hecht, M. H., Kounaves, S. P., Quinn, R. C., West, S. J., Young, S. M. M., Ming, D. W., Catling, D. C., Clark, B. C., Boynton, W. V., Hoffman, J., DeFlores, L. P., Gospodinova, K., Kapit, J., Smith, P. H., 2009. Detection of Perchlorate and the Soluble Chemistry of Martian Soil at the Phoenix Lander Site. Science 325, 5936, 64-67.

Hiesinger, H., Head, J. W., III, 2000. Characteristics and origin of polygonal terrain in southern Utopia Planitia, Mars: Results from Mars Orbiter Laser Altimeter and Mars Orbiter Camera data. J. Geophys. Res. 105, E5, 11999-12022, 10.1029/1999JE001193.

Hoefen, T. M., Clark, R. N., Bandfield, J. L., Smith, M. D., Pearl, J. C., Christensen, P. R., 2003. Discovery of Olivine in the Nili Fossae Region of Mars. Science 302, 627-630.

Hoffman, N., 2000. Ideas About the Surface Runoff Features on Mars. Science 290, 5492, 711-714.

Hoffman, N., 2002. Active Polar Gullies on Mars and the Role of Carbon Dioxide. Astrobiology 2, 3, 313-323.

Höller, H., 1967. Experimentelle Bildung von Alunit-Jarosit durch die Einwirkung von Schwefelsäure auf Mineralien und Gesteine. Contrib. Mineral. Petrol. 15, 4, 309-329.

Holt, J. W., Safaeinili, A., Plaut, J. J., Head, J. W., Phillips, R. J., Seu, R., Kempf, S. D., Choudhary, P., Young, D. A., Putzig, N. E., Biccari, D., Gim, Y., 2008. Radar Sounding Evidence for Buried Glaciers in the Southern Mid-Latitudes of Mars. Science 322, 5905, 1235-1238.

Horgan, B. H., Bell, J. F., Noe Dobrea, E. Z., Cloutis, E. A., Bailey, D. T., Craig, M. A., Roach, L. H., Mustard, J. F., 2009. Distribution of hydrated minerals in the

north polar region of Mars. J. Geophys. Res. (Planets) 114, 01005.

Howard, A. D., Moore, J. M., 2004. Scarp-bounded benches in Gorgonum Chaos, Mars: Formed beneath an ice-covered lake? Geophys. Res. Lett. 31, 1, L01702, 10.1029/2003GL018925

Howard, A. D., Moore, J. M., 2011. Late Hesperian to early Amazonian midlatitude Martian valleys: Evidence from Newton and Gorgonum basins. J. Geophys. Res. 116, E5, E05003, 10.1029/2010JE003782

Howard, A. D., Moore, J. M., Irwin, R. P., III, 2005. An intense terminal epoch of widespread fluvial activity on early Mars: 1. Valley network incision and associated deposits. J. Geophys. Res. 110, E12, E12S14.

Hunt, G. R., 1977. Spectral Signatures of Particulate Minerals in the Visible and Near Infrared. Geophysics 42, 3, 501-513.

Hunt, G. R., Salisbury, J. W., 1971. Visible and near infrared spectra of minerals and rocks. II. Carbonates. Modern Geology 2, 23-30.

Hunt, G. R., Salisbury, J. W., Lenhoff, C. J., 1971. Visible and near infrared spectra of minerals and rocks. III. Oxides and hydroxides. Modern Geology 2, 195-205.

Hynek, B. M., Beach, M., Hoke, M. R. T., 2010. Updated global map of Martian valley networks and implications for climate and hydrologic processes. J. Geophys. Res. 115, E9, E09008.

Irwin, R. P., III, Howard, A. D., Craddock, R. A., Moore, J. M., 2005. An intense terminal epoch of widespread fluvial activity on early Mars: 2. Increased runoff and paleolake development. J. Geophys. Res. 110, E12, E12S15.

Irwin, R. P., III, Howard, A. D., Maxwell, T. A., 2004. Geomorphology of Ma'adim Vallis, Mars, and associated paleolake basins. J. Geophys. Res. 109, E12, E12009, 10.1029/2004JE002287.

Ivanov, B. A., 2001. Mars/Moon Cratering Rate Ratio Estimates. Space Science Reviews 96, 1, 87-104.

Jaumann, R., 1989, Spectrophotometrische Analyse der chemisch-mineralogischen Zusammensetzung lunarer Oberflächenmaterialien. DLR, Oberpfaffenhofen, 284.

Jaumann, R., Neukum, G., Behnke, T., Duxbury, T. C., Eichentopf, K., Flohrer, J., Gasselt, S. V., Giese, B., Gwinner, K., Hauber, E., Hoffmann, H., Hoffmeister, A., Köhler, U., Matz, K. D., McCord, T. B., Mertens, V., Oberst, J., Pischel, R., Reiss, D., Ress, E., Roatsch, T., Saiger, P., Scholten, F., Schwarz, G., Stephan, K., Wählisch, M., the HRSC Co-Investigator Team, 2007. The high-resolution stereo camera (HRSC) experiment on Mars Express: Instrument aspects and experiment conduct from interplanetary cruise through the nominal mission. Planet. Space Sci. 55, 928-952.

Jöns, H.-P., 2002. Junge/Rezente nichtäolische exogene Dynamik auf dem Mars: Großflächige Beeinflussung durch zerfallende CO2-Hydrate? Zeitschrift für Geologische Wissenschaften 30, 6, 403-421.

JPL, 2011, SPIRIT UPDATE: Spirit Remains Silent at Troy. Jet Propulsion Laboratory, http://marsrover.nasa.gov/mission/status.html, accessed 21.01.2012.

Kass, D. M., Yung, Y. L., 1995. Loss of atmosphere from Mars due to solar wind-induced sputtering. Science 268, 5211, 697-699.

Kaufmann, H., Segl, K., Itzerott, S., Bach, H., Wagner, A., Hill, J., Heim, B., Oppermann, K., Heldens, W., Stein, E., Müller, A., van der Linden, S., Leitao, P. J., Rabe, A., Hostert, P., 2009, Hyperspectral Algorithms. Report in the frame of EnMAP preparation activities. Scientific Technical Report. Helmholtz Zentrum Potsdam, Deutsches GeoForschungszentrum, Potsdam, 268.

Kieffer, H. H., Jakosky, B. M., Snyder, C. W., 1992. 1. The Planet Mars: From Antiquity to the Present. in: H. H. Kieffer, *et al.*, (Eds.), Mars The University of Arizona Press, Tuscon, 1-33.

King, P. L., Lescinsky, D. T., Nesbitt, H. W., 2004. The composition and evolution of primordial solutions on Mars, with application to other planetary bodies. Geochim. Cosmochim. Acta 68, 23, 4993-5008.

Kirk, R. L., Lee, E. M., Sucharski, R. M., Richie, J., Grecu, A., Castro, S. K., 2000. MDIM 2.0: A Revised Global Digital Image Mosaic of Mars. 31st Lunar and Planetary Science Conference Houston, TX, USA.

Kirkland, L. E., Herr, K. C., 2000. Spectral anomalies in the 11 and 12 μm region from the Mariner Mars 7 Infrared Spectrometer. J. Geophys. Res. 105, E9, 22507-22515.

Klingelhöfer, G., DeGrave, E., Morris, R. V., Alboom, A., Resende, V. G., Souza, P. A., Rodionov, D., Schröder, C., Ming, D.

W., Yen, A., Lippens, P. E., Jumas, J. C., Génin, J. M. R., 2007. Mössbauer spectroscopy on Mars: goethite in the Columbia Hills at Gusev crater
ICAME 2005. Springer Berlin Heidelberg, 549-554.

Klingelhöfer, G., Morris, R. V., Bernhardt, B., Schröder, C., Rodionov, D. S., de Souza, P. A., Yen, A., Gellert, R., Evlanov, E. N., Zubkov, B., Foh, J., Bonnes, U., Kankeleit, E., Gütlich, P., Ming, D. W., Renz, F., Wdowiak, T., Squyres, S. W., Arvidson, R. E., 2004. Jarosite and Hematite at Meridiani Planum from Opportunity's Mössbauer Spectrometer. Science 306, 1740-1745.

Kneissl, T., Reiss, D., van Gasselt, S., Neukum, G., 2009. Distribution and orientation of northern-hemisphere gullies on Mars from the evaluation of HRSC and MOC-NA data. Earth Planet. Sci. Lett. 294, 3-4, 357-367.

Kneissl, T., van Gasselt, S., Neukum, G., 2010. Measurement of Strike and Dip of Geologic Layers from Remote Sensing Data - New Software Tool for ArcGIS. 41st Lunar and Planetary Science Conference The Woodlands, TX, USA.

Kneissl, T., van Gasselt, S., Neukum, G., 2011. Map-projection-independent crater size-frequency determination in GIS environments - New software tool for ArcGIS. Planet. Space Sci. 59, 11-12, 1243-1254.

Komatsu, G., Geissler, P. E., Strom, R. G., Singer, R. B., 1993. Stratigraphy and erosional landforms of layered deposits in Valles Marineris, Mars. J. Geophys. Res. 98, E6, 11105 - 11121.

Kubelka, P., 1948. New Contributions to the Optics of Intensely Light-Scattering Materials. Part I. J. Opt. Soc. Am. 38, 5, 448-448.

Kuzmin, R. O., Mironenko, M. V., Evdokimova, N. A., 2008. Mars: Spectral and Thermodynamic Restrictions on the Gypsum Existence in the Juventae Chasma. 39th Lunar and Planetary Science Conference, League City, TX, USA.

Langevin, Y., Poulet, F. o., Bibring, J.-P., Gondet, B., 2005. Sulfates in the North Polar Region of Mars Detected by OMEGA/Mars Express. Science 307, 1584-1586.

Lapen, T. J., Righter, M., Brandon, A. D., Debaille, V., Beard, B. L., Shafer, J. T., Peslier, A. H., 2010. A Younger Age for ALH84001 and Its Geochemical Link to Shergottite Sources in Mars. Science 328, 5976, 347-351.

Laskar, J., Correia, A. C. M., Gastineau, M., Joutel, F., Levrard, B., Robutel, P., 2004. Long term evolution and chaotic diffusion of the insolation quantities of Mars. Icarus 170, 2, 343-364.

Laskar, J., Levrard, B., Mustard, J. F., 2002. Orbital forcing of the martian polar layered deposits. Nature 419, 6905, 375-377.

Lawson, C. L., Hanson, R. J., 1974. Solving Least Squares Problems, Prentice-Hall, Englewood Cliffs, NJ.

Le Deit, L., Bourgeois, O., Mège, D., Hauber, E., Le Mouélic, S., Massé, M., Jaumann, R., Bibring, J. P., 2010. Morphology, stratigraphy, and mineralogical composition of a layered formation covering the plateaus around Valles Marineris, Mars: Implications for its geological history. Icarus 208, 684-703.

Le Deit, L., Le Mouélic, S., Bourgeois, O., Combe, J.-P., Mège, D., Sotin, C., Gendrin, A., Hauber, E., Mangold, N., Bibring, J.-P., 2008. Ferric oxides in East Candor Chasma, Valles Marineris (Mars) inferred from analysis of OMEGA/Mars Express data: Identification and geological interpretation. J. Geophys. Res. (Planets) 113, 07001.

Le Deit, L., Mège, D., Bourgeois, O., Le Mouélic, S., Sotin, C., Mangold, N., Hauber, E., Gendrin, A., Bibring, J. P., 2007. Morphological and Mineralogical Analysis of East Candor Chasma in Valles Marineris on Mars. 7th International Conference on Mars, Pasadena, CA, USA.

LeDeit, L., 2008. Les dépôts stratifiés dans la région de Valles Marineris (Mars): composition minéralogique et morphologie. 288, Université de Nantes, Nantes.

Levine, J. S., Kraemer, D. R., Kuhn, W. R., 1977. Solar radiation incident on Mars and the outer planets: Latitudinal, seasonal, and atmospheric effects. Icarus 31, 1, 136-145.

Levy, J. S., Head, J. W., Marchant, D. R., 2011. Gullies, polygons and mantles in Martian permafrost environments: cold desert landforms and sedimentary processes during recent Martian geological history. Geological Society, London, Special Publications 354, 1, 167-182.

Lewis, K. W., Aharonson, O., 2006. Stratigraphic analysis of the distributary fan in Eberswalde crater using stereo imagery. J. Geophys. Res. 111, E6, E06001.

Lichtenberg, K. A., Arvidson, R. E., Morris, R. V., Murchie, S. L., Bishop, J. L., Fernandez Remolar, D., Glotch, T. D., Noe Dobrea, E., Mustard, J. F., Andrews-Hanna, J., Roach, L. H., 2010. Stratigraphy of hydrated sulfates in the sedimentary deposits of Aram Chaos, Mars. J. Geophys. Res. 115, E00D17.

Loizeau, D., Mangold, N., Poulet, F., Ansan, V., Hauber, E., Bibring, J. P., Gondet, B., Langevin, Y., Masson, P., Neukum, G., 2010. Stratigraphy in the Mawrth Vallis region through OMEGA, HRSC color imagery and DTM. Icarus 205, 396-418.

Loizeau, D., Mangold, N., Poulet, F., Bibring, J. P., Gendrin, A., Ansan, V., Gomez, C., Gondet, B., Langevin, Y., Masson, P., Neukum, G., 2007. Phyllosilicates in the Mawrth Vallis region of Mars. J. Geophys. Res. (Planets) 112, E8, E08S08.

Lucchitta, B. K., 1987. Valles Marineris, Mars - Wet debris flows and ground ice. Icarus 72, 411-429.

Lucchitta, B. K., 1999. Geologic Map of Ophir and Central Candor Chasmata (MTM - 5072) of Mars. U. S. Geological Survey, Flagstaff, AZ, USA.

Lucchitta, B. K., 2002. Late Mafic Volcanism in Valles Marineris, Mars. 33rd Lunar and Planetary Science Conference, Houston, TX, USA.

Lucchitta, B. K., 2009a. Lakes in Valles Marineris, Mars (I): Walls, Mounds, Moats, and Volcanoes. 40th Lunar and Planetary Science Conference The Woodlands, TX, USA.

Lucchitta, B. K., 2009b. Lakes in Valles Marineris, Mars (II): Valleys, Channels, Shallow Lakes, and Age. 40th Lunar and Planetary Science Conference The Woodlands, TX, USA.

Lucchitta, B. K., Isbell, N. K., Howington-Kraus, A., 1994. Topography of Valles Marineris: Implications for erosional and structural history. J. Geophys. Res. 99, E2, 3783-3798.

Lucchitta, B. K., McEwen, A. S., Clow, G. D., Geissler, P. E., Singer, R. B., Schultz, R. A., Squyres, S. W., 1992. The canyon system on Mars. Mars, 453-492.

Madden, M. E., Bodnar, R. J., Rimstidt, J. D., 2004. Jarosite as an indicator of water-limited chemical weathering on Mars. Nature 431, 821-823.

Madejová, J., Pentrák, M., Pálková, H., Komadel, P., 2009. Near-infrared spectroscopy: A powerful tool in studies of acid-treated clay minerals. Vibrational Spectroscopy 49, 2, 211-218.

Madeleine, J. B., Forget, F., Head, J. W., Levrard, B., Montmessin, F., Millour, E., 2009. Amazonian northern mid-latitude glaciation on Mars: A proposed climate scenario. Icarus 203, 2, 390-405.

Malin, M. C., Bell, J. F., Cantor, B. A., Caplinger, M. A., Calvin, W. M., Clancy, R. T., Edgett, K. S., Edwards, L., Haberle, R. M., James, P. B., Lee, S. W., Ravine, M. A., Thomas, P. C., Wolff, M. J., 2007. Context Camera Investigation on board the Mars Reconnaissance Orbiter. J. Geophys. Res. (Planets) 112, E510.1029/2006JE002808.

Malin, M. C., Danielson, G. E., Ingersoll, A. P., Masursky, H., Veverka, J., Ravine, M. A., Soulanille, T. A., 1992. Mars Observer camera. J. Geophys. Res. 97, 7699-7718, 10.1029/92JE00340.

Malin, M. C., Edgett, K. S., 2000a. Evidence for Recent Groundwater Seepage and Surface Runoff on Mars. Science 288, 2330-2335.

Malin, M. C., Edgett, K. S., 2000b. Sedimentary Rocks of Early Mars. Science 290, 5498, 1927 -1937.

Malin, M. C., Edgett, K. S., 2001. Mars Global Surveyor Mars Orbiter Camera: Interplanetary cruise through primary mission. J. Geophys. Res. 106, 23429-23570.

Malin, M. C., Edgett, K. S., Cantor, B. A., Caplinger, M. A., Danielson, G. E., Jensen, E. H., Ravine, M. A., Sandoval, J. L., Supulver, K. D., 2010. An overview of the 1985-2006 Mars Orbiter Camera science investigation. International Journal of Mars Science and Exploration 5, 1-60.

Mangold, N., Costard, F., Forget, F., 2003. Debris flows over sand dunes on Mars: Evidence for liquid water. J. Geophys. Res. 108, E4, 5027.

Mangold, N., Gendrin, A., Gondet, B., Lemouelic, S., Quantin, C., Ansan, V., Bibring, J.-P., Langevin, Y., Masson, P., Neukum, G., 2008. Spectral and geological study of the sulfate-rich region of West Candor Chasma, Mars. Icarus 194, 519-543.

Mangold, N., Gendrin, A., Quantin, C., Bibring, J. P., Gondet, B., Langevin, Y., Poulet, F., Arvidson, R., Griffes, J. L., Hauber, H., Masson, P., Neukum, G., Omega Team, HRSC Co-Investigator Team, 2007a. An Overview of the Sulfates Detected in the Equatorial Regions by the OMEGA/MEx Spectrometer. LPI Contributions 1353, 3141.

Mangold, N., Poulet, F., Mustard, J. F., Bibring, J. P., Gondet, B., Langevin, Y., Ansan, V.,

Masson, P., Fassett, C., Head, J. W., Hoffmann, H., Neukum, G., 2007b. Mineralogy of the Nili Fossae region with OMEGA/Mars Express data: 2. Aqueous alteration of the crust. J. Geophys. Res. (Planets) 112.

Mangold, N., Quantin, C., Ansan, V., Delacourt, C., Allemand, P., 2004. Evidence for Precipitation on Mars from Dendritic Valleys in the Valles Marineris Area. Science 305, 5680, 78-81.

Márquez, A., de Pablo, M. Á., Oyarzun, R., Viedma, C., 2005. Evidence of gully formation by regional groundwater flow in the Gorgonum-Newton region (Mars). Icarus 179, 2, 398-414.

Marzo, G. A., Davila, A. F., Tornabene, L. L., Dohm, J. M., Fairén, A. G., Gross, C., Kneissl, T., Bishop, J. L., Roush, T. L., McKay, C. P., 2010. Evidence for Hesperian impact-induced hydrothermalism on Mars. Icarus 208, 667-683.

Mason, B. H., 1966. Principles of Geochemistry, J. Wiley & Sons, New York.

Massé, M., Bourgeois, O., Le Mouélic, S., Verpoorter, C., Le Deit, L., Bibring, J. P., 2010. Martian polar and circum-polar sulfate-bearing deposits: Sublimation tills derived from the North Polar Cap. Icarus 209, 434-451.

Matthes, S., 1993. Mineralogie: eine Einführung in die spezielle Mineralogie, Petrologie und Lagerstättenkunde, 4. vollst. überarb. Aufl. ed., Springer, Berlin, Heidelberg, New York, London, Paris, Tokyo, Hong Kong, Barcelona, Budapest.

McConnochie, T. H., Bell, J. F., III, Savransky, D., Mehall, G., Caplinger, M., Christensen, P. R., Cherednik, L., Bender, K., Dombovari, A., 2006. Calibration and in-flight performance of the Mars Odyssey Thermal Emission Imaging System visible imaging subsystem (THEMIS VIS). J. Geophys. Res. 111, E6, E06018.

McCord, T. B., Adams, J. B., Bellucci, G., Combe, J. P., Gillespie, A. R., Hansen, G., Hoffmann, H., Jaumann, R., Neukum, G., Pinet, P., Poulet, F., Stephan, K., 2007. Mars Express High Resolution Stereo Camera spectrophotometric data: Characteristics and science analysis. J. Geophys. Res. (Planets) 112, E6.

McCord, T. B., Huguenin, R. L., Johnson, G. L., 1977. Photometric imaging of Mars during the 1973 opposition. Icarus 31, 293-314.

McCubbin, F. M., Tosca, N. J., Smirnov, A., Nekvasil, H., Steele, A., Fries, M., Lindsley, D. H., 2009. Hydrothermal jarosite and hematite in a pyroxene-hosted melt inclusion in martian meteorite Miller Range (MIL) 03346: Implications for magmatic-hydrothermal fluids on Mars. Geochim. Cosmochim. Acta 73, 4907-4917.

McEwen, A. S., Eliason, E. M., Bergstrom, J. W., Bridges, N. T., Hansen, C. J., Delamere, W. A., Grant, J. A., Gulick, V. C., Herkenhoff, K. E., Keszthelyi, L., Kirk, R. L., Mellon, M. T., Squyres, S. W., Thomas, N., Weitz, C. M., 2007. Mars Reconnaissance Orbiter's High Resolution Imaging Science Experiment (HiRISE). J. Geophys. Res. (Planets) 112, E510.1029/2005JE002605.

McEwen, A. S., Tornabene, L., Grant, J., Wray, J., Mustard, J., 2008. Noachian Megabreccia on Mars. AGU Fall Meeting Abstracts 43, 03.

McGuire, P. C., Bishop, J. L., Brown, A. J., Fraeman, A. A., Marzo, G. A., Frank Morgan, M., Murchie, S. L., Mustard, J. F., Parente, M., Pelkey, S. M., Roush, T. L., Seelos, F. P., Smith, M. D., Wendt, L., Wolff, M. J., 2009. An improvement to the volcano-scan algorithm for atmospheric correction of CRISM and OMEGA spectral data. Planet. Space Sci. 57, 809-815.

McGuire, P. C., Wolff, M. J., Smith, M. D., Arvidson, R. E., Murchie, S. L., Clancy, R. T., Roush, T. L., Cull, S. C., Lichtenberg, K. A., Wiseman, S. M., Green, R. O., Marti, T. Z., Milliken, R. E., Cavender, P. J., Humm, D. C., Seelos, F. P., Seelos, K. D., Taylor, H. W., Ehlmann, B. L., Mustard, J. F., Pelkey, S. M., Titus, T. N., Hash, C. D., Malaret, E. R., 2008. MRO/CRISM Retrieval of Surface Lambert Albedos for Multispectral Mapping of Mars With DISORT-Based Radiative Transfer Modeling: Phase 1 -Using Historical Climatology for Temperatures, Aerosol Optical Depths, and Atmospheric Pressures. IEEE Transactions on Geoscience and Remote Sensing 46, 4020-4040.

McKay, C. P., Nedell, S. S., 1988. Are there carbonate deposits in the Valles Marineris, Mars? Icarus 73, Jan. 1988, 142-148.

McKeown, N. K., Bishop, J. L., Noe Dobrea, E. Z., Ehlmann, B. L., Parente, M., Mustard, J. F., Murchie, S. L., Swayze, G. A., Bibring, J.-P., Silver, E. A., 2009.

Characterization of phyllosilicates observed in the central Mawrth Vallis region, Mars, their potential formational processes, and implications for past climate. J. Geophys. Res. 114, E00D10, 10.1029/2008JE003301

McLennan, S. M., Bell Iii, J. F., Calvin, W. M., Christensen, P. R., Clark, B. C., de Souza, P. A., Farmer, J., Farrand, W. H., Fike, D. A., Gellert, R., Ghosh, A., Glotch, T. D., Grotzinger, J. P., Hahn, B., Herkenhoff, K. E., Hurowitz, J. A., Johnson, J. R., Johnson, S. S., Jolliff, B., Klingelhöfer, G., Knoll, A. H., Learner, Z., Malin, M. C., McSween Jr, H. Y., Pocock, J., Ruff, S. W., Soderblom, L. A., Squyres, S. W., Tosca, N. J., Watters, W. A., Wyatt, M. B., Yen, A., 2005. Provenance and diagenesis of the evaporite-bearing Burns formation, Meridiani Planum, Mars. Earth Planet. Sci. Lett. 240, 1, 95-121.

McSween, H. Y., 2002. The rocks of Mars, from far and near. Meteoritics & Planetary Science 37, 1, 7-25.

Mège, D., Bourgeois, O., 2010. Destabilization of Valles Marineris Wallslopes by Retreat of Ancient Glaciers. 41st Lunar and Planetary Science Conference The Woodlands,TX, USA.

Metz, J. M., Grotzinger, J. P., Mohrig, D., Milliken, R., Prather, B., Pirmez, C., McEwen, A. S., Weitz, C. M., 2009. Sublacustrine depositional fans in southwest Melas Chasma. J. Geophys. Res. (Planets) 114, 10002.

Meunier, A., 2005. Clays, Springer, Berlin, Heidelberg, New York.

Michael, G., Neukum, G., 2009. Image Enhancement of the Super Resolution Channel (SRC) of the Mars Express HRSC Experiment. 40th Lunar and Planetary Science Conference, The Woodlands, TX, USA. .

Michael, G. G., Neukum, G., 2010. Planetary surface dating from crater size-frequency distribution measurements: Partial resurfacing events and statistical age uncertainty. Earth Planet. Sci. Lett. 294, 3-4, 223-229.

Michalski, J. R., Noe Dobrea, E. Z., 2007. Evidence for a sedimentary origin of clay minerals in the Mawrth Vallis region, Mars. Geology 35, 10, 951-954.

Milkovich, S. M., Head, J. W., III, 2005. North polar cap of Mars: Polar layered deposit characterization and identification of a fundamental climate signal. J. Geophys. Res. 110, E1, E01005.

Milliken, R. E., Bish, D. L., 2010. Sources and sinks of clay minerals on Mars. Philosophical Magazine 90, 17-18, 2293-2308.

Milliken, R. E., Fischer, W. W., Hurowitz, J. A., 2009. Missing salts on early Mars. Geophys. Res. Lett. 36, 11, L11202.

Milliken, R. E., Grotzinger, J. P., Thomson, B. J., 2010. Paleoclimate of Mars as captured by the stratigraphic record in Gale Crater. Geophys. Res. Lett. 37, 4, L04201.

Milliken, R. E., Swayze, G., Arvidson, R. E., Bishop, J. L., Clark, R. N., Ehlmann, B. L., Grotzinger, J., Morris, R. V., Murchie, S. L., Mustard, J. F., Weitz, C. M., Team, C. S., 2008a. Spectral Evidence for Sedimentary Silica on Mars. 39th Lunar and Planetary Science Conference, League City, Texas.

Milliken, R. E., Swayze, G. A., Arvidson, R. E., Bishop, J. L., Clark, R. N., Ehlmann, B. L., Green, R. O., Grotzinger, J. P., Morris, R. V., Murchie, S. L., Mustard, J. F., Weitz, C., 2008b. Opaline silica in young deposits on Mars. Geology 36, 11, 847-850.

Ming, D. W., Mittlefehldt, D. W., Morris, R. V., Golden, D. C., Gellert, R., Yen, A., Clark, B. C., Squyres, S. W., Farrand, W. H., Ruff, S. W., Arvidson, R. E., Klingelhöfer, G., McSween, H. Y., Rodionov, D. S., Schröder, C., de Souza, P. A., Jr., Wang, A., 2006. Geochemical and mineralogical indicators for aqueous processes in the Columbia Hills of Gusev crater, Mars. J. Geophys. Res. 111, E2, E02S12.

Minitti, M. E., Weitz, C. M., Lane, M. D., Bishop, J. L., 2007. Morphology, chemistry, and spectral properties of Hawaiian rock coatings and implications for Mars. J. Geophys. Res. 112, E5, E05015.

Mittlefehldt, D. W., 1994. ALH84001, a cumulate orthopyroxenite member of the Martian meteorite clan. Meteoritics 29, 214-221.

Miyamoto, H., Dohm, J. M., Baker, V. R., Beyer, R. A., Bourke, M., 2004. Dynamics of unusual debris flows on Martian sand dunes. Geophys. Res. Lett. 31, 13, L13701.

Moehlmann, D. T. F., Niemand, M., Formisano, V., Savijärvi, H., Wolkenberg, P., 2009. Fog phenomena on Mars. Planet. Space Sci. 57, 1987-1992.

Moore, J. M., Howard, A. D., Stansbery, E., 2003. Ariadnes-Gorgonum Knob Fields of North-Western Terra Sirenum, Mars. Lunar Planet. Sci., League City, TX, USA.

Moroz, L., Schade, U., Wäsch, R., 2000. Reflectance Spectra of Olivine-Orthopyroxene-Bearing Assemblages at Decreased Temperatures: Implications for Remote Sensing of Asteroids. Icarus 147, 1, 79-93.

Morris, R. V., Golden, D. C., 1998. Goldenrod Pigments and the Occurrence of Hematite and Possibly Goethite in the Olympus-Amazonis Region of Mars. Icarus 134, 1, 1-10.

Morris, R. V., Klingelhöfer, G., Schröder, C., Rodionov, D. S., Yen, A., Ming, D. W., de Souza, P. A., Wdowiak, T., Fleischer, I., Gellert, R., Bernhardt, B., Bonnes, U., Cohen, B. A., Evlanov, E. N., Foh, J., Gütlich, P., Kankeleit, E., McCoy, T., Mittlefehldt, D. W., Renz, F., Schmidt, M. E., Zubkov, B., Squyres, S. W., Arvidson, R. E., 2006. Mössbauer mineralogy of rock, soil, and dust at Meridiani Planum, Mars: Opportunity's journey across sulfate-rich outcrop, basaltic sand and dust, and hematite lag deposits. J. Geophys. Res. (Planets) 111.

Morris, R. V., Lawson, C. A., Gibson, E. K., Jr., Lauer, H. V., Jr., Nace, G. A., Stewart, C., 1985. Spectral and other physicochemical properties of submicron powders of hematite (alpha-Fe2O3), maghemite (gamma-Fe2O3), magnetite (Fe3O4), goethite (alpha-FeOOH), and lepidocrocite (gamma-FeOOH). J. Geophys. Res. 90, 3126-3144.

Morris, R. V., Ruff, S. W., Gellert, R., Ming, D. W., Arvidson, R. E., Clark, B. C., Golden, D. C., Siebach, K., Klingelhöfer, G., Schröder, C., Fleischer, I., Yen, A. S., Squyres, S. W., 2010. Identification of Carbonate-Rich Outcrops on Mars by the Spirit Rover. Science 329, 421-424.

MSSS, 2010, Mars Reconnaissance Orbiter (MRO) Context Camera (CTX). accessed 18.10.2011.

Mukhin, L. M., Koscheev, A. P., Dikov, Y. P., Huth, J., Wänke, H., 1996. Experimental simulations of the photodecomposition of carbonates and sulphates on Mars. nature 379, 141-143.

Murchie, S., Arvidson, R., Bedini, P., Beisser, K., Bibring, J. P., Bishop, J., Boldt, J., Cavender, P., Choo, T., Clancy, R. T., Darlington, E. H., Des Marais, D., Espiritu, R., Fort, D., Green, R., Guinness, E., Hayes, J., Hash, C., Heffernan, K., Hemmler, J., Heyler, G., Humm, D., Hutcheson, J., Izenberg, N., Lee, R., Lees, J., Lohr, D., Malaret, E., Martin, T., McGovern, J. A., McGuire, P., Morris, R., Mustard, J., Pelkey, S., Rhodes, E., Robinson, M., Roush, T., Schaefer, E., Seagrave, G., Seelos, F., Silverglate, P., Slavney, S., Smith, M., Shyong, W. J., Strohbehn, K., Taylor, H., Thompson, P., Tossman, B., Wirzburger, M., Wolff, M., 2007a. Compact Reconnaissance Imaging Spectrometer for Mars (CRISM) on Mars Reconnaissance Orbiter (MRO). J. Geophys. Res. (Planets) 112, E510.1029/2006JE002682.

Murchie, S., Guinness, E., Slavney, S., 2007b, Mars Reconnaissance Orbiter CRISM DATA PRODUCT SOFTWARE INTERFACE SPECIFICATION. PDS Geosciences Node, NASA.

Murchie, S., Roach, L., Seelos, F., Milliken, R., Mustard, J., Arvidson, R., Wiseman, S., Lichtenberg, K., Andrews-Hanna, J., Bishop, J., Bibring, J.-P., Parente, M., Morris, R., 2009a. Evidence for the origin of layered deposits in Candor Chasma, Mars, from mineral composition and hydrologic modeling. J. Geophys. Res. (Planets) 114, E12.

Murchie, S. L., Mustard, J. F., Ehlmann, B. L., Milliken, R. E., Bishop, J. L., McKeown, N. K., Noe Dobrea, E. Z., Seelos, F. P., Buczkowski, D. L., Wiseman, S. M., Arvidson, R. E., Wray, J. J., Swayze, G., Clark, R. N., Des Marais, D. J., McEwen, A. S., Bibring, J.-P., 2009b. A synthesis of Martian aqueous mineralogy after 1 Mars year of observations from the Mars Reconnaissance Orbiter. J. Geophys. Res. 114.

Murchie, S. L., Seelos, F. P., Hash, C. D., Humm, D. C., Malaret, E., McGovern, J. A., Choo, T. H., Seelos, K. D., Buczkowski, D. L., Morgan, M. F., Barnouin-Jha, O. S., Nair, H., Taylor, H. W., Patterson, G. W., Harvel, C. A., Mustard, J. F., Arvidson, R. E., McGuire, P., Smith, M. D., Wolff, M. J., Titus, T. N., Bibring, J.-P., Poulet, F., 2009c. Compact Reconnaissance Imaging Spectrometer for Mars investigation and data set from the Mars Reconnaissance Orbiter's primary science phase. J. Geophys. Res. 114, E00D07, 10.1029/2009JE003344

Mustard, J. F., Ehlmann, B. L., Murchie, S. L., Poulet, F., Mangold, N., Head, J. W., Bibring, J. P., Roach, L. H., 2009. Composition, Morphology, and Stratigraphy of Noachian Crust around the Isidis basin. J. Geophys. Res. (Planets) 114.

Mustard, J. F., Murchie, S. L., Pelkey, S. M., Ehlmann, B. L., Milliken, R. E., Grant, J. A., Bibring, J. P., Poulet, F., Bishop, J.,

Dobrea, E. N., Roach, L., Seelos, F., Arvidson, R. E., Wiseman, S., Green, R., Hash, C., Humm, D., Malaret, E., McGovern, J. A., Seelos, K., Clancy, T., Clark, R., Marais, D. D., Izenberg, N., Knudson, A., Langevin, Y., Martin, T., McGuire, P., Morris, R., Robinson, M., Roush, T., Smith, M., Swayze, G., Taylor, H., Titus, T., Wolff, M., 2008. Hydrated silicate minerals on Mars observed by the Mars Reconnaissance Orbiter CRISM instrument. Nature 454, 305-309.

Mustard, J. F., Poulet, F., Gendrin, A., Bibring, J. P., Langevin, Y., Gondet, B., Mangold, N., Bellucci, G., Altieri, F., 2005. Olivine and Pyroxene Diversity in the Crust of Mars. Science 307, 1594-1597.

NASA, 2007, Report Reveals Likely Causes of Mars Spacecraft Loss. NASA, http://www.nasa.gov/mission_pages/mgs/mgs-20070413.html, accessed 21.01.2012.

Nascimento, J. M. P., Dias, J. M. B., 2007. Unmixing Hyperspectral Data: Independent and Dependent Component Analysis. in: C.-I. Chang, (Ed.), Hyperspectral Data Exploitation: Theory and Application, 149-177.

Nedell, S. S., Squyres, S. W., Andersen, D. W., 1987. Origin and evolution of the layered deposits in the Valles Marineris, Mars. Icarus 70, June 1987, 409-441.

Neukum, G., Basilevsky, A. T., Kneissl, T., Chapman, M. G., van Gasselt, S., Michael, G., Jaumann, R., Hoffmann, H., Lanz, J. K., 2010. The geologic evolution of Mars: Episodicity of resurfacing events and ages from cratering analysis of image data and correlation with radiometric ages of Martian meteorites. Earth Planet. Sci. Lett. 294, 3-4, 204-222.

Neukum, G., Hiller, K., 1981. Martian Ages. J. Geophys. Res. 86, B4, 3097-3121.

Neukum, G., Ivanov, B. A., Hartmann, W. K., 2001. Cratering Records in the Inner Solar System in Relation to the Lunar Reference System. Space Science Reviews 96, 1, 55-86.

Neukum, G., Ivanov, B. A., Matthews, M. S., Schumann, A. M., 1994. Crater Size Distributions and Impact Probabilities on Earth from Lunar, Terrestrial-planet, and Asteroid Cratering Data. Hazards Due to Comets and Asteroids,

Neukum, G., Jaumann, R., 2004, HRSC: the High Resolution Stereo Camera of Mars Express. Mars Express: the Scientific Payload, 17-35.

Neukum, G., Jaumann, R., Hoffmann, H., Hauber, E., Head, J. W., Basilevsky, A. T., Ivanov, B. A., Werner, S. C., van Gasselt, S., Murray, J. B., McCord, T., Team, H. C.-I., 2004. Recent and episodic volcanic and glacial activity on Mars revealed by the High Resolution Stereo Camera. Nature 432, 971-979.

Neukum, G., Wise, D. U., 1976. Mars: A Standard Crater Curve and Possible New Time Scale. Science 194, 4272, 1381-1387.

Newman, M. J., Rood, R. T., 1977. Implications of Solar Evolution for the Earth's Early Atmosphere. Science 198, 4321, 1035-1037.

Noe Dobrea, E. Z., 2007. Ariadnes Colles. Second MSL Landing Site Workshop, Pasadena, CA.

Noe Dobrea, E. Z., Moore, J., Howard, A., Catling, D., Grant, J., 2008. Spectral and Geomorphic Evidence for a Past Inland Sea in Eridania Basin, Mars. AGU Fall Meeting Abstracts 32, 03.

Noe Dobrea, E. Z., Swayze, G., 2010. Acid Pedogenesis on Mars? Evidence for Top-Down Alteration on Mars from CRISM and HiRISE Data. 42nd Lunar and Planetary Institute Science Conference The Woodlands, TX, USA.

Osterloo, M. M., Anderson, F. S., Hamilton, V. E., Hynek, B. M., 2010. Geologic context of proposed chloride-bearing materials on Mars. J. Geophys. Res. 115, E10, E10012, 10.1029/2010JE003613

Osterloo, M. M., Hamilton, V. E., Bandfield, J. L., Glotch, T. D., Baldridge, A. M., Christensen, P. R., Tornabene, L. L., Anderson, F. S., 2008. Chloride-Bearing Materials in the Southern Highlands of Mars. Science 319, 5870, 1651-1654.

Owen, T., Biemann, K., Rushneck, D. R., Biller, J. E., Howarth, D. W., Lafleur, A. L., 1977. The Composition of the Atmosphere at the Surface of Mars. J. Geophys. Res. 82, 28, 4635-4639.

Palomba, E., Zinzi, A., Cloutis, E. A., D'Amore, M., Grassi, D., Maturilli, A., 2009. Evidence for Mg-rich carbonates on Mars from a 3.9 µm absorption feature. Icarus 203, 58-65.

Papike, J. J., Karner, J. M., Shearer, C. K., 2006. Comparative planetary mineralogy: Implications of martian and terrestrial jarosite. A crystal chemical perspective. Geochim. Cosmochim. Acta 70, 1309-1321.

Parente, M., 2008. A New Approach to Denoising CRISM Images. 39th Lunar and

Planetary Science Conference League City, TX, USA.

Parkhurst, D. L., Appelo, C. A. J., 1999, User's Guide to PHREEQC (Version 2) -A computer program for speciation, batch-reaction, one-dimensional transport, and inverse geochemical calculations. U.S. Geological Survey Water-Resources Investigations Report, 310.

Pechmann, J. C., 1980. The origin of polygonal troughs on the Northern Plains of Mars. Icarus 42, 2, 185-210.

Pelkey, S. M., Mustard, J. F., Murchie, S., Clancy, R. T., Wolff, M., Smith, M., Milliken, R., Bibring, J. P., Gendrin, A., Poulet, F., Langevin, Y., Gondet, B., 2007. CRISM multispectral summary products: Parameterizing mineral diversity on Mars from reflectance. J. Geophys. Res. (Planets) 112, E810.1029/2006JE002831.

Pepin, R. O., 1991. On the origin and early evolution of terrestrial planet atmospheres and meteoritic volatiles. Icarus 92, 1, 2-79.

Peterson, C. M., 1981. Hebes Chasma - Martian Pyroclastic Sink. 12th Lunar and Planetary Science Conference, Houston, TX, USA.

Pieters, C. M., 1983. Strength of Mineral Absorption Features in the Transmitted Component of Near-Infrared Reflected Light: First Results From RELAB. J. Geophys. Res. 88, B11, 9534-9544.

Pinet, P., Chevrel, S., 1990. Spectral identification of geological units on the surface of Mars related to the presence of silicates from earth-based near-infrared telescopic charge-coupled device imaging. J. Geophys. Res. 95, 14435-14446.

Poulet, F., Arvidson, R. E., Gomez, C., Morris, R. V., Bibring, J. P., Langevin, Y., Gondet, B., Griffes, J., 2008. Mineralogy of Terra Meridiani and western Arabia Terra from OMEGA/MEx and implications for their formation. Icarus 195, 106-130.

Poulet, F., Gomez, C., Bibring, J. P., Langevin, Y., Gondet, B., Pinet, P., Belluci, G., Mustard, J., 2007. Martian surface mineralogy from Observatoire pour la Minéralogie, l'Eau, les Glaces et l'Activité on board the Mars Express spacecraft (OMEGA/MEx): Global mineral maps. J. Geophys. Res. (Planets) 112.

Poulet, F., Mangold, N., Platevoet, B., Bardintzeff, J. M., Sautter, V., Mustard, J. F., Bibring, J. P., Pinet, P., Langevin, Y., Gondet, B., Aléon-Toppani, A., 2009. Quantitative compositional analysis of martian mafic regions using the MEx/OMEGA reflectance data. 2. Petrological implications. Icarus 201, 84-101.

Poulleau, G., Gondet, B., Langevin, Y., 2005, OMEGA Experiment Archive Interface Control Document. Institut d'Astrophysique Spatiale, Centre National de la Recherche Scientifique

Putzig, N. E., Mellon, M. T., Kretke, K. A., Arvidson, R. E., 2005. Global thermal inertia and surface properties of Mars from the MGS mapping mission. Icarus 173, 2, 325-341.

Quantin, C., Allemand, P., Mangold, N., Delacourt, C., 2004. Ages of Valles Marineris (Mars) landslides and implications for canyon history. Icarus 172, 555-572.

Quantin, C., Mangold, N., Hauber, E., Flahaut, J., Le Deit, L., Fueten, F., Zegers, T., 2010. Timing Constrains of Interior Layered Deposit Emplacement in Valles Marineris. First International Conference on Mars Sedimentology and Stratigraphy, El Paso, TX, USA.

Ramsey, M. S., Christensen, P. R., 1998. Mineral abundance determination: Quantitative deconvolution of thermal emission spectra. J. Geophys. Res. 103, B1, 577-596.

Rees, W. G., 2001. Physical Principles of Remote Sensing 2ed., Cambridge University Press, Cambridge, New York, Melbourne, Madrid, Cape Town, Singapore, Sao Paolo

Reiss, D., Jaumann, R., 2003. Recent debris flows on Mars: Seasonal observations of the Russell Crater dune field. Geophys. Res. Lett. 30, 6, 3-6.

Reiss, D., van Gasselt, S., Neukum, G., Jaumann, R., 2004. Absolute dune ages and implications for the time of formation of gullies in Nirgal Vallis, Mars. J. Geophys. Res. 109, E6, E06007.

Rencz, A. N., 1999. Remote Sensing for the Earth Sciences - Manual of Remote Sensing (3rd Edition) Volume 3, John Wiley & Sons.

Rieder, R., Gellert, R., Anderson, R. C., Brückner, J., Clark, B. C., Dreibus, G., Economou, T., Klingelhöfer, G., Lugmair, G. W., Ming, D. W., Squyres, S. W., d'Uston, C., Wänke, H., Yen, A., Zipfel, J., 2004. Chemistry of Rocks and Soils at Meridiani Planum from the Alpha Particle X-ray Spectrometer. Science 306, 5702, 1746-1749.

Roach, L. H., 2009. Sulfates in Valles Marineris as Indicators of the Aqueous Evolution

of Mars. 296, Brown University, Providence, RI.

Roach, L. H., Mustard, J. F., Lane, M. D., Bishop, J. L., Murchie, S. L., 2010a. Diagenetic haematite and sulfate assemblages in Valles Marineris. Icarus 207, 659-674.

Roach, L. H., Mustard, J. F., Swayze, G., Milliken, R. E., Bishop, J. L., Murchie, S. L., Lichtenberg, K., 2010b. Hydrated mineral stratigraphy of Ius Chasma, Valles Marineris. Icarus 206, 253-268.

Rogers, A. D., Bandfield, J. L., Christensen, P. R., 2007. Global spectral classification of Martian low-albedo regions with Mars Global Surveyor Thermal Emission Spectrometer (MGS-TES) data. J. Geophys. Res. 112, E2, E02004.

Rossi, A. P., Neukum, G., Pondrelli, M., van Gasselt, S., Zegers, T., Hauber, E., Chicarro, A., Foing, B., 2008. Large-scale spring deposits on Mars? J. Geophys. Res. (Planets) 113, E8.

Rossi, A. P., van Gasselt, S., 2010. Geology of Mars after the first 40 years of exploration. Research in Astronomy and Astrophysics 10, 7, 621.

Sánchez España, J., López Pamo, E., Santofimia, E., Aduvire, O., Reyes, J., Barettino, D., 2005. Acid mine drainage in the Iberian Pyrite Belt (Odiel river watershed, Huelva, SW Spain): Geochemistry, mineralogy and environmental implications. Appl. Geochem. 20, 7, 1320-1356.

Sanders, L. C., Schott, J. R., Raqueño, R., 2001. A VNIR/SWIR atmospheric correction algorithm for hyperspectral imagery with adjacency effect. Remote Sensing of Environment 78, 3, 252-263.

Saunders, R. S., Arvidson, R. E., Badhwar, G. D., Boynton, W. V., Christensen, P. R., Cucinotta, F. A., Feldman, W. C., Gibbs, R. G., Kloss, C., Landano, M. R., Mase, R. A., McSmith, G. W., Meyer, M. A., Mitrofanov, I. G., Pace, G. D., Plaut, J. J., Sidney, W. P., Spencer, D. A., Thompson, T. W., Zeitlin, C. J., 2004. 2001 Mars Odyssey Mission Summary. Space Science Reviews 110, 1, 1-36.

Schiffman, P., Zierenberg, R., Marks, N., Bishop, J. L., Darby Dyar, M., 2006. Acid-fog deposition at Kilauea volcano: A possible mechanism for the formation of siliceous-sulfate rock coatings on Mars. Geology 34, 921-924.

Schorghofer, N., 2007. Dynamics of ice ages on Mars. Nature 449, 7159, 192-194.

Schultz, P. H., Lutz, A. B., 1988. Polar wandering of Mars. Icarus 73, 1, 91-141.

Schwertmann, U., 1985. The effect of pedogenic environments on iron oxide minerals. Advances in Soil Sciences 1, 171-200.

Scott, D. H., Carr, M. H., 1978. Geologic Map of Mars I-1083. U. S. Geological Survey, Reston.

Scott, D. H., Tanaka, K. L., 1986. Geologic Map of the Western Equatorial Region of Mars I-1802-A. U. S. Geological Survey, Flagstaff, AZ, USA.

Segura, T. L., Toon, O. B., Colaprete, A., Zahnle, K., 2002. Environmental Effects of Large Impacts on Mars. Science 298, 5600, 1977-1980.

Settle, M., 1979. Formation and deposition of volcanic sulfate aerosols on Mars. J. Geophys. Res. 84, 8343-8354.

Sherman, D. M., Burns, R. G., Mee Burns, V., 1982. Spectral characteristics of the iron oxides with application to the Martian bright region mineralogy. J. Geophys. Res. 87, 10169-10180.

Singer, R. B., 1982. Spectral Evidence for the Mineralogy of High-Albedo Soils and Dust on Mars. J. Geophys. Res. 87, B12, 10159-10168.

Singer, R. B., Clark, R. N., McCord, T. B., Adams, J. B., Huguenin, R. L., 1979. Mars surface composition from reflectance spectroscopy - A summary. J. Geophys. Res. 84, 8415-8426.

Smith, D. E., Neumann, G. A., Arvidson, R., Guinness, E., Slavney, S., 2003. Mars Global Surveyor Laser Altimeter Mission Experiment Gridded Data Record. MGS-M-MOLA-5-MEGDR-L3-V1.0 ed., NASA Planetary Data System

Smith, D. E., Zuber, M. T., Frey, H. V., Garvin, J. B., Head, J. W., Muhleman, D. O., Pettengill, G. H., Phillips, R. J., Solomon, S. C., Zwally, H. J., Banerdt, W. B., Duxbury, T. C., Golombek, M. P., Lemoine, F. G., Neumann, G. A., Rowlands, D. D., Aharonson, O., Ford, P. G., Ivanov, A. B., Johnson, C. L., McGovern, P. J., Abshire, J. B., Afzal, R. S., Sun, X., 2001. Mars Orbiter Laser Altimeter: Experiment summary after the first year of global mapping of Mars. J. Geophys. Res. 106, E10, 23689-23722, 10.1029/2000JE001364

Smith, P. H., Tamppari, L. K., Arvidson, R. E., Bass, D., Blaney, D., Boynton, W. V., Carswell, A., Catling, D. C., Clark, B. C., Duck, T., DeJong, E., Fisher, D., Goetz, W., Gunnlaugsson, H. P., Hecht, M. H., Hipkin, V., Hoffman, J., Hviid, S. F., Keller, H. U., Kounaves, S. P., Lange, C. F., Lemmon, M. T., Madsen, M. B., Markiewicz, W. J., Marshall, J., McKay,

C. P., Mellon, M. T., Ming, D. W., Morris, R. V., Pike, W. T., Renno, N., Staufer, U., Stoker, C., Taylor, P., Whiteway, J. A., Zent, A. P., 2009. H2O at the Phoenix Landing Site. Science 325, 5936, 58-61.

Snyder, C. W., Moroz, V. I., 1992. Spacecraft Exploration of Mars. in: H. H. Kieffer, *et al.*, (Eds.), Mars. The University of Arizona Press, Tuscon, 71-119.

Sowe, M., Wendt, L., McGuire, P. C., Neukum, G., 2011. Hydrated minerals in the deposits of Aureum Chaos. Icarus, 0.

Squyres, S. W., Arvidson, R. E., Ruff, S., Gellert, R., Morris, R. V., Ming, D. W., Crumpler, L., Farmer, J. D., Des Marais, D. J., Yen, A., McLennan, S. M., Calvin, W., Bell, J. F., Clark, B. C., Wang, A., McCoy, T. J., Schmidt, M. E., de Souza, P. A., 2008. Detection of Silica-Rich Deposits on Mars. Science 320, 1063-1067.

Squyres, S. W., Grotzinger, J. P., Arvidson, R. E., Bell, J. F., Calvin, W., Christensen, P. R., Clark, B. C., Crisp, J. A., Farrand, W. H., Herkenhoff, K. E., Johnson, J. R., Klingelhöfer, G., Knoll, A. H., McLennan, S. M., McSween, H. Y., Morris, R. V., Rice, J. W., Rieder, R., Soderblom, L. A., 2004. In Situ Evidence for an Ancient Aqueous Environment at Meridiani Planum, Mars. Science 306, 1709-1714.

Squyres, S. W., Kasting, J. F., 1994. Early Mars: How Warm and How Wet? Science 265, 5173, 744-749.

Stöffler, D., Ryder, G., 2001. Stratigraphy and Isotope Ages of Lunar Geologic Units: Chronological Standard for the Inner Solar System. Space Science Reviews 96, 1, 9-54.

Strom, R. G., Malhotra, R., Ito, T., Yoshida, F., Kring, D. A., 2005. The Origin of Planetary Impactors in the Inner Solar System. Science 309, 5742, 1847-1850.

Sunshine, J. M., Pieters, C. M., 1990. Extraction of Compositional Information from Olivine Reflectance Spectra: A New Capability for Lunar Exploration. 21st Lunar and Planetary Science Conference Houston, TX, USA.

Sunshine, J. M., Pieters, C. M., Pratt, S. F., 1990. Deconvolution of Mineral Absorption Bands: An Improved Approach. J. Geophys. Res. 95, B5, 6955-6966.

Tanaka, K. L., 1986. The Stratigraphy of Mars. J. Geophys. Res. 91, B13, E139-E158.

Tanaka, K. L., 2005. Geology and insolation-driven climatic history of Amazonian north polar materials on Mars. Nature 437, 7061, 991-994.

Tanaka, K. L., Rodriguez, J. A. P., Skinner Jr, J. A., Bourke, M. C., Fortezzo, C. M., Herkenhoff, K. E., Kolb, E. J., Okubo, C. H., 2008. North polar region of Mars: Advances in stratigraphy, structure, and erosional modification. Icarus 196, 2, 318-358.

Tanaka, K. L., Scott, D. H., Greeley, R., 1992. Global Stratigraphy. in: H. H. Kieffer, *et al.*, (Eds.), Mars. University of Arizona Press, Tuscon, 345-382.

Tera, F., Papanastassiou, D. A., Wasserburg, G. J., 1974. Isotopic evidence for a terminal lunar cataclysm. Earth Planet. Sci. Lett. 22, 1, 1-21.

Tosca, N. J., McLennan, S. M., 2006. Chemical divides and evaporite assemblages on Mars. Earth Planet. Sci. Lett. 241, 1-2, 21-31.

Tosca, N. J., McLennan, S. M., Clark, B. C., Grotzinger, J. P., Hurowitz, J. A., Knoll, A. H., Schröder, C., Squyres, S. W., 2005. Geochemical modeling of evaporation processes on Mars: Insight from the sedimentary record at Meridiani Planum. Earth Planet. Sci. Lett. 240, 122-148.

Tosca, N. J., McLennan, S. M., Dyar, M. D., Sklute, E. C., Michel, F. M., 2008a. Fe oxidation processes at Meridiani Planum and implications for secondary Fe mineralogy on Mars. J. Geophys. Res. (Planets) 113, 05005.

Tosca, N. J., McLennan, S. M., Lindsley, D. H., Schoonen, M. A. A., 2004. Acid-sulfate weathering of synthetic Martian basalt: The acid fog model revisited. J. Geophys. Res. (Planets) 109, 05003.

Tosca, N. J., Milliken, R. E., Michel, F. M., 2008b. Smectite Formation on Early Mars: Experimental Constraints. LPI Contributions 1441, 77-78.

Toulmin, P., III, Baird, A. K., Clark, B. C., Keil, K., Rose, H. J., Jr., Christian, R. P., Evans, P. H., Kelliher, W. C., 1977. Geochemical and Mineralogical Interpretation of the Viking Inorganic Chemical Results. J. Geophys. Res. 82, 28, 4625-4634.

Triantafyllidis, S., Skarpelis, N., 2006. Mineral formation in an acid pit lake from a high-sulfidation ore deposit: Kirki, NE Greece. J. Geochem. Explor. 88, 1-3, 68-71.

Tucker, M. E., 1985. Einführung in die Sedimentpetrologie, Enke Verlag, Stuttgart.

van Gasselt, S., 2007. Cold-Climate Landforms on Mars. 272, Dissertation, Freie Universität Berlin, Berlin.

Védie, E., Costard, F., Font, M., Lagarde, J. L., 2008. Laboratory simulations of Martian gullies on sand dunes. Geophys. Res. Lett. 35, 21, L21501.

Wagner, C., Schade, U., 1996. Measurements and Calculations for Estimating the Spectrometric Detection Limit for Carbonates in Martian Soil. Icarus 123, 256-268.

Walter, S., Gasselt, S. V., Michael, G., Neukum, G., 2006. Footprint Representation of Planetary Remote Sensing Data European Planetary Science Congress Berlin.

Weitz, C. M., Lane, M. D., Staid, M., Dobrea, E. N., 2008. Gray hematite distribution and formation in Ophir and Candor chasmata. J. Geophys. Res. (Planets) 113, 02016.

Weitz, C. M., Milliken, R. E., Grant, J. A., McEwen, A. S., Williams, R. M. E., Bishop, J. L., Thomson, B. J., 2010. Mars Reconnaissance Orbiter observations of light-toned layered deposits and associated fluvial landforms on the plateaus adjacent to Valles Marineris. Icarus 205, 73-102.

Wendt, L., Combe, J.-P., McGuire, P. C., Bishop, J. L., Neukum, G., 2009, Linear spectral unmixing of near-infrared hyperspectral data from Juventae Chasma, Mars. in: L. Bruzzone, *et al.*, Image and Signal Processing for Remote Sensing XV. SPIE, Berlin, Germany.

Wendt, L., Combe, J. P., McCord, T. B., Neukum, G., 2008. Mapping of Martian Surface Units using HRSC Color Data. 39th Lunar and Planetary Science Conference League City, TX, USA.

Wendt, L., Gross, C., Kneissl, T., Sowe, M., Combe, J.-P., Ledeit, L., McGuire, P. C., Neukum, G., 2011. Sulfates and iron oxides in Ophir Chasma, Mars, based on OMEGA and CRISM observations. Icarus 213, 86-103.

Werner, S. C., 2005. Major Aspects of the Chronostratigraphy and Geologic Evolutionary History of Mars. Dissertation, Freie Universität Berlin, Berlin.

White, A. F., 1984. Weathering characteristics of natural glass and influences on associated water chemistry. J. Non-Cryst. Solids 67, 1-3, 225-244.

Williams, D. A., Greeley, R., Fergason, R. L., Kuzmin, R., McCord, T. B., Combe, J.-P., Head, J. W., Xiao, L., Manfredi, L., Poulet, F. o., Pinet, P., Baratoux, D., Plaut, J. J., Raitala, J., Neukum, G., the HRSC Co-Investigator Team, 2009. The Circum-Hellas Volcanic Province, Mars: Overview. Planet. Space Sci. 57, 895-916.

Wilson, L., Head, J. W., III, 2002. Tharsis-radial graben systems as the surface manifestation of plume-related dike intrusion complexes: Models and implications. J. Geophys. Res. 107, E8, 5057, 10.1029/2001JE001593

Winter, M. E., Shen, S. S., 1999, N-FINDR: an algorithm for fast autonomous spectral end-member determination in hyperspectral data. in: M. R. Descour, S. S. Shen, Imaging Spectrometry V. SPIE.

Wray, J. J., Murchie, S. L., Squyres, S. W., Seelos, F. P., Tornabene, L. L., 2009. Diverse aqueous environments on ancient Mars revealed in the southern highlands. Geology 37, 11, 1043-1046.

Wyatt, M. B., McSween, H. Y., 2002. Spectral evidence for weathered basalt as an alternative to andesite in the northern lowlands of Mars. Nature 417, 6886, 263-266.

Yanai, K., 1997. General view of twelve martian meteorites. Mineralogical Journal 19, 2, 65-74.

Zegers, T. E., Dabekaussen, W., Hauber, E., Gwinner, K., Scholten, F., Fueten, F., Stesky, R., MacKinnon, P., Neukum, G., the HRSC Co-Investigator Team, 2006, 3D Structural Analysis of Ophir Chasma Based on HRSC Image Data and Stereo-derived DTM. 37th Lunar and Planetary Science Conference, League City, TX, USA, 1605.

Zorzano, M. P., Mateo-Martí, E., Prieto-Ballesteros, O., Osuna, S., Renno, N., 2009. Stability of liquid saline water on present day Mars. Geophys. Res. Lett. 36.

Zurek, R. W., Smrekar, S. E., 2007. An overview of the Mars Reconnaissance Orbiter (MRO) science mission. J. Geophys. Res. 112, E5, E05S01.

Appendix

Selected Summary Parameters

Name	Parameter	Formulation	Rationale
BD530	0.53 µm band depth	1-(R530/(a*R709+b*R440))	Ferric minerals, especially nanophase ferric oxide and hematite
OLINDEX	Olivine index	(R1695/(0.1*R1050+ 0.1*R1210+0.4*R1330+0.4*R1470)) - 1	Olivine and Fe-containing phyllosilicate
LCPINDEX	Low-Ca pyroxene index	((R1330 - R1050)/(R1330 + R1050))*((R1330-R1815)/(R1330 + R1815)	Pyroxene, favoring low-Ca pyroxene
HCPINDEX	High-Ca pyroxene index	((R1470 - R1050)/(R1470 + R1050)) *((R1470 - R2067)/(R1470 + R2067)	Pyroxene, favoring high-Ca pyroxene
BD1900	1.9 micron H2O band depth	1 - (((R1930 + R1985)*0.5) /(a*R1875 + b*R2067)	Bound H2O in most minerals
BD2210	2.21 micron Al-OH band depth	1-(R2210/(a*R2140+b*R2250))	Al-OH and Si-OH bonds in glass and phyllosilicates
D2300	2.3 micron drop-off	1-(R2290+R2330 + R2330) /(R2140 + R2170 + R2210)	Mg-OH and Fe-OH bonds in phyllosilicate
SINDEX	Detects convexity at 2.29 mm due to absorptions at 1.9– 2.1, 2.4 mm	1-(R2100 + R2400) /(2*R2290)	Hydrated minerals

Values beginning with R are used to represent atmospherically and photometrically corrected I/F at given wavelength in nanometers. From Murchie *et al.*, 2009b.

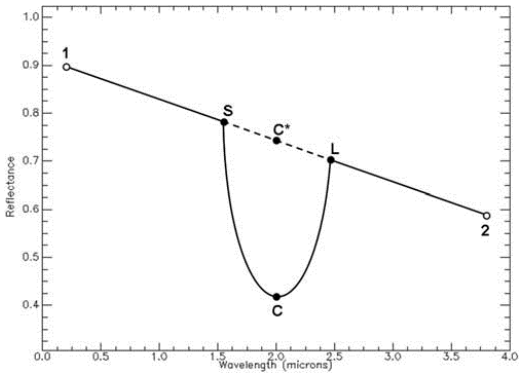

An idealized spectral absorption band centered at wavelength λC superimposed on a sloped continuum. The band depth is calculated as 1-RC/RC*. RC is the reflectance at the defined center of the absorption band. The value of RC* is calculated from the continuum and is equal to a*RS+b*RL, where a=1-b and b=(λC-λS)/(λL-λS). From Pelkey et al., 2007.

table 0-1: Absorption band positions for selected sulfates

Mineral Formula	Electronic transition feature due to Fe^{3+}	Crystal field transition due to Fe^{2+}	OH stretching overtones (1.4 µm region)	H_2O overtones/combinations (1.4 µm region)	$OH/H_2O/SO_4$ combinations/overtones (1.7-1.8 µm region)	H_2O combinations (1.9 µm region)	$OH/H_2O/SO_4$ combinations/overtones (2.0-2.7 µm region)
Szomolnokite $[Fe^{2+}(SO_4)(H_2O)]$		~0.9				1.98	2.10[d], 2.41[c], 2.55
Kieserite $[Mg(SO_4)(H_2O)]$				1.461, 1.53[a]	1.75[d]	1.974, 2.06	2.13, 2.42, 2.55
Gypsum $[CaSO_4(H_2O)_2]$				1.39[a], 1.449, 1.488, 1.534	1.751, 1.78[a]	1.944, 1.97[a]	2.17, 2.22, 2.28, 2.43[a], 2.48, 2.55[a]
Romerite $[Fe^{3+}(SO_4)2(H_2O)_4]2[Fe^{2+}(H_2O)_6]$	-	~0.947[b], ~1.17			1.75[a,c]	2.0[a]	2.10, 2.40, 2.60
Rozenite $[Fe^{2+}(SO_4)(H_2O)_4]$		~0.92[b], ~1.17		1.450, 1.5[a]	1.75[c]	1.95, 1.98	2.44[a], 2.53
Melanterite $FeSO_4*7H_2O$		~0.92[b], ~1.17					
Copiapite $[Fe^{3+}2\ (OH)(H_2O)4(SO_4)_3]2\{Fe^{2+}(H_2O)_6\}(H_2O)_6$	0.430, 0.55[a], 0.855–0.866	0.9?[c], 1.17?[c]	1.36	1.452, 1.48[a]	1.78[a,c]	1.940, 2.0[a]	2.42a, 2.47a, 2.53
Coquimbite $[Fe^{3+}3\ (SO4)_6(H2O)_6]\{Fe^{3+}(H_2O)_6\}(H_2O)_6$	0.423-0.433, 0.553-0.558, 0.774-0.775			1.412, 1.48	1.75[a,c]	1.911, 1.984	2.1[a], 2.55[a]
Ferricopiapite $[Fe^{3+}2(OH)(H_2O)4(SO_4)_3]2\{(Fe^{3+}_{0.67/0.33})(H_2O)_6\}(H_2O)_6$	0.431, 0.55, 0.860-0.873			1.453, 1.5[d]	1.78[a,c]	1.943, 1.98	2.41[a], 2.46[a], 2.55[a]
Hexahydrite $\{Mg(H_2O)_6\}(SO_4)$				1.441, 1.46[a]	1.75[c]	1.938, 1.97[a]	2.45[a], 2.54[a]
Jarosite $K[Fe^{3+}\ 3(OH)_6(SO_4)_2]$	0.43–0.436, 0.5[a], 0.63[a], 0.915–0.922		1.465-1.468, 1.51-1.52		1.84-1.85		2.08[a], 2.21, 2.27, 2.30, 2.41, 2.46, 2.51, 2.59, 2.61
Natrojarosite $Na[Fe^{3+}\ 3\ (OH)_6(SO_4)_2]$	0.43–0.434, 0.5[a], 0.63[a], 0.914–0.919		1.477-1.48, 1.541-1.546				2.07[a], 2.23, 2.27, 2.30[c], 2.42, 2.46, 2.52, 2.61
H_3O-Jarosite $(H_3O)[Fe^{3+}\ 3\ (OH)_6(SO_4)_2]$	0.43, 0.68, 0.895					1.93[d]	2.28[d], 2.45[a,c], 2.6[a,c]

() and {}denote polyhedron groups, [] denote linked polyhedra. [a] shoulder, approx. band position. [b] Band due to Fe^{2+} or Fe^{3+}. [c] weak band. [d] broad band, approx. band position. From Cloutis *et al.*, 2006.

Curriculum Vitae

Der Lebenslauf ist aus Datenschutzgründen in der Online-Version nicht enthalten.

Publications

peer-reviewed articles

Wendt, L., Bishop, J.L., Neukum, G., **2012**. Knob fields in the Terra Cimmeria/Terra Sirenum Region of Mars: Stratigraphy, Mineralogy, Morphology. submitted to Icarus.

Sowe, M., **Wendt, L.,** McGuire, P. C., Neukum, G. **2011.** Hydrated minerals in the deposits of Aureum Chaos. Icarus, 218, 406-419.

Wendt, L., Gross, C., Kneissl, T., Sowe, M., Combe, J.-P., Le Deit, L., McGuire, P. C., Neukum, G., **2011**. Sulfates and iron oxides in Ophir Chasma, Mars, based on OMEGA and CRISM observations. Icarus 213, 86-103.

Roush, T. L., Marzo, G. A., Fonti, S., Orofino, V., Blanco, A., Gross, C., **Wendt, L., 2011**. Assessing spectral evidence of aqueous activity in two putative martian paleolakes. Icarus 214, 240-245.

Foing, B. H., Stoker, C., Zavaleta, J., Ehrenfreund, P., Thiel, C., Sarrazin, P., Blake, D., Page, J., Pletser, V., Hendrikse, J., Direito, S., Kotler, J. M., Martins, Z., Orzechowska, G., Gross, C., **Wendt, L**., Clarke, J., Borst, A. M., Peters, S. T. M., Wilhelm, M. B., Davies, G. R., Davies, **2011**. Field astrobiology research in Moon-Mars analogue environments: instruments and methods. International Journal of Astrobiology 10, 141-160.

McGuire, P. C., Gross, C., **Wendt, L**., Bonnici, A., Souza-Egipsy, V., Ormö, J., Díaz-Martínez, E., Foing, B. H., Bose, R., Walter, S., Oesker, M., Ontrup, J., Haschke, R., Ritter, H., **2010**. The Cyborg Astrobiologist: testing a novelty detection algorithm on two mobile exploration systems at Rivas Vaciamadrid in Spain and at the Mars Desert Research Station in Utah. International Journal of Astrobiology 9, 11-27.

McGuire, P. C., Bishop, J. L., Brown, A. J., Fraeman, A. A., Marzo, G. A., Frank Morgan, M., Murchie, S. L., Mustard, J. F., Parente, M., Pelkey, S. M., Roush, T. L., Seelos, F. P., Smith, M. D., **Wendt, L.,** Wolff, M. J., **2009**. An improvement to the volcano-scan algorithm for atmospheric correction of CRISM and OMEGA spectral data. Planet. Space Sci. 57, 809-815.

conference proceedings

Wendt, L., Combe, J.-P., McGuire, P. C., Bishop, J. L., Neukum, G., **2009**. Linear spectral unmixing of near-infrared hyperspectral data from Juventae Chasma, *Mars*. In: Image and Signal Processing for Remote Sensing XV, edited by Bruzzone, L., Notarnicola, C., Posa, F., Proceedings of SPIE Vol. 7477, #7747A-21.

selected conference abstracts

Al-Samir, M., van Berk, W., Kneissl, T., van Gasselt, S., Gross, C., **Wendt, L**., Jaumann, R., **2012**. A Model Scenario for Kieserite-Dominated Evaporites in Juventae Chasma, Mars. Lunar. Planet Sci 43, The Woodlands, Texas.

Gross, C., **Wendt, L**., Combe, J.-Ph., Jodlowski, P., Marzo, G.A., Roush, T.L., McCord, T., Halbach, P., Neukum, G., **2012**. Investigating the Phyllosilicate Bearing Micoud Crater in the Northern Plains of Mars. Lunar Planet Sci. 43. The Woodlands, Texas.

Gross, C., Sowe, M., **Wendt, L.,** Bishop, J.L., Fairén, A.G., **2012**. Phyllosilicates in Bamberg Crater, Mars. Lunar Planet Sci. 43. The Woodlands, Texas.

Wendt, L., Bishop, J.L., Neukum, G. **2012**, Knob fields in the Terra Cimmeria/Terra Sirenum Region of Mars: Stratigraphy, Mineralogy, Morphology. Lunar Planet Sci. 43, The Woodlands, Texas.

Wendt, L., Gross, C., Kneissl, T., Sowe, M., Combe, J. P., Le Deit, L., McGuire, P. C., Neukum, G., **2011.** Mineralogy and Stratigraphy of Sulfates and Ferric Oxides in Ophir Chasma, Mars. Lunar Planet. Sci. 42, Woodlands, Texas.

Gross, C., **Wendt, L.,** Combe, J. P., Jodlowski, P., Marzo, G. A., Roush, T. L., McCord, T., Halbach, P., Neukum, G., **2011**. Investigation on a Pyllosilicate-Bearing Crater in the Northern Plains of Mars. Lunar Planet. Sci. 42. The Woodlands, Texas.

Jodlowski, P., Gross, C., **Wendt, L.,** Halbach, P., Neukum, G., **2011**. Geologic/Geomorphologic Mapping of a Complex Impact Crater in the Northern Plains of Mars. Lunar Planet. Sci. 42. Woodlands, Texas.

Roush, T. L., Marzo, G. A., Fonti, S., Orofino, V., Blanco, A., Gross, C., **Wendt, L**., **2011**. Assessing Spectral Evidence of Aqueous Activity in Two Putative Martian Paleolakes. Lunar Planet. Sci. 42, Woodlands, Texas.

Wendt, L., Gross, C., Kneissl, T., Sowe, M., Combe, J. P., Le Deit, L., McGuire, P. C., Neukum, G., **2010**. Sulfates and Iron Oxides in Ophir Chasma, Mars. Lunar Planet. Sci. 41. Woodlands, Texas.

Sowe, M., **Wendt, L.,** Kneissl, T., McGuire, P. C., Neukum, G., **2010**. Hydrated Minerals in Aureum Chaos, Mars. Lunar Planet. Sci. 41, Woodlands, Texas.

Gross, C., **Wendt, L.,** McGuire, P. C., Bonnici, A., Foing, B. H., Souza-Egipsy, V., Bose, R., Walter, S., Ormö, J., Díaz-Martínez, E., Oesker, M., Ontrup, J., Haschke, R., Ritter, H., **2010**. The Cyborg Astrobiologist: Testing a Novelty Detection Algorithm at the Mars Desert Research Station (MDRS), Utah. Lunar Planet. Sci. 41. Woodlands, Texas.

Basilevsky, A. T., Neukum, G., Werner, S. C., Dumke, A., van Gasselt, S., Kneissl, T., Zuschneid, W., Rommel, D., **Wendt, L.**, Chapman, M., Head, J. W., Greeley, R., **2009**. Episodes of floods in Mangala Valles, Mars, from the analysis of HRSC, MOC and THEMIS images. Planet. Space Sci. 57, 917-943.

Gross, C., **Wendt, L.,** Dumke, A., Neukum, G., **2009**. Episodic Floodings at Maja Valles and Juventae Chasma. European Planetary Science Congress 2009, Potsdam.

Wendt, L., Gross, C., McGuire, P. C., Combe, J. P., Neukum, G., **2009**. Analysis of Juventae Chasma Sulfate Mound B using the Multiple-Endmember Linear Spectral Unmixing Model (MELSUM) on CRISM Data. Lunar Planet. Sci. 40, Woodlands, Texas.

Wendt, L., Gross, C., McGuire, P. C., Combe, J. P., Neukum, G., **2009**. Analyzing CRISM Data from mound B in Juventae Chasma, Mars, with the Multiple-Endmember Linear Spectral Unmixing Model MELSUM. EGU General Assembly 2009, 2009 in Vienna, Austria.

Wendt, L., Mahapatra, P., Gross, C., Borst, A., Foing, B. H., Exogeolab, T., Eurogeomars, T., **2009**. Raman investigations of the EuroGeoMars Campaign. European Planetary Science Congress 2009, Potsdam.

Wendt, L., Combe, J. P., McCord, T. B., Neukum, G., **2008**. Mapping of Martian Surface Units using HRSC Color Data. Lunar Planet. Sci. 38, League City, Texas.